Etude de l'amortissement piézoélectrique shunté appliqué aux roues aubagées désaccordées

Biao Zhou

Numéro d'ordre: 2012-55 Année 2008

MÉMOIRE DE THÈSE

PRÉSENTÉ POUR OBTENIR LE TITRE DE

DOCTEUR

DE L'ÉCOLE CENTRALE DE LYON

SPÉCIALITÉ: MÉCANIQUE

ÉCOLE DOCTORALE DE MÉCANIQUE DE LYON

(UCBL/INSA/ECL)

PAR

Biao ZHOU

ÉTUDE DE L'AMORTISSEMENT PIÉZOÉLECTRIQUE SHUNTÉ APPLIQUÉ AUX ROUES AUBAGÉES DÉSACCORDÉES

Soutenu publiquement le 7 décembre 2012,

devant le jury d'examen

F. LEBOEUF, Professeur, École Centrale de Lyon,	Examinateur
L. PANNING-VON SCHEIDT, Professeur, Universität Hannover,	Rapporteur
G. KERSCHEN, Professeur, Université de Liège,	Rapporteur
L. LI, Professeur, Beijing University of Aeronautics & Astronautics,	Examinateur
M. GRUIN, Ingénieur, SNECMA,	Examinateur
F. THOUVEREZ, Professeur, École Centrale de Lyon,	Directeur de thèse
D. LENOIR, Ingénieur de Recherche, École Centrale de Lyon,	Co-directeur de thèse

THESIS

SUBMITTED FOR THE DEGREE OF

DOCTOR OF PHILOSOPHY

OF ÉCOLE CENTRALE DE LYON

SPECIALITY: MECHANICAL ENGINEERING

ÉCOLE DOCTORALE DE MÉCANIQUE DE LYON

(UCBL/INSA/ECL)

BY

Biao ZHOU

STUDY OF PIEZOELECTRIC SHUNT DAMPING APPLIED TO MISTUNED BLADED DISKS

Defended publicly on 7 december 2012

Doctoral Committee

F. LEBOEUF, Professor, École Centrale de Lyon,	Examiner
L. PANNING-VON SCHEIDT, Professor, Universität Hannover,	Reviewer
G. KERSCHEN, Professor, Université de Liège,	Reviewer
L. LI, Professor, Beijing University of Aeronautics & Astronautics,	Examiner
M. GRUIN, Engineer, SNECMA,	Examiner
F. THOUVEREZ, Professor, École Centrale de Lyon,	Thesis supervisor
D. LENOIR, Research Engineer, École Centrale de Lyon,	Thesis co-supervisor

ÉCOLE CENTRALE LYON **Direction de la recherche**

Liste des personnes Habilitées à Diriger des Recherches en poste à l'Ecole Centrale de Lyon

Nom-Prénom	*Corps grade*	Laboratoire ou à défaut département ECL	Etablissement
BEROUAL Abderrahmane	*professeur*	AMPERE	ECL
BURET François	*professeur*	AMPERE	ECL
JAFFREZIC-RENAULT Nicole	*directeur de recherche*	AMPERE	CNRS/ECL
KRÄHENBÜHL Laurent	*directeur de recherche*	AMPERE	CNRS/ECL
NICOLAS Alain	*professeur*	AMPERE	ECL
NICOLAS Laurent	*directeur de recherche*	AMPERE	CNRS/ECL
SCORLETTI Gérard	*professeur*	AMPERE	ECL
SIMONET Pascal	*directeur de recherche*	AMPERE	CNRS/ECL
VOLLAIRE Christian	*professeur*	AMPERE	ECL
		Nbre Ampère 9	
HELLOUIN Yves	*maître de conférences*	DER EEA	ECL
		Nbre DER EEA 1	
GUIRALDENQ Pierre	*professeur émérite*	DER STMS	ECL
VINCENT Léo	*professeur*	DER STMS	ECL
		Nbre DER STMS 2	
LOHEAC Jean-Pierre	*maître de conférences*	ICJ	ECL
MAITRE Jean-François	*professeur émérite*	ICJ	ECL
MARION Martine	*professeur*	ICJ	ECL
MIRONESCU Elisabeth	*professeur*	ICJ	ECL
MOUSSAOUI Mohand	*professeur*	ICJ	ECL
MUSY François	*maître de conférences*	ICJ	ECL
ZINE Abdel-Malek	*maître de conférences*	ICJ	ECL
		Nbre ICJ 7	
CALLARD Anne-Ségolène	*professeur*	INL	ECL
CLOAREC Jean-Pierre	*maître de conférences*	INL	ECL
GAFFIOT Frédéric	*professeur*	INL	ECL
GAGNAIRE Alain	*maître de conférences*	INL	ECL
GARRIGUES Michel	*directeur de recherche*	INL	CNRS/ECL
GENDRY Michel	*directeur de recherche*	INL	CNRS/ECL
GRENET Geneviève	*directeur de recherche*	INL	CNRS/ECL
HOLLINGER Guy	*directeur de recherche*	INL	CNRS/ECL
KRAWCZYK Stanislas	*directeur de recherche*	INL	CNRS/ECL
LETARTRE Xavier	*chargé de recherche*	INL	CNRS/ECL
O'CONNOR Ian	*professeur*	INL	ECL
PHANER-GOUTORBE Magali	*professeur*	INL	ECL
ROBACH Yves	*professeur*	INL	ECL
SAINT-GIRONS Guillaume	*chargé de recherche*	INL	CNRS/ECL
SEASSAL Christian	*directeur de recherche*	INL	CNRS/ECL

SOUTEYRAND Eliane	*directeur de recherche*	INL	CNRS/ECL
TARDY Jacques	*directeur de recherche*	INL	CNRS/ECL
VIKTOROVITCH Pierre	*directeur de recherche*	INL	CNRS/ECL

Nbre INL 18

CHEN Liming	*professeur*	LIRIS	ECL
DAVID Bertrand	*professeur*	LIRIS	ECL

Nbre LIRIS 2

BAILLY Christophe	*professeur*	LMFA	ECL
BERTOGLIO Jean-Pierre	*directeur de recherche*	LMFA	CNRS/ECL
BLANC-BENON Philippe	*directeur de recherche*	LMFA	CNRS/ECL
BOGEY Christophe	*chargé de recherche*	LMFA	CNRS/ECL
CAMBON Claude	*directeur de recherche*	LMFA	CNRS/ECL
CARRIERE Philippe	*directeur de recherche*	LMFA	CNRS/ECL
CHAMPOUSSIN J-Claude	*professeur émérite*	LMFA	ECL
COMTE-BELLOT geneviève	*professeur émérite*	LMFA	ECL
FERRAND Pascal	*directeur de recherche*	LMFA	CNRS/ECL
GALLAND Marie-Annick	*professeur*	LMFA	ECL
GODEFERD Fabien	*directeur de recherche*	LMFA	CNRS/ECL
GOROKHOVSKI Mikhail	*professeur*	LMFA	ECL
HENRY Daniel	*directeur de recherche*	LMFA	CNRS/ECL
JEANDEL Denis	*professeur*	LMFA	ECL
JUVE Daniel	*professeur*	LMFA	ECL
LE RIBAULT Catherine	*chargée de recherche*	LMFA	CNRS/ECL
LEBOEUF Francis	*professeur*	LMFA	ECL
PERKINS Richard	*professeur*	LMFA	ECL
ROGER Michel	*professeur*	LMFA	ECL
SCOTT Julian	*professeur*	LMFA	ECL
SHAO Liang	*directeur de recherche*	LMFA	CNRS/ECL
SIMOENS Serge	*chargé de recherche*	LMFA	CNRS/ECL
TREBINJAC Isabelle	*maître de conférences*	LMFA	ECL

Nbre LMFA 23

BENAYOUN Stéphane	*professeur*	LTDS	ECL
CAMBOU Bernard	*professeur*	LTDS	ECL
COQUILLET Bernard	*maître de conférences*	LTDS	ECL
DANESCU Alexandre	*maître de conférences*	LTDS	ECL
FOUVRY Siegfrid	*chargé de recherche*	LTDS	CNRS/ECL
GEORGES Jean-Marie	*professeur émérite*	LTDS	ECL
GUERRET Chrystelle	*chargé de recherche*	LTDS	CNRS/ECL
HERTZ Dominique	*past*	LTDS	ECL
ICHCHOU Mohamed	*professeur*	LTDS	ECL
JEZEQUEL Louis	*professeur*	LTDS	ECL
JUVE Denyse	*ingénieur de recherche*	LTDS	ECL
KAPSA Philippe	*directeur de recherche*	LTDS	CNRS/ECL
LE BOT Alain	*directeur de recherche*	LTDS	CNRS/ECL
LOUBET Jean-Luc	*directeur de recherche*	LTDS	CNRS/ECL
MARTIN Jean-Michel	*professeur*	LTDS	ECL
MATHIA Thomas	*directeur de recherche*	LTDS	CNRS/ECL
MAZUYER Denis	*professeur*	LTDS	ECL
PERRET-LIAUDET Joël	*maître de conférences*	LTDS	ECL
SALVIA Michelle	*maître de conférences*	LTDS	ECL
SIDOROFF François	*professeur*	LTDS	ECL
SINOU Jean-Jacques	*professeur*	LTDS	ECL
STREMSDOERFER Guy	*professeur*	LTDS	ECL

THOUVEREZ Fabrice	*professeur*	LTDS	ECL
TREHEUX Daniel	*professeur*	LTDS	ECL
VINCENS Eric	*maître de conférences*	LTDS	ECL
		Nbre LTDS 25	
	Total HdR ECL	91	

Acknowledgements

I would like to express appreciation to those who have helped me through my doctoral studies. First of all, my most sincere gratitude goes to my supervisor Prof. Fabrice Thouverez and co-supervisor, Mr. David Lenoir, with whom it is my honor to work. It is them that gave me this unique opportunity to experience research in France. There is no doubt that this is one of the most exciting journeys in my life. I gratefully acknowledge their keen insights and clear guidance, as well as their patience, leading to a good completion of my doctoral life.

I am pleased to acknowledge my colleagues in the D2S group. Special acknowledge is given to Aurelien Grolet and Emmanuelle Sarrouy for their helpful scientific discussion and friendly support. I really appreciate the companion of other chinese colleagues: Tianli Huang, Kai Zhang and Changwei Zhou in this laboratory.

I am grateful to Prof. Francis Leboeuf, who has honored me as the president of doctoral committee. I would like to also thank Prof. Lars Panning-von Scheidt, Prof. Gaëtan Kerschen, Prof. Lin Li and Miss Marion Gruin for their review work of my thesis and presence in my defence.

Finally, I would like to deeply express my love and gratitude to my parents, my brother and Rong Li, who are always being there for me. Their understanding has encouraged me throughout my PhD.

Thanks go to the Ecole Centrale de Lyon and Chinese Scholarship Council for their financial supports on this research project.

Abstract

This study deals with piezoelectric shunt damping in the mistuned bladed disks. Bladed disks are rich dynamical systems that are known to suffer from severe vibration problems. Blade mistuning is an issue of major concern since it is responsible for high cycle fatigue and failure risks. In the mitigation practice, additional damping is usually introduced into the structure to reduce vibration amplitudes. Here, we are interested in piezoelectric shunt damping applied into mistuned bladed disks.

In our proposed damping strategy, shunted piezoelectrics are attached onto the disk surface between adjacent blades in order to dissipate the disk mechanical energy. Consequently the blade vibration can be reduced due to the blade-disk coupling. This strategy is of engineering interest since piezoelectric transducers are placed outside of the main stream in turbomachinery. This idea is developed based on a lumped-parameter bladed disk model. Resonant shunt circuits are adopted. Both piezoelectric shunt damping and optimized piezoelectric mistuning are introduced to minimize the blade mistuning effect. Piezoelectric mistuning can be seen as a kind of damping mistuning; it is modeled as a small variation of the inductance value of each shunt circuit.

In reality the blade mistuning pattern is not constant in the long run. Due to various complexities, a perturbation of the blade mistuning pattern might result. In benefitting from the manageability and controllability of piezoelectric shunt circuits, an adaptive control strategy is developed to adjust the optimal piezoelectric mistuning pattern according to the perturbation. Numerical simulations reveal that a fine

performance is achieved in terms of reducing the blade vibration of slowly time-variant, mistuned bladed disks.

An essentially nonlinear piezoelectric shunt circuit is proposed as practical realization of nonlinear energy sink (NES). This piezoelectric-based NES is featured by nonexistence of preferential resonant frequency. It is therefore able to act in essence, as a passive, adaptive, broadband vibration absorber, when integrated into a mechanical structure. A variable-coefficient harmonic balance method for quasi-periodic responses is devised. It helps gain insights into the complex dynamics of forced response when the coupled electromechanical system is under harmonic external forcing.

The appealing property of the piezoelectric-based NES enables it especially suitable for applications in mistuned bladed disks since it is capable of adaptively interacting with each sector of mistuned bladed disks in a broadband fashion. Promising results obtained in the numerical studies further demonstrate this viewpoint.

Key words: piezoelectric shunt damping, blade mistuning, adaptive control, nonlinear energy sink.

Résumé

Ce travail porte sur l'étude d'amortissement piézoélectrique shunté pour les roues aubagées désaccordées de turbomachines. Les problèmes vibratoires sont de première importance pour les motoristes aéronautiques et, parmi ceux-ci, les vibrations causées par le désaccordage des aubes tiennent une place importante puisqu'elles sont à l'origine des phénomènes de fatigue oligocyclique et des risques de défaillance associés. L'usage de technologies d'amortissement est donc assez répandu pour réduire l'amplitude vibratoire. Ici, on s'intéresse à l'étude de l'amortissement piézoélectrique shunté appliqué aux roues aubagées désaccordées.

Dans notre stratégie, des patchs piézoélectriques shuntés sont attachés sur la surface de la roue entre les aubes adjacentes afin de dissiper l'énergie mécanique de la roue. Par conséquent, l'amplitude des aubes peut être réduite du fait du couplage entre les aubes et la roue. Cette stratégie est d'intérêt pour l'ingénieur car les transducteurs piézoélectriques sont placés en dehors du flux principal des turbomachines. Un modèle numérique a été développé intégrant des circuits piézoélectriques shuntés résonnants. L'amortissement piézoélectrique shunté et un motif optimisé de désaccordage piézoélectrique sont tous les deux introduits afin de minimiser l'effet du désaccordage des aubes.

En pratique, le désaccordage des aubes change au cours de la vie du moteur. Les raisons peuvent être multiple comme l'usure, des endommagement par impacts qui vont conduire inévitablement à une évolution du motif du désaccordage. En s'appuyant sur la stratégie de contrôle adaptatif, nous avont proposé un shunt piézoélectrique resonant capable de suivre l'évolution de la structure au cours du temps. Les simulations numériques montrent qu'une bonne efficacité

est obtenue en termes de réduction des vibrations de roues aubagées désaccordées.

Dans cette thèse, une dernière stratégie est proposée qui correspond à la mise en place d'un système de pompage énergetique nonlinéaire basé sur les élements piézoélectriques. Une fois intégrées dans une structure mécanique, il est donc en mesure d'agir en tant qu'amortisseur de vibrations, adaptatif et large bande. Une méthode numérique, à *coefficient variables de balance harmonique*, a été développée afin de calculer les réponses quasi-périodiques associés à ce type de problème.

Ce dispositif de pompage énergetique piézoélectrique semble particulièrement intéressant dans le cadre des roues aubagées désaccordées, car il est capable d'interagir de façon adaptative avec chaque secteur de la roue désaccordé. Des résultats prometteurs ont été obtenus et illustrent démontrent ce point de vue.

Mots clés: amortissement piézoélectrique shunté, roues aubagées, désaccordage, contrôle adaptatif, pompage énergetique nonlinéaire.

Contents

Introduction

Bladed disk structures are used in a number of propulsion and power generation applications. Bladed disks, as the name implies, consists of a central circular disk surrounded by blades. A bladed disk is featured by cyclic symmetry in the design phase. The structure can be divided into a number of identical substructures or sectors, which are arranged symmetrically around the central axis. In practice, however, the sectors are never perfectly identical due to manufacturing tolerances, material defects, and uneven wear in the operation. The small discrepancies between sectors are known as *mistuning*. It is well known that mistuning has a profound effect on the dynamic behavior of the bladed disk structure.

Vibration in mistuned bladed disks has received significant attention from the academic and industrial community in the last decades. In general, various research efforts in this domain can naturally fall into three categories.

The first category concerns the comprehensive understanding of the mistuning mechanism. Early research efforts on the phenomenological aspects of blade mistuning have been conducted in the area of structural dynamics. In fact, the subject matter is an interdisciplinary one requiring expertise in aerodynamics of cascades as well as structural dynamics of bladed disk assemblies leading to aeroelasticity of blades. The current trend is to include effects either previously absent or ignored from the early mistuned bladed disk analyses. For example, specific features of the aerodynamic damping and aerocoupling are now taken into account in the modeling of mistuned bladed disks.

The second category is more methodological in the field of structural dynamics. These research works focus on both a better representation of modeling and reducing computational cost. Studies on this subject are often initially motivated by the request for phenomenological representation of mistuned bladed

disks. For example, nowadays, more and more investigations are performed on reduced-order models generating from large scale modern industrial finite element models of a full bladed disk. The reduced order models could reduce the computational models of the full bladed disk to manageable size, while retaining the model accuracy.

Finally, the last category focuses on blade vibration reduction. To this end, several schemes have emerged in the literature. One possibility is to act at the level of excitation to reduce their impact on the structure (e.g., symmetry breaking excitations). One can also optimize the distribution of vibrational energy in the mistuned bladed disks and accordingly limit vibration levels in critical areas (structural optimization, or intensional mistuning). In the mitigation practice, additional damping is usually introduced into the bladed disk. In this thesis, we will pay special attention to the *piezoelectric shunt damping* in mistuned bladed disks.

Thesis outline

This thesis is dedicated to applying piezoelectric shunt damping into bladed disks in order to suppress blade mistuning effects. Chapter 1 is devoted to introducing dynamics and vibration phenomenons in bladed disks. The modeling methodology of tuned bladed disks is then illustrated in taking advantage of cyclic symmetry property. Of particular interest is the vibration in mistuned bladed disks. A range of fundamental research issues are briefly presented.

In Chapter 2, conceptions of piezoelectric shunt damping are fully discussed. We present a detailed discussion on physical principles and constitutive models of piezoelectric materials and structures. The concept of piezoelectric shunt damping is illustrated when piezoelectric materials are connected with classical shunt circuits, i.e. the resistive shunt circuit and resonant shunt circuit. Recent advances in this area will be also covered in the end of this chapter.

We propose a new piezoelectric damping strategy especially suitable for blisks, i.e., using resonant shunted piezoelectrics solely attached onto the disk, in Chapter 3. Both the piezoelectric shunt damping and piezoelectric mistuning effect will be utilized to achieve a maximum blade vibration reduction. Piezoelectric

mistuning can be seen herein, to some extent, as a kind of damping mistuning; it is modeled as a small variation of the inductance value of each shunt circuit. More specifically, an optimal piezoelectric mistuning, obtained by genetic algorithm optimization, could be introduced into a bladed disk with a given blade mistuning to achieve further blade vibration mitigation.

Chapter 4 presents an adaptive control strategy based on the piezoelectric shunt technique. This adaptive control strategy has focused on more realistic cases where the blade mistuning pattern is slowly time-varying. By taking advantage of the controllability of piezoelectric shunt circuits, the piezoelectric mistuning pattern can be adjusted to keep "optimal" in terms of maintaining low blade vibration levels.

An essentially nonlinear piezoelectric shunt circuit is proposed in Chapter 5 as practical realization of nonlinear energy sink (NES). This piezoelectric-based NES is featured by nonexistence of preferential resonant frequency. It is therefore able to act in essence, as a passive, adaptive, broadband vibration absorber, when integrated into a mechanical structure. This appealing property enables it especially suitable for application in mistuned bladed disks.

In Chapter 6, essentially nonlinear piezoelectric shunt circuits are applied into mistuned bladed disks as an attempt. These essentially nonlinear shunt circuits are capable of adaptively interacting with each sector of mistuned bladed disks in a broadband fashion. Consequently, a sound damping performance can be expected.

Finally, main contributions of the research work presented in this thesis are summarized and a brief discussion on future directions for piezoelectric shunt damping in bladed disks is given at the end of this thesis.

Chapter 1

Dynamics of the bladed disk

This chapter is dedicated to introducing dynamics and vibration phenomenons in bladed disks. Following a general overview on the functional environment of bladed disks, excitation sources and principal blade vibratory phenomenons are described. The modeling methodology of tuned bladed disks is then illustrated in taking advantage of cyclic symmetry property. Of particular interest is the vibration in mistuned bladed disks. A range of fundamental research issues will be briefly presented.

1.1 Overview of turbomachinery, compressors and bladed disks

A turbomachine is a device that exchange energy with a fluid using continuously flowing fluid and rotating blades [1; 2]. Examples of these devices include aircraft engines (see Fig. 1.1) and wind turbine. Although aircraft engines have been built and operated successfully for the past century, their inherent complexity still gives rise to unexpected behavior.

In a basic aircraft engine, air enters the front inlet and is compressed through a compressor. The compressor is made up of many blades that are attached to a disk mounted onto a shaft. These rotating blades compress the air and raise the pressure. Then the compressed air is mixed with sprayed fuel and an electric spark lights the mixture. The hot gases are expanded either through a turbine

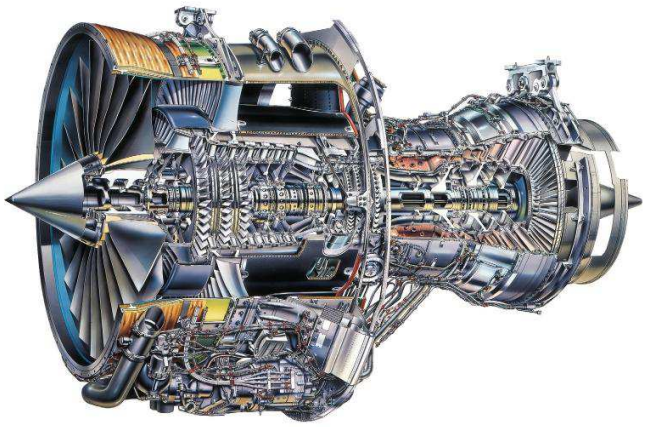

Figure 1.1: The aircraft engine RB211-535E4 manufactured by Rolls-Royce (UK)

to generate shaft power or through a nozzle to create thrust. This shaft power, drives the compressor or the fan in turn, therefore bringing in a fresh air supply through the inlet. Aircraft engines are self sustaining machines. As long as fuel is provided they will keep operating.

The turbine and compressor components are mated by a shaft, since the former powers the latter. A single shaft aeroengine has only one shaft connecting the compressor and turbine components. A twin-spool aeroengine has two concentric shafts, a longer one connecting a low-pressure compressor (LPC) to a low pressure turbine (the low spool), which rotates inside a shorter, larger-diameter shaft. The latter connects the high-pressure turbine with the higher pressure compressor (HPC), which rotates at higher speeds than the low spool. A triples pool engine would have a third, intermediate-pressure compressor-turbine spool.

The more efficient, higher capacity axial flow compressor is widely used on most gas turbines for high level of compression and thrust generation (see Fig. 1.2a). A stationary row in the form of inlet guide vanes is located at the start of the passage. Air or any other working fluid is first accelerated and then diffused to obtain the right pressure increment in an axial compressor stage. Rotating blades (airfoils) mounted on the disk impart kinetic energy to the fluid; stationary blades (stator vanes) then convert it into potential energy in the form of increased pressure (see Fig. 1.2b). Multiple stages are required to attain the proper compression,

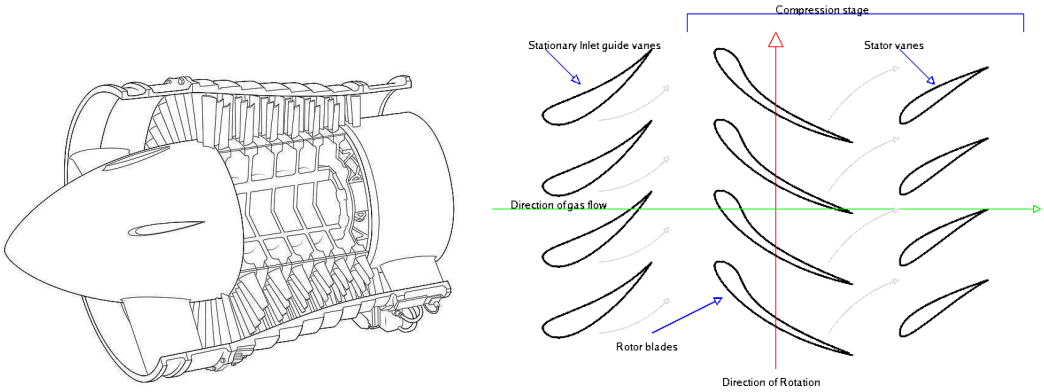

(a) (b)

Figure 1.2: a)Low pressure axial compressor scheme of the Olympus BOl.1 turbojet; b)Diagram of an axial flow compressor.

each row of stationary and moving blades constituting a stage.

Bladed disks are therefore essential components of compressors and turbines. A bladed disk assembly is represented in Figure 1.3. Vibration-induced fatigue failure of rotating blades has been a problem of major concern to the designer [3]. Vibration reduction technologies are needed for high performance and lifespan requirement in modern aeroengines.

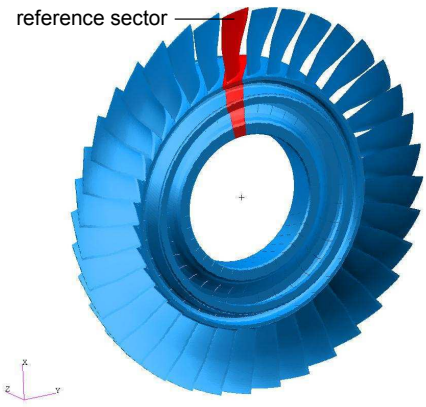

Figure 1.3: A blade disk assemble model

In the following, the principal excitation sources and vibratory phenomenons in bladed disks will be discussed.

1.2 Vibratory phenomenons in bladed disk

There are several excitation sources, arising out of aerodynamic and structural environment in aeroengine, which can lead to vibration phenomenons of engine blades. The most common vibration problems of rotating bladed disks in operation include: a) resonant vibration occurring at multiple of rotation speed (integral order vibration); b) flutter, which is an aeroelastic instability (nonintegral order vibration), having the potential to escalate into larger and larger amplitude and leading to severe damage to the blades. The associate failures of engine blades are referred to as high cycle fatigue (HCF) failures. Both the resonance and flutter are induced by aerodynamic excitation. In addition, mechanical sources of excitation are also briefly referred.

1.2.1 Aeroelastic aspect

The principal sources of excitation in bladed disk is related to the aerodynamic loading acting on the blade. As remarked earlier, air flow entering the engine inlet meets with the rotating bladed disks and static obstructions (stator vanes) in its path from the inlet to the exhaust. The flow field inside the engine is inherently unsteady. Various of aerodynamic unsteady phenomenons, such as wakes, potential pressure disturbances, circumferential flow distortions, shocks in passages, secondary flows, coexist in either upstream or downstream of any rotor stage. The unsteady flow produces pressure variations, which is experienced by the spinning blades as a time-varying forces. A more detailed introduction is given by Srinivasan [3] and numerous research efforts in this domain are presented by Hall and Kielb [4]. In this section, we mainly introduce the aforementioned two principal phenomenons in brief.

Resonant response

The flow conditions of air drawn through fan stages of an engine and delivered to compressors generally vary in space and time at any engine stage. Similar conditions prevail in the turbine stages. Therefore, blades experiencing pressures, velocities, incidence, temperatures, etc., that vary periodically in time. From the viewpoint of the structural dynamics, the key point relates to an accurate estimate of aerodynamic forcing and determining the resonant conditions under which the pattern of varying aerodynamic forces match any blade-disk modes both in time and space. If the resonant condition is met, the resulting vibration amplitude is controlled by attainable aerodynamic and structural damping in aeroengines. Therefore, the reliability of predicting resonant stresses depends upon the accuracy of prediction of aerodynamic forces, bladed disk modes and damping available in the operational environment. All these efforts are made to avoid resonant conditions based on a Campbell diagram, which will be introduced in Section 1.4.

Flutter

Susceptibility of rotor blades to flutter instabilities is a major consideration in the design of turbomachines. A principal reason is that flutter is an aeroelastic instability leading to very high vibration amplitudes. Flutter is caused by an interaction between the blade vibratory motions and the aerodynamic forces resulting from these motions. In the instable condition the aerodynamic forces feed energy into the blade, and thus stresses escalate with each sequential cycle of vibration. Vibration amplitude of blade can thus cumulate. Unless the energy dissipated by aerodynamic and mechanical damping matches the energy input, blade vibration will not be limited, which can result in large amplitude vibration and potentially lead to rapid failure.

Because of this, the blades are designed carefully within known parameters to avoid flutter. However, usually both the unsteady aerodynamics and the mechanical properties of the bladed disks in aeroengines are not fully understood, flutter can only be kept under control through detailed testing. An important feature of flutter is that the resulting vibration is nonintegral and therefore the

frequency-speed characteristic does not "ride" the engine order line in the Campbell diagram. On the contrary, resonant conditions at an integral order are met when the frequency speed characteristic goes across the engine order line. When it departs from the engine order line, then the aeroelastic instability of flutter could take place.

1.2.2 Mechanical sources of excitation

In addition to the aerodynamic sources, there also exist mechanical sources of excitation that can produce forces at frequencies that may lead to forced vibration in an individual blade mode or a system mode. For example, foreign object damage occurs when either the low compressor blades are impacted by a bird (or a block of ice) at take-off/landing, or if a downstream blade is impacted by debris of an upstream blade. Whatever the case is, the metal pieces must be contained by the casing. Fan blade-off and bird ingestion are two tests used in the certification process of an engine.

Among various effects of mechanical excitation, the nonlinearity caused by contact interface are receiving more and more attention. In fact, there are nonlinearities caused by contact at shroud interface, at dovetail attachments for inserted blades [5; 6], and caused by the blade-tips/casing contact phenomenons [7; 8]. A number of emerging studies in this area are beyond the scope of this work. Hence they are not listed here.

Above all, vibrations of bladed disks occur in an aerodynamical environment in aeroengines. Therefore, apart from structural dynamic characteristics, significant advances in the aerodynamic aspect is also required for the prediction of blade vibration risks. Next we will turn to the structural dynamic aspect of bladed disks.

1.3 Bladed disk modeling: cyclic symmetry strategy

The bladed disk modeling methodology takes advantage of the cyclic symmetry property in this periodic structure. A structure is said to present cyclic symmetry when it is composed of a number of geometrically identical substructures, i.e. sectors. For instance, Fig. 1.3 depicts a full model of bladed disk and its reference sector.

The assumption of perfect cyclic symmetry greatly simplifies the tuned bladed disk vibration analysis. It enables equations of motion to be uncoupled by spatial Fourier decomposition. Instead of analyzing the full bladed disk as a whole, we could therefore have an insight of the full structure by only investigating the dynamic behavior of the reference sector. For more details, readers are referred to early research efforts by Thomas [9], Wildheim [10] and Sternchuss [11].

1.3.1 Cyclic components

Let's consider a cyclic structure that is composed of N sectors numbered from 0 to $N-1$. It is generated by rotation of the reference sector with a phase difference $\alpha = 2\pi/N$. A vector u_j represents a certain quantity (displacements, forces etc.) in physical coordinates for the j^{th} sector. As usual, u_0 stands for the quantity in the reference sector. According to the cyclic symmetry condition, we have:

$$u_{N+j} = u_j, \qquad j = 0, 1, \cdots, N-1 \tag{1.1}$$

From the theory of cyclic components, the vector u_j in physical coordinates for all N sectors may be expressed as a linear combination of the corresponding quantity $\tilde{u}_0$ in cyclic coordinates for the reference sector as:

$$u_j = \sum_{k=0}^{N-1} \tilde{u}_0^k e^{ijk\alpha}, \qquad i^2 = -1 \tag{1.2}$$

The amplitude $\tilde{u}_0^k$ is named cyclic component of harmonic order k on the reference sector. The "tilde" notation is used throughout this thesis to indicate

that a quantity is represented in cyclic coordinates. For each cyclic component of harmonic order k, the inter-sector phase difference is fixed and equals $k\alpha$.

The cyclic components $\tilde{u}_0^k$ is defined as a function of physical coordinates u_j:

$$\tilde{u}_0^k = \frac{1}{N}\sum_{j=0}^{N-1} u_j e^{-ijk\alpha} \tag{1.3}$$

Transforms (1.2) and (1.3) are (inverse) discrete spatial Fourier transforms, in essence. Since the physical quantity u is considered in the real-valued form, a real-valued matrix presentation of the discrete spatial Fourier transform is preferable for convenience. The complex cyclic components could be written as:

$$\tilde{u}_0^k = \tilde{u}_0^{k,c} + i\tilde{u}_0^{k,s} \tag{1.4}$$

A real form of cyclic representation is introduced as:

$$\tilde{u} = [\tilde{u}_0^0 \cdots \tilde{u}_0^{k,c} \quad \tilde{u}_0^{k,s} \cdots \tilde{u}_0^{N/2}]^T \tag{1.5}$$

where the last term $\tilde{u}_0^{N/2}$ only exists if N is even.

The physical representation is:

$$u = [u_0 \cdots u_j \cdots u_{N-1}]^T \tag{1.6}$$

Since cyclic components are represented by trigonometric series, the physical quantity u_j for j^{th} sector can be expressed as:

$$u_j = \frac{1}{\sqrt{N}}\tilde{u}_0^0 + \sqrt{\frac{2}{N}}\sum_{k=1}^{\kappa}\left[\tilde{u}_0^{k,c}cos(jk\alpha) + \tilde{u}_0^{k,s}sin(jk\alpha)\right] + \frac{(-1)^{j-1}}{\sqrt{N}}\tilde{u}_0^{N/2} \tag{1.7}$$

In the above expression, the harmonic index k varies from 0 to κ. κ is defined as:

$$\kappa = \begin{cases} N/2-1 & \text{if N is even;} \\ (N-1)/2 & \text{if N is odd.} \end{cases} \tag{1.8}$$

We can therefore define the real-valued matrix representation of the inverse

discrete spatial Fourier transform:

$$u = [E]\tilde{u} \tag{1.9}$$

The unitary Fourier matrix $[E]$ is defined as:

$$[E] = \frac{1}{\sqrt{N}} \begin{bmatrix} 1 & \sqrt{2} & 0 & \cdots & 0 & 1 \\ 1 & \sqrt{2}cos\alpha & \sqrt{2}sin\alpha & \cdots & \sqrt{2}sin\kappa\alpha & -1 \\ 1 & \sqrt{2}cos2\alpha & \sqrt{2}sin2\alpha & \cdots & \sqrt{2}sin2\kappa\alpha & 1 \\ \vdots & \vdots & \vdots & & \vdots & \vdots \\ 1 & \sqrt{2}cos(N-1)\alpha & \sqrt{2}sin(N-1)\alpha & \cdots & \sqrt{2}sin(N-1)\kappa\alpha & (-1)^{N-1} \end{bmatrix} \tag{1.10}$$

where the last column only exists if N is even.

Similarly, the cyclic components could also be expressed with the inverse matrix of $[E]$. Let's note that the matrix $[E]$ is orthonormal, or unitary, such that $[E]^T[E] = I$, where I is an identity matrix of size N and the superscript $(.)^T$ denotes the transpose. This implies that $[E]^T = [E]^{-1}$. We have:

$$\tilde{u} = [E]^{-1}u = [E]^T u \tag{1.11}$$

where the corresponding backward transform from physical to cyclic coordinates could also be given by the following series of relations:

$$\tilde{u}_0^0 = \frac{1}{\sqrt{N}} \sum_{j=0}^{N-1} u_j \tag{1.12}$$

$$\begin{aligned} \tilde{u}_0^{k,c} &= \sqrt{\frac{2}{N}} \sum_{j=0}^{N-1} cos(jk\alpha)u_j \\ \tilde{u}_0^{k,s} &= \sqrt{\frac{2}{N}} \sum_{j=0}^{N-1} sin(jk\alpha)u_j \\ \tilde{u}_0^{N/2} &= \frac{1}{\sqrt{N}} \sum_{j=0}^{N-1} (-1)^{j-1}u_j \end{aligned} \tag{1.13}$$

In the rest of this thesis, the real-valued form of spatial Fourier transform is preferred. The physical representation $u = \{u_j,\, j = 0, \cdots, N-1\}$ and cyclic representation $\tilde{u}_0 = \{\tilde{u}_0^0, \tilde{u}_0^{k,c}, \tilde{u}_0^{k,s},\, \tilde{u}_0^{N/2},\, k = 1, \cdots, \kappa\}$ are equivalent. Due to the fact that the cyclic components contain the complete set of admissible circumferential mode shapes of the cyclic assembly, this transform is not an approximation, but an accurate description of the global system behavior.

1.3.2 Spatial Fourier transform of matrices

In finite element formulations (Ritz-Galerkin procedure), the continuous field u is discretized which leads to a physical vector of degree of freedom (DOF) U on the full bladed disk structure. We can gather all the DOFs as a series of vectors U_j defined on j^{th} sector. Since it is assumed the full bladed disk has a perfect cyclic symmetry, it is possible to compute cyclic components defined on the reference sector by the spatial Fourier transform. Let $U = [U_0, U_1, \cdots, U_{N-1}]^T$, we have:

$$\tilde{U} = ([E]^T \otimes I_n)U \tag{1.14}$$

where $\tilde{U}$ is the vector in cyclic coordinates in the form of

$$\tilde{U} = [\tilde{U}_0^0, \cdots, \tilde{U}_0^{k,c}, \tilde{U}_0^{k,s}, \cdots, \tilde{U}_0^{N/2}]^T \tag{1.15}$$

As aforementioned, the last term $\tilde{U}_0^{N/2}$ only exists if N is even. I_n is $n \times n$ identity matrix and n is the number of DOFs in each sector. The symbol $\otimes$ denotes the Kronecker product. U could also be recovered by the inverse discrete Fourier transform:

$$U = ([E] \otimes I_n)\tilde{U} \tag{1.16}$$

At this stage, the physical discretized fields defined in two adjacent sectors are assumed disjoint. The continuity condition will be discussed in Section 1.3.3.

The spatial Fourier transform of a field, either continuous or discretized, only requires a periodic distribution of points. A matrix representation of the operator that acts on the physical field is to be examined below.

Let A_j be any finite element matrix associated with j^{th} sector. The matrix A

results from the assembly of the disjoint sector matrices:

$$A = \begin{bmatrix} A_0 & \cdots & 0 & \cdots & 0 \\ \vdots & \ddots & \vdots & & \vdots \\ 0 & \cdots & A_j & \cdots & 0 \\ \vdots & & \vdots & \ddots & \vdots \\ 0 & \cdots & 0 & \cdots & A_{N-1} \end{bmatrix} \tag{1.17}$$

The bladed disk is said to be tuned when all sectors share exactly the same set of mechanical properties, i.e. perfect cyclic symmetry. In this particular case, the matrix A could be derived from the submatrix A_0 associated with the reference sector so that:

$$A = I_N \otimes A_0 \tag{1.18}$$

The spatial Fourier transform could then be applied to the the matrix A:

$$\tilde{A} = ([E]^T \otimes I_n)(I_N \otimes A_0)([E] \otimes I_n) \tag{1.19}$$

Taking into account properties of the unitary Fourier transform matrix $[E]$, we have a block-form matrix of $\tilde{A}$:

$$\tilde{A} = \begin{bmatrix} \tilde{A}^0 & \cdots & 0 & \cdots & 0 \\ \vdots & \ddots & \vdots & & \vdots \\ 0 & \cdots & \tilde{A}^k & \cdots & 0 \\ \vdots & & \vdots & \ddots & \vdots \\ 0 & \cdots & 0 & \cdots & \tilde{A}^{N/2} \end{bmatrix} \tag{1.20}$$

Blocks in $\tilde{A}$ depend on the mechanical properties of the reference sector A_0 and the harmonic index k:

$$\tilde{A}^0 = \tilde{A}^{N/2} = A_0 \tag{1.21}$$

$$\tilde{A}^k = \begin{bmatrix} A_0 & 0 \\ 0 & A_0 \end{bmatrix}, \qquad k = 1, \cdots, \kappa \tag{1.22}$$

For each block $\tilde{A}^k$, the upper and bottom row correspond to the real and

imaginary part of the spatial Fourier harmonic with index k.

The property exhibited in this section reveals that in the tuned bladed disk, structure matrices do not couple the Fourier harmonics to each other if sectors in the full bladed disk are considered disjoint. Next, it is necessary to define continuity conditions between the reference sector and its neighboring sectors.

1.3.3 Continuity conditions in neighboring sectors

Continuity conditions are imposed on the interface of the reference sector. Fig. 1.4 gives an illustration of interfaces between the reference sector and its neighboring sectors. Let us consider that an arbitrary vector U_0 defined on the reference sector could be partitioned into the DOFs on the left interface ${}^{l}U_0$, on the right interface ${}^{r}U_0$ and interior DOFs ${}^{i}U_0$:

$$U_0 = [{}^{l}U_0 \quad {}^{r}U_0 \quad {}^{i}U_0] \tag{1.23}$$

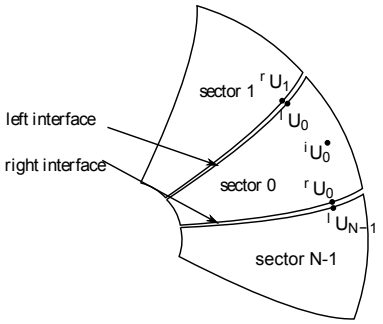

Figure 1.4: Illustration of interfaces of the reference sector

Continuity conditions on interfaces of the reference sectors with the neighboring sector numbered 1 and $N-1$ are given by:

$${}^{l}U_0 = {}^{r}U_1 \tag{1.24}$$

$${}^{r}U_0 = {}^{l}U_{N-1} \tag{1.25}$$

Substituting the relation in Eq. (1.3) into Eq. (1.24) and Eq. (1.25), one could express the continuity conditions based on the cyclic components with harmonic

index k:

$$
\begin{aligned}
{}^{l}\tilde{U}_0^k &= {}^{r}\tilde{U}_0^k e^{ik\alpha} && (1.26)\\
{}^{r}\tilde{U}_0^k &= {}^{l}\tilde{U}_0^k e^{i(N-1)k\alpha} && (1.27)
\end{aligned}
$$

These propagation equations in cyclic coordinates allow to relate the DOFs on the left interface to that on the right interface. They are completely equivalent. Eq. (1.26) is then adopted to eliminate the DOFs on the left interface. Once again, we can write continuity conditions in the real-valued form:

- $k = 0$,

$$
{}^{l}\tilde{U}_0^0 = {}^{r}\tilde{U}_0^0 \tag{1.28}
$$

- $k = 1, \cdots, \kappa$,

$$
\begin{bmatrix} {}^{l}\tilde{U}_0^{k,c} \\ {}^{l}\tilde{U}_0^{k,s} \end{bmatrix} = \begin{bmatrix} cosk\alpha & sink\alpha \\ -sink\alpha & cosk\alpha \end{bmatrix} \begin{bmatrix} {}^{r}\tilde{U}_0^{k,c} \\ {}^{r}\tilde{U}_0^{k,s} \end{bmatrix} \tag{1.29}
$$

- $k = N/2$,

$$
{}^{l}\tilde{U}_0^{N/2} = -{}^{r}\tilde{U}_0^{N/2} \tag{1.30}
$$

With inter-sector continuity conditions, it enables to carry out the bladed disk structure analysis based on the reference sector. This will considerably reduce the size of vibration problems. In the next section, the method of formulating bladed disk structure problems with cyclic symmetry is to be presented.

1.4 Structure problems formulated with cyclic symmetry

Consider a discrete structure problem of the bladed disk in physical coordinates:

$$
M\ddot{U}(t) + C\dot{U}(t) + KU(t) = F(t) \tag{1.31}
$$

where M, C and K are mass matrix, damping matrix and stiffness matrix, respectively. $U(t)$ is the vector of displacement and $F(t)$ denotes the external

excitation.

As described in the precedent sections, the physical quantities U and F could be reformulated in cyclic coordinates according to the relation in Eq. (1.14). Consequently, the problem presented by Eq. (1.31) in physical coordinates could be reformulated in cyclic coordinates. This reformulation consists of a set of independent subproblems for each harmonic order k:

$$\tilde{M}^k\ddot{\tilde{U}}_0^k(t) + \tilde{C}^k\dot{\tilde{U}}_0^k(t) + \tilde{K}^k\tilde{U}_0^k(t) = \tilde{F}_0^k(t) \tag{1.32}$$

For each subproblem corresponding to harmonic order k, the continuity conditions defined in Eq. (1.28), (1.29) and (1.30) should be taken into account.

After resolving each subproblem, the complete response $U(t)$ could be obtained by the superposition of all cyclic components (see Eq. (1.16)). We discuss the details of the modal analysis and the force response respectively in this section.

1.4.1 Modal analysis

The modal analysis of a tuned bladed disk is realized through solving the eigenvalue problems defined in the reference sector for each harmonic index k:

$$(\tilde{K}^k - \omega^2\tilde{M}^k)\tilde{X}_0^k = 0 \tag{1.33}$$

For the harmonic index $k = 0$ and $k = N/2$, the system matrix in cyclic coordinates are of size n (see Eq. (1.21)) and the corresponding modes are *non-degenerate*; for the other harmonic index $k = 1, \cdots, \kappa$, system matrices in cyclic coordinates are of size $2n$ (see Eq. (1.22)). The rows in system matrices are decoupled into the real and imaginary part of the spatial Fourier harmonic. Note that these system matrices are symmetric and that their two diagonal blocks are identical. The eigenvalue problems belongs to a *degenerate* class of structural eigenvalue problems, which will yield pairs of real eigenvalues. The circumferential positioning of mode shapes pertaining to double harmonics is arbitrary. As a result, these mode shape pairs can also be represented by complex, counter-rotating waves [12].

Mode shapes of the full bladed disk are obtained by applying the relation Eq. (1.16) to the eigenmode $\tilde{X}_0^k$ in the cyclic coordinates. Let's note that each subproblem for harmonic index k is independent. For practical consideration, it is possible to only solve the subproblems with some particular harmonic index k. Then the full blade-disk mode with respect to harmonic index k is reconstructed separately:

$$X^k = \begin{cases} ([E]^0 \otimes I_n)\tilde{X}_0^0 & k = 0; \\ ([E]^k \otimes I_n) \begin{pmatrix} \tilde{X}_0^{k,c} \\ \tilde{X}_0^{k,s} \end{pmatrix} & k = 1, \cdots, \kappa; \\ ([E]^{N/2} \otimes I_n)\tilde{X}_0^{N/2} & k = N/2. \end{cases} \tag{1.34}$$

with

$$[E]^0 = \frac{1}{\sqrt{N}} \begin{bmatrix} 1 \\ 1 \\ 1 \\ \vdots \\ 1 \end{bmatrix} \qquad [E]^{N/2} = \frac{1}{\sqrt{N}} \begin{bmatrix} 1 \\ -1 \\ 1 \\ \vdots \\ (-1)^{N-1} \end{bmatrix} \tag{1.35}$$

$$[E]^k = \sqrt{\frac{2}{N}} \begin{bmatrix} 1 & 0 \\ \vdots & \vdots \\ cos(jk\alpha) & sin(jk\alpha) \\ \vdots & \vdots \\ cos(N-1)k\alpha & sin(N-1)k\alpha \end{bmatrix}$$

It is a classical strategy to plot the eigenfrequency of a tuned bladed disk with respect to the number of nodal diameters (harmonic index k). A typical frequency/nodal diameters plot is shown in Fig. 1.5 for a monobloc disk with 36 blades [13].

As remarked earlier, blade-disk mode can be represented by counter-rotating waves propagating in the circumferential direction. Blade vibration is thus related to energy transfer among consecutive sectors in the blade-disk structure. In most cases, the structure coupling, particularly blade-disk coupling, plays the key role as the dominant mechanism for inter-sector energy transfer. The blade-disk coupling strength can be examined in the frequency/nodal diameters plot [14]. Generally, two different types of blade-disk modes are observed in this plot:

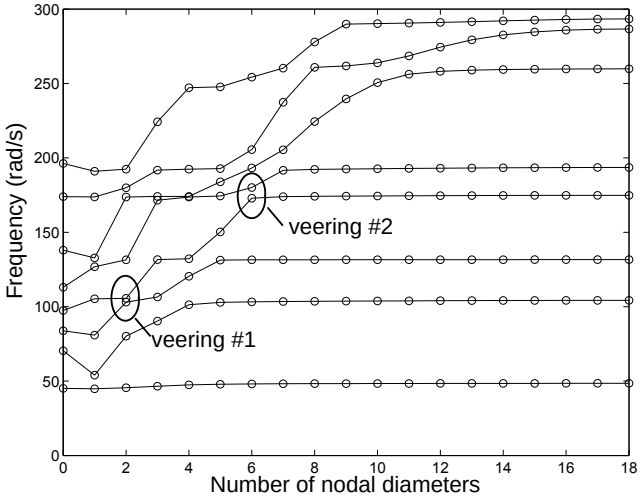

Figure 1.5: Example of Frequency/ Nodal diameters diagram

blade-dominated mode

Modes dominated by blade motion tend to appear as horizontal lines in the plot. They feature little disk motion and thus they have weak inter-blade coupling. This feature tends to confine the strain energy to the blades. There may be numerous blade-dominated modes corresponding to moderate or high nodal diameters. These regions of high modal density are referred to as clustered mode area.

disk-dominated mode

The modal stiffness of a disk increases rapidly as the number of nodal diameters is increased. So disk-dominated modes appear as slanted lines in this plot. In disk-dominated modes, the inter-blade coupling is high enough so that the strain energy spreads over the blades and the disk.

There are several regions where the disk and blade modes appear to veer away from each other, as indicated by "veering" in Fig. 1.5. For example, in the veering area #2, blade-dominated modes at 5 nodal diameters loses its blade characteristics through the veering, becoming disk-dominated mode at 6 nodal diameters; on the other hand, the disk-dominated mode at 5 nodal diameter

gains more blade participation through the veering, becoming blade-dominated at higher nodal diameters. Modes in the veering regions tend to be featured by mixed disk-blade motion. Therefore, the blades will have significant vibration response if these modes are excited. There is also a mechanism for transferring energy between blades through the disk. This combination of conditions can lead to the blade vibration energy being localized in a few blades when blade mistuning is present [14]. Blade mistuning will be discussed in detail in Section 1.5.

The relationship between the veering and inter-blade coupling has been investigated extensively [15–17]. From curve veering theory, it is known that the strength of the blade-disk interaction, and thus the inter-sector coupling, is a function of veering curvature. If the interaction between disk-dominated and blade-dominated motion is negligible, then the disk-dominated and the blade-dominated frequency curves will appear to "pass through" each other (veering #1 in Fig. 1.5). The veering is therefore extremely sharp with high curvature. In contrast, a lower-curvature veering indicates a higher level of modal interaction, and accordingly, stronger inter-sector coupling (veering #2 in Fig. 1.5).

The veering theory has been further developed by Bladh et al. [18] to obtain continuous natural frequency curves. The continuous veering plot offers a tool to better determine the type of the examined blade-disk modes. Thus, the inter-sector coupling strength can be quantified by examining the veering characteristics.

Another benefit of examining blade-to-blade coupling through the disk is that it enables one to affect the blade response through variation of the disk parameters [19]. This finding also raise possibility of introducing some kind of damping to the disk for the purpose of affecting the blade response. For example, friction rings are usually arranged inside the integral blisk grooves in order to enhance the structural damping.

1.4.2 Forced response

When it comes to compute the response of a tuned bladed disk under an external excitation, a similar procedure as described in the modal analysis is adopted.

This procedure consists of three typical steps:

- Decomposition of the external excitation into spatial Fourier harmonics;
- Resolving subproblems for each harmonic;
- Reconstructing the displacement vector of the full bladed disk in physical coordinates from the cyclic coordinates.

First, the external excitation $F(t)$ is decomposed into its spatial Fourier components using the Fourier transform Eq. (1.14). This transform allows to obtain the cyclic component $\tilde{F}_0^k$ of external force defined in the reference sector using the physical representation F_j acting on each sector:

$$\begin{aligned}
\tilde{F}_0^0 &= \frac{1}{\sqrt{N}} \sum_{j=0}^{N-1} F_j \\
\tilde{F}_0^{k,c} &= \sqrt{\frac{2}{N}} \sum_{j=0}^{N-1} cos(jk\alpha) F_j \\
\tilde{F}_0^{k,s} &= \sqrt{\frac{2}{N}} \sum_{j=0}^{N-1} sin(jk\alpha) F_j \\
\tilde{F}_0^{N/2} &= \frac{1}{\sqrt{N}} \sum_{j=0}^{N-1} (-1)^{j-1} F_j
\end{aligned} \tag{1.36}$$

Following the spatial Fourier decomposition, we can solve a series of subproblems corresponding to each harmonic component:

- $k = 0$,

$$\begin{cases} \tilde{M}^0 \ddot{\tilde{U}}_0^0(t) + \tilde{C}^0 \dot{\tilde{U}}_0^0(t) + \tilde{K}^0 \tilde{U}_0^0(t) &= \tilde{F}_0^0(t) \\ {}^l\tilde{U}_0^0 &= {}^r\tilde{U}_0^0 \end{cases} \tag{1.37}$$

- $k = 1, \cdots, \kappa$,

$$\begin{cases} \tilde{M}^k \begin{bmatrix} \ddot{\tilde{U}}_0^{k,c}(t) \\ \ddot{\tilde{U}}_0^{k,s}(t) \end{bmatrix} + \tilde{C}^k \begin{bmatrix} \dot{\tilde{U}}_0^{k,c}(t) \\ \dot{\tilde{U}}_0^{k,s}(t) \end{bmatrix} + \tilde{K}^k \begin{bmatrix} \tilde{U}_0^{k,c}(t) \\ \tilde{U}_0^{k,s}(t) \end{bmatrix} = \begin{bmatrix} \tilde{F}_0^{k,c}(t) \\ \tilde{F}_0^{k,s}(t) \end{bmatrix} \\ \\ \begin{bmatrix} {}^l\tilde{U}_0^{k,c} \\ {}^l\tilde{U}_0^{k,s} \end{bmatrix} = \begin{bmatrix} cosk\alpha & sink\alpha \\ -sink\alpha & cosk\alpha \end{bmatrix} \begin{bmatrix} {}^r\tilde{U}_0^{k,c} \\ {}^r\tilde{U}_0^{k,s} \end{bmatrix} \end{cases} \tag{1.38}$$

- $k = N/2$,

$$\begin{cases} \tilde{M}^{N/2}\ddot{\tilde{U}}_0^{N/2}(t) + \tilde{C}^{N/2}\dot{\tilde{U}}_0^{N/2}(t) + \tilde{K}^{N/2}\tilde{U}_0^{N/2}(t) &= \tilde{F}_0^{N/2}(t) \\ {}^l\tilde{U}_0^{N/2} &= -{}^r\tilde{U}_0^{N/2} \end{cases} \tag{1.39}$$

After resolving each subproblems, the complete forced response $U(t)$ could be obtained by the superposition of all cyclic components:

$$U = ([E] \otimes I_n)\tilde{U} \tag{1.40}$$

Equivalently, this principle of superposition could be expressed by trigonometric series:

$$U_j = \frac{1}{\sqrt{N}}\tilde{U}_0^0 + \sqrt{\frac{2}{N}}\sum_{k=1}^{\kappa}\left[\tilde{U}_0^{k,c}cos(jk\alpha) + \tilde{U}_0^{k,s}sin(jk\alpha)\right] + \frac{(-1)^{j-1}}{\sqrt{N}}\tilde{U}_0^{N/2} \tag{1.41}$$

Engine order excitation

The primary form of excitation in the analysis of forced response in turbomachinery is that of engine order excitation. As remarked in Section 1.2.1, this forcing condition occurs due to the fact that the rotors are rotating through a unsteady flow that is non-uniform in the circumferential direction. The non-uniformity of the flow stems from the multiple obstructions in the flow field. Each blade on the rotating assembly experiences these spatial variations in the steady flow as time-varying and therefore responds by vibrating with frequencies that are directly related to the speed of rotation.

The forcing function is characterized by a frequency which is an integer multiple of the rotation speed; on the other hand, it has also a characteristic shape since it is applied simultaneously to all the blades around the assembly. By performing a spatial Fourier transform of the flow field it may be broken into its spatial harmonics. In assuming linear dynamics, the response of the assembly to each of these harmonics can be analyzed separately. An engine order excitation is therefore assumed, which is harmonic in time and differs only in phase from blade to blade. The forcing function of an engine order EO with excitation frequency ω on blade j can be expressed as:

$$F_j = F_{amp} e^{i\omega t} e^{i2\pi EO \frac{j-1}{N}} \tag{1.42}$$

which is a traveling wave excitation of amplitude F_{amp} traveling in the positive j direction with wave speed:

$$\frac{\omega N}{2\pi EO}$$

The advantage of examining individually the spatial harmonics of the excitation is that each harmonic excites only modes with a harmonic index that matches the engine order. The relationship between the number of nodal diameters (N_d) of the excited mode and the excitation order p (excitation harmonic EO multiplied by the number of obstacles (stator blades) in the upstream of the considered bladed disk) is determined analytically by: $N_d = |kN - p|$ with $0 \leq k \leq N/2$ and $0 \leq |kN - p| \leq N/2$. For example, the nodal diameter 3 mode shown in Fig. 1.5 would be excited by engine order excitation $EO = 3$. If there are 36 blades in the system, this mode would be excited by an excitation of order $p = 33$, and $p = 39$, and so forth. This relationship could also be intuitively illustrated in a Zig-zag diagram [10].

Campbell diagram

Let's turn to the realistic case where the bladed disk is rotating at speed Ω. As remarked above, the engine order EO excitation will excite all blade-disk modes that contain a component of EO nodal diameters in their mode shape, and will do so at a frequency experienced by the bladed disk of $EO\Omega$. A convenient way

to present the characteristics of forced response due to engine order excitation is with a Campbell or interference diagram (see Figure 1.6 for a 18-sector bladed disk).

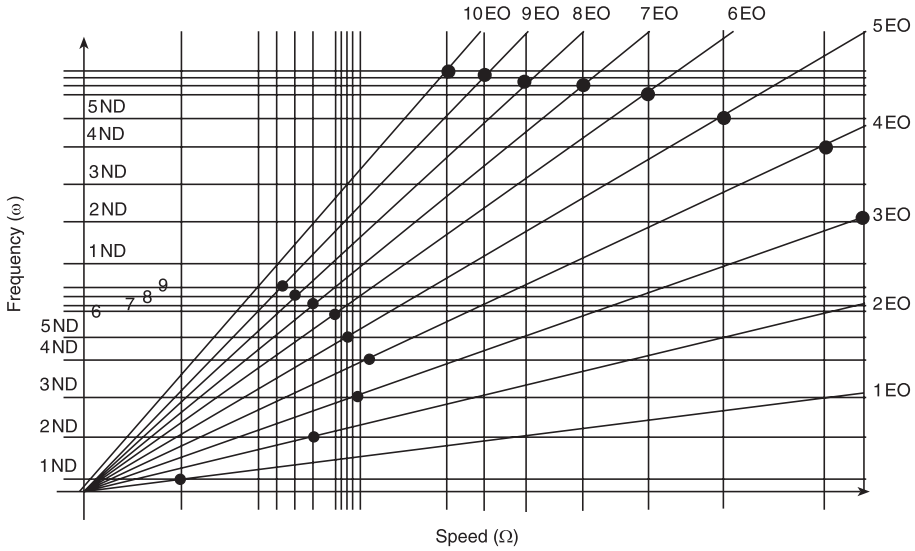

Figure 1.6: Example of Campbell diagram

Campbell diagram in Figure 1.6 plots the vibration frequency (as experienced on the rotating bladed disk) against rotation speed. When the bladed disk is subjected to an engine order excitation, resonance vibration can be expected. It can be clearly seen on this diagram that each *EO* selectively picks out the vibration mode with the matching number of nodal diameters and generates resonance accordingly. Furthermore, coincidence of excitation frequencies with natural frequencies does not necessarily satisfy the additional requirement of matching engine order and number of nodal diameters; consequently it does not lead to resonance vibration [20]. Hence, in the design phase, resonant conditions are always carefully identified and further avoided at a glance of the Campbell diagram.

At this point, it should be emphasized that all the analyses presented in Section 1.3 and Section 1.4 are based on a common hypothesis: the bladed disk is tuned with perfect cyclic symmetry. In the following, a special vibration phe-

nomenon in the realistic blade disk where the perfect cyclic symmetry is destroyed, i.e. mistuning vibration, is introduced.

1.5 Vibration in mistuned bladed disks

Bladed disks, as shown in precedent sections, are rich dynamical systems that are known to suffer from severe vibration problems. Although a bladed disk in the ideal, tuned design has uniform blades, there are always random, inevitable deviations among the blades, which is called mistuning. Blade mistuning could be caused by manufacturing tolerances, wear, and other causes in operation. Even though mistuning is typically small (e.g. blade properties deviate on the order of a few percent of the nominal values), it has a profound effect on the system dynamics of bladed disks. The most important and dangerous consequence is that the mistuned bladed disk can have drastically larger forced response levels than the tuned design. The attendant increase in vibration amplitude can lead to unexpected high cycle fatigue (HCF) of the blades. HCF is widely supposed to be related to blade failures in aeroengines. The comprehensive modeling, analysis, and understanding of bladed disk vibration is thus critical to reducing the occurrence of HCF and improving the performance and reliability of aeroengines [14]. To gain an insight to the mistuning phenomenon, modeling the entire blade-disk structure is indispensable since each blade differs from the others. This process is certainly much more computationally expensive compared to the tuned case. In this section, some fundamental issues in the mistuned bladed disk are briefly covered.

1.5.1 Mistuning sources

Vibration in mistuned bladed disks has received significant attention from the research community in the last decades. To understand the basic vibration characteristics, bladed disks have often been modeled as cyclic chains of spring-mass oscillators in early mistuning studies. The simplest such model of an N-sector bladed disk is a chain of N single-degree-of-freedom oscillators coupled by linear springs. Additional oscillators can be added at each sector to have both blade and

disk degrees of freedom. In the literature, we observe a general classification into structural coupling methods for forced response predictions of mistuned bladed disks, incorporating deterministic and statistical approaches [21], and aerodynamic methods for turbomachinery applications [22; 23].

Nowadays, more and more investigations are performed on reduced-order models generating from large scale modern industrial finite element models of a full bladed disk. The reduced order models could reduce the computational models of the full bladed disk to manageable, smaller size, while retaining adequate model accuracy. Numerous studies on this subject reveals that there exist a set of parameters whose spatial variations have a significant impact on the behavior of the nominally tuned bladed disks. These identified structure parameters range over:

blade mass

The bladed disk is mistuned by the addition of small, unequal weights to the blade tips [24] or by the perturbation of blade mass matrices [25–27].

blade stiffness

The mistuning model can be represented by perturbation of the individual sector partition of the bladed disk stiffness matrix. Blade stiffness mistuning models are adopted in most of publications [28–32].

damping

In reality, blade energy is dissipated by a combination of mechanisms such as material damping, Coulomb friction at the interfaces between sectors and aerodynamic damping. Early studies have used lumped parameter models to investigate the damping mistuning effect [28; 33]. Using large scale finite element models, Petrov and Ewins [30] have studied friction damping mistuning and its effects on the dynamics of bladed disks. In recent researches, damping mistuning has been characterized at the sector level as variations in the modal damping values of each sector [27] or by deviations of the structural damping coefficients of the blades from their average value [34; 35].

natural frequencies of the cantilevered blades

Natural frequencies of the cantilevered blades [36; 37] or of bladed sectors whose inter-sector interfaces are fixed [38–41] differ from each other. This can be interpreted as a combined effect of the blade mass and stiffness.

geometry

Geometry mistuning could originate from the manufacturing process [42; 43], from in service wear or from an accidental damage (a foreign object crash leading to a permanent blade deformation)[44], etc. Generally, geometric mistuning is considered to cause simultaneous perturbations in mass and stiffness matrices, which alter mode shapes associated with the blade. In the case of severe foreign object crash, some blades undergo drastic geometric deformation, which definitely changes the mode deformation of blades. This characterizes geometric mistuning from "frequency mistuning", which does not alter the blade mode shapes, but only the blade alone frequencies [45].

Besides these various mistuning sources, there are still many potentially important phenomena that are typically neglected in early vibration models of mistuned bladed disks, such as aerodynamic coupling and Coriolis force effect.

aerodynamic coupling effect

The aerodynamic coupling effect has been first included in a lumped parameter model of mistuned bladed disk by Pierre and Murthy [23]. The authors state that aerodynamic coupling has an effect qualitatively similar to that of structural interblade coupling. In particular, the blade-disk assemblies with weak aerodynamic inter-blade coupling (e.g. high solidity assemblies, for which aerodynamic forces are small compared to structural forces) are highly sensitive to mistuning. In recent years, Mayorca and Vogt et al [46] present a Multimode Least Square method for stability and forced response analyses of aerodynamically coupled blades considering the interaction of various mode families. The mistuned forced response calculated with aerocoupling effects included has been studied for cases of random blade mistuning and for mistuned blade rearrangements by Petrov [47].

Coriolis force effect

The effect of Coriolis forces is neglected in most of studies in the domain of bladed disk dynamics. In general, Coriolis forces are derived as components of blade and disk motion along the axes, which are perpendicular to the axis of disk rotation. At the same time the force components related with the disk motion in the parallel direction do not participate in the effect. The effects of Coriolis forces and magnitude of disorder on the localization phenomenon of a rotating bladed-disk system are investigated numerically by Huang [48]. Obtained results indicate that Coriolis forces may enhance the localization phenomenon. Coriolis effects and their mutual interaction with mistuning is studied in [49] numerically with a lumped mass model and experimentally by means of a specially designed so-called swept test piece with 24 blades allowing a strong Coriolis coupling of blade vibrations. Typical changes in the dynamics induced by Coriolis effect are shown and quantified experimentally and numerically in [31]. It is concluded that modes affected by Coriolis effects are rather low nodal diameters coupled modes for which significant splits of frequencies appear with increase of the rotating speed. In cases where these modes are concerned by forced responses, it is recommended to take into account the demonstrated effects for accurate prediction of bladed disks dynamic properties. Similar conclusions are also reported in another numerical investigation by Xin and Wang [50].

In summary, a trend toward including effects either previously absent or ignored from the mistuned bladed disk analysis is highlighted in recent years. Involving these aforementioned aerodynamic effects or Coriolis force effect may give rise to new insights into mistuned bladed disk analysis.

1.5.2 Mistuning, coupling and mode localization

As described in Section 1.4, mode shapes of a periodic structure with perfect cyclic symmetry are characterized by sinusoidal shapes that are extended throughout the structure (see Fig. 1.7a). However, mistuning in bladed disks could have a drastic effect on system behaviors of the full structure. In particular, the mode shapes can become spatially confined in a small region of the structure, as shown in Fig. 1.7b. This phenomenon is known as mode localization. In early times,

Hodges [51] pointed out that the degree of mode localization depends largely on the mistuning-to-coupling ratio. In other words, mode localization increases monotonically with increasing mistuning strength or decreasing mechanical coupling strength between substructures.

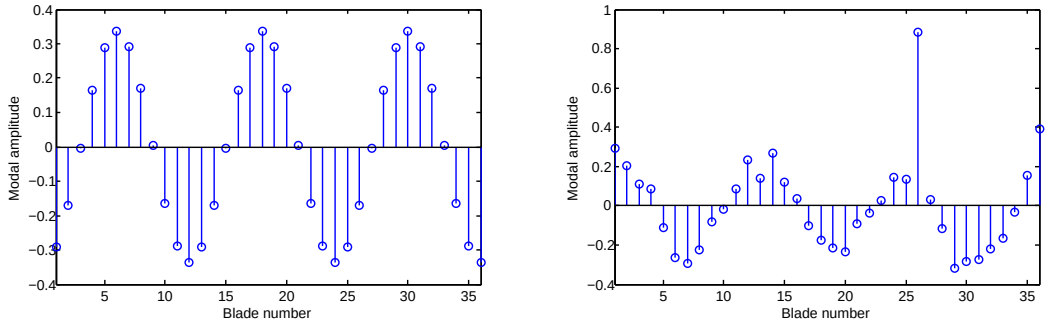

(a) (b)

Figure 1.7: Mode shape of a lumped-parameter bladed disk model (which will be described in Chapter 3): a) 3 nodal diameter-mode of a tuned bladed disk; b) localized mode of a mistuned bladed disk.

In bladed disks, the coupling includes: the structural coupling arising from blade-disk coupling or shroud coupling (in shrouded cases), and the aerodynamic coupling between blades. For an ideal, cyclic bladed disk, engine order excitation will excite only those modes whose number of nodal diameters meets the harmonic index of the excitation (see Section 1.4). For a mistuned bladed disk, the localized modes could be decomposed into multiple harmonic contents. Consequently many tuned mode components will be excited by a single engine order excitation. Among those excited modes, the one that retains significant harmonic content matching the engine order of excitation will be strongly excited, leading to exceptional large forced response level [14].

When it comes to the maximum forced-response levels, things become different. Unlike the phenomenon that mode localization increases monotonically with respect to the mistuning-to-coupling ratio, it is shown in Fig. 1.8 that vibration amplitude magnification tends to exhibit a peak value when blade mistuning is of a moderate level. Based on this finding, Óttarsson [52] has declaimed that

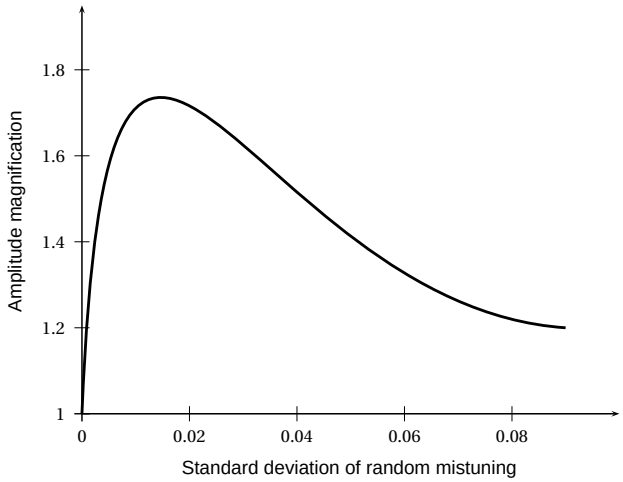

Figure 1.8: Amplitude magnification as a function of mistuning strength. Calculation is based on a lumped-parameter bladed disk model described in Chapter 3.

moderately weak interblade coupling is required for significant increases in forced-response amplitudes. Neither weak coupling nor extremely strong coupling could lead to spatial vibration localization and further amplitude magnification.

1.5.3 Mistuning sensitivity

With the identified mistuning sources and the basic understanding of the mistuning mechanism in the bladed disk, additional research issues to assess and improve the bladed disk design with respect to its sensitivity are presented.

Blade-disk coupling

As just mentioned, the inter-sector coupling plays an important role in the system dynamics because it governs the communication of vibration energy among blades. Moreover, inter-sector coupling is largely dependent on the blade-disk interaction. This is deduced throgh an examination of the frequency/nodal diameters diagram, as presented in Fig. 1.5.

In Section 1.4.1, the relationship between the veering and the inter-blade coupling is discussed. It is said that quantifying the veering characteristics can yield

key information for the quantification of blade-disk coupling strength. Naturally, these quantitative coupling strength could be used for predicting mistuning sensitivity [15].

Blade-disk coupling can also be quantitatively measured through so-called "coupling index" proposed by Javier and Mignolet [53]. The coupling index allows to intuitively qualify the blade-disk coupling by observing the impact of blade stiffness drifts on the variation of blade-disk mode frequencies. Furthermore, an examination of blade-disk coupling also raises the possibility of influencing blade response by damping the disk. This concept will be discussed and calculated in Chapter 3.

Maximum forced response

A major concern in the academic community of mistuning is the prediction of maximum attainable forced response levels. The maximum amplification factor is traditionally defined as a ratio of the largest amplitude of mistuned bladed disk to the corresponding value of tuned response. Prediction of the maximum forced response increase due to mistuning has been one of the most challenging mistuning questions. A number of studies have attempted to provide a definitive answer.

The first research effort to address this issue was by Whitehead [54] who concluded that the amplitude of blade response on a mistuned N-blade disk could be as large as $(1 + \sqrt{N})/2$. A single degree of freedom per blade model with a negligible damping is used to obtain this upper limit to the amplification factor. This expression reveals that the number of blades is a major factor influencing the maximum forced response amplification.

Subsequent analyses [55–57] typically have supported and qualified the occurrence of such amplitude, and also extended the discussion to multi-degree of freedom per blade models [58; 59] and further multi-stage assemblies [60]. The maximum amplification factors were announced ranging from about 1.2 to 5.3 in these research efforts. On the other hand, these studies have also argued that the maximum amplification factor is affected by a range of possible factors, such as the mistuning strength, coupling level, attainable damping and the specificity of

operating conditions, etc. For this reason, the conflicting results tend to be case-dependent and difficult to generalize. A better understanding of the interaction of important factors affecting the maximum forced response is needed.

Mistuning pattern

It is well known that some particular pattern of the blade mistuning has a large effect on the forced response amplification, even for small mistuning. It is then natural to wonder what kind of mistuning patterns lead to high or low forced response and whether there exist common characteristics among these worst/best mistuning pattern.

Ewins [61] has first noted that by careful rearrangement of the same set of non-identical blades on the disk, it is possible to reduce the maximum forced response levels. There have been several studies on using optimization methods to find the worst and best overall mistuning pattern in terms of forced response amplification in recent decades [62; 63]. Petrov and Ewins [57] showed that the same set of 92 blades can be rearranged into a pattern, such that the maximum forced response could have a value less than 2 for the best arrangement and greater than 5 for the worst blade arrangement. If the industrial blades are detachable, this indicates a considerable potential for vibration reduction of mistuned bladed disks by simply rearranging the blade locations.

Mistuning identification

For mistuned bladed disk vibration research, how to identify the mistuning pattern existing in a manufactured bladed disk is also of engineering interest. For disks with detachable blades, the standard method consists of removing the individual blades for measurements of their natural frequencies. But problems arise when it comes to the integrally bladed disk structures (blisks), where the blades and disk form one integral piece and blades can not be removed from the assembly. Therefore, in order to accurately identify mistuning pattern in blisks, mistuning identification techniques based on experimental measurements of system response have been therefore developed recently to determine the individual blade mistuning pattern.

Mistuning identification is achieved through global measurements on the whole blisk structure followed by a global model updating procedure. Early work toward this goal has been reported by Judge et al. [64], in which the authors have developed a method of using free response system measurements to identify the blade modal stiffnesses present in a reduced-order model of a blisk and described preliminary experimental validation of this technique. Other early works on mistuning identification have made use of lumped parameter models [28; 65]; more recently, several alternative reduced-order models have been applied to mistuning identification [66–68]. Mistuning identification can also be beneficial in terms of damage detection applications in bladed disks, such as crack monitoring [44].

1.5.4 Mistuning is always adverse?

The answer is "no" ! Early studies reveal that mistuning is not only a phenomenon with adverse effects. In some special cases, mistuning tends to be beneficial. For instance, periodic structure can become stable in terms of flutter with a small mistuning between sectors of this structure [69]. Several studies have also shown numerically that frequency mistuning has the effect of increasing the flutter stability by distributing the energy of unstable flutter modes over a range of stable modes [70; 71].

In particular, a new phenomenon of reducing blade disk forced response by random mistuning is reported by Petrov [47; 72]. In these studies, a high-fidelity method is proposed which allows the use of industrial-size sector models of bladed disks for analysis of forced response of mistuned structures in the gas flow. This method consists of two decoupled steps:

1. CFD (Computational Fluid Dynamic) analysis. During this step the modal aerodynamic forces are calculated for a tuned bladed disk vibrating with a frequency of interest, i.e. the excitation frequency.

2. Mistuned forced response analysis. The CFD characteristics obtained in the previous step are then combined with different mistuned bladed disks for forced response calculations.

Aerodynamic damping, the interaction of vibrating blades through gas flow

and the effects of structural/aerodynamic mistuning are thus involved in the model. A newly observed phenomenon has been declared by Petrov: forced response levels for any randomly mistuned bladed disk can be smaller than those of its tuned counterpart by several times.

This conclusion is astonishing because it is traditionally and widely believed that mistuning is generally adverse for forced response levels, although it is favorable for flutter suppression. The involved aerodynamic effects definitively determines the new finding in the mistuned bladed disk analysis.

It is explained that a major cause of this reported vibration reduction phenomenon by any random mistuning are the differences in modal damping values. These differences are introduced by aerodynamic forces. As remarked earlier, localized modes caused by mistuning contains multiple harmonic contents. The mistuned modes containing tuned mode shapes with all numbers of nodal diameters are excited even by a single engine order excitation. Therefore, in the expansion of a mode shape of the mistuned bladed disk over mode shapes of a tuned bladed disk, contributions of tuned modes with numbers of nodal diameters different from excitation EO can be significant. When mode shapes corresponding to the engine order excitation have smaller damping values than the rest of the modes, then excitation of modes with higher modal damping factors makes the resulting damping factor higher than that for a tuned bladed disk. When this situation is arrived, a reduced forced response level is observed.

Finally, this phenomenon is expected to occur for most industrial bladed disks for which aerodynamic damping is significant. Moreover, such reduction of the forced response does not require any special intentional mistuning pattern: any random mistuning can be beneficial. Hence, a series of questions naturally arise:

- The research work is based on the hypothesis that flow fields in the tuned and mistuned bladed disk share the same CFD characteristics. However, does this strong assumption really hold?

- What is the realistic aerodynamic damping level for a mistuned bladed disk in gas flow?

- If this vibration reduction phenomenon due to mistuning could manifest

in many other bladed disks, then how to explain the excessive amplitudes responsible for occasional blade high cycle fatigue failures?

It is also admirable that this high-fidelity method is capable of including all aerodynamics effects that are typically absent in the literature. With the development in CFD, it can be seen that more and more research efforts will taken into account the aerodynamic environment for the mistuned bladed disk analysis. Let's terminate this section by quoting Srinivasan in 1997 [3]: "Vibrations of bladed disks occur in an aerodynamical environment and therefore it is only appropriate that significant advances in the aerodynamic and structural dynamic characteristics be realized. The subject matter is an interdisciplinary one requiring expertise in aerodynamics of cascades as well as structural dynamics of bladed disk assemblies leading to aeroelasticity of blades."

1.6 Vibration reduction in mistuned bladed disks

Vibration of mistuned bladed disks have been widely investigated, as presented in the precedent section; while studies of methods to reduce the blade vibration have been conducted to a less extent. The worsening effects of mistuning have challenged researchers to seek means of vibration reduction and prevention of the worst case. Intentional mistuning is an appealing design strategies from many viewpoints. In the mitigation practice, additional damping is usually introduced into the structure in order to reduce vibration amplitudes. The latter will receive special attention in this thesis.

1.6.1 Intentional mistuning

Intentional mistuning refers to a deliberate mistuning pattern that can be implemented in the nominal design that will make the bladed disk less sensitive to random mistuning in operation.

The first study that have used an intentional mistuning in design of mistuned bladed disks is attributed to Castanier and Pierre [73] in 1997. They have demonstrated a feasibility of employing the intentional mistuning in harmonic (sinusoidal) patterns to significantly decrease the maximum forced response on

a simple 12-bladed spring-mass model. Subsequent studies [74–77] supporting this finding have also examined a range of intentional mistuning patterns. For example, square-wave patterns of intentional mistuning, which only require two different blade types, is a more practical consideration for its easy implementation.

Furthermore, intentional mistuning makes the bladed disk design much more robust with respect to extra random mistuning. It is explained that the amplitude magnification often exhibits a peak with respect to a moderate mistuning strength, as discussed in Sec.1.5.2. If the intentional mistuning is put on the right side of the peak, the extra random mistuning would barely affect the forced response level. Further studies considered the optimization of intentional mistuning patterns by means of simple genetic algorithm [78] and sequential quadratic programming method [79].

1.6.2 Additional damping

Intentional mistuning is not the only feasible forced response reduction strategy. Escalation of stresses due to resonant responses and flutter can be minimized only if there is adequate damping in the system. System damping of bladed disks in gas flow is the sum of available aerodynamic damping and mechanical damping. It is widely thought that bladed disks are weakly damped in the functional environment. In the mitigation practice, additional damping is introduced into the structure to reduce vibration amplitudes. Different types of mechanical damping and new emerging damping technologies are presented below.

Friction damping

Since the 1980s, friction damping becomes the most common approach to effectively damping the resonance mode of interest. Vibration energy is herein dissipated in frictional contacts between two adjacent blades or in a blade-disk interfaces. Friction dampers consists of underplatform dampers (Fig. 1.9) [80], snubbers and tip shrouds (Fig. 1.10) [81], friction rings (Fig. 1.11) [82]. All friction dissipation systems or mechanisms, except snubbers, are designed at the blade tip (e.g. shrouds) or under the airfoil platform, so that the aerodynamic

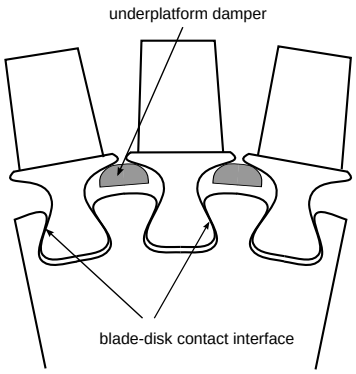

Figure 1.9: Illustration of underplatform damper

performance in the cascade is not perturbed by the presence of friction dampers.

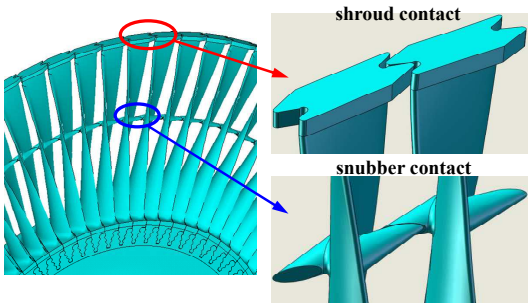

Figure 1.10: Contact configuration of snubbers and shrouds

The phenomenon of friction between contacting surfaces is an elusive physical mechanism. The complexity of friction damping arises from variations in the type of time-dependent motions at the contact interfaces. To predict the vibration amplitudes including frictional sliding, nonlinear dynamic contact models have to be considered and sophisticated computational strategies are necessary [83; 84]. Various physical parameters such as friction coefficients, contact stiffness and time-varying normal load are difficult to estimate and model. Microslip behavior (small relative displacements in the tangential directions) at the contact interface also have a damaging effect, since fretting-wear appears and can induce

cracking [85]. Besides, large finite element model of full bladed disks describing the contact interactions usually requires prohibitive computational resources. Effective computational strategies are devised by Petrov [30; 86].

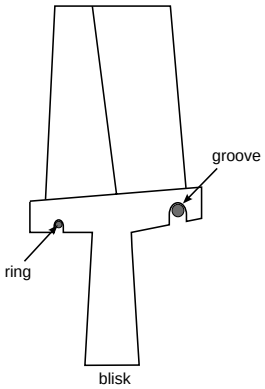

Figure 1.11: Friction ring dampers in their grooves

Coating materials

For the materials currently in use for manufacturing blades (titanium-based and nickel-based alloys), contributions to mechanical damping is essentially negligible [3]. To increase the material damping, damping materials are treated over the blade surface. Although such coatings applied to blades are generally quite thin, they have been shown to add significant damping to the system [87]. A study on improving material damping of blades due to coating is presented with measuring and modeling results [88]. Such coatings are found to display nonlinear mechanical properties in the stiffness. Thus, system nonlinearity arising from a nonlinear coating should be incorporated into the forced response prediction of blades. This issue is addressed in the recent research by Filippi and Torvik [89].

Eddy current damping

A non-contact damping mechanism based on eddy current damping applied in bladed disk has been investigated by Laborenz and Krack et al.[90; 91]. In this non-contacting approach permanent magnets and copper plates are embedded

into the blades facing each other between adjacent blades. In case of vibrations the relative movement between magnets and copper plates induces eddy currents in the conducting material such that mechanical energy is converted to electrical energy which then dissipates into heat and, therefore, leads to an amplitude reduction.

Piezoelectric shunt damping

Another vibration damping technology, piezoelectric shunt damping, is receiving a growing awareness for its possible application in bladed disks. The piezoelectric effect is the ability of a material to generate electric charges when subjected to external forces. Thus the piezoelectric material bonded to flexible structures is capable of converting mechanical energy into electrical energy. If the piezoelectric material is connected to a shunt circuit, then the shunted impedance enables to dissipate the converted energy into heat, leading to an amplitude reduction. The term *shunt damping* is therefore used for a single piezoelectric ceramic connected to a shunt circuit. Passive shunt circuit only consists of discrete electric components, such as inductance, resistance and capacitance. An overview on the piezoelectric shunt damping will be presented in the following chapter.

1.7 Conclusion

To conclude, for tuned bladed disks, there are considerable savings in both computing cost and data storage associated with the application of cyclic symmetry property. With a real-valued spatial Fourier transform, it enables to carry out the full bladed disk structure analysis using only one sector, i.e. the reference sector.

Much insight to the vibration in mistuned bladed disk have been gained to date. In essence, the interaction between the disk and blade dynamics provides the dominant mechanism for energy transfer among blades. This blade-disk coupling enables vibration energy to be communicated and confined around certain blades, potentially determining the mistuning sensitivity of a bladed disk design. This may also raise the possibility of influencing the blade response through

damping the disk.

Excessive blade vibration level is usually observed in mistuned bladed disks. Additional damping is considered for the purpose of forced response reduction and increasing aerodynamic stability in terms of flutter. Several damping technologies for bladed disks are briefly introduced. Special attention will be paid to the piezoelectric shunt damping in this dissertation. The conception of piezoelectric shunt damping and modeling methodologies will be fully discussed in the next chapter.

Chapter 2

Conceptions of piezoelectric shunt damping

Conceptions of piezoelectric shunt damping will be fully discussed in this chapter, which will pave the way for its application to bladed disks. This chapter is initialized by an overview of piezoelectric materials. Constitutive equations and different transduction modes of piezoelectric materials are described. The concept of piezoelectric shunt damping is illustrated when piezoelectric materials are connected with classical shunt circuits, i.e. the resistive shunt circuit and resonant shunt circuit. Piezoelectric-based system modeling methodologies are presented both in the time domain and frequency domain. Recent advances in this area will be also covered in the end of this chapter.

2.1 Overview of piezoelectric materials

It was first demonstrated by Curie brothers in 1880 that when piezoelectric materials undergo mechanical deformation, an electric charge can be produced. This is referred to as piezoelectricity that these materials exhibit a coupling between their electrical, mechanical states. Piezoelectricity exists in materials either naturally or synthetically. Synthetic piezoelectric materials extensively used nowadays include lead zirconate titanate ($PbZrTiO_3 - PbTiO_3$, known as PZT), barium titanate, barium strontium titanate (BaSTO), etc [92; 93].

An important characteristic of piezoelectric material is the "Curie temperature". A manufactured piezoelectric ceramic consists of electric dipoles in random directions. This ceramic shows no piezoelectricity as a whole since the responses of these dipoles subjected to an externally applied electric field tend to cancel one another. If the ceramic is heated above the Curie temperature and exposed to a very strong electric field, the dipoles can change and align their orientation in the solid phase material. The direction of this electric field is referred to as the polarization direction. It determines the direction along which the dipoles are aligned. The material is then cooled below its Curie temperature with the polling field is maintained. This process is called as "polling". As a result of this process the alignment of the electric dipoles is permanently formed. Piezoelectricity then exists in this piezoelectric ceramic under Curie temperature.

When a poled piezoelectric material undergoes mechanical deformation, electric charges can be produced on the surface of ceramic and form an electric field in the polarization direction (direct effect). Conversely, if it is subjected to an electric field in the polarization direction, a mechanical deformation is formed in response, which produces an expansion along the polling direction and contraction in the perpendicular plane (converse effect). In general, piezoelectrics have the capability efficiently to transform mechanical energy to electrical energy and vice versa. It is this dual transformation ability that makes them useful as actuators or sensors.

2.1.1 Constitutive equations

Assuming linear characteristics and constant temperature, the standardized Piezoelectric constitutive equations [94] can be written as:

$$\begin{bmatrix} D \\ S \end{bmatrix} = \begin{bmatrix} \xi^T & d \\ d_t & s^\epsilon \end{bmatrix} \begin{bmatrix} \epsilon \\ T \end{bmatrix} \tag{2.1}$$

In matrix form of this expression, $D \in R^{3\times 1}$ is a vector of electrical displacement ($charge/area$); ϵ is the vector of electrical field in the material ($volts/meter$); S is the vector of material engineering strains, and T is the vector of material

stresses ($force/area$).

$$D = \begin{bmatrix} D_1 \\ D_2 \\ D_3 \end{bmatrix}, \epsilon = \begin{bmatrix} \epsilon_1 \\ \epsilon_2 \\ \epsilon_3 \end{bmatrix}, S = \begin{bmatrix} S_{11} \\ S_{22} \\ S_{33} \\ 2S_{23} \\ 2S_{13} \\ 2S_{12} \end{bmatrix} = \begin{bmatrix} S_1 \\ S_2 \\ S_3 \\ S_4 \\ S_5 \\ S_6 \end{bmatrix}, T = \begin{bmatrix} T_{11} \\ T_{22} \\ T_{33} \\ T_{23} \\ T_{13} \\ T_{12} \end{bmatrix} = \begin{bmatrix} T_1 \\ T_2 \\ T_3 \\ T_4 \\ T_5 \\ T_6 \end{bmatrix} \tag{2.2}$$

The direction 3 is associated with the polarization direction. These direction conventions are shown in Fig. 2.1. s^{ϵ} is the (6×6) compliance matrix, which

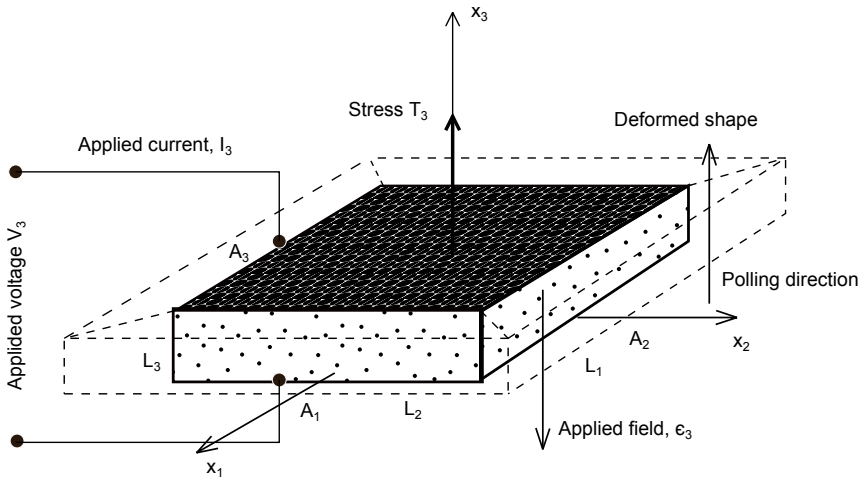

Figure 2.1: A typical piezoelectric material with the top and bottom surfaces electrode and x_3 axis in the polarization direction [94]

relate the two elastic variables, stain S and stress T. The superscripts, such as $[.]^{\epsilon}$, on material properties typically denote the mechanical or electrical boundary conditions under which the constants are valid. Hereby $[.]^{\epsilon}$ is to emphasize the fact that it has been measured at constant electric field (e.g. short circuit).

ξ^T is the (3×3) dielectric or permittivity constants matrix, which relates the two electrical variables, electrical displacement D and electrical field ϵ. The superscript $[.]^T$ signifies that these values are measured at constant stress.

Finally, d is another (3×6) coupling matrix in $Coulomb/Newton$ or $m/Volt$.

It is a matrix of piezoelectric constants, which couples the mechanical and electrical equations through the piezoelectric effect. The subscript $[.]_t$, represents the conventional matrix transpose temporarily in this section.

2.1.2 Different transduction modes

In taking advantage of the transverse isotropic property of piezoelectrics, the constitutive equation Eq. (2.1) can be further developed explicitly [93]. For PZT ceramics, they are:

- Actuation:

$$\begin{bmatrix} S_{11} \\ S_{22} \\ S_{33} \\ 2S_{23} \\ 2S_{13} \\ 2S_{12} \end{bmatrix} = \begin{bmatrix} s^{\epsilon}_{11} & s^{\epsilon}_{12} & s^{\epsilon}_{13} & 0 & 0 & 0 \\ s^{\epsilon}_{12} & s^{\epsilon}_{22} & s^{\epsilon}_{23} & 0 & 0 & 0 \\ s^{\epsilon}_{13} & s^{\epsilon}_{23} & s^{\epsilon}_{33} & 0 & 0 & 0 \\ 0 & 0 & 0 & s^{\epsilon}_{44} & 0 & 0 \\ 0 & 0 & 0 & 0 & s^{\epsilon}_{55} & 0 \\ 0 & 0 & 0 & 0 & 0 & s^{\epsilon}_{66} \end{bmatrix} \begin{bmatrix} T_{11} \\ T_{22} \\ T_{33} \\ T_{23} \\ T_{13} \\ T_{12} \end{bmatrix} + \begin{bmatrix} 0 & 0 & d_{31} \\ 0 & 0 & d_{32} \\ 0 & 0 & d_{33} \\ 0 & d_{24} & 0 \\ d_{15} & 0 & 0 \\ 0 & 0 & 0 \end{bmatrix} \begin{bmatrix} \epsilon_1 \\ \epsilon_2 \\ \epsilon_3 \end{bmatrix} \tag{2.3}$$

- Sensing:

$$\begin{bmatrix} D_1 \\ D_2 \\ D_3 \end{bmatrix} = \begin{bmatrix} 0 & 0 & 0 & 0 & d_{15} & 0 \\ 0 & 0 & 0 & d_{24} & 0 & 0 \\ d_{31} & d_{32} & d_{33} & 0 & 0 & 0 \end{bmatrix} \begin{bmatrix} T_{11} \\ T_{22} \\ T_{33} \\ T_{23} \\ T_{13} \\ T_{12} \end{bmatrix} + \begin{bmatrix} \xi^T_1 & 0 & 0 \\ 0 & \xi^T_2 & 0 \\ 0 & 0 & \xi^T_3 \end{bmatrix} \begin{bmatrix} \epsilon_1 \\ \epsilon_2 \\ \epsilon_3 \end{bmatrix} \tag{2.4}$$

As just mentioned, the direction 3 coincides with the polarization direction of the piezoelectric materials. PZT materials are isotropic in the plane, and thus have $d_{31} = d_{32}$ and $d_{24} = d_{15}$. Typical values for piezoelectric constants are given for PZT-4 [93]: $d_{33} = 289$, $d_{31} = -123$, $d_{15} = 496$ (units: $10^{-12}C/N$).

According to Eq. (2.3), three different piezoelectric transduction mode could be derived in engineering applications. The transduction modes illustrated in Fig. 2.2 mainly depend on the directions of applied force and electrical field:

- d_{33} mode or thickness mode. Force and field are both in 3 direction. In this case, several thin slices of PZT are usually stacked together and separated by electrodes. When an electric field ϵ_3 is applied, the piezo transducers may expand along its thickness (d_{33}) and shrink in the in-plane directions, because the d_{31} and d_{32} coefficients are negative.

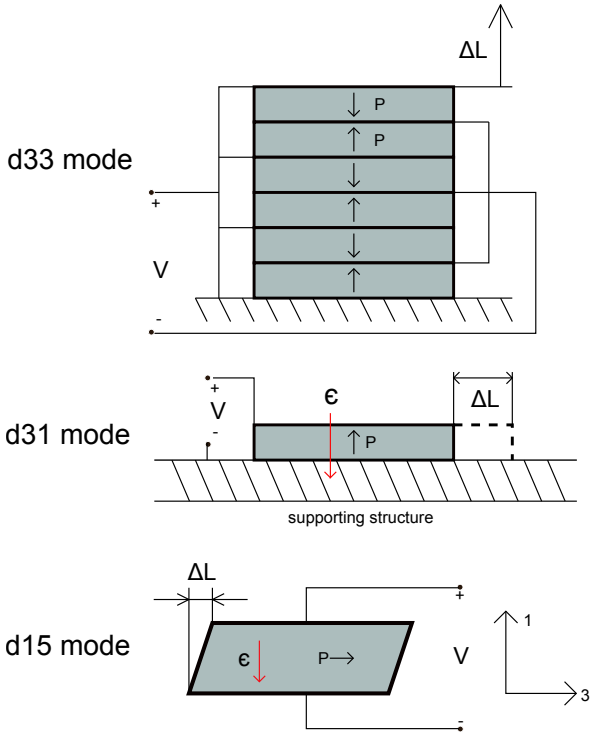

Figure 2.2: Different piezoelectric transduction modes [95]; P: polarization direction, ϵ: electric field.

- d_{31} mode or transverse mode. A thin piezoelectric patch is usually bonded onto a plate structure. The expansion or contraction is generated along with the movement of the supporting structure. The direction of expansion or contraction is perpendicular to the electric field.

- d_{15} mode or shear mode, the application of electric field ϵ_1 or ϵ_2 (normal to the polarization direction 3) produces a shear deformation S_5 or S_4. d_{15} typically has the largest values among all piezoelectric constants.

This thesis mainly deals with the transverse d_{31} mode in Chapter 3 and the thickness d_{33} mode in Chapter 5.

We recall that the existence of piezoelectricity in piezoelectric materials is observed below the Curie temperature. High temperature usually changes the crystal structure of ceramics, resulting in no net macroscopic dipole in the materials. The Curie temperature is usually in the range of $300\,°\mathrm{C} - 400\,°\mathrm{C}$. Although typically fixed, this range can be changed and tuned accordingly if needed [93]. This issue is hereby addressed out of practical consideration for its application in aeroengine since the working environment of bladed disks is featured by high temperature.

Electromechanical coupling factor

Piezoelectric electromechanical coupling factors are material constants that measure the effectiveness of the conversion of mechanical energy into electrical energy (and vice versa). In the direct piezoelectric effect, it is quantitatively defined as the ratio of the stored electrical energy to applied mechanical energy [93]:

$$k_{ij}^2 = \frac{\text{stored electrical energy (electric field and electric displacement) in direction } i}{\text{applied mechanical energy (stress and strain) in direction } j} \tag{2.5}$$

This factor plays a vital role in shunt damping of piezoelectric shunted structures in the rest of this chapter. Three different factors for different transduction modes are determined by:

- d_{33} mode: $k_{33} = d_{33}/\sqrt{s_{33}^{\epsilon}\xi_3^T}$
- d_{31} mode: $k_{31} = k_{32} = d_{31}/\sqrt{s_{11}^{\epsilon}\xi_3^T}$
- d_{15} mode: $k_{15} = k_{24} = d_{15}/\sqrt{s_{55}^{\epsilon}\xi_1^T}$

Accordingly, the higher the value of this factor, the more efficient the energy conversion is. PZT ceramics typically have $k_{33} \approx k_{15} \approx 0.7$ and $k_{31} \approx 0.3$ [93].

2.2 Piezoelectric shunt damping

Passive piezoelectric damping applications have been investigated completely by Hagood and Von Flotow [94] in 1990. In this research, the derivation for analysis of general structural systems with shunted piezoelectrics are established. In energy dissipation applications, the electrodes of the piezoelectric are shunted with some electrical impedance; hence the term *piezoelectric shunt damping* is used. The electrical impedance is designed to dissipate the electrical energy which has been converted from mechanical energy by the piezoelectric. In the following sections, the shunted piezoelectric's interaction with external circuits will be modeled, and classic passive shunt circuits will be compared. The derivation for analysis of resonant shunt circuits will also benefit the nondimensionalization process of essentially nonlinear shunt circuits in Chaper 6. The methodology adopted here is the impedance-based formulation put forward by Hagood and Von Flotow and recently applied by Benjedou and Ranger-Vieillard [96; 97]. Alternatively, a time-domain modeling method is also presented.

2.2.1 Piezoelectric-based system modeling: in the frequency domain

A typical application of piezoelectric working in the d_{31} mode is shown in Fig. 2.3. In engineering applications,two identical piezoelectric patches are usually attached onto surfaces of a beam-like structure in order to enhance the energy conversion. Note that both patches are poled in the same direction 3. The deformation of piezoelectric patches along with bending movement of the beam will thus create opposite electric field directions due to their relative location. Piezoelectric transducers behave electrically like a charged capacitance C_p, since electric charges arising out of piezoelectricity cumulate on the ceramic surface. Connected with shunt impedances Z_{sh}, piezoelectric patches are capable of converting the mechanical energy into electrical energy and dissipating this converted energy.

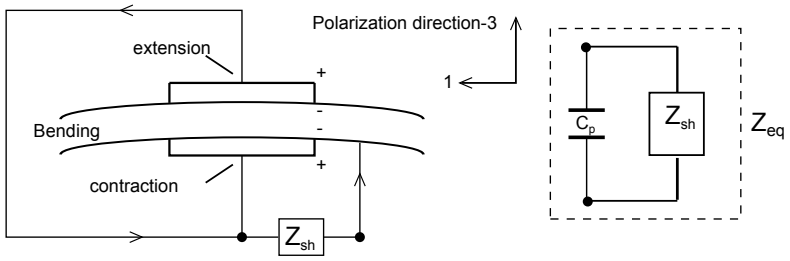

Figure 2.3: Piezoelectric in transverse mode connected with shunt impedance

Shunted piezoelectric model

For the piezoelectric patches working in the transverse mode with one-dimensional stress loading in the longitudinal direction 1, according to Eq. (2.1), the reduced constitutive equation can be written as follows:

$$\begin{bmatrix} D_3 \\ S_1 \end{bmatrix} = \begin{bmatrix} \xi_3^T & d_{31} \\ d_{31} & s_{11}^{\epsilon} \end{bmatrix} \begin{bmatrix} \epsilon_3 \\ T_1 \end{bmatrix} \tag{2.6}$$

It is assumed that both the electric field and electric displacement are constant through the thickness direction. We then introduce a linear relationship for the capacitance of the piezoelectric patch at constant stress C_p^T:

$$D_3 = \frac{q_3}{A_3}, \quad \epsilon_3 = \frac{V_3}{h}, \quad C_p^T = \frac{\xi_3^T A_3}{h} \tag{2.7}$$

where q_3 is the charge collected on the electrode surface A_3; V_3 is the difference of electric potential in the upper and lower electrodes, and h is the piezoelectric thickness along direction 3.

According to the impedance-based formulation in [94], the electric current in the Laplace domain is expressed by $I_3 = sq_3$, where s is the Laplace variable. Furthermore the open circuit electrical impedance at constant stress Z_{oc}^T is introduced by:

$$Z_{oc}^T = \frac{1}{sC_p^T} \tag{2.8}$$

It enables us to express Eq. (2.7) in terms of the piezoelectric impedance:

$$\begin{bmatrix} I_3 \\ S_1 \end{bmatrix} = \begin{bmatrix} 1/Z_{oc}^T & sA_3d_{31} \\ d_{31}/h & s_{11}^\epsilon \end{bmatrix} \begin{bmatrix} V_3 \\ T_1 \end{bmatrix} \tag{2.9}$$

When the piezoelectric patch is connected by a shunt impedance Z_{sh} , as shown in Fig. 2.3, the piezoelectric impedance Z_{oc}^T can be replaced by an equivalent impedance Z_{eq}:

$$Z_{eq} = \frac{Z_{oc}^T Z_{sh}}{Z_{oc}^T + Z_{sh}} \tag{2.10}$$

We recall the electromechanical coupling factor k_{31} and non-dimensional electrical impedance:

$$k_{31} = \frac{d_{31}}{\sqrt{s_{11}^\epsilon \xi_3^T}}, \quad \bar{Z}_{eq} = \frac{Z_{eq}}{Z_{oc}^T} \tag{2.11}$$

Substituting Eq. (2.10) and Eq. (2.11) into Eq. (2.9) yields an expression of the strain S_1 in terms of the stress T_1 and electric current I_3:

$$S_1 = s_{11}^\epsilon (1 - k_{31}^2 \bar{Z}_{eq}) T_1 + \left(\frac{d_{31}}{h} Z_{eq} \right) I_3 \tag{2.12}$$

The shunted piezoelectric compliance is then defined as:

$$s_{11}^{sh} = s_{11}^\epsilon (1 - k_{31}^2 \bar{Z}_{eq}) \tag{2.13}$$

It indicates that the shunted impedance Z_{sh} imposes a modification on the piezoelectric compliance s_{11}^ϵ. In the open circuit condition characterized by $Z_{sh} \to \infty$, we have

$$\bar{Z}_{eq} = 1, \quad s_{11}^{oc} = s_{11}^\epsilon (1 - k_{31}^2) \tag{2.14}$$

and conversely a short circuit condition is achieved for a null shunt impedance $Z_{sh} = 0$, so that:

$$\bar{Z}_{eq} = 0, \quad s_{11}^{sc} = s_{11}^\epsilon \tag{2.15}$$

We can also write the shunted elastic modulus in terms of the short circuit one $c_{11}^{sc} = 1/s_{11}^\epsilon$ as:

$$c_{11}^{sh} = \frac{c_{11}^{sc}}{(1 - k_{31}^2 \bar{Z}_{eq})} \tag{2.16}$$

Following the simplification in the classic beam theory, piezoelectric patch's stiffness along direction 1 can be approximated by:

$$k_{11} = \frac{c_{11} A_1}{L_1} \tag{2.17}$$

where A_1 and L_1 are the area of the cross section along direction 1, respectively.

Using equation (2.16), when bonded on the surface of structures, the shunted piezoelectric patch's stiffness k_{11}^{sh} can be obtained in terms of the short circuit one k_{11}^{sc}:

$$k_{11}^{sh} = \frac{c_{11}^{sh} A_1}{L_1} = \frac{c_{11}^{sc} A_1}{(1 - k_{31}^2 \bar{Z}_{eq}) L_1} = \frac{k_{11}^{sc}}{1 - k_{31}^2 \bar{Z}_{eq}} \tag{2.18}$$

Accordingly, different shunt circuits lead to various $\bar{Z}_{eq}$, and exerts a significant impact on the damping capability of piezoelectric transducers. Two classical shunt circuits, i.e. resistive shunt circuit and resonant shunt circuit will be covered below.

Resistive & Resonant shunt circuit

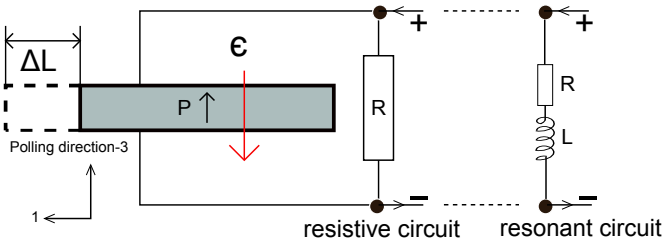

Figure 2.4: Piezoelectric connected with resistive & resonant shunt circuit

For a resistive shunt circuit, the impedance Z_{sh} is a resistance R as illustrated in Fig. 2.4. In this case, the normalized equivalent electrical impedance is:

$$\bar{Z}_{eq} = \frac{sRC_p^T}{1 + sRC_p^T} \tag{2.19}$$

In considering a harmonic excitation with frequency ω , such that $s = i\omega, i^2 = -1$, and using Eq. (2.18), the shunted piezoelectric stiffness k_{11}^{sh} can be rewritten

as the following frequency dependent complex stiffness:

$$k_{11}^{sh}(i\omega) = \frac{1 + i\omega RC_p^T}{1 + i\omega RC_p^T(1 - k_{31}^2)}\, k_{11}^{sc} \tag{2.20}$$

Another case of interest is to create a resonant circuit by shunting the piezoelectric inherent capacitance C_p with a resistance R and inductance L in series forming a LRC circuit for Z_{eq}. This circuit is also shown in Fig. 2.4. The normalized equivalent electrical impedance is:

$$\bar{Z}_{eq} = \frac{s^2 LC_p^T + sRC_p^T}{1 + s^2 LC_p^T + sRC_p^T} \tag{2.21}$$

In a similar way, substituting the expression Eq. (2.21) into Eq. (2.18), we have the following frequency dependent complex stiffness of resonant shunted piezoelectrics:

$$k_{11}^{sh}(i\omega) = k_{11}^{sc} \frac{1 + i\omega RC_p^T - \omega^2 LC_p^T}{1 + i\omega RC_p^S - \omega^2 LC_p^S} \tag{2.22}$$

Performance comparison of classic shunt circuits

Now that the expressions of the shunted piezoelectric stiffness have been established. The objective is then to evaluate the effective dissipation of the vibration energy for a targeted structural mode, using resistive & resonant shunted piezoelectric materials. For this purpose, the damping of a single-mode mechanical system with shunted piezoelectric is now considered, through the study of the single degree of freedom (SDOF) system shown in Fig. 2.5.

Given the single modal parameters m, k of a mechanical structure, denote the modal mechanical displacement $x(t) = Xe^{i\omega t}$ and the modal excitation $f(t) = Fe^{i\omega t}$, the equation of motion of this SDOF system can be written now in the frequency domain as

$$[-\omega^2 m + k + k_{11}^{sh}(i\omega)]X = F \tag{2.23}$$

The problem associated with the parameter optimization of two different shunt circuits is to add maximum damping to the targeted structural mode. Conventionally known as "tuning" design, it is briefly introduced, respectively.

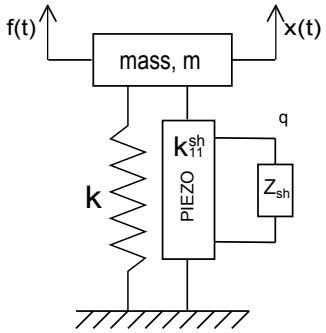

Figure 2.5: A SDOF mechanical system with shunted piezoelectric patches

For the resistive shunt circuit, introducing C_p^S as the piezoelectric capacitance at constant strain, such that $C_p^S = C_p^T(1 - k_{31}^2)$, and defining a non-dimensional frequency:

$$\rho = RC_p^S\omega \tag{2.24}$$

then one can represent the complex stiffness Eq. (2.20) in the standard complex modulus form:

$$k_{11}^{sh} = K_{11}^{sh}(1 + i\eta^{sh}) \tag{2.25}$$

where the real part of k_{11}^{sh} is defined as the modulus K_{11}^{sh}, and the ratio between the imaginary and real parts η^{sh} is defined as the loss factor. The key point for resistive circuit tuning is that a maximum loss factor turns out at a transition point:

$$\rho_{opt} = RC_p^S\omega = \sqrt{1 - k_{31}^2} \tag{2.26}$$

Consequently, by appropriate choice of resistance, the peak of the loss factor can be move to any target modal frequency. The optimal resistance that maximizes the loss factor at a given frequency ω can be obtained as

$$R_{opt} = \frac{1}{\omega C_p^T\sqrt{1 - k_{31}^2}} \tag{2.27}$$

For the resonant shunt circuit, key similarities have been observed between a system containing a resonant shunted piezoelectric and a system containing a mechanical vibration absorber or proof mass damper. In order to make the

expressions non-dimensional, the following parameters are introduced:

- $\omega_n = \sqrt{k/m}$, resonance frequency of the mechanical system;
- $\omega_e = \sqrt{1/LC_p^S}$, electrical resonance frequency;
- $\delta^t = \omega_e/\omega_n$, nondimensional tuning ratio;
- $\omega_n^{sc} = \sqrt{(k + k_{11}^{sc})/m}$, short circuit natural frequency of the SDOF system;
- $\omega_n^{oc} = \sqrt{(k + k_{11}^{oc})/m}$, open circuit natural frequency of the SDOF system;
- $r = RC_p^S\omega_n^{sc}$, electric damping ratio;
- $g = \omega/\omega_n$, nondimensional frequency;
- $K_{31}^2 = \left(\frac{k_{11}^{sc}}{k+k_{11}^{sc}}\right)\left(\frac{k_{31}^2}{1-k_{31}^2}\right) = \bar{K}\left(\frac{k_{31}^2}{1-k_{31}^2}\right)$, generalized electromechanical coupling coefficient.

The generalized electromechanical coupling proposed by Hagood and Von Flotow [94] is a direct measurement of a shunted piezoelectric's influence on the global system. It is widely used for determining the optimal nondimensional tuning ratio δ_{opt}^t and electric damping ratio r_{opt}:

$$\delta_{opt}^t = \sqrt{1 + K_{31}^2} \tag{2.28}$$

$$r_{opt} = \frac{\sqrt{2K_{31}^2}}{1 + K_{31}^2} \tag{2.29}$$

The optimal resistance and inductance values of the resonant shunt circuit for a targeted structural mode could then be calculated by:

$$R_{opt} = \frac{r_{opt}}{C_p^S\omega_n^{sc}} \tag{2.30}$$

$$L_{opt} = \frac{1}{C_p^S(\delta_{opt}^t\omega_n^{sc})^2} \tag{2.31}$$

Fig. 2.6 typically illustrates the performance of vibration reduction due to different piezoelectric shunt damping. The nondimensional ratios given for optimal tuning and electrical damping of the resonant shunt circuit is used to minimize

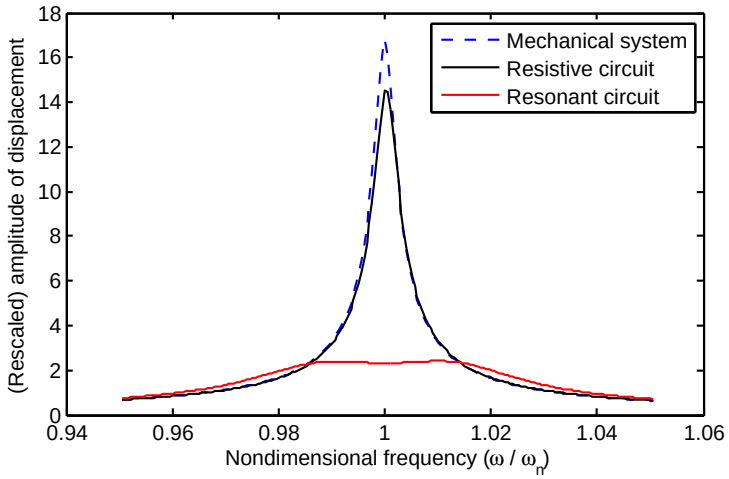

Figure 2.6: Performance of piezoelectric shunted mechanical system

the maximum response of the targeted mode in the way analogous to proof mass damper tuning. The effectiveness of the resonant shunted piezoelectric damper at optimal tuning is dependent on the generalized electromechanical coupling efficient. Moreover, a tuned resonant shunt circuit (———) can increase the structural mode damping several orders of magnitude above a simple resistive shunt circuit (———). Considering that the damping level in the realistic bladed disk arising from aerodynamic and structural environment is very low, we expect to introduce piezoelectric shunt damping into the structure as much as possible. For this reason, we confine to the resonant shunt circuit in terms of passive piezoelectric shunt damping in the rest of this thesis.

Despite the good prospect of resonant shunted piezoelectric as additional damping, it also exhibits some disadvantages:

- Impractical large and massive inductance is required for the low-frequency electrical resonance with the small inherent piezoelectric capacitance. The size required for the inductance is proportional to the inverse square of the frequency;

- In the tuning design, the electrical resonance is tuned very close to the structural resonance. The behavior of resonant shunted piezoelectrics is

very sensitive to the deviation of both structural parameters and optimal electrical parameters.

2.2.2 Piezoelectric-based system modeling: in the time domain

In this subsection, a time-domain modeling method for shunted piezoelectric integrated into the SDOF structure [98] is also presented, which will also be used in this thesis.

Let's recall the configuration in Fig. 2.5. Performing a force balance on the mass yields

$$m\ddot{x} + k\,x + f_p = f(t) \tag{2.32}$$

where f_p is the force due to the piezoelectric element. The force f_p could be derived by examining the reduced piezoelectric constitutive equation Eq. (2.6). Using relations presented in Eq. (2.7). The piezoelectric constitutive equation can be rearranged as:

$$q_3 = C_p^T V_3 + A_3 d_{31} T_1 \tag{2.33}$$

$$S_1 = s_{11}^{\epsilon} T_1 + d_{31} V_3 / h \tag{2.34}$$

The stress and strain along the direction 1 can be defined as:

$$S_1 = \frac{x}{L_1}, \quad T_1 = \frac{f_p}{A_1} \tag{2.35}$$

Substituting equation (2.35) into (2.32) and (2.34) yields:

$$q_3 = C_p^S V_3 + k_{11}^{sc} d_{31} \frac{L_1}{h} x \tag{2.36}$$

$$f_p = k_{11}^{sc} x - k_{11}^{sc} d_{31} \frac{L_1}{h} V_3 \tag{2.37}$$

Combining Eq. (2.32) with (2.36) and (2.37) gives the equation of motion for

the SDOF modal structure with a piezoelectric element:

$$m\ddot{x} + (k + k_{11}^{sc})\, x = f(t) + \frac{k_{11}^{sc} d_{31} L_1}{C_p^S h} q_3 - \frac{(k_{11}^{sc} d_{31} L_1 / h)^2}{C_p^S} x \tag{2.38}$$

or

$$m\ddot{x} + (k + k_{11}^{oc})\, x = f(t) + \frac{k_{11}^{sc} d_{31} L_1}{C_p^S h} q_3 \tag{2.39}$$

From Eq. (2.14) and (2.15) a relation can be readily obtained:

$$k_{11}^{oc} = \frac{k_{11}^{sc}}{1 - k_{31}^2} \tag{2.40}$$

The voltage across the piezoelectric electrode is:

$$V_3 = \frac{q_3}{C_p^S} - \frac{k_{11}^{sc} d_{31} L_1}{C_p^S h} x \tag{2.41}$$

Furthermore, when the piezoelectric material is connected with a RL shunt circuit, the governing equation for the shunt circuit is written as

$$L\ddot{q}_3 + R\dot{q}_3 + \frac{1}{C_p^S} q_3 - \frac{k_{11}^{sc} d_{31} L_1}{C_p^S h} x = 0 \tag{2.42}$$

Denoting $x = Xe^{i\omega t}$, $q_3 = Q_3 e^{i\omega t}$ and $f = Fe^{i\omega t}$, let us substitute these expressions into Eq. (2.38)-(2.42). The electric degree of freedom can be eliminated after mathematic manipulations by use of piezoelectric constitutive equations, which leads to:

$$[-\omega^2 m + k + k_{11}^{sc} \frac{1 + i\omega R C_p^T - \omega^2 L C_p^T}{1 + i\omega R C_p^S - \omega^2 L C_p^S}] X = F \tag{2.43}$$

Note that this express is the same as that one obtains in Eq. (2.23). Hence, the different modeling methodologies presented by Eq. (2.23) and Eq. (2.38)-(2.42) are equivalent in terms of describing the behavior of shunted piezoelectrics.

2.3 Recent advances in piezoelectric shunt damping

Hagood and Von Flotow [94] have initialized the complete and brilliant study about classical shunt circuits. In the past decades, there emerge a variety of research efforts on this subject [99; 100]. A number of recent advances in piezoelectric shunt damping will be briefly listed in this section.

Synthetic inductance

Resonant circuits require impractical high values for the inductance (typically hundreds or even thousands of Henries) in low frequency vibration cases. To overcome this limitation, synthetic inductance (or gyrators) are obtained by using operational amplifiers, as depicted in Fig. 2.7. The inductance value that can be achieved with these circuits is much larger (up to thousands of Henries); it however requires the supply of a power source [101]. These two different configurations, known as a) Riordan circuit and b) Antoniou circuit, yield equivalent attainable inductance values.

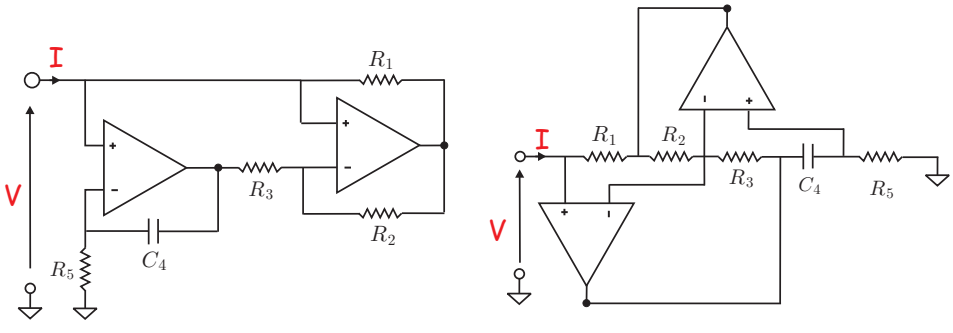

$$L = \frac{R_1 R_3 R_5 C_4}{R_2}$$

Figure 2.7: Synthetic inductances (gyrators) made of operational amplifiers: a) Riordan circuit; b) Antoniou circuit [95].

Multimodal damping

A question puzzling the academic community of piezoelectric has been: how can one extend the resonant shunt circuit to achieve multiple mode vibration suppression? One can attach a number of piezoelectric transducers to a structure, each one shunted by a RL circuit tuned to a specific mode [102]. The main focus in this area has been on finding multiple-mode vibration damping methods using a single piezoelectric transducer. Extension of a resonant shunt circuit for single-mode damping to multi-mode damping has been first considered by Hollkamp [103], who have used several RLC circuits connected in parallel (Fig. 2.8a). Wu [104] has proposed current-blocking parallel LC circuits to realize multimodal damping (Fig. 2.8b). More recently, parametric analyses have been performed to evaluate optimal configurations of a sole piezoelectric transducer for a set of damped modes [97; 105].

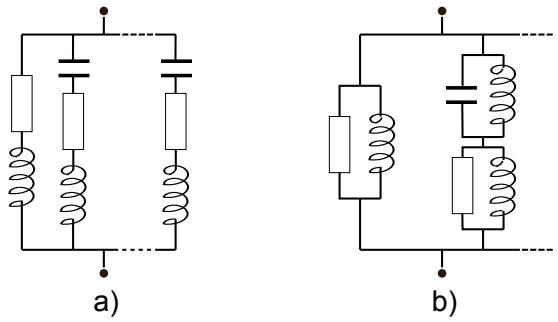

Figure 2.8: Electric circuits for multimodal damping

Negative capacitance

The electro-mechanical coupling coefficient, as shown in Section. (2.2), exerts a critical impact on piezoelectric shunt damping. This coefficient can be increased by introducing a negative capacitance. By connecting a negative capacitance in series with the piezoelectric material, the overall capacitance of the circuit is increased, resulting in a larger electro-mechanical coupling coefficient.

Although the negative capacitance cannot be realized passively and one needs to use an operational amplifier to form a negative impedance converter circuit

that requires a power source (see Fig. 2.9), the power consumption is little and it is an attractive approach for its multiple benefits in many situations. The negative capacitance increases the overall capacitance value of the shunt circuit, and directly reduces the required optimal inductance value. On one hand, the synthetic inductor becomes unnecessary if the required inductance is reduced to an acceptable low level; on the other hand, the negative inductance can share the power source with the synthetic inductor [106]. It is reported that the negative capacitance connected in series with piezoelectrics is capable of enhancing the electromechanical coupling and improving the shunt damping accordingly [95; 107].

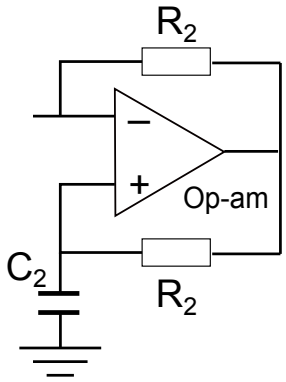

Figure 2.9: Circuit diagram of the negative capacitor. The equivalent negative capacitance value is expressed as: $C_n = -R_2C_2/R_2 = -C_2$.

Active shunt circuit

Piezoelectric shunt damping is not limited to passive circuits. A number of research works [106; 108] have investigated the use of hybrid circuits, in which the integration of the passive and active approach, often referred to as an active-passive hybrid piezoelectric network, has shown promising results.

Adaptive shunt circuit

The damping performances of the resonant circuit (both single-mode and multi-modes) are extremely sensitive to circuit tuning on the targeted structural natural

frequencies. Since synthetic inductance has been introduced as implementation of piezoelectric shunt impedances, the electric parameters are easily tuned online. Consequently Niederberger and Fleming et al. [109; 110] have proposed the use of adaptive circuits to compensate for a drift of the system characteristics.

Distributed shunt circuit

Thorp and Ruzzene et al. [111] have proposed that shunted piezoelectric patches are periodically distributed along rods (Fig. 2.10) to control the longitudinal wave propagation in the rods. Wave propagation over specified frequency bands, namely stop bands can be filtered in this periodic structure. Furthermore, it is found that disorder in the shunt parameters of periodically piezoelectrics typically extends the stop bands into adjacent propagation zones and produces vibration energy localization near the excitation source. Motivated by this research, we are also going to introduce intentional disorder of shunt parameters into periodic bladed disks. A number of sophisticated periodic electric networks have been further reported to achieve multimodal damping [112; 113].

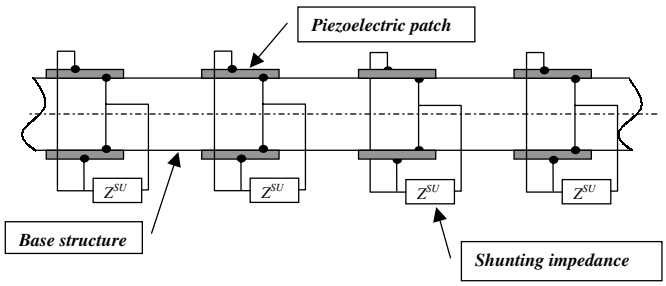

Figure 2.10: A rod with periodically distributed shunted piezoelectric patches [111]

Switched shunt circuit

The switched shunt circuit has also received much attention during the last decade. Lawrence and Clark [98] have proposed the "state switching" technique (Fig. 2.11a) in which piezoelectric elements play the role of a variable stiffness

actuator. A simple control law is employed to switch the piezoelectric element between high and low stiffness conditions in order to dissipate the vibration energy.

More recently, a nonlinear vibration control method, called the synchronized switch damping (SSD) technique, has been developed by Guyomar [114; 115]. This technique consists of adding a switching device (a switch and an inductance connected in series) in parallel with the piezoelectric elements (Fig. 2.11b). It allows to briefly inverse the voltage measured in the piezoelectric electrodes at selected instants. The switch is almost always open, except at selected instants. The switch is then kept closed until the voltage V on the piezoelectric elements has been inverted. Waveforms of the voltage V and displacement u are shown in the case of a sinusoidal excitation and when the voltage inversion instants correspond to the displacement extremes. Compared with resonant circuits, this technique does not require a high inductance value for a single structural mode. A multimodal control law for this SSD technique has also been developed.

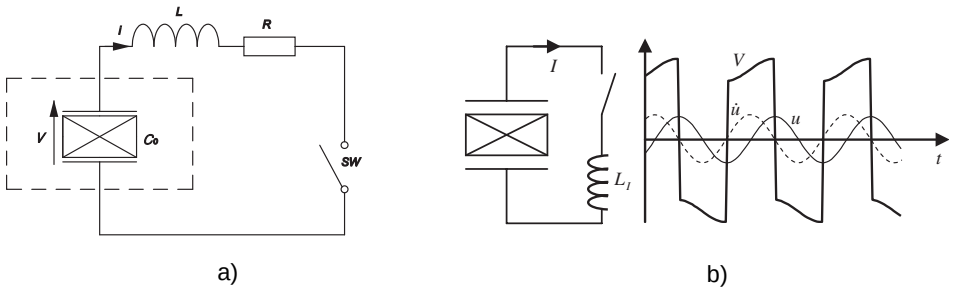

Figure 2.11: Various switched shunts: a) state switching shunt [98]; b) SSD device and waveforms of the voltage V and displacement u for a sinusoidal excitation [115].

Energy harvest device

In the last few years, there has been a surge of research in the area of power harvesting. The process of acquiring the energy surrounding a system and converting it into usable electrical energy is termed energy harvesting. Different from the

shunt damping, piezoelectric materials can also be used as mechanisms to transfer mechanical energy, usually ambient vibration, into electrical energy that can be stored and used to power other devices. With the recent advances in wireless and micro-electro-mechanical-systems (MEMS) technology, sensors can be placed in exotic and remote locations. As these devices are wireless it becomes necessary that they have their own power supply. The energy harvest device based on piezoelectrics thus provides promising prospects in powering small electronic components [116].

2.4 Conclusion

Piezoelectric shunt damping techniques exploit the capability of piezoelectric materials to transform mechanical (strain) energy into electrical energy, which is then dissipated in the electrical circuit. In a piezoelectric shunted structure, this conversion capability highly depends on 1) the ability to absorber the strain energy of the structure into the active piezoelectric material and 2) the capability of the piezoelectric materials to transform this strain energy into electrical energy. The former depends on the distribution of modal strain energy in the structure, which requires that piezoelectric materials should be located in the proper zone; the latter is determined by the piezoelectric electromechanical coupling factor, which can be increased by a negative capacitance for example.

In summary, the classic resonant shunt circuits exhibit the advantage of simplicity and compactness and high efficiency when properly tuned; while at the same time the use of resonant shunt circuits is limited by the massive inductance required in low-frequency cases and sensitivity to drifts in both structural frequencies and optimal electric parameters. Various semi-passive or active-passive strategies for improving the piezoelectric shunt damping should be well reflected before applying into bladed disks since special considerations is to be taken into account for this special situation, such as rotor balance and installation problems. In the next chapter, both the piezoelectric shunt damping and piezoelectric mistuning will be exploited with respect to minimizing the blade mistuning effect.

Chapter 3

Resonant shunt circuits applied into mistuned bladed disks

This chapter is devoted to applications of piezoelectric shunt damping in mistuned bladed disks. State-of-art of piezoelectric shunt damping in turbomachinery is first presented. Different piezoelectric-based damping strategies in turbomachinery are compared. Then we propose to damp blades by attaching resonant shunted piezoelectric materials solely onto the disk surface. Both the piezoelectric shunt damping and piezoelectric mistuning effect will be taken into account to achieve a maximum blade vibration reduction.

3.1 Introduction

Piezoelectric materials have been extensively used as sensors and actuators for vibration controls because of their ideal properties: light weight, high bandwidths, efficient energy conversion and easy integration. Embedded or bonded onto the vibrating structures, piezoelectric materials can convert mechanical energy into electric energy and vice versa. In exploiting this energy conversion capability, several research efforts have been dedicated to applications of piezoelectric materials in blade vibration reduction. In this section, a brief overview on the recent advances of piezoelectric shunt damping in blades will be first presented; then a new piezoelectric shunt damping strategy for bladed disks will be proposed.

3.1.1 State-of-art: piezoelectric shunt damping in turbomachinery

The application of passive piezoelectric shunt damping for turbomachine blades has been first investigated through experiments performed by Cross and Fleeter [117]. An array of piezoelectric elements is bonded to an airfoil in the stator row (see Fig. 3.1). This airfoil is excited in a resonant chordwise bending mode by upstream rotor-generated wakes. The piezoelectrics experience a strain and in response produce an electric field. Tuned electrical circuits connected to the piezoelectrics as shunts dissipate this electrical energy, with multi-mode shunting techniques utilized. The authors state that this electrical energy dissipation and the corresponding reduction in the airfoil mechanical energy result in a reduction in the magnitude of the resonant vibrations.

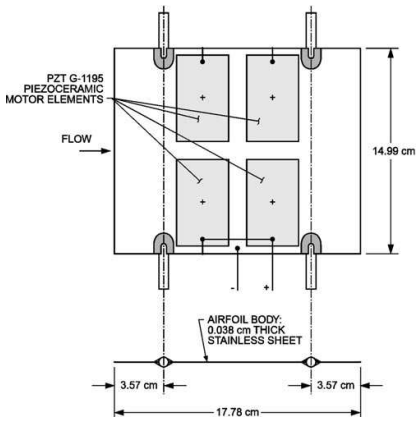

Figure 3.1: Flat plate airfoil boned with multiple piezoelectric elements [117]

Livet and Berthillier et al. [118] have studied vibration suppression by piezoelectric shunt damping using a simplified blade model. A piezoelectric patch is bonded close to the cantilever beam root. The authors have presented a finite element modeling methodology to describe the Euler-Bernoulli beam model with piezoelectric materials in order to optimize electrically the shunted piezoelectric element and its location. It is concluded that a significant vibration reduction is possible with both passive and semi-active shunting.

Schwarwendahl and Szwedowicz et al have proposed the integration of the piezoelectric material into the blade in order to protect the material from the centrifugal loading and environmental degradation [119]. As shown in Fig. 3.2a, the piezoelectric stack is put into an artificial cavity into the top section of a simplified blade. The size and location of piezoelectric stack is optimized based on a finite element piezo-blade model with respect to a specified blade chord-wise bending mode. Additionally, a sensitivity analysis reveals that the piezoelectric damping performance depends on the frequency ratio of the electrical to the mechanical resonance of interest. For high blade mistuning above 1%, the detuned piezodamper loses its desired damping effect.

Figure 3.2: Blade with cavity and piezoelectric stack [119].

In addition to passive piezoelectric shunting, a number of active piezoelectric control approaches applied to blades have been also devised to improve structure damping. Watanabe et al. [120] performed analysis and testing of piezoelectric actuators on airfoil trailing edges to actively control flutter on airfoils in a linear transonic cascade. In order for a piezoelectric patch to absorber vibration energy as much as possible, it needs to be placed in an blade area of high modal strain. However, as the blade spins, centrifugal loading causes the blade to stiffen, and modal strain contours to shift, changing the effectiveness of the patch to sense or actuate the target mode. Considering the practical implementation of piezoelectric elements within rotor blades, Duffy et al. [121; 122] showed the effectiveness of a piezoelectric-damped plate under centrifugal loading. Testing shows that active piezoelectric control can significantly reduce vibrations of subscale composite fan blades. State switching shunt circuits have also been adopted by Kauffman

and Lesieutre [123] and Sénéchal [124] in blade vibration suppression.

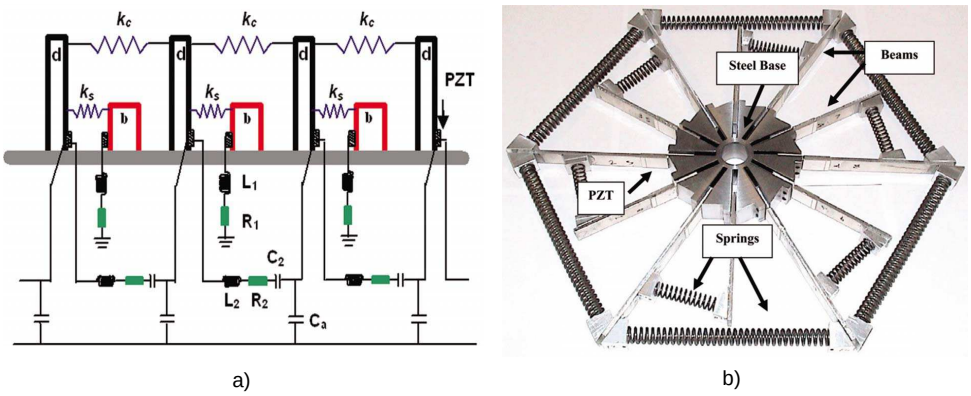

Figure 3.3: a) Bladed-disk model with piezoelectric network; b) Base line bladed-disk model system with piezoelectric patches [125].

In particular, Yu and Wang et al. [125–127] have recently explored the feasibility of utilizing piezoelectric materials attached onto both the blade and disk for the vibration reduction of mistuned periodic structures. A simplified bladed-disk model in Fig. 3.3a is used so that the disk dynamics are included. Capacitor C_a is used to couple these local shunt circuits. The additional capacitor C_2 is added to cancel out mechanical blade-disk coupling effects. The bladed-disk test structure with piezoelectric patches is shown in Fig. 3.3b. A tuned passive piezoelectric network is derived to achieve multiple spatial harmonic suppression. This research effort offers a very good start in applying piezoelectric shunt damping to simplified bladed disk structures. A symmetric piezoelectric network [128] combining energy harvesting and vibration reduction has been also proposed for vibration suppression in simplified periodic structures.

In summary, passive resonant shunt circuits for a single blade mode require huge and massive inductance in low-frequency cases, even though these circuits exhibit the advantage of simplicity and compactness. Moreover, they are sensitive to drifts in the structural resonance frequencies. Once the blade becomes mistuned, the resonant shunt circuit loses its desired damping performance.

For active piezoelectric control approaches, more sophisticated electronic components such as operational amplifies, diodes and voltage sources are needed. Out

of practical considerations such as rotor imbalance and installation problems in bladed disks, those aforementioned active control strategies are greatly limited by power supply needs as well as complex signal processing.

Another issue of major concern is the location of piezoelectric transducers in bladed disks. In most of current applications, piezoelectric patches are mounted onto blade surfaces. In general however, it is not thought to be practical since objects attached onto blades will disturb the flow field in the cascade. A trend is toward a compact integration of piezoelectric materials into the blade [119]. For instance, it is stated that the full-size fan blade does have adequate thickness to incorporate embedded piezoelectric elements [122]. While for small-sized blades in higher stage, it seems that there is not enough space inside. In addition, such incorporation itself may also bring about new problems, like manufacturing difficulties and blade strength degradation.

3.1.2 Problem Statement and Research Objective

A piezoelectric application as actuators is given in our previous research concerning the friction ring damper [82]. 24 PZT piezoelectric transducers ($30 \times 10 \times 1mm$) working in d_{31} mode are attached onto the disk circumferentially to provide excitation for experimental validation of friction damping (see Fig. 3.4). In this case, blade vibration is successfully excited only by shaking the disk through piezoelectric actuators. Therefore, an inverse energy transfer from blades to the disk is naturally desired. A similar arrangement of piezoelectric materials as damping device for industrial bladed disks has been also proposed in the latest research by Mokrani and Bastaits et al in 2012 [129].

Based on the above arguments, this thesis is devoted to reducing the vibration of mistuned bladed disks using shunted piezoelectrics solely attached onto the disk (see the position of piezoelectric transducers in Fig. 3.4). In this chapter, resonant shunted piezoelectric patches are bonded onto the disk surface between adjacent blades in order to dissipate the disk's mechanical energy. Consequently, the blade vibration level can be reduced because of coupling between blades and the disk. This strategy is of engineering interest since the piezoelectric transducers are placed outside of the main stream in turbomachinery. It is particularly suitable

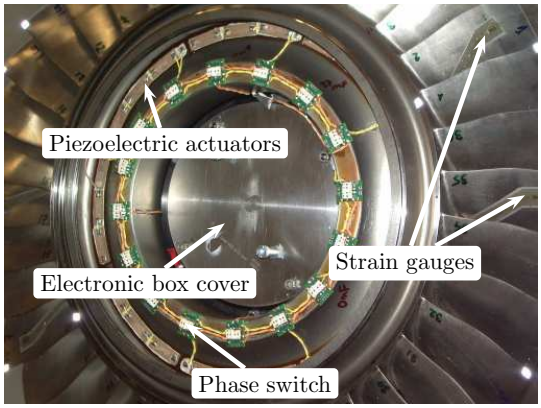

Figure 3.4: Position of piezoelectric transducers in the bladed disk [82]

for the integral bladed disk ("blisk") where the friction damping is not favorable due to the absence of a frictional contact interface. This idea is developed based on a lumped-parameter bladed disk model, in which the coupling effect of blade and disk is taken into account. An initial piezoelectric configuration that includes optimal inductance and resistance values will be sought to damp a certain blade-disk mode in Section 3.2.

The effectiveness of resonant shunt circuits relies on the internal resonance between electrical and mechanical systems. U. Andreaus and M. Porfiri [130] have investigated the damping effectiveness of RL circuits under electrical impedance variation with respect to their optimal values. Results from sensitivity analyses reveal that small uncertainties of the inductance value lead to a huge variance of the performance of the resonant shunted structures; while the variance of damping parameter (resistance) does not significantly influence the system performance.

In this chapter, similar phenomena will be observed that piezoelectric shunted bladed disks are very sensitive to inductance value perturbations. It is naturally desirable to seek further vibration reduction by introducing a piezoelectric mistuning pattern. As a result, both piezoelectric shunt damping and piezoelectric mistuning will be introduced to minimize the blade mistuning effects. Piezoelectric mistuning can be seen herein, to some extent, as a kind of damping mistuning [27]; it is modeled as a small variation of the inductance value of each shunt circuit. As the synthetic inductance value can be determined by a digital filter, the

piezoelectric mistuning is considered controllable. More specifically, an optimal piezoelectric mistuning δ_L, obtained by genetic algorithm optimization, could be introduced into a blisk with a given blade mistuning δ to achieve further blade vibration mitigation (see the definition of δ_L and δ in Section 3.2).

3.2 Piezoelectric shunt damping in the tuned bladed disk

The piezoelectric shunt damping will be investigated for a tuned bladed disk in this section. A theoretical model for the bladed disk with resonant shunted piezoelectric patches will be first presented. Both the time-domain and frequency-domain modeling methods are developed. Optimal electrical parameters are sought in order to damp a specified blade-disk mode.

3.2.1 Piezoelectric shunted bladed disk model

A lumped-parameter bladed disk model is presented in Fig. 3.5. This cyclic periodic structure consists of N identical sectors. Blade masses $(m_{1,j}, m_{2,j})$ and disk mass $m_{3,j}$ are linked by coupling springs $(k_{1,j}, \cdots, k_{4,j})$. The external engine order excitation acts upon the blade mass 1 $(m_{1,j})$.

Identical piezoelectric patches working in the d_{31} mode are attached onto both the front and rear disk surface circumferentially between adjacent blades. The schematic of two equally sized piezoelectric patches attached to the disk is shown in Fig. 2.3. It is assumed that only uniaxial loading of piezoelectric patches in the longitudinal direction 1 has been considered in this lumped-parameter model. Accordingly, piezoelectric patches are modeled as coupling components in parallel with disk coupling stiffness $k_{3,j}$.

We begin with an investigation into the original 9-sector bladed disk without piezoelectric patches. Modal analysis for the tuned bladed disk is carried out according to the method presented in Chapter 1.4.1. Numerical values of the mechanical system generating the frequency/nodal diameters diagram (see Fig. 3.6) are listed in Table 3.1, where γ denotes structure damping. This model is built so that it represents as much as possible a real bladed disk, particularly

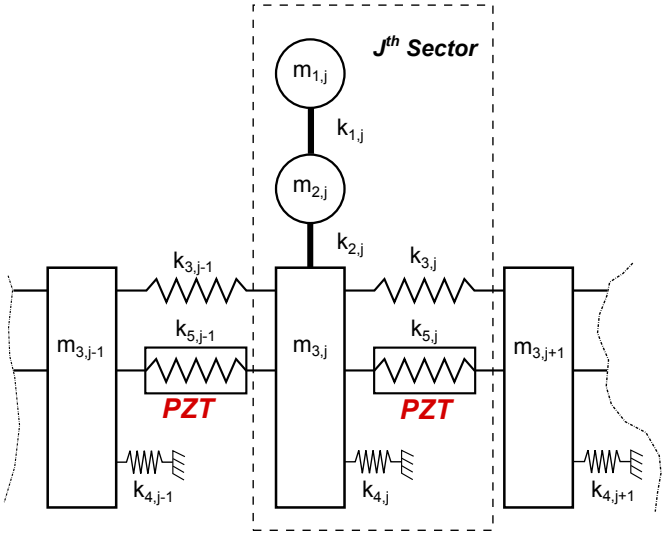

Figure 3.5: Lumped-parameter model of piezoelectric shunted bladed disks

in terms of blade-disk coupling. As concluded in Chapter 1, examining the blade-disk coupling strength may raise the possibility of influencing the blade response through damping the disk. A quantitative measurement of the coupling, namely the coupling index, has been proposed by Javier and Mignolet [53].

Table 3.1: Numerical values of the lumped-parameter bladed disk model

$m_{1,j}$	$m_{2,j}$	$m_{3,j}$	$k_{1,j}$	$k_{2,j}$	$k_{3,j}$	$k_{4,j}$	γ
$0.25kg$	$0.35kg$	$1.2kg$	$2 \times 10^6 N/m$	$10^6 N/m$	$5 \times 10^7 N/m$	$10^5 N/m$	0.2%

Coupling index

It is declared that the interblade coupling plays a crucial role in the dynamics of the system because it governs the communication of vibration energy among blades. The interblade coupling is largely dependent on the blade-disk coupling. An qualitative analysis of the natural frequency versus nodal diameter plot is often conducted that intuitively qualify this coupling, as discussed in Section 1.4.1. The coupling index, as quantitative measurement of blade-disk coupling, is based on observing the impact of blade

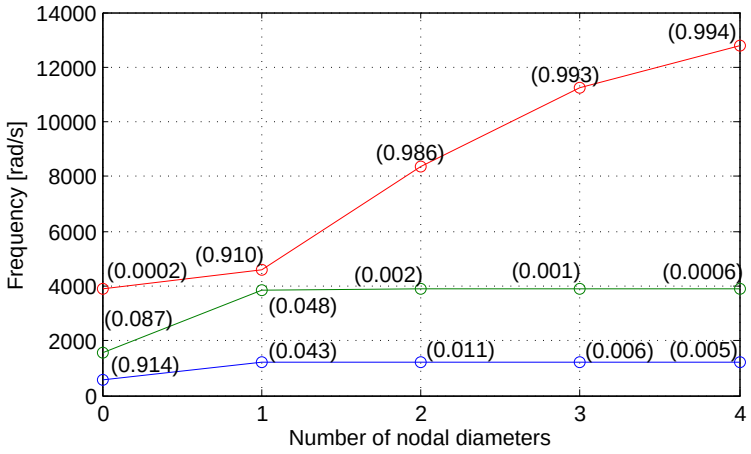

Figure 3.6: Frequency/nodal diameter diagram of 9-sector bladed disk without piezoelectric patches; coupling indices are included for each blade-disk mode.

stiffness drifts on the variation of blade-disk mode frequency. Note that a relative change δE of blade Young's modulus would affect the blade-alone frequencies by the factor $\sqrt{1+\delta E}$ while the frequencies of disk-alone modes would not be affected. Thus the variation of the blade-disk mode natural frequencies will be between these two extreme cases and the coupling index is defined as:

$$CI = 1 - \frac{\omega_r(1+\delta E) - \omega_r(1)}{(\sqrt{1+\delta E} - 1)\omega_r(1)} \tag{3.1}$$

where $\omega_r(1+\delta E)$ corresponds to the appropriate bladed disk natural frequency associated with r nodal diameters and a blade Young's modulus of $E+\delta E$. Similarly, $\omega_r(1)$ corresponds to $\delta E = 0$. Clearly, a coupling index $CI = 0$ indicates a purely blade alone mode, while $CI = 1$ corresponds to a disk mode with rigid blades. Moderate blade-disk mode coupling is necessary for significant forced amplitude magnification in mistuned bladed disks. Similar definition of coupling index could be readily extended to the lumped-parameter bladed disk model. A plot of coupling indices for all blade-disk modes is shown in Fig. 3.6. Note the excellent correlation between the coupling index values and a qualitative analysis discussed in Section 1.4.1.

According to coupling indices, in the first two mode families (i.e. low frequency), the coupling is weak for high nodal diameters, whereas in small nodal diameters the coupling is stronger. Let's also note a strong coupling appears in the 1st and 2nd modes (low frequency) of 1 nodal diameter while the 3rd mode (high frequency) tends to be disk-dominant in Fig. 3.6. This coupling parameter is an important factor relative to the efficiency of the piezoelectric shunt damping since it determines disk participation in the global motion. The energy dissipation due to piezoelectric shunt damping depends on the relative displacement between different disk areas; this is achieved when the strong coupling mode of the structure is excited and that both the blades and disk move.

Next, let's turn to the system description in the time domain, which contains shunt circuit governing equations. Let q_j be the electric charge generated on the j^{th} piezoelectric patch. k_j^c reflects the electromechanical coupling effect and k_j^{oc} is the open circuit piezoelectric stiffness. At first structural damping is not taken into account. Following the time-domain modeling methodology presented in Eq. (2.38)-(2.42), the equation of motion (EOM) for the j^{th} sector can be written as:

$$\begin{aligned}
m_{1,j}\ddot{x}_{1,j} + k_{1,j}x_{1,j} - k_{1,j}x_{2,j} &= f_{1,j}e^{i\omega t} \\
m_{2,j}\ddot{x}_{2,j} - k_{1,j}x_{1,j} + (k_{1,j}+k_{2,j})x_{2,j} - k_{2,j}x_{3,j} &= 0 \\
m_{3,j}\ddot{x}_{3,j} - k_{3,j-1}x_{3,j-1} - k_{j-1}^{oc}x_{3,j-1} - k_{j-1}^{c}q_{j-1} - k_{2,j}x_{2,j} + (k_{3,j-1} + & \\
k_{2,j} + k_{3,j} + k_{4,j})x_{3,j} + (k_{j-1}^{oc} + k_j^{oc})x_{3,j} + k_j^c q_j - k_{3,j}x_{3,j+1} - k_j^{oc}x_{3,j+1} &= 0 \\
L_j\ddot{q}_j + R_j\dot{q}_j + \frac{1}{C_{p,j}^s}q_j + k_j^c x_{3,j} - k_j^c x_{3,j+1} &= 0
\end{aligned} \tag{3.2}$$

With structure damping γ, a compact matrix form of EOM is presented:

$$\mathbf{M_p}\,\ddot{y} + \mathbf{D_p}\,\dot{y} + \mathbf{K_p}\,y = f_p e^{i\omega t} \tag{3.3}$$

$$y = [y_1, \cdots, y_N]^T,\ f_p = [f_{p,1}, \cdots, f_{p,N}]^T,\ \mathbf{M_p} = \mathbf{Bdiag}\,(\mathbf{M_{p,1}}, \cdots, \mathbf{M_{p,N}})$$

$$y_j = [x_{1,j}, x_{2,j}, x_{3,j}, q_j]^T,\ f_{p,j} = [f_{1,j}, 0, 0, 0]^T,\ \mathbf{M_{p,j}} = diag(m_{1,j}, m_{2,j}, m_{3,j}, L_j)$$

where the subscript p indicates that the electrical degree of freedom of piezoelectric patches is involved. Other submatrices are given in Appendix A.

An alternative frequency-domain system description is also proposed. Here, the piezoelectric patches connected with R_j and L_j are modeled as frequency-dependent coupling stiffness $k_{5,j}(i\omega)$, which is derived from Eq. (2.22). After a similar transformation presented in Eq. (2.43), we furthermore have the following equations of motion in the frequency domain:

$$[-\omega^2\mathbf{M} + i\gamma\mathbf{K}_{mech} + \mathbf{K}_{mech} + \mathbf{K}_{piezo}]X = F \tag{3.4}$$
$$X = [X_1, \cdots, X_N]^T, \quad F = [F_1, \cdots, F_N]^T, \quad \mathbf{M} = \mathbf{Bdiag}\,(\mathbf{M}_1, \cdots, \mathbf{M}_N)$$
$$X_j = [X_{1,j}, X_{2,j}, X_{3,j}]^T, \quad F_j = [f_{1,j}, 0, 0]^T, \quad \mathbf{M}_j = diag(m_{1,j}, m_{2,j}, m_{3,j})$$

In this equation, the mechanical stiffness matrix $\mathbf{K}_{mech}$ and piezoelectric stiffness matrix $\mathbf{K}_{piezo}$ are separated. Readers are referred to Appendix A for details on the submatrices. Note that only the mechanical degrees of freedom have been included in Eq. (3.4).

Given a blade mistuning pattern δ and tuned blade stiffness $k_{1,t}, k_{2,t}$, the blade mistuning is modeled as a variation in blade-alone stiffness:

$$k_{1,j} = k_{1,t}(1+\delta_j), \quad k_{2,j} = k_{2,t}(1+\delta_j), \quad j = 1, 2, \cdots, N \tag{3.5}$$

Similarly, the piezoelectric mistuning is modeled as a variation in inductance values. R_{opt} and L_{opt} denote the optimal electric parameters obtained by tuning design.

$$L_j = L_{opt}(1+\delta_{L,j}) \tag{3.6}$$

A piezoelectric configuration is to be sought in order to damp a specified blade-disk mode, i.e. tuning design.

3.2.2 Tuning design

Previous research efforts have demonstrated that the behavior of resonant shunted piezoelectric is almost like that of a dynamic vibration absorber when integrated into the host structure. Considering the analogy of the dynamic absorber, as discussed in Chapter 2.2, the optimal electric parameters for a targeted structural mode can be obtained through optimization methods presented by Hagood and

Von Flotow [94]. In particular, the tuning design could benefit from the cyclic symmetry in periodic structures. For instance, a so-called U-transform technique was adopted by Yu and Wang [125]. In essence, this U-transform is a spatial Fourier transform widely used in the tuned bladed disk modeling.

We propose herein a numerical procedure for obtaining the optimal electrical parameters based on strain energy considerations. The objective function is set as the strain energy of the global tuned piezo-mechanical system over a given frequency range:

$$E^s(R,L) = \int_{\omega_l}^{\omega_u} X^T(\mathbf{K}_{mech} + \mathbf{K}_{piezo})X \, d\omega \tag{3.7}$$

where X is the response vector ; $\mathbf{K}_{mech}$ and $\mathbf{K}_{piezo}$ are defined in Eq. (3.4).

The optimal resistance R_{opt} and inductance L_{opt} are sought so as to obtain the minimum global strain energy over the frequency interval $[\omega_l, \omega_u]$ around the targeted blade-disk mode. Note that these tuning parameters only make sense in the tuned bladed disk.

Table 3.2: Dimensions and material properties of piezoelectric patches

Dimension($:cm$)	Material property
width: 1.5	Young's modulus (E): 63Gpa
thickness: 0.05	OC capacitance C_p^T: $9.93 \times 10^{-8} F$
length: 10	SC stiffness k^{sc}: $2.4 \times 10^6 N/m$
	electro-mechnical factor k_{31}: 0.35

The numerical values of piezoelectric materials are given in Table 3.2. Note that in most cases the piezoelectric stiffness should be much smaller than disk stiffness. The geometry is chosen so that the ratio between the short circuit stiffness k^{sc} and mechanical coupling stiffness k_3 is approximately 5%. The piezoelectric patches are tuned to damp the 1st mode of 1 nodal diameter (low frequency), which is a blade-dominant mode, while at the same time the blade-disk coupling is strong enough. The corresponding optimal electric parameters are given below

by minimizing the global system strain energy defined in Eq. (3.7):

$$R_{opt} = 148\Omega \qquad L_{opt} = 7.79H$$

A highly concerned issue regarding resonant shunt circuit is the realization of huge and massive inductance. The size required for the inductance is proportional to the inverse square of the frequency and thus decreased rapidly with higher structural frequencies. It is true that when targeting low-frequency structural modes, impractically large inductance values are required. However, in the real rotating bladed disk with high speed, the blade vibration frequency induced by aerodynamic loading is typically up to $5 \sim 35kHz$ [14]. We can draw an evident conclusion that relatively much smaller inductances are needed, with an increasing frequency of damped bladed disk mode. In other words, the resonant shunted piezoelectric is more favorable in cases of relatively high-frequency vibration. On the other hand, the large inductance value $7.79H$ is obviously caused by the low frequency of this lumped-parameter model (i.e. approx. 192 Hz), though it is still acceptable in the numerical simulation. This situation can be immediately verified by checking the tuning electrical parameters for the 2nd mode of 1 nodal diameter:

$$R_{opt}^{'} = 44.3\Omega \qquad L_{opt}^{'} = 0.76H$$

With a relatively small inductor requirement, such a passive piezoelectric shunt technique is therefore well suited to the high-frequency case of bladed disks.

3.3 Blade mistuning

The blade mistuning effect is to be examined from both a determined and statistic viewpoint. Most of studies in blade mistuning have been of deterministic type, in which a model is generated and mistuned by a specified pattern, then the results are analyzed. However, deterministic approaches by themselves are not sufficient since blade mistuning is a random phenomenon. Statistical approaches to mistuned bladed disk analysis become therefore necessary. An additional remark is that the shunted piezoelectrics are assumed to be distributed on the disk in a "tuned" pattern, i.e. no piezoelectric mistuning is introduced in this section.

3.3.1 Blade mistuning: deterministic viewpoint

Blade mistuning effect is first examined from a deterministic viewpoint. With optimal electrical parameters damping a 1 nodal diameter mode, an engine order 1 excitation is imposed on the bladed disk. Blade mistuning is added as random variables δ, as in the expressions in Eq. (3.5). Blade vibration levels of tuned/mistuned mechanical/piezo-mechanical systems are then compared in Fig. 3.7 by examining responses under engine order excitation with fixed frequency (chosen as the damped modal frequency).

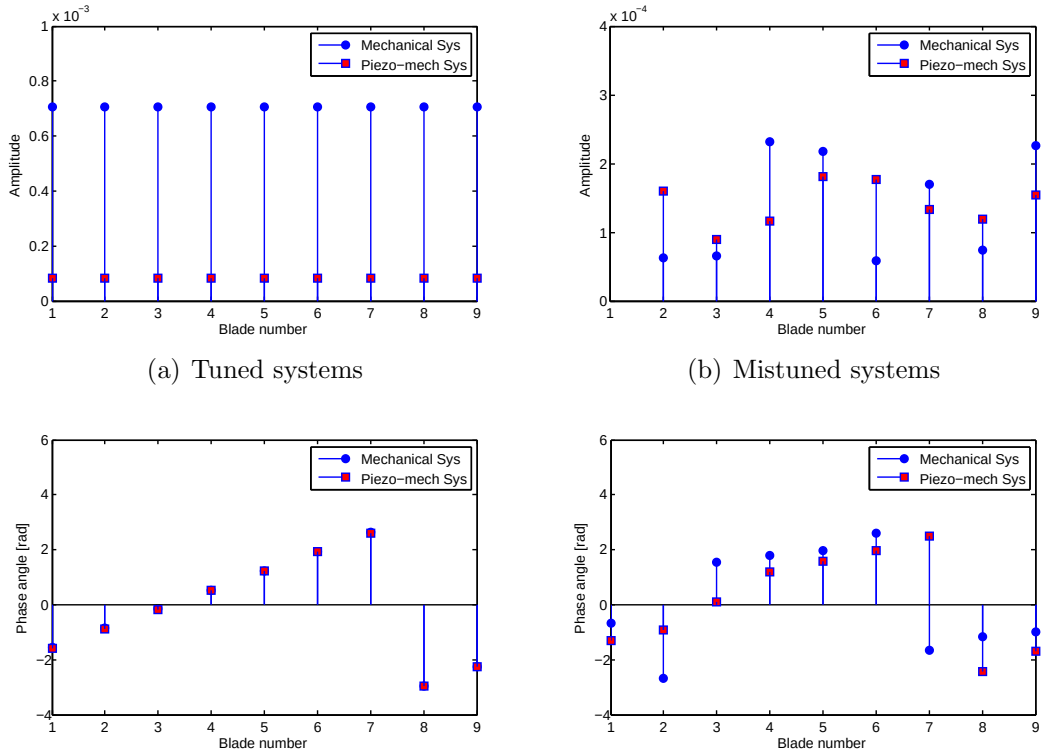

(a) Tuned systems

(b) Mistuned systems

(c) Tuned systems

(d) Mistuned systems

Figure 3.7: Responses of blade mass 1 at the fixed excitation frequency.

The tuned assembles possess constant inter-blade phase angle modes. When the tuned mode is excited, all blades throughout the structure vibrate at the same amplitude level yet with a fixed phase difference, which is determined by the number of nodal diameters of the excited blade-disk mode (see Fig. 3.7a,c).

A significant vibration reduction is seen due to the added piezoelectric shunt damping. An uniform blade amplitude indicates that vibration energy is still equally distributed among all the sectors.

When blade mistuning takes place, the perfect cyclic symmetry is destroyed. The small blade mistuning alters mode shapes drastically, which leads to vibration energy localization around a few blades. Because of the spatial confinement of vibration energy, certain blades in a mistuned system can suffer a higher vibration level than the others, as depicted in Fig. 3.7b,d. Even though the piezoelectric shunt damping lower the vibration level, localization phenomenon does still exist.

Frequency sweeps on the basis of Eq. (3.4) are then performed with respect to blade-tuned/ blade-mistuned mechanical/ piezo-mechanical bladed disk systems. Various responses are compared by examining the maximum amplitudes throughout the bladed disk versus excitation frequency, as illustrated in Fig. 3.8, where only the amplitudes of blade mass 1 are plotted.

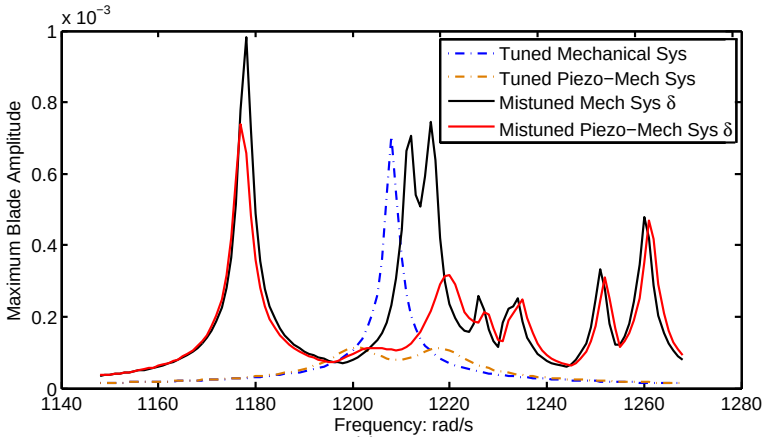

Figure 3.8: Maximum blade amplitude versus frequency

In Fig. 3.8, for tuned systems, resonant shunt circuit are sought to minimize response of bladed disk in a way analogous to dynamic damper tuning. Two resonance peaks are generated in the frequency response of the tuned piezo-mechanical system (– · –), and a significant vibration reduction (up to nearly 80% compared to the mechanical counterpart (– · –)) is achieved within the frequency band limited by the two peak points.

The mistuned blade-disk mode shape is no longer a pure modal diameter mode, but instead has multiple harmonic content. The modes that retain significant harmonic content matching the engine order of excitation will be strongly excited. As a result, several peak response amplitudes arise around the damped modal frequency and some of them exhibit excessive vibration level than that of a tune system. Due to the same blade stiffness mistuning, the piezo-mechanical bladed disk (———) yields several peak amplitudes over the frequency range where the peak response of the mistuned mechanical counterpart (———) is exposed. The vibration level of this mistuned system is depressed because of piezoelectric shunt damping. The blade mistuning effect is greatly alleviated especially around the the tuning frequency.

3.3.2 Blade mistuning: statistic viewpoint

To estimate the statistics of the forced response for a population of randomly mistuned bladed disks with the same nominal design, a Monte Carlo simulation is performed. First, given a value $\sigma = 0.03$ for the standard deviation of random mistuning, the blade mistuning pattern δ for one realization of a mistuned bladed disk are assigned by a pseudo-random-number generator (normal distribution). Second, a frequency sweep is performed to find the largest peak response amplitude of any blade on the bladed disk. Third, this process is repeated for many realizations (5000 realizations in this section) of mistuned bladed disks. In order to facilitate the comparison, amplitude magnification factors are defined based on the maximum blade amplitude $A_{\max}$ of the tuned mechanical system:

$$AMF = \frac{A_{\max}(\text{blade-mistuned systems})}{A_{\max}(\text{blade-tuned mechanical system})} \tag{3.8}$$

Post-processing of this simulation results in an approximation of the response statistics, e.g., the probability density function. The probability distribution function (PDF) of a random variable X, $F_X(x)$, corresponds to the probability that $X < x$. Fig. 3.9 shows PDFs of the maximum blade amplitudes versus (AMF) of blade mass 1. It is clearly seen that the piezoelectric shunt damping is efficient to suppress the vibration level of mistuned bladed disks at this given

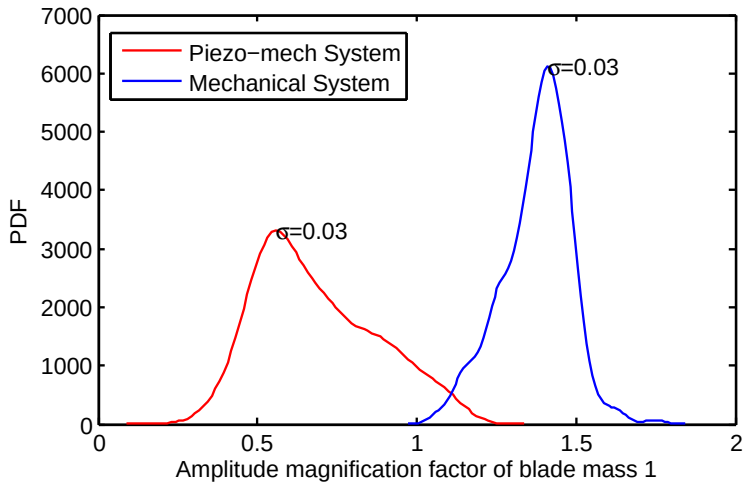

Figure 3.9: Probabilistic density function (PDF) of the maximum blade amplitudes versus amplitude magnification factor (AMF) of blade mass 1

blade mistuning strength.

Early research efforts reveal that the maximum response amplitude of mistuned bladed disks is sensitive to the mistuning strength. Fig. 3.10 shows how the statistics of the largest response of mistuned bladed disks evolve as the level of mistuning strength is varied. Mistuning strength is measured by the standard deviation of the blade mistuning pattern distribution. Of greatest importance is the curve labeled 99%. The values on this curve denote the mistuning-induced amplification of largest response that will only be surpassed by 1% of all realizations of mistuned systems. When this value deviates greatly from unity, mistuning effects are high.

As blade mistuning strength increases from weak to strong, we note that for mechanical systems (blue lines) the mistuning effect reaches a maximum at moderate blade mistuning level. This result is in agreement with that in the literature. With the presence of piezoelectric shunt damping (red lines), This feature is not seen any more. Instead, mistuning effects are greatly suppressed at the weak and moderate blade mistuning level. It indicates that the piezoelectric shunt damping is promising in reducing the blade mistuning effect from a statistic viewpoint.

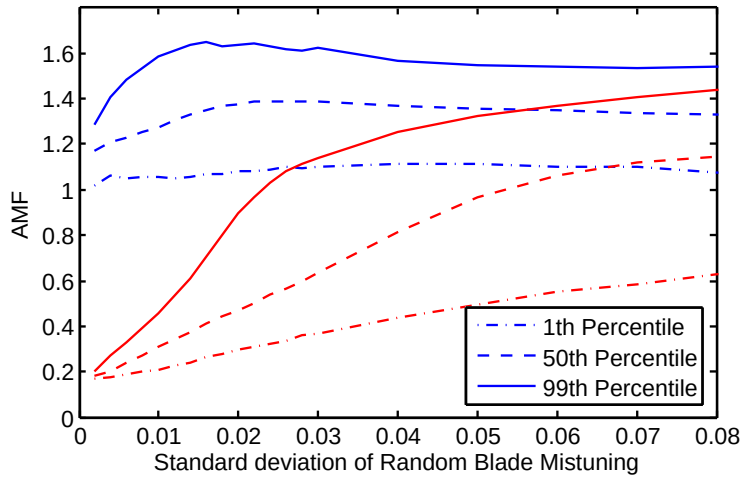

Figure 3.10: Amplitude magnification factor as a function of blade mistuning strength. blue lines: mechanical systems; red lines: piezo-mechanical systems

3.4 Piezoelectric mistuning

In this section, the effect of random piezoelectric mistuning in a blade-mistuned is first examined. Piezoelectric shunt damping together with piezoelectric mistuning effect will be then utilized to achieve maximum blade vibration reduction. To this end, the genetic algorithm is employed to search for an optimal piezoelectric mistuning pattern with regard to a given blade mistuning pattern.

3.4.1 Piezoelectric mistuning effect

Previous sections have provided the tuning electric parameters for a tuned piezoelectric shunted bladed disk. When blade mistuning δ is taken into account, as we see, the vibration level of the mistuned piezo-mechanical system is depressed in comparison with the mechanical counterpart because of added piezoelectric damping. The blade mistuning effect, however, does still exist. Inspired by the sensitivity of the resonant shunt circuits to inductance uncertainty, we perform an investigation of the piezoelectric mistuning effect below. A random piezoelectric mistuning pattern δ_L is added into the blade-mistuned system in a fashion presented in Eq. (3.6).

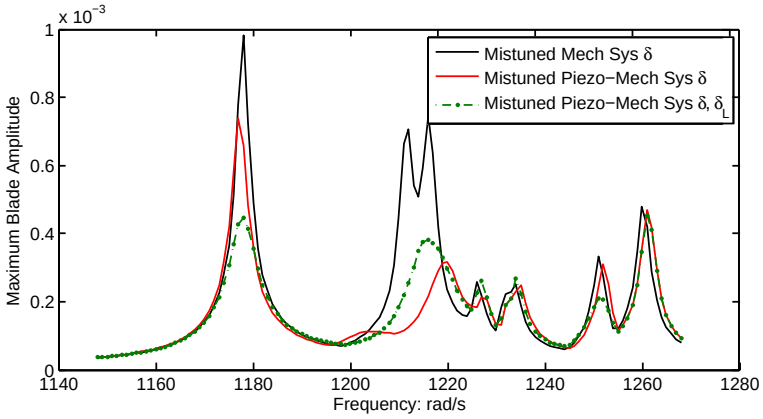

Figure 3.11: Maximum blade amplitude versus frequency

Fig. 3.11 reveals that with a random piezoelectric perturbation δ_L, the response curve of the blade-mistuned disk (green line) changes significantly near the first peak value. This implies that the blade-mistuned disk is also sensitive to piezoelectric mistuning, which is thought to be controllable. This interesting phenomenon provides the possibility to derive the genetic algorithm optimization presented in the next subsection.

3.4.2 Piezoelectric mistuning pattern optimization

Let's note that the blade mistuning identification technique has been well developed in recent years [67; 68]. Hence, it is reasonable to assume that the initial blade mistuning pattern δ could be derived experimentally. It is found that the resonant shunted bladed disk, to some extent, is very sensitive to inductance mistuning. As a result, it is desirable to find a special piezoelectric patch arrangement pattern to obtain a more acceptable vibration level for a blisk with an known blade mistuning pattern. The problem of searching for a better piezoelectric mistuning pattern can thus be formulated as a pattern optimization problem. Such optimization problems are also encountered in some worst mistuning pattern analyses [57] as well as intentional mistuning optimization [78].

A glimpse of genetic algorithm

Generally, one can categorize the optimization methods into two major classes, namely gradient-based methods and global-based methods. In some engineering applications conventional gradient-based algorithms are ineffective due to the problem of local minima or the difficulty in calculating gradients. The genetic algorithm (GA) is one of the optimization methods that require no gradient and can achieve a global optimal solution. GAs are so-called because they attempt to use the supposition of evolution, i.e. learning/survival of the fittest, as a basic mechanism for improvement in solving an optimization problem. GAs are computationally simple but powerful and not limited by assumptions about the search space.

The genetic algorithm solves optimization problems on the basis of natural selection, the process that drives biological evolution [131]. The genetic algorithm repeatedly modifies a population of individual solutions. At each step, the genetic algorithm selects individuals at random from the current population to be parents and uses them produce the children for the next generation. Over successive generations, the population "evolves" toward an optimal solution. The genetic algorithm uses three main types of rules at each step to create the next generation from the current population:

- *Selection rules* select the individuals, called parents, that contribute to the population at the next generation;
- *Crossover rules* combine two parents to form children for the next generation;
- *Mutation rules* apply random changes to individual parents to form children.

The genetic algorithm differs from a standard optimization algorithm in two main ways, as summarized in Table 3.3 [131]:

Overall, GAs are global optimizers because of mutation and their general probabilistic non-gradient nature.

Table 3.3: Differences between standard algorithm and genetic algorithm

Standard algorithm	Genetic algorithm
Generates a single point at each iteration.The sequence of points approaches an optimal solution.	Generates a population of points at each iteration. The population approaches an optimal solution.
Selects the next point in the sequence by a deterministic computation.	Selects the next population by computations that involve random choices.

Piezoelectric mistuning optimization by genetic algorithm

Above all, the optimal piezoelectric mistuning pattern δ_L for a given blade-mistuned disk is a special arrangement that minimizes the piezo-mechanical system's amplitude magnification factor (AMF_{piezo}) over a specified frequency range, i.e.:

$$\delta_L = argmin_{|\delta_{L,j}|<\mu} \{AMF_{piezo}\{[\omega_l, \omega_u], \delta_L\}\} \tag{3.9}$$

μ is the upper bound of perturbation parameters. AMF_{piezo} is defined based on the maximum blade amplitude $A_{\max}$ of the blade-mistuned disk with tuned piezoelectric patches:

$$AMF_{piezo} = \frac{A_{\max}(\text{blade-mistuned disk \& mistuned piezoelectric})}{A_{\max}(\text{blade-mistuned disk \& tuned piezoelectric})} \tag{3.10}$$

In numerical simulations, the pulsation range has been set at $[1150, 1300](rad/s)$, which is wide enough to cover all the possible peak amplitudes around the damped modal frequency. The upper bound of inductance perturbation is 0.06. When the genetic algorithm is implemented, the initial population of optimization parameter δ_L is set at zero, which means that the iteration begins from the tuned case with the same inductance value L_{opt}. The number of population in each generation of GA is 200; the crossover rate is 90% and the mutation rate is 1%. The objective function AMF_{piezo} (fitness value) converges on a value 0.46 after 66

generations, as shown in Fig. 3.12. In Fig. 3.13a it is rewarding to see that the

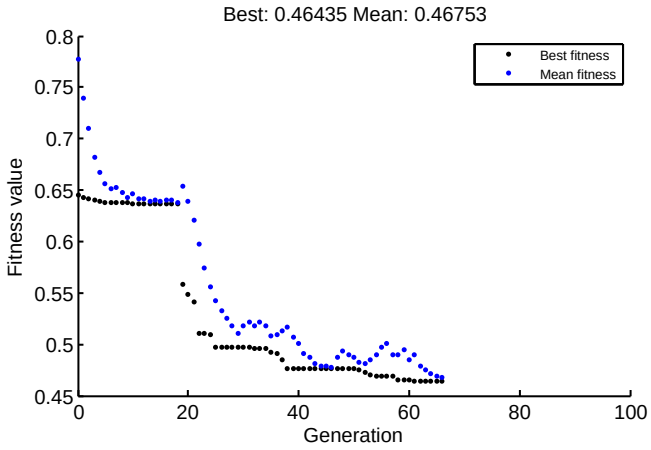

Figure 3.12: Evolving fitness values in genetic algorithm

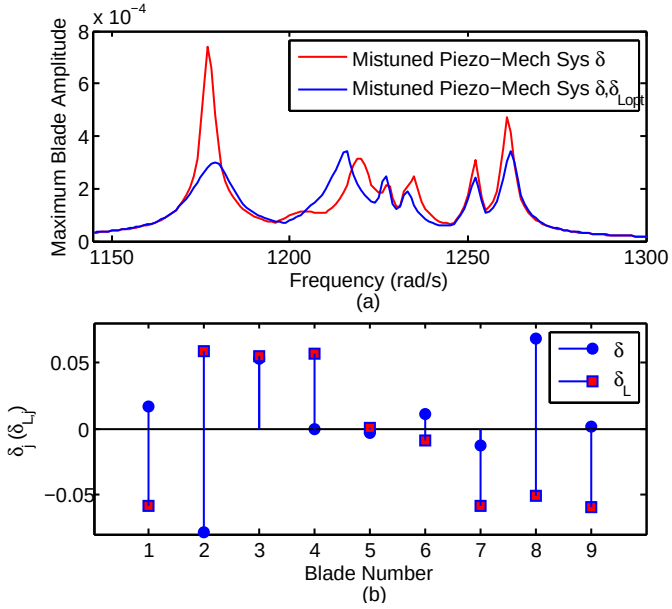

Figure 3.13: Results of genetic algorithm optimization: a) frequency sweep results; b) blade and optimal piezoelectric mistuning pattern.

optimal piezoelectric mistuning pattern does effectively lower the vibration level

around several peaks. This encouraging result demonstrates complete feasibility of reducing the blade mistuning effect by introducing piezoelectric mistuning. The given blade stiffness mistuning pattern δ and optimized inductance mistuning pattern (hereafter denoted δ_L) are plotted in Fig. 3.13b.

The derived piezoelectric mistuning pattern δ_L is optimal only in conjunction with the initial blade mistuning pattern δ. As blade mistuning evolves and causes blade amplitude augmentation, a corresponding adjustment of piezoelectric mistuning will be sought.

3.5 Conclusion

In this chapter, the passive piezoelectric shunt technique has been explored to derive the effective vibration suppression of mistuned bladed disks. Resonant shunted piezoelectric transducers attached onto the disk, combined with the piezoelectric mistuning effect, provide a practical means for blade vibration reduction in turbomachinery. This strategy is of engineering interest since all the piezoelectric patches are placed outside of the main stream. It is also important to demonstrate that relatively small inductances are required for the high-frequency vibration in bladed disks.

Piezoelectric mistuning, to some extent, is a kind of damping mistuning. The optimized piezoelectric mistuning pattern is demonstrated effective in blade vibration reduction for a given mistuned bladed disk. However, for such a pattern optimization, GA needs exhaustive computation resources and is time-consuming. If blade mistuning evolves, repeated blade mistuning identification in terms of δ is also required, which is obviously cumbersome. For this reason, an adaptive control strategy is to be developed in case of blade mistuning evolution in the next chapter.

Chapter 4

Adaptive control strategy for mistuned piezoelectric shunted blisks

In the previous chapter we have succeeded in suppressing blade vibration in mistuned blisks by introducing piezoelectric shunt damping combined with piezoelectric mistuning. Provided that the blade mistuning pattern δ is known by mistuning identification techniques, the optimal piezoelectric mistuning pattern δ_L is obtained by genetic algorithm, as Step 1 illustrated in Fig. 4.1.

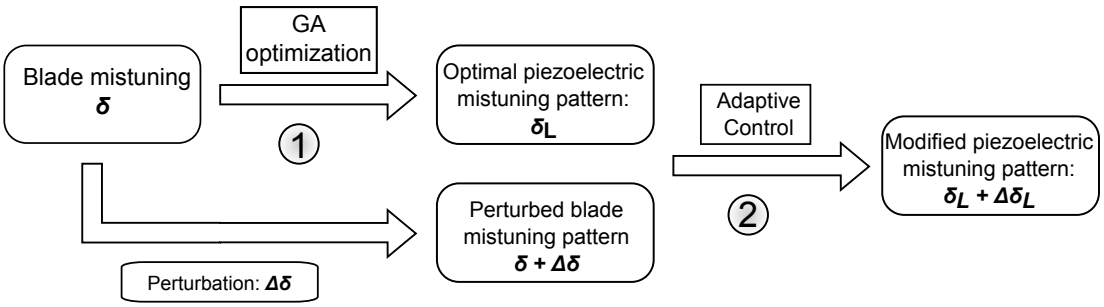

Figure 4.1: Overview of blade vibration control strategy based on piezoelectric shunt techniques

In the actual operation, the blade mistuning pattern is not constant. Due to various complexities including wear, cracked blades and geometric damage (e.g.

caused by missing materials in the blade tip), a perturbation $\Delta\delta$ might arise. Cracks or other types of blade damage can have very small effects on the blade-alone frequencies yet still cause major changes in some of the system mode shapes [44]. The perturbation $\Delta\delta$ usually leads to unexpected response augmentation within a certain frequency range. In benefitting from the manageability and controllability of piezoelectric shunt circuits, an adaptive control strategy has been developed, with the aim of adjusting the piezoelectric mistuning pattern by $\Delta\delta_L$ to maintain a low blade vibration level in the event that the blade mistuning evolves and $\Delta\delta$ generates. That is exactly what we are going to do during Step 2 in Fig. 4.1.

4.1 Framework of the adaptive control strategy

The idea of adaptive control has been around for at least five decades. In the 1950s the topic was enthusiastically pursued by many people, especially in relation to autopilot design. Up to date many apparently different approaches to adaptive control have been proposed in the literature. The design of an adaptive control system is conceptually simple. Essentially, a very natural approach is to combine a particular parameter estimation technique with any control law [132].

One can distinguish two broad classes of adaptive control algorithms depending on the complexity of the design calculation. The simplest conceptual scheme is when the system is parameterized in a natural way and the design calculations are carried out based on the estimated system model. For example, one might adaptively solve the closed-loop pole assignment problem by estimating the system parameters online and calculating the corresponding feedback law. This class of algorithm is commonly called indirect since the evaluation of the control law is indirectly achieved via the system model. These schemes are also sometimes called explicit since the design is based on an explicit process model.

In some cases it is possible to parameterize the system directly in terms of the control law parameters. If this is done, the design calculation necessary to determine the control law becomes essentially trivial. An example is the one-step-ahead design, in which the control law parameters are simply the parameters in a one-step-ahead predictor. This class of algorithm is commonly called direct since

the control law is directly estimated. These schemes are also called implicit since the design is based on estimation of an implicit process model.

In this chapter we turn our attention to the mistuned piezoelectric shunted bladed disk. Of course, as is the case with any design technique, the basic adaptive control theory must be augmented with practical considerations relevant to the system under study.

The general block diagram of the adaptive control system for mistuned bladed disk is shown in Fig. 4.2. Two basic assumptions are given as prerequisites: 1) the engine order excitation $f_p(t)$ as system input is known in experimental cases; 2) the response $y(t)$ as system output is known by measurements and expansion techniques. Measurement noise has been neglected. This adaptive control system is generally viewed within a determined framework in order to simplify parameter estimation process. The strategy presented in this chapter does not strictly belong to neither of the above two classification because the control law, as we shall show later, is devised quite differently from the existent direct and indirect schemes. Keeping the basic block diagram of Fig. 4.2 in mind, we shall take an overview of this strategy at first.

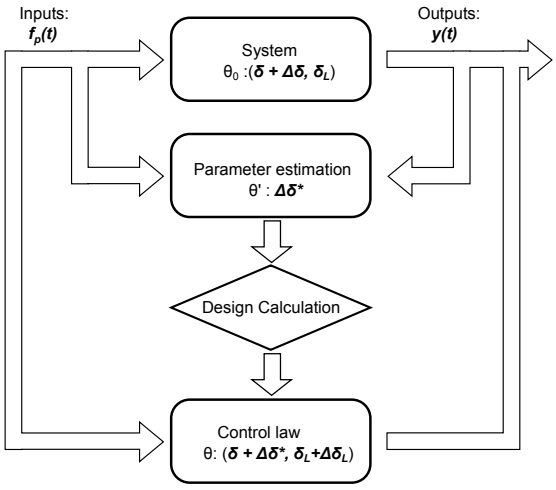

Figure 4.2: Block diagram of the adaptive control strategy for mistuned bladed disks

In the block diagram of the adaptive control system, the dynamic system parameter θ_0 contains the unknown blade mistuning perturbation $\Delta\delta$. As a

wide class of linear and nonlinear deterministic dynamic systems, input-output characteristics can be described by the model that may be expressed succinctly in the following simple form [133]:

$$y(t) = \varphi(t-1)^T \theta_0 \tag{4.1}$$

where $y(t)$ denotes system output at time t;
θ_0 denotes the unknown parameter vector;
$\varphi(t-1)$ denotes a vector that is a linear or nonlinear function of present and past observations of system outputs and inputs.

Although Eq. (4.1) appears very simple, the parameter estimation algorithm can in fact be motivated by many different objective functions. In particular, an online parameter estimation algorithm is preferred in this research. "Online" means that this algorithm handles sequential data; it requires that parameter estimation be recursively updated within the time limit imposed by the sampling period. The online parameter estimation algorithm is capable therefore of continuously tracking time-varying blade stiffness mistuning patterns.

With the estimation $\Delta\delta^*$, the control law is intended to yield a new piezoelectric mistuning pattern $\delta_L + \Delta\delta_L$, which minimizes the blade vibration amplitude at a specified frequency. The basic idea here is to derive a linear approximation of the response vector. The design calculation can then be formulated as a least-squares problem to search a minimal blade response in the neighborhood of δ_L. Details of this adaptive control strategy are organized in this manner: the online parameter estimation algorithm in Section 4.2 along with the response expansion in Section 4.3 correspond to the "parameter estimation" in the block diagram of Fig. 4.2. The "control law" block will be presented in Section 4.4. Numerical simulations are lastly performed in Section 4.5.

4.2 Estimation of random perturbation $\Delta\delta$

In the previous section we saw that a compact mathematical model could be used to describe the dynamical behavior of deterministic systems. The precise nature

of the model response is determined by the values of certain parameters, such as $\delta + \Delta\delta$. In these instances it may be possible to deduce the values of the parameters by observing the nature of the system's response under appropriate experimental conditions. This procedure is called parameter estimation.

In terms of estimation algorithm, we may distinguish two main classes of algorithm: online and offline. In the offline case, it is presumed that all the data are available prior to analysis. Consequently, the data may be treated as a complete block of information, with no strict time limit on the process of analysis. In contrast, the online case deals with sequential data, which requires that the parameter estimates be recursively updated within the time limit imposed by the sampling period. In this section we are concerned primarily with online algorithm for estimation of $\Delta\delta$. Before the parameter estimation, a proper model is required to describe the blade mistuning pattern evolution, which will be discussed next.

4.2.1 Modeling gradual degradation of blade stiffness

It is noted that Tserpes [134] has proposed a progress damage modeling method to assess fatigue damage accumulation and residual strength of aircraft composite materials. In cases of fatigue loading, the nature of cyclic loading implies an additional material degradation plus some sudden material property degradation. The so-called gradual material property degradation is driven by the increased number of cycles.

Based on theoretical and experimental methods, the gradual degradation of stiffness is modeled as function of number of cycles and a linear equation is derived from fitting of the data in Fig. 4.3. The general form of the linear equations in terms of normalized residual stiffness and normalized number of cycles is:

$$E^{res} = \left[A \left(\frac{n}{N_f} \right) + 1 \right] E^{static} \tag{4.2}$$

where E^{res} and E^{static} are the residual stiffness and the static stiffness, respectively; n is the number of cycles; N_f is the number of cycles to failure and A is an experimental fitting parameter.

Inspired by the residual stiffness model in the reference, a similar expression

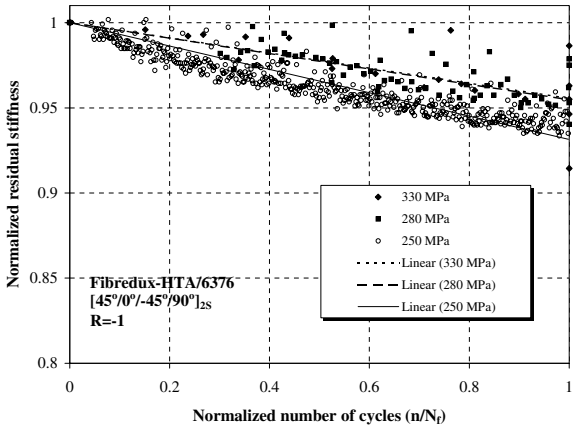

Figure 4.3: Normalized residual stiffness of composite material subjected to fatigue at various stress level

of the time-varying residual blade stiffness in the lumped-parameter model is written as:

$$k_j^{res} = k_{j,t}(1+\delta_j)\left[1-\alpha(t)\right] \tag{4.3}$$

α is a time-dependent parameter related to the number of cycles. Consequently, the perturbation of blade mistuning pattern $\Delta\delta$ can be extracted from the above expression and a proper value of α can be assigned for the numerical simulation.

$$\Delta\delta_j = -\alpha(t)(1+\delta_j) \tag{4.4}$$

Generally speaking, the gradual degradation of blade stiffness is a very slow physical phenomenon compared with the blade vibration phenomenon and the "online" identification strategy presented in this section. It is thus reasonable to assume that the blade mistuning pattern remains time-invariant during the parameter estimation. This assumption is of great importance for the proposed adaptive control strategy.

4.2.2 Online parameter estimation algorithm

To identify the blade mistuning perturbation $\Delta\delta$, a description of the input-output characteristics similar to Eq. (4.1) is necessary. First, we can derive the

perturbed damping matrix ΔD_p and stiffness matrix ΔK_p caused by the blade mistuning perturbation $\Delta\delta$ based on Eq. (3.3).

$$\begin{aligned} \mathbf{M_p}\,\ddot{y} + (\mathbf{D_p} + \Delta\mathbf{D_p})\,\dot{y} + (\mathbf{K_p} + \Delta\mathbf{K_p})y &= f_p e^{i\omega t} \\ \Delta\mathbf{D_p} &= \mathbf{Bdiag}(\Delta\mathbf{D}_{\mathbf{p},1}, \Delta\mathbf{D}_{\mathbf{p},2}, \cdots, \Delta\mathbf{D}_{\mathbf{p},N}) \\ \Delta\mathbf{K_p} &= \mathbf{Bdiag}(\Delta\mathbf{K}_{\mathbf{p},1}, \Delta\mathbf{K}_{\mathbf{p},2}, \cdots, \Delta\mathbf{K}_{\mathbf{p},N}) \end{aligned} \tag{4.5}$$

For j^{th} sector:

$$\begin{aligned} \Delta\mathbf{K}_{\mathbf{p},j} &= \begin{bmatrix} \Delta\mathbf{K}_j & 0 \\ 0 & 0 \end{bmatrix}, \quad \Delta\mathbf{D}_{\mathbf{p},j} = \begin{bmatrix} \frac{\gamma}{\omega}\Delta\mathbf{K}_j & 0 \\ 0 & 0 \end{bmatrix} = \frac{\gamma}{\omega}\Delta\mathbf{K}_{\mathbf{p},j} \\ \Delta\mathbf{K}_j &= \Delta\delta_j K_{base} = \Delta\delta_j \begin{bmatrix} k_{1,t} & -k_{1,t} & 0 \\ -k_{1,t} & k_{1,t}+k_{2,t} & -k_{2,t} \\ 0 & -k_{2,t} & k_{2,t} \end{bmatrix} \end{aligned} \tag{4.6}$$

Therefore, $\Delta\mathbf{K_p}$ can be expressed as a linear sum of mistuning submatrices K^j_{mist}:

$$\begin{aligned} \Delta\mathbf{K_p} &= \Delta\delta_1 K^1_{mist} + \Delta\delta_2 K^2_{mist} + \cdots + \Delta\delta_N K^N_{mist} \\ K^j_{mist} &= \mathbf{Bdiag}(e_j \otimes \begin{bmatrix} K_{base} & 0 \\ 0 & 0 \end{bmatrix}), \quad e_j = [0, \cdots, 1_j, \cdots, 0] \end{aligned} \tag{4.7}$$

It is assumed that the response of bladed disks could be obtained by the "tip-timing" measuring technique [135] and the expansion technique [136]. The "tip-timing" technique allows measuring one DOF in the tip of each blade with far fewer sensors. The expansion technique could expand the limited measured DOFs to obtain all DOFs in the model. In reality, all the measurements are discrete time signals. Eq. (3.3) can be discretized by use of finite differences:

$$\begin{aligned} \dot{y}(t) &= \frac{y(t) - y(t-1)}{T} \\ \ddot{y}(t) &= \frac{y(t+1) - 2y(t) + y(t-1)}{T^2} \end{aligned} \tag{4.8}$$

where T is the sampling interval. The resulting discretized model is described in

a regression form:

$$\begin{aligned} y(t+1) &= \underbrace{2y(t) - y(t-1) - T\mathbf{M_p^{-1}D_p}\left[y(t) - y(t-1)\right] - T^2\mathbf{M_p^{-1}K_p}\,y(t)}_{y_a(t)} \\ &\quad \underbrace{+\,T^2\mathbf{M_p^{-1}}f_p(t)}_{y_a(t)} + \mathbf{M_p^{-1}\Delta K_p}\underbrace{\left\{-\frac{\gamma T}{\omega}\left[y(t) - y(t-1)\right] - T^2 y(t)\right\}}_{y_b(t)} \\ &= y_a(t) + \mathbf{M_p^{-1}\Delta K_p} y_b(t) \end{aligned} \tag{4.9}$$

Substituting Eq. (4.7) into Eq. (4.9) yields:

$$\begin{aligned} y(t+1) &= y_a(t) + \mathbf{M_p^{-1}}\left(\sum_{j=1}^{N}\Delta\delta_j K_{mist}^{j}\right) y_b(t) \\ &= \left[\; y_a(t) \;\middle|\; \mathbf{M_p^{-1}}K_{mist}^{1}\, y_b(t) \;\middle|\; \cdots \;\middle|\; \mathbf{M_p^{-1}}K_{mist}^{N}\, y_b(t) \;\right] \times \\ &\quad \left[\; 1, \quad \Delta\delta_1, \quad \ldots, \quad \Delta\delta_N \;\right]^T \\ &= \varphi(t)^T\theta \end{aligned} \tag{4.10}$$

We succeed here in separating the perturbation of the blade mistuning pattern. The expression above can be used for a variety of parameter estimation algorithms to minimize the following cost function [132]:

$$\begin{aligned} J_n(\theta) &\triangleq \frac{1}{2}(\theta - \theta_0)^T P_0^{-1}(\theta - \theta_0) + \\ &\quad \frac{1}{2}\sum_{t=1}^{n}\left[y(t) - \varphi(t-1)^T\theta\right]^T W^{-1}\left[y(t) - \varphi(t-1)^T\theta\right] \end{aligned} \tag{4.11}$$

Basically, the cost in Eq. (4.11) represents the sum of weighted squares of errors (the second term) $e(t) = y(t) - \varphi(t-1)^T\theta$, which is the difference between the actual observation $y(t)$ and the value predicted by the model with parameter vector θ. W is the weight matrix. The first term has been included to account for initial conditions. P_0 can be seen as a measure of confidence in the initial estimate θ_0. Usually P_0 and W are both identity matrices.

The adopted multivariable least-squares algorithm for parameter estimation

is thus:

$$\begin{aligned}
\hat{\theta}(t) &= \hat{\theta}(t-1) + P(t-2)\varphi(t-1) \times \left[\varphi(t-1)^T P(t-2)\varphi(t-1) + W\right]^{-1} \times \\
&\quad \left[y(t) - \varphi(t-1)^T \hat{\theta}(t-1)\right] \\
P(t-1) &= P(t-2) - P(t-2)\varphi(t-1) \times \left[\varphi(t-1)^T P(t-2)\varphi(t-1) + W\right]^{-1} \times \\
&\quad \varphi(t-1)^T P(t-2) \\
P(-1) &= P_0 \quad \text{(any positive definite matrix)}
\end{aligned} \tag{4.12}$$

The perturbation of the blade mistuning pattern $\Delta\delta^*$ can be extracted from the final estimation of θ. Before proceeding to the second step in this strategy, some practical considerations concerning response expansion should be taken into account in the following.

4.3 Response expansion

In real cases, experimental data often provide less information than that one needs for analyses. For the purpose of identifying perturbation $\Delta\delta$, each degree of freedom (DOF) in the model should be measured. Unfortunately only a limited number of DOFs could actually be measured . The problem arises from the use of measured experimental data because of incompleteness. Expansion of these measured data is required for parameter estimation.

It is assumed that by making one measurement per blade, the time history of tip displacements $x_{1,j}(t)$ can be measured and reconstructed by the "tip-timing" measurement strategy [135]. The tip-timing method is a new-emerging non-invasive method in aeroengine. Blade tip deflections can be measured by making use of the blade tip arriving time when a blade tip passes the stationary probes installed on the engine casing (see Fig. 4.4). When the blade is experiencing vibration, the blade tip arriving time depends on the blade vibration amplitude as well as the rotation speed. The tip-timing method can be thus used to create an on-line monitoring system for blade dynamic performance. For this purpose, the "tip-timing" measurement strategy has the capabilities listed below:

- initial data measurement (time of blade tip passing through the probe)

using single or multiple probes;

- calculation of characteristic parameters including vibration amplitude, blade tip deflection etc, on the basis of measured data;
- processing of characteristic parameters in order to describe a specified blade dynamic behavior.

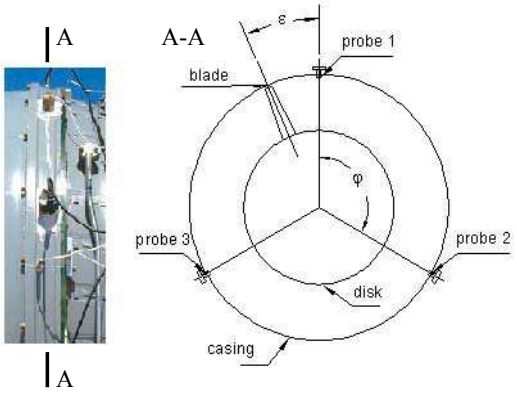

Figure 4.4: Illustration of the tip-timing method [135].

Consequently the forced response $X_{1,meas}$ in the frequency domain can be obtained. Besides, some high-precision current measurement techniques could be used to determine the current in each shunt circuit. Under harmonic excitation the electrical DOF $q_j(t)$ and Q_{meas} are also available. The objective is to expand $x_{1,j}(t), q_j(t)$ so that all other DOFs in each sector $x_{1,j}(t)$, $x_{2,j}(t)$, $x_{3,j}(t)$, $q_j(t)$ can be obtained. Classical expansion techniques make use of the analytical modes of structures [136]. At first, let's turn our attention to the free vibration equations of tuned piezoelectric shunted bladed disks derived from Eq. (3.3).

$$\mathbf{M_p}\,\ddot{y} + \mathbf{D_p}\,\dot{y} + \mathbf{K_p}\,y = \mathbf{0} \tag{4.13}$$

Due to the piezoelectric shunt damping, the damping matrix $\mathbf{D_p}$ can not be considered as either small or proportional to $\mathbf{M_p}$ and $\mathbf{K_p}$. Complex modes should thus be used for the response expansion. Eq. (4.13) is therefore rewritten in the

following generalized state-space form:

$$\begin{bmatrix} \mathbf{D_p} & \mathbf{M_p} \\ \mathbf{M_p} & \mathbf{0} \end{bmatrix} \begin{Bmatrix} \dot{y} \\ \ddot{y} \end{Bmatrix} + \begin{bmatrix} \mathbf{K_p} & \mathbf{0} \\ \mathbf{0} & -\mathbf{M_p} \end{bmatrix} \begin{Bmatrix} y \\ \dot{y} \end{Bmatrix} = \mathbf{0} \tag{4.14}$$

In all, $8N$ complex modes $\Psi = [\Phi, \lambda\Phi]^T$ could be obtained by solving the eigenvalue problem:

$$\left(\begin{bmatrix} \mathbf{D_p} & \mathbf{M_p} \\ \mathbf{M_p} & \mathbf{0} \end{bmatrix} \lambda + \begin{bmatrix} \mathbf{K_p} & \mathbf{0} \\ \mathbf{0} & -\mathbf{M_p} \end{bmatrix} \right) \Psi = \mathbf{0} \tag{4.15}$$

The proposed response expansion method makes use of the analytical modes of the tuned piezoelectric shunted bladed disk. First, a measurement vector Y_{meas} is built using $X_{1,meas}$ and Q_{meas}.

$$Y_{meas} = [X_{1,meas}, Q_{meas}, i\omega X_{1,meas}, i\omega Q_{meas}]^T \tag{4.16}$$

The measurement vector Y_{meas} can then be expressed as a linear combination of selective modes Ψ_{sel}, i.e.:

$$B\Psi_{sel}\mathbb{U} = Y_{meas} \tag{4.17}$$

where B is the Boolean matrix for the measured DOFs and $\mathbb{U}$ is an unknown vector to be estimated.

To avoid underdetermined problems, only a selected collection of $4N$ modes Ψ_{sel} is utilized in the above equation. It is found that inadequate system information in the selected mode set usually leads to poor expanded responses. In order to improve the accuracy of this response expansion, some auxiliary equations are sought to include more modes in Ψ_{sel}.

Let's recall the forced vibration equation Eq. (3.3) of the mistuned bladed disk and simply transform it into the frequency domain:

$$\left\{-\omega^2\mathbf{M_p} + i\omega\mathbf{D_p} + \mathbf{K_p}\right\} Y = A_p Y = f_p \tag{4.18}$$

where $y(t) = Ye^{i\omega t}$ and obviously we have $Y = \Phi_{sel}\mathbb{U}$.

Let's now rearrange the matrix A_p and extract the corresponding $2N$ rows in the bottom $A_{p,b}$ for coupled DOFs $X_{3,j}$ and Q_j. Let's note the absence of external excitation imposed on these coupled DOFs, i.e. $f_{p,b} = \mathbf{0}$.

$$\begin{bmatrix} A_{p,t} \\ A_{p,b} \end{bmatrix} Y = \begin{bmatrix} A_{p,t} \\ A_{p,b} \end{bmatrix} \Phi_{sel} \mathbb{U} = f_p = \begin{bmatrix} f_{p,t} \\ f_{p,b} \end{bmatrix} \tag{4.19}$$

$$A_{p,b} \Phi_{sel} \mathbb{U} = \mathbf{0} \tag{4.20}$$

Next, combine the equations Eq. (4.17) and Eq. (4.20):

$$\begin{bmatrix} B\Psi_{sel} \\ A_{p,b}\Phi_{sel} \end{bmatrix} \mathbb{U} = \begin{bmatrix} Y_{meas} \\ \mathbf{0} \end{bmatrix} \tag{4.21}$$

Finally, a set of $6N$ modes Ψ_{sel} could be utilized in this equation. Generally speaking, both tuned blade-dominant and disk-dominant modes near the excitation frequency should be involved. Once $\mathbb{U}$ is solved, the expanded response vector Y^{exp} is given by:

$$Y^{exp} = \Phi_{sel} \mathbb{U} \tag{4.22}$$

We can reproduce the time history of all DOFs in the j^{th} sector:

$$\begin{aligned} [x_{1,j}(nT), x_{2,j}(nT), x_{3,j}(nT), q_j(nT)]^T &= e^{i\omega nT} Y_j^{exp} \\ n &= 0, 1, 2, \cdots \end{aligned} \tag{4.23}$$

This expanded response is to be used for the online parameter estimation algorithm presented in the previous section.

4.4 Control law about the adjustment of piezoelectric mistuning $\Delta\delta_L$

Let's imagine that after parameter estimation an "initial" system equation Eq. (3.4) with $\Delta\delta^*$ can be rewritten in the frequency domain as follows:

$$\left[-\omega^2\mathbf{M} + i\gamma\mathbf{K}_{mech}^{\delta+\Delta\delta^*} + \left(\mathbf{K}_{mech}^{\delta+\Delta\delta^*} + \mathbf{K}_{piezo}^{\delta_L}\right)\right] X_0^{\delta+\Delta\delta^*,\delta_L} = F \tag{4.24}$$

In this equation, blade mistuning $\delta + \Delta\delta^*$ and piezoelectric mistuning δ_L are respectively incorporated into the stiffness matrices. If the piezoelectric mistuning pattern is the perturbation such that $\delta_L^{pert} = \delta_L + \Delta\delta_L$, in assuming a first order Taylor expansion, then the corresponding response vector $X^{\delta_L+\Delta\delta_L}$ is perturbed as:

$$X(\delta_L + \Delta\delta_L) = X_0 + \mathbf{J}\Delta\delta_L \tag{4.25}$$

The perturbed response vector is a function of the initial response vector X_0, the perturbation $\Delta\delta_L$ and the Jacobian matrix (or derivative) $\mathbf{J}$. The Jacobian is available mathematically (see Appendix B.1). We thus have a linear approximation of the response vector X in the neighborhood of δ_L at a specified frequency ω. Naturally, the adjustment of piezoelectric mistuning pattern $\Delta\delta_L$ can be obtained by minimizing the 2-norm of $X^{\delta_L+\Delta\delta_L}$, i.e.:

$$\Delta\delta_L = argmin_{\Delta\delta_L}\left\{\|X(\delta_L + \Delta\delta_L)\|_2\right\} \tag{4.26}$$

This objective function aims to minimize the response at a specified frequency ω. Alternatively, a more reasonable objective function defined over a frequency range $[\omega_l, \omega_u]$ is proposed:

$$\begin{aligned}\Delta\delta_L = argmin_{\Delta\delta_L}\left\{\Pi(\delta_L + \Delta\delta_L)\right\} \quad &= \quad argmin_{\Delta\delta_L}\left\{\int_{\omega_l}^{\omega_u} \|X(\delta_L + \Delta\delta_L, \omega)\|_2^2\, d\omega\right\} \\ &\text{subject to} \quad \Delta\delta_L - \Delta\delta_L^* = 0\end{aligned} \tag{4.27}$$

The response vector $X(\delta_L + \Delta\delta_L, \omega)$ and Jacobian matrix $\mathbf{J}(\delta_L, \omega)$ are both complex matrices (vectors). An additional constraint is necessary to ensure that $\Delta\delta_L$ is a real vector ($\Delta\delta_L^*$ denotes conjugation of $\Delta\delta_L$). The latter objective

function can easily be expanded as:

$$\begin{aligned}\Pi(\delta_L+\Delta\delta_L) &= \int_{\omega_l}^{\omega_u}\|X(\delta_L+\Delta\delta_L,\omega)\|_2^2 d\omega = \sum_{j=1}^{n}\|X(\delta_L+\Delta\delta_L,\omega_j)\|_2^2\Delta\omega \\ &= \Delta\omega\sum_{j=1}^{n}\big\{X_0^H(\omega_j)X_0(\omega_j)+2\Delta\delta_L^T Re[\mathbf{J}^H(\omega_j)X_0(\omega_j)]+ \\ &\quad \Delta\delta_L^T\mathbf{J}^H(\omega_j)\mathbf{J}(\omega_j)\Delta\delta_L\big\} \\ &= \Pi(\delta_L)+2\Delta\delta_L^T\sum_{j=1}^{n}Re[\mathbf{J}^H(\omega_j)X_0(\omega_j)]+ \\ &\quad \Delta\delta_L^T\sum_{j=1}^{n}[\mathbf{J}^H(\omega_j)\mathbf{J}(\omega_j)]\Delta\delta_L \end{aligned} \tag{4.28}$$

The Gauss-Newton method for such a nonlinear least-squares problem (see Appendix B.2) Eq. (4.27) is adopted to find a local minimizer in the vicinity of δ_L [137]. The final δ_L is found by the following typical iterative steps:

$$\begin{aligned}\text{Solve:}\quad Re[\sum_{j=1}^{n}\mathbf{J}^H(\omega_j)\mathbf{J}(\omega_j)](\Delta\delta_L)_{gn} &= -\sum_{j=1}^{n}Re[\mathbf{J}^H(\omega_j)X_0(\omega_j)] \\ \text{line search:}\quad \bar{\delta_L} &= \delta_L+\beta(\Delta\delta_L)_{gn} \\ \text{next iterate:}\quad \delta_L &= \bar{\delta_L};\end{aligned} \tag{4.29}$$

Here, $(\Delta\delta_L)_{gn}$ is the Gauss-Newton step and β is found by conducting a line search [137]. In combination with a line search, this hybrid method can be shown to guarantee convergence.

4.5 Numerical simulation and results

In this section, we will present the results of computer simulations using the formulas derived in the previous sections.

Table 4.1: Numerical values of the lumped-parameter bladed disk model

No.	$\Delta\delta_{real}$	$\Delta\delta^*$	$\Delta\delta_L$	$\Delta\delta^*_{exp}$	$\Delta\delta_L^{exp}$
1	0	7.10e-5	-0.0064	0.0054	0.0401
2	0	6.52e-5	0.0059	-0.0041	-0.0005
3	0	6.62e-5	0.0050	0.0163	0.0079
4	0	6.84e-5	0.0142	0.0028	0.0079
5	-0.0090	-0.0097	-0.0090	-0.0184	-0.0061
6	0	6.82e-5	-0.0073	-0.0100	0.0214
7	-0.0099	-0.0098	-0.0149	-0.0167	-0.0315
8	0	6.47e-5	0.0391	0.0161	0.0465
9	0	7.04e-5	0.0241	0.0039	0.0249

4.5.1 Performance of the adaptive control strategy

It is assumed that the initial blade mistuning δ and the corresponding optimal piezoelectric mistuning pattern δ_L are both obtained after the optimization routine in Chapter 3. Numerical simulations concerning the adaptive control strategy have been carried out. It is moreover assumed that the perturbation takes place randomly in two cracked blades with blade No.: 5,7 in Table 4.1. The time-varying parameter $\alpha(t)$ in Eq. (4.3) is set at 0.01 and remains constant during parameter estimation. As shown in Fig. 4.5a, when the perturbation $\Delta\delta$ is exposed, an amplitude augmentation occurs around the frequency $1213\,rad/s$. If the bladed disk is experiencing vibration at this frequency and the steady response is observed sequentially, then the online parameter estimation presented in Section 4.2 is performed.

In the simulation, the observation of a steady response is generated numerically. Provided exact and complete measurements of all DOFs in the bladed disk model, an "accurate" estimation of perturbation $\Delta\delta^*$ is derived by the parameter estimation.

To validate the response expansion technique forwarded in Section 4.3, the measured blade tip displacement $X_{1,meas}$ and the electrical DOF Q_{meas} are given by exact numerical values. The estimated perturbation derived from the incomplete measurements is denoted $\Delta\delta^*_{exp}$.

It is shown in Table 4.1 that the online parameter estimation provides a very good estimation of $\Delta\delta$ when the exact response from the analytical calculation is used. In contrast, the expanded response leads to a poorly estimated perturbation $\Delta\delta^*_{exp}$. This can be explained by the high sensitivity of the blade response to the blade mistuning pattern. Since no "exact" response could be obtained using the response expansion technique, a totally spurious perturbation pattern might be caused by the small error from the expanded response.

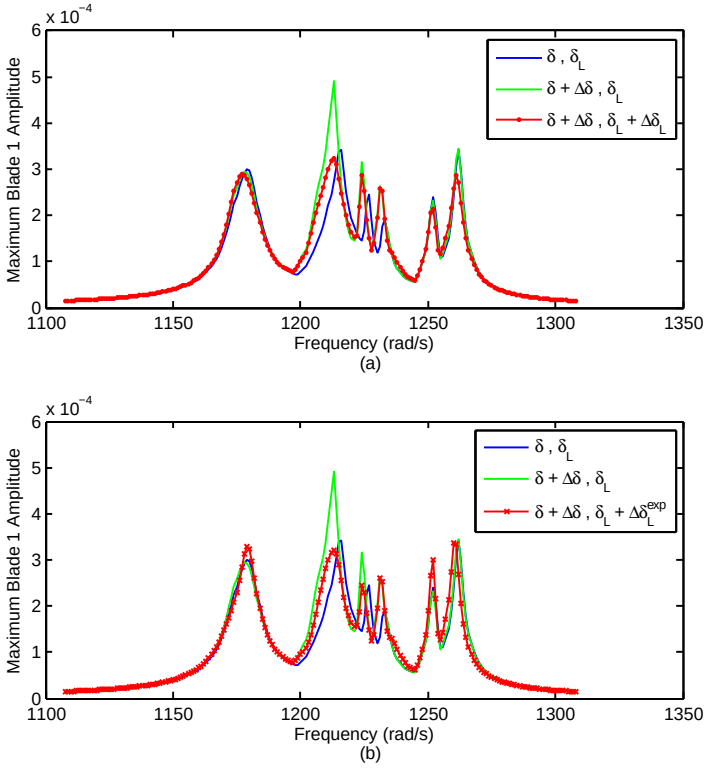

Figure 4.5: Results of the adaptive control strategy

However, let's be clear that in the adaptive control strategy the perturbation is not necessary to be identified precisely. It is the adjustment of piezoelectric mistuning $\Delta\delta_L$ that plays the role of control variable. Following the estimated perturbation $\Delta\delta^*$ (or $\Delta\delta^*_{exp}$), the optimal adjustment $\Delta\delta_L$ (or $\Delta\delta_L^{exp}$) is searched by the iterative Gauss-Newton method combined with a line search (see

Eq. (4.29)). With the new mistuning patterns $(\delta + \Delta\delta, \delta_L + \Delta\delta_L)$ in Fig. 4.5a ($(\delta + \Delta\delta, \delta_L + \Delta\delta_L^{exp})$ in Fig. 4.5b), frequency sweep results are plotted below. The red curve shows that a further vibration reduction around the excitation frequency is achieved due to $\Delta\delta_L$. Moreover, the deduced adjustment $\Delta\delta_L^{exp}$ still provides very good vibration suppression results, as indicated in Fig 4.5b.

4.5.2 Adaptive control strategy applied to time-varying mistuned bladed disks

The performance of the adaptive control strategy applied to time-varying mistuned bladed disks will be investigated in this subsection. The "time-varying" blade mistuning perturbation will be modeled in a step-increasing manner. Considering that the blade stiffness evolves slowly, the blade mistuning pattern is thought to be constant over each step interval. Similar to Eq. (4.3), a series of values with a constant increment are assigned to $\alpha(t)$ in order to describe the gradual degradation of blade stiffness. α remains invariant in each parameter estimation step.

Note that the perturbation $\Delta\delta$ exerts a great impact on the distribution of peak amplitudes in the frequency range. In particular, the location of peaks may change. On the other hand, the objective function Π (see Eq. (4.28)) could be treated as a generalized Euclidean norm of response over the frequency range. It takes into account all possible peaks in this frequency band with the evolution in blade mistuning. Consequently, the function Π (instead of the maximum peak values of the blade amplitude) is used to measure performance of the adaptive control strategy.

Fig. 4.6 shows the effectiveness of this adaptive control strategy ($\triangle$) with blade stiffness mistuning evolution. For purpose of comparison, performances of the blade-mistuned disk without piezoelectric mistuning ($\square$) and of the mistuned bladed disk with an invariant piezoelectric mistuning pattern δ_L ($\odot$) are also illustrated. Starting from the tuned case, it can be seen that as compared with the invariant piezoelectric mistuning pattern $\Delta\delta_L$, the variant piezoelectric mistuning by the adaptive control strategy is more effective in suppressing the vibration of time-varying mistuned bladed disks.

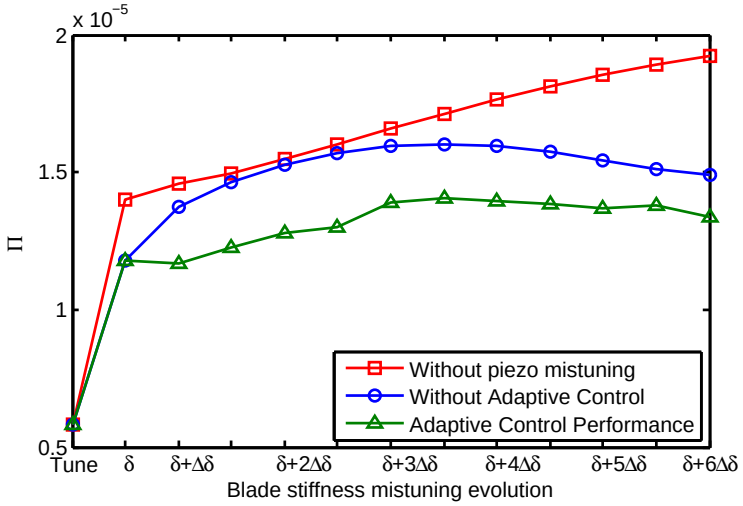

Figure 4.6: Performance of the adaptive control strategy applied to time-varying mistuned bladed disks

4.6 Conclusion

The adaptive control strategy based on the piezoelectric shunt technique has focused on more realistic cases where the blade mistuning pattern is slowly time-varying. By taking advantage of the controllability of piezoelectric shunt circuits, the piezoelectric mistuning pattern can be adjusted to keep "optimal" in terms of maintaining low blade vibration levels.

When the blade mistuning is evolving, the adaptive control strategy is relatively more effective compared with the genetic algorithm optimization. Repeating blade mistuning identification in terms of δ is avoided; the optimization of piezoelectric mistuning is greatly simplified since the piezoelectric mistuning pattern is only slightly adjusted based on the precedent pattern. This is the motivation for the proposed adaptive control strategy. Numerical studies have shown that a fine performance is achieved with respect to reducing the vibration of a time-variant mistuned bladed disk.

Chapter 5

Essentially nonlinear piezoelectric shunt circuit

An essentially nonlinear piezoelectric shunt circuit is proposed for practical realization of nonlinear energy sink in this chapter. First, targeted energy transfer phenomenons from a linear primary structure to a nonlinear attachment, i.e., nonlinear energy sink, are introduced. Various methods for nonlinear dynamic problems and stability analysis are listed. Special attention is paid to the harmonic balance method since it is employed as a main tool in this thesis. The configuration of essentially nonlinear shunt circuits is described. Both the nonlinear normal modes and forced response under harmonic forcing are investigated extensively. A special section is devoted to a numerical method , namely, *variable-coefficient harmonic balance method*, to calculate quasi-periodic responses arising in the coupled electromechanical nonlinear system. Finally, the concept of nonlinear damping ratio is discussed.

5.1 Targeted energy transfer and nonlinear energy sink

The nonlinear targeted energy transfer phenomenon (or nonlinear energy pumping) has been first observed by Gendelman [138] in 2001. In this research, redistribution of energy in a highly asymmetric two-DOF system consisting of

weakly coupled linear oscillator (with a high linear frequency) and highly nonlinear damped oscillator (with a small linear frequency) is investigated. The need for *essential (strong) nonlinearity* in the nonlinear oscillator is emphasized. It was late demonstrated that the transition of mode localization in nonlinear systems raises the possibility of energy transfer from one mode to another [139].

Gendelman has investigated the transient dynamics of the global system when the primary linear oscillator undergoes impulsive loads. It is shown that, whereas input energy is initially stored to the linear oscillator (LO), a nonlinear normal mode (NNM) localized to the nonlinear attachment can be excited provided that the input energy is above a critical threshold. As a result, TET occurs and a significant portion of the input energy to the LO gets passively absorbed and locally dissipated by the essentially nonlinear attachment. With the capacity of absorbing external energy, the nonlinear attachment is termed as nonlinear energy sink (NES).

Another attractive feature of such essentially nonlinear oscillators is that they do not have preferential resonant frequencies of oscillation. It enables them to resonantly interact with modes of the primary linear system at arbitrary frequency ranges. This characterizes NES from traditional vibration absorbers, such as resonant shunted piezoelectrics. As remarked in Chapter 1, the behavior of resonant shunted piezoelectrics is very sensitive to the deviation of both structural parameters and optimal electrical parameters.

5.1.1 Configurations of nonlinear energy sink

A basic NES configuration (see Fig .5.1a) has been proposed by Vakakis and Gendelman [140; 141]. The grounded nonlinear oscillator (the NES) is coupled to the impulsively loaded primary structure by means of essential nonlinearity. In this configuration, grounded and relatively heavy nonlinear attachments clearly limit their application in practice. For this reason, another lightweight and ungrounded NES configuration (see Fig .5.1b) has been devised and widely studied [142]. It has been shown that the dynamics of these two NES configurations bears strong resemblance.

According to the classic NES configuration in Fig .5.1b, the simplest two-DOF

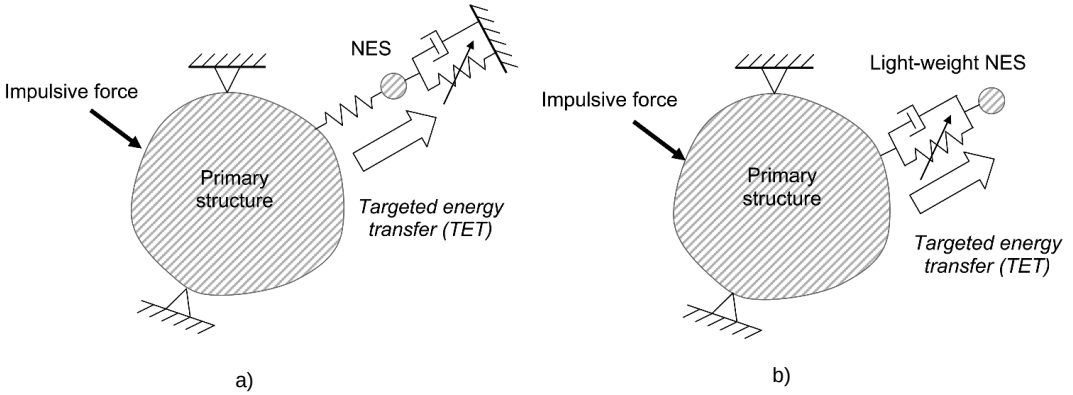

Figure 5.1: NES configurations [139]: a) grouded and heavy weighted NES; b) ungrounded and lightweight NES.

system capable of exhibiting targeted energy transfer phenomenons is constructed as follows [139]:

$$m_1\ddot{x} + c_1\dot{x} + c_2(\dot{x} - \dot{v}) + k_1 x + k_2(x - v)^3 = 0 \tag{5.1}$$

$$m_2\ddot{v} + c_2(\dot{v} - \dot{x}) + k_2(v - x)^3 = 0 \tag{5.2}$$

This system consists of a grounded, damped SDOF linear oscillator (LO), which acts as the primary system with mass m_1 and viscous damper c_1, coupled to an ungrounded attachment m_2 through a pure cubic stiffness in parallel to a viscous damper c_2. The equation of motion for this integrated system clearly characterizes NES by: a) strong mass asymmetry, $m_2 << m_1$; b) essentially nonlinear coupling between the primary structure and NES.

5.1.2 Analysis method and NES design

TET has then been defined as the one-way (irreversible) channel of vibrational energy from the directly excited linear primary structure to the attached NES. Weak damping of the global system is a prerequisite for effective realization of TET in the dynamics discussed. Without the presence of damping, the integrated system typically can only exhibit nonlinear beat phenomena, whereby the conserved energy flows back and forth between the linear primary system and the

NES, and that no targeted energy transfer, even energy dissipation can occur.

The triggering mechanism of nonlinear energy pumping has been further investigated in several recent studies. A criterion (critical threshold) for inducing nonlinear energy pumping has been formulated by Vakakis [143]. In particular, for the case of a two DOF system it is shown that nonlinear energy pumping coincided with the zero crossing of a frequency of envelope modulation.

A trend is seen that the theory of nonlinear mode localization has become a powerful tool in pursuing the mechanism of nonlinear energy transfer. At early times, the complexification-averaging method [139] is adopted to have a grasp of the dynamics and nonlinear localization phenomena that occur in different frequency/energy ranges of the global system. More recently, the bifurcation structure of the nonlinear normal modes (NNMs) has been studied in-depth for the undamped linear primary system coupled to an undamped NES attachment [144; 145]. Stemming from the classic theory of NNM by Rosenberg, a slightly different definition of NNM is proposed by Kerschen [146; 147]. Not only the the resonant dynamics under condition of 1:1 internal resonance, but also nonsynchronous periodic motions are included in the calculation of NNMs. The influence of damping on the resonant dynamics and TET phenomena in the weakly damped system has been further studied in [148]. In these research efforts, two useful tools are proved effective in seeking the underlying dynamical mechanism governing TETs:

- Frequency-energy plot (FEP). As a suitable graphic representation of nonlinear normal modes, it offers an intuitive observation of their energy-dependence. For the weakly damped dynamics, it also reveals how the decaying global system energy exerts an impact on the transition of nonlinear mode localization, and further leads to nonlinear energy transfer.

- Wavelet transform (WT). When superposed to a frequency-energy plot, the wavelet transform (WT) spectra of the weakly damped responses is used extensively for analyzing energy exchanges and transfers taking place between the primary structure and NES [148; 149].

The response of harmonically forced linear oscillator with attached nonlinear energy sink (NES) has been investigated by Starosvetsky and Gendelman

[150; 151]. Even in the case of single-frequency excitation, quasi-periodic response regimes is demonstrated to typically exist together with periodic response regimes. The complicated response regimes give rise to essential problems that in such situations, NES requires careful tuning design for optimal performance and may be only efficient in limited range of external forcing amplitudes.

In terms of NES design, a design procedure has been developed by Musienko et al. [152]. Efficient energy pumping in the presence of uncertain parameters (in particular, nonlinear parameters and damping) has been assessed by Gourdon and Lamarque [153]. Kozmin et al. [154] have performed studies of optimal energy pumping mode using global optimization. Experimental verification of analytic and numerical results of nonlinear energy pumping has been performed by means of appropriately small designed building model [155].

5.1.3 Implementation of nonlinear energy sink

Among a number of experimental studies of nonlinear energy transfers [156; 157], the design and practical implementation of essentially nonlinear elements is always of major concern. As remarked earlier, this is due to the fact that essential nonlinearity characterizes the nonlinear energy sink systems.

In most of existing NES devices, essential nonlinearity is realized by sophisticated wire-based rigs. For example, the design, application and performance of nonlinear energy sink in suppressing aeroelastic instability has been reported by Lee et al. [158; 159]. This research interests us because the rotating blades in the flow field also experience possible aeroelastic instabilities. In this experimental study, a 2DOF in-flow rigid wing model interacts with a mechanical NES device. Since the NES provides a one-way irreversible channel of vibration energy from the wing to the NES, it is feasible to partially or even completely suppress aeroelastic instability of the wing in flow field. Naturally, NES is also expected to give promising prospect if applied to bladed disks.

Let's focus on the NES used in this nonlinear aeroelastic test apparatus (NATA) depicted in Fig .5.2. A small "car", representing the mass of NES, is supported on an air track and connected to the NATA through the viscous damper and the essentially nonlinear spring. This spring is formed by fastening

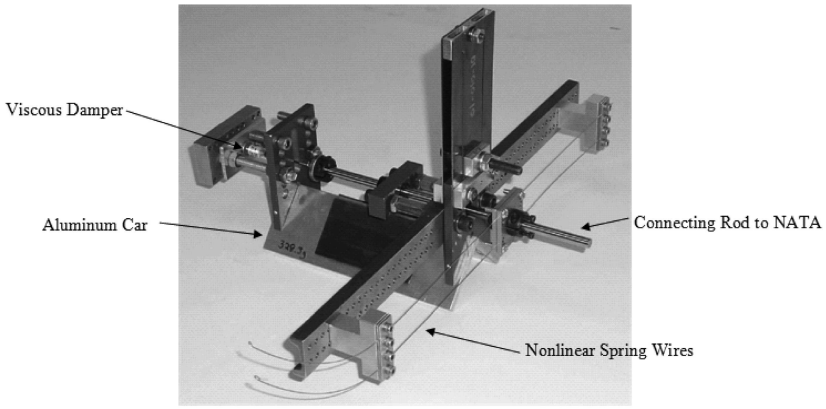

Figure 5.2: Configuration of NES used in NATA [159]

a pair of thin metal wires. As a consequence, geometrically nonlinear overall stiffness characteristic between the NATA and NES is obtained when the NATA moves with respect to the NES in the direction perpendicular to the wires.

In another applications of nonlinear energy pumping to problems in acoustics, essential nonlinearity depending on the thin circular visco-elastic membrane experiencing large amplitude oscillation has been demonstrated experimentally by Cochelin et al. [160].

As pointed out in the literature [161], such geometrically nonlinear stiffness designs at this stage also introduce a weight penalty to the primary structure and need significant installation space for efficient vibration mitigation. These inherent limitations stimulate us to seek new intermedia for practical realizations of nonlinear energy sinks. A nonlinear piezoelectric shunting strategy has been proposed in a previous research effort [162]. In this chapter, we attempt to construct a piezoelectric-based NES through shunting the piezoelectric materials by a so-called essentially nonlinear shunt circuit.

5.2 Methods in nonlinear analyses

In this section, we will briefly discuss different methods that can be used to characterize the response of nonlinear systems. Let's consider a non-autonomous nonlinear dynamic system described by the following second order differential

equation:

$$M\ddot{u} + D\dot{u} + Ku + f_{nl}(t, u, \dot{u}) = f(\omega, t) \tag{5.3}$$

where M, D and K are mass, damping and stiffness matrix of size $n \times n$, respectively; f_{nl} represents nonlinear force and $f(\omega, t)$ the external periodic excitation with a frequency ω. We are mainly interested in periodic solutions of the nonlinear system.

For time-periodic solutions, there is a minimum time interval $T > 0$ (the "period") after which the system returns to its original state:

$$u(t) = u(t + T) \tag{5.4}$$

for all t.

There exist numerous approaches to analyzing periodic solutions for a nonlinear dynamic system. These approaches can be naturally divided into two categories:

- *analytical methods*, such as perturbation methods [163] and averaging method [164], are limited in small-sized systems possessing certain types of nonlinearities. In this thesis, a complexification-averaging technique [139] that is especially suitable for analyzing strong nonlinear systems is to be adopted in our studies of targeted energy transfer in a 2DOF system;

- *numerical methods* can be further categorized into two groups:

  1. methods in the time domain based on time integrations [165]; the time history of motions are progressively constructed from the system in question;
  2. methods in the frequency domain based on Galerkin method (i.e. a projection procedure) [166].

  There are also some other kinds of numerical methods, such as Describing Function Method [167] and Cell Mapping method [168], etc, which are beyond the scope of this thesis.

In particular, the harmonic balance method (HBM) has been shown computationally efficient for simple nonlinear problems as well as complex industrial

nonlinear systems. Employed as a principal tool in this thesis, it will be introduced in detail. Continuation technique is also covered in order to follow the branch of solutions by HBM.

5.2.1 Harmonic balance method

For all linear systems subjected to mono-harmonic excitation their responses will also be mono-harmonic. This consideration is derived from the theory of linear differential equations. But it cannot be directly applied to the non-linear system case. It is only possible to suppose that nonlinear system response is periodic. Sometimes it happens that non-linear response is quasi-periodic or even chaotic. But in majority of cases the periodic solution is obtained. Solutions periodic in time, and of an unique fundamental frequency, may be expressed in terms of a Fourier series:

$$\begin{aligned} u(t) &= U^0 + \sum_{k=1}^{N_h} U^{ck} cos(k\omega t) + U^{sk} sin(k\omega t) \\ &= [I, cos(\omega t)I, sin(\omega t)I, \cdots, cos(k\omega t)I, sin(k\omega t)I, \cdots] \\ &\quad \times [U^0, U^{c1}, U^{s1}, \cdots, U^{ck}, U^{sk}, \cdots]^T \\ &= T(t)U \end{aligned} \tag{5.5}$$

where I is the $n \times n$ identity matrix and N_h is the number of retained harmonics. The $(2N_h + 1)n \times 1$ vector U contains unknown Fourier coefficients:

$$U = [U^0, U^{c1}, U^{s1}, \ldots, U^{ck}, U^{sk}, \ldots, U^{cN_h}, U^{sN_h}]^T \tag{5.6}$$

$T(t)$ is the $n \times (2N_h + 1)n$ matrix containing trigonometric functions:

$$T(t) = [I, cos(\omega t)I, sin(\omega t)I, \cdots, cos(N_h\omega t)I, sin(N_h\omega t)I] \tag{5.7}$$

The same procedure is then applied for the external force f and nonlinear

force f_{nl}:

$$f(t) = T(t) \times [F^0, F^{c1}, F^{s1}, \cdots, F^{ck}, F^{sk}, \cdots]^T = T(t)F \quad (5.8)$$

$$f_{nl}(t, u, \dot{u}) = T(t) \times [F^0_{nl}, F^{c1}_{nl}, F^{s1}_{nl}, \cdots, F^{ck}_{nl}, F^{sk}_{nl}, \cdots]^T = T(t)F_{nl}(U) \quad (5.9)$$

In order to compute velocities and accelerations, a frequential derivative operator is defined:

$$\nabla = diag(\mathbf{0}_{n\times n}, \nabla_1, \cdots, \nabla_{N_h}) \quad \text{with} \nabla_k = \begin{bmatrix} \mathbf{0} & I \\ -I & \mathbf{0} \end{bmatrix} \quad (5.10)$$

We may thus write:

$$\dot{u}(t) = \omega T(t)\nabla U \quad (5.11)$$

$$\ddot{u}(t) = \omega^2 T(t)\nabla^2 U \quad (5.12)$$

Substituting Eq. (5.6)-(5.12) into Eq. (5.3) yields:

$$\omega^2 MT(t)\nabla^2 U + \omega DT(t)\nabla U + KT(t)U + T(t)F_{nl}(U) = T(t)F \quad (5.13)$$

Considering that for a $n \times n$ matrix W and a $(2N_h + 1)n \times 1$ vector U, we have:

$$WT(t)U = T(t)N_w U \quad (5.14)$$

with $N_w = Bdiag(W, W, \cdots)$.

Eq. (5.13) becomes:

$$T(t)[(\omega^2 N_M \nabla^2 + \omega N_D \nabla + N_K)U + F_{nl}(U)] = T(t)F \quad (5.15)$$

Time dependency may be suppressed and a frequency algebraic equation linking Fourier coefficient may be obtained using a Galerkin method, which is a projection of the equation on trigonometric functions. Indeed these trigonometric functions define a scalar product:

$$\langle f, g \rangle = \frac{\omega}{2\pi} \int_0^{2\pi/\omega} f(t)g(t)dt \quad (5.16)$$

We thus may write:

$$\frac{\omega}{2\pi}\int_0^{2\pi/\omega} {}^T T(t)T(t)dt = \frac{1}{2}\begin{bmatrix} 2I & & & 0 \\ & I & & \\ & & I & \\ 0 & & & \ddots \end{bmatrix} = L \tag{5.17}$$

Applying this scalar production Eq. (5.15) leads to:

$$L[(\omega^2 N_M \nabla^2 + \omega N_D \nabla + N_K)U + F_{nl}(U)] = LF \tag{5.18}$$

L is a diagonal matrix so Eq. (5.18) may be simplified into a $(2N_h + 1)n$ equation system:

$$G(\omega, U) = P(\omega)U + F_{nl}(U) - F = 0 \tag{5.19}$$

where $P(\omega) = \omega^2 N_M \nabla^2 + \omega N_D \nabla + N_K$.

The problem of searching for periodic solutions to the nonlinear dynamic system Eq. (5.3) is therefore equivalent to finding zeros of the algebraic function $G(U) : \mathbb{R}^{(2N_h+1)n} \rightarrow \mathbb{R}^{(2N_h+1)n}$. Roots of Eq. (5.19) are found by using a quasi-newton algorithm, variants of which are available in Fortran libraries or in Matlab's optimization toolbox. A critical issue in the formulation of harmonic balance method is the treatment of nonlinear force, i.e., the determination of the nonlinear term $F_{nl}(U)$, which is to be discussed next.

Treatment of nonlinear force

In the standard harmonic balance method, the nonlinear force $f_{nl}(t)$ is expressed by a Fourier expansion:

$$f_{nl}(t) = F_{nl}^0 + \sum_{k=1}^{N_h} F_{nl}^{ck} cos(k\omega t) + F_{nl}^{sk} sin(k\omega t) \tag{5.20}$$

where

$$F_{nl}^{0} = \frac{\omega}{2\pi}\int_{0}^{2\pi/\omega} f_{nl}(t, T(t)U, \omega T(t)\nabla U)dt \tag{5.21}$$

$$F_{nl}^{ck} = \frac{\omega}{\pi}\int_{0}^{2\pi/\omega} f_{nl}(t, T(t)U, \omega T(t)\nabla U)cos(k\omega t)dt \tag{5.22}$$

$$F_{nl}^{sk} = \frac{\omega}{\pi}\int_{0}^{2\pi/\omega} f_{nl}(t, T(t)U, \omega T(t)\nabla U)sin(k\omega t)dt \tag{5.23}$$

Apparently if the nonlinear function $f_{nl}(t, u, \dot{u})$ is of a simple form (e.g., a cubic nonlinearity), analytical expression of F_{nl} can be readily obtained for small valued N_h. When the nonlinearity is strong, the solution may not be strictly harmonic. Also higher harmonics may significantly contribute to the overall solution. Moreover, when more harmonics are included in the analysis the resulting expression from Eq. (5.20) may be long and complex. Consequently the classical HBM becomes cumbersome or even impractical.

In the case that no analytical expression can be written between F_{nl} and U, nonlinearities of all kinds could be treated by using the alternating frequency/time-domain (AFT) technique [169] based on fast Fourier transform. Eq. (5.19) is nonlinear and it must be solved iteratively. AFT technique in this iteration process can be sketched in Fig. 5.3:

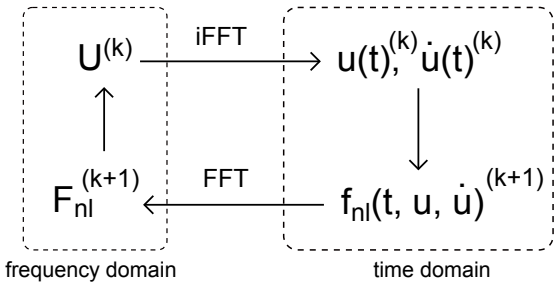

Figure 5.3: Alternating frequency/time-domain technique

At each iterative step, an evaluation of the approximate temporal terms $u(t)$ and $\dot{u}(t)$ is carried out from an initial value $U^{(k)}$ using the inverse fast Fourier transform (iFFT); it also allows to evaluate temporarily the nonlinear term $f_{nl}(t, u, \dot{u})^{(k+1)}$, and then to deduce Fourier coefficients F_{nl} by a fast Fourier trans-

form (FFT) procedure. As a result, an explicit evaluation of $F_{nl}(U)$ is avoided and HBM could be applied with a large number of harmonics.

Besides AFT technique, the determination of the nonlinear term $F_{nl}(U)$ could also be solved by a Trigonometrical Collocation Method [170; 171].

5.2.2 Continuation technique

The task of finding a periodic solution for the the nonlinear dynamic system Eq. (5.3) can be transformed into an equivalent root-finding problem Eq. (5.19), by means of HBM:

$$G(\omega, U) = 0 \tag{5.24}$$

where ω is an independent, externally controlled scalar parameter, excitation frequency over a range in which the solution to Eq. (5.3) is of interest; U is the $(2N_h + 1)n \times 1$ unknown Fourier coefficient vector and G a nonlinear algebraic function in a $(2N_h + 1)n$ dimensional space.

Once a solution to Eq. (5.24) is found for a certain parameter, i.e. (ω^0, U^0), one can use this information in order to find the other solutions when the control parameter of the system ω is varied. The variation of ω yields a branch of solutions in the solution-parameter space.

Here, we consider continuation technique for the periodic solutions of the system Eq. (5.24). This technique provides algorithmic procedures to generate a continuum of periodic solutions (ω^j, U^j) so that:

$$G(\omega^j, U^j) \leq \epsilon \tag{5.25}$$

where ϵ is the prescribed accuracy of the solution.

In general, the continuation technique proceeds step-wise, due to the fact that each previous periodic solution is the initial guess for finding the next periodic solution. There exist various continuation methods that differ in the parameterization strategy, predictor, corrector and step control [172; 173]. The arc-length continuation method employed in this chapter is based on a prediction step tangent to the solution branch and subsequent correction steps to converge to the branch (see Fig. 5.4).

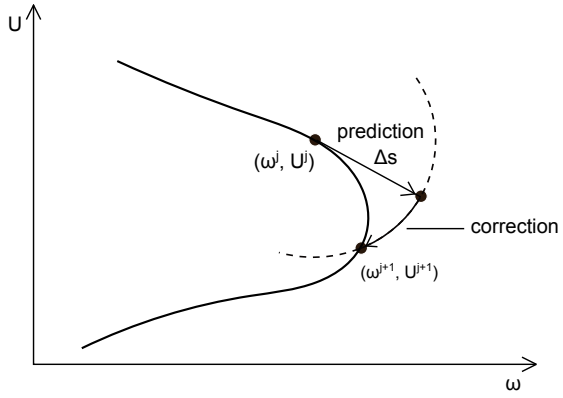

Figure 5.4: Arc-length continuation

In an arc-length continuation, periodic solutions are parameterized by the arc length s, so that $(\omega^j, U^j) = (\omega(s_j), U(s_j))$. The subsequent solution is to be obtained by:

$$U^{j+1} = U^j + \Delta U^{pred} + \sum_k \Delta U_k^{cor} \tag{5.26}$$

$$\omega^{j+1} = \omega^j + \Delta\omega^{pred} + \sum_k \Delta\omega_k^{cor} \tag{5.27}$$

Prediction step

At step j, ΔU^{pred} and $\Delta\omega^{pred}$ are generated along the tangent vector to the branch at the current point (ω^j, U^j). An expansion is first performed:

$$\begin{aligned} G(\omega^j + \Delta\omega^{pred}, U^j + \Delta U^{pred}) = {} & G(\omega^j, U^j) + \frac{\partial G(\omega^j, U^j)}{\partial U}\Delta U^{pred} + \\ & \frac{\partial G(\omega^j, U^j)}{\partial \omega}\Delta\omega^{pred} + \text{H.O.T} = 0 \end{aligned} \tag{5.28}$$

Neglecting the high order terms and substituting Eq. (5.25) into the above expression yields:

$$\frac{\partial G(\omega^j, U^j)}{\partial U}\Delta U^{pred} + \frac{\partial G(\omega^j, U^j)}{\partial \omega}\Delta\omega^{pred} = 0 \tag{5.29}$$

Eq. (5.29) is underdetermined. An auxiliary condition is desired to obtain

an unique prediction. For this purpose, the arc-length is normalized so that the tangent vector $[\Delta U^{pred} \,|\, \Delta\omega^{pred}]^T$ has a unit length:

$$\frac{||\Delta U^{pred}||^2}{||\Delta s||^2} + \frac{||\Delta\omega^{pred}||^2}{||\Delta s||^2} = 1 \tag{5.30}$$

Combining Eq. (5.29) with Eq. (5.30), we obtain expressions of $\Delta\omega^{pred}$ and ΔU^{pred}:

$$\Delta\omega^{pred} = \pm\Delta s / \sqrt{||[\frac{\partial G(\omega^j, U^j)}{\partial U}]^{-1} \frac{\partial G(\omega^j, U^j)}{\partial \omega}||^2 + 1} \tag{5.31}$$

$$\Delta U^{pred} = -[\frac{\partial G(\omega^j, U^j)}{\partial U}]^{-1} \frac{\partial G(\omega^j, U^j)}{\partial \omega} \Delta\omega^{pred} \tag{5.32}$$

It is observed that there are two possibilities for $\Delta\omega^{pred}$, which correspond to two different prediction directions. In order to follow the branch in the same direction, a scalar product condition is imposed between two consecutive prediction steps:

$$[\Delta U^{pred} \,|\, \Delta\omega^{pred}]_{j-1}^T \cdot [\Delta U^{pred} \,|\, \Delta\omega^{pred}]_j \geq 0 \tag{5.33}$$

Correction step

The prediction solution $(\omega^j + \Delta\omega^{pred}, U^j + \Delta U^{pred})$ usually does not meet the criterion in Eq. (5.25). A Newton-Raphson corrector is utilized to make the prediction solution converge to the branch. Values of ΔU_k^{cor} and $\Delta\omega_k^{cor}$ corresponding to k^{th} correction are determined by:

$$\frac{\partial G(\omega, U)}{\partial U}\Delta U_k^{cor} + \frac{\partial G(\omega, U)}{\partial \omega}\Delta\omega_k^{cor} = -G(\omega, U) \tag{5.34}$$

where (ω, U) is the updating point expressed by:

$$U = U^j + \Delta U^{pred} + \sum_{l=1}^{k-1} \Delta U_l^{cor} \tag{5.35}$$

$$\omega = \omega^j + \Delta\omega^{pred} + \sum_{l=1}^{k-1} \Delta\omega_l^{cor} \tag{5.36}$$

Eq. (5.34) is also underdetermined. An additional equation is given by:

$$||U - U^j||^2 + ||\omega - \omega^j||^2 = ||\Delta s||^2 \tag{5.37}$$

It means that the distance between the two consecutive periodic solution is always kept equaling to Δs.

This iterative process is carried out until convergence is achieved. Convergence is achieved when $G(\omega, U) \approx 0$ approaches to the desired accuracy. In summary, the algorithm for periodic solutions based on HBM and arc-length continuation method is illustrated in Fig. 5.5.

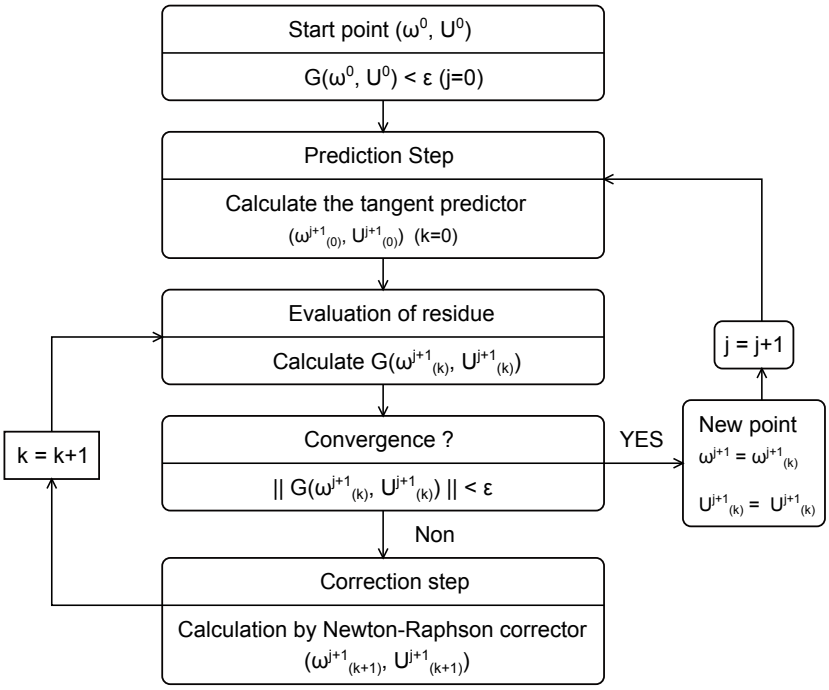

Figure 5.5: Algorithm for continuation of periodic solutions

Step control

The evolution path of this predictor-corrector method is parameterized by the distance Δs along the tangent predictor, also referred to as arc-length continuation parameter in the literature. In simple problems the principles introduced

above may work effectively without a step-length control. That is, constant step lengths are taken throughout, with $\Delta s = 0.1$. If the step size is small enough, such a step strategy may be successful for a wide range of problems. But such results are often obtained in an inefficient manner, involving too many steps along "flat" branches. The step length should be adapted to the actual convergence behavior. Ultimately, it is the flexibility of a step control that decides whether a continuation algorithm works well. Step-length algorithms should therefore be specifically designed.

As pointed out in the literature [173], step-length algorithms can be based on empirical arguments. The costs of a continuation are moderate for a certain medium step length, which is related to an optimal number N^*_{iter} of iterations of during the correction step. This number depends on the type of corrector and on the prescribed error tolerance ϵ. For example, with quasi-Newton correctors and $\epsilon = 10^{-4}$, the optimal number is about $N^*_{iter} = 6$.

The step control strategy used herein relies on the evaluation of the convergence quality by the number of iterations of the corrector step. The step size is controlled so that the corrector step requires on average the desirable number of iterations N^*_{iter}. At each step, the step size is updated according to the ratio between the desirable number N^*_{iter} and the previous number N^{j-1}_{iter} of iterations:

$$\Delta s^{(j)} = \frac{N^*_{iter}}{N^{j-1}_{iter}} \Delta s^{(j-1)} \tag{5.38}$$

In practice,the ratio $N^*_{iter}/N^{j-1}_{iter}$ is often bounded to make the adaptation step-size more robust and to prevent the continuation from jumping between different branches. The step size can also be bounded $\Delta s \leq \Delta s_{max}$ to obtain enough discretized points on the branch during the continuation. In case of no convergence, the step size can be halved until convergence is achieved.

5.3 Stability analysis

When tracing a branch of periodic solutions, the question arises whether the periodic solutions are stable and where and in which way stability is lost. Deter-

mining the local stability of a dynamical system periodic solution is of primary interest in an engineering context since only stable solutions are experimentally encountered. In this section, we will mainly discuss the stability analysis scheme based on the well-known Floquet theory. A newly emerging Hill method is to be also introduced in short.

5.3.1 Notion of stability

We usually consider the continuous-time dynamic system governed by the general equation of first order. To this end, the second order equation of motion Eq. (5.3) is rearranged in the following form:

$$\begin{bmatrix} \dot{u} \\ \ddot{u} \end{bmatrix} = \begin{bmatrix} \mathbf{0} & I \\ -M^{-1}K & -M^{-1}D \end{bmatrix} \begin{bmatrix} u \\ \dot{u} \end{bmatrix} + \begin{bmatrix} \mathbf{0} \\ M^{-1}[-f_{nl}(t,u,\dot{u}) + f(\omega,t)] \end{bmatrix} \tag{5.39}$$

or in a succinct form:

$$\dot{v}(t) = g(v;\omega) \tag{5.40}$$

where $v(t) = [u(t), \dot{u}(t)]^T$ is a $2n$-dimensional state vector and g is a nonlinear $2n$-dimensional vector field that depends on a control parameter ω. In the following, g may explicitly depend on t (in non-autonomous systems) or not (in autonomous systems).

Global stability

In nonlinear dynamics, the most common definition is Lyapunov stability.

Definition 1. A solution $v(t)$ of the differential equation in Eq. (5.40) is said to be Lyapunov stable if, given a small number $\epsilon > 0$, there exists a number $\delta = \delta(\epsilon) > 0$ such at any other solution $w(t)$ for which $||v(t) - w(t)|| < \delta$ at time $t = t_0$ satisfies $||v(t) - w(t)|| < \epsilon$ for all $t > t_0$.

If $v(t)$ is Lyapunov stable, then any other solution that is close to it initially remains so and is confined to a tube formed by the union of spheres of radius ϵ centered on points along the trajectory $v(t)$, the so-called ϵ tube.

Another widely used definition in mechanic dynamics is asymptotic stability:

Definition 2. A solution $v(t)$ of Eq. (5.40) is said to be asymptotically stable if it is Lyapunov stable and $\lim_{t\to\infty} ||v(t) - w(t)|| \to 0$.

Lyapunov functions are often employed to determine the global stability of a nonlinear solution. However, there is no general method for determining these functions. There still exist various definitions of global stability in the literature, such as Poincaré stability and Lagrange stablity [172]. But all the notions of global stability above do not provide any explicit schemes to determine the stability of a solution. Studies focusing principally on local stability are discussed below. On the contrary, explicit schemes for determining local stability can be derived.

Local stability

We consider a periodic solution $v_0(t)$ of Eq. (5.40) with minimal period T, at the particular control parameter value ω_0. The stability of this periodic solution is studied by superimposing a small disturbance $w(t)$:

$$v(t) = v_0(t) + w(t) \tag{5.41}$$

Substituting Eq. (5.41) into Eq. (5.40), assuming that g is at least twice continuously differentiable, expanding the result in a Taylor series about v_0, and retaining only linear terms in the disturbance, we obtain:

$$\dot{w}(t) = J_v(v_0; \omega_0)w(t) \tag{5.42}$$

where $J_v(v_0; \omega_0)$ is the Jacobian matrix of g at $(v_0; \omega_0)$.

The stability study of the periodic solution $v_0(t)$ consists in finding if the disturbance $w(t)$, solution of Eq. (5.42), fades away or is amplified as t is increased. Since $v_0(t)$ is T-periodic in time, J_v is also T-periodic in time considering its definition. Consequently, the system in Eq. (5.42) is a linearized system with periodic coefficients. The Floquet theory discussed in the following, specifically deals with this kind of dynamical systems.

5.3.2 Floquet theory

Assuming that a fundamental matrix solution of Eq. (5.42) $W(t)$ is expressed as:

$$W(t) = [w_1(t), w_2(t), \ldots, w_{2n}(t)] \tag{5.43}$$

$W(t+T)$ should therefore be also a fundamental matrix solution and moreover, be linear combinations of $w_1(t), w_2(t), \ldots, w_{2n}(t)$. That is:

$$W(t+T) = W(t)\Phi \tag{5.44}$$

where the matrix Φ is called the monodromy matrix.

Specifying the initial condition $W(0) = I$ (I is $2n \times 2n$ identity matrix) and setting $t = 0$ yields $\Phi = W(T)$. The monodromy matrix can be thus obtained by calculating $w_j(T)$ using time integration from an initial condition $w_j(0) = I_j$, where I_j is the j^{th} column of I. In particular, the monodromy matrix is simply a by-product of a shooting continuation method [147].

The monodromy matrix Φ has $2n$ eigenvalues ρ_j, called Floquet multipliers. One of the Floquet multipliers is always equal to +1, say $\rho_{2n} = 1$. The other $2n-1$ multipliers determine local stability of periodic solution $(v_0; \omega_0)$ by the following rule:

1. $v_0(t)$ is stable if $|\rho_j| < 1$ for all j = 1,2, ..., 2n-1;
2. $v_0(t)$ is unstable if $|\rho_j| > 1$ for some j;
3. if $\max \rho_j = 1$, a nonlinear analysis is necessary to determine the stability of such a nonhyperbolic periodic solution $v_0(t)$.

Stability analysis based on Floquet theory is usually of good precision. However, it is necessary to perform time integrations for $2n$ differential equations in the construction of the monodromy matrix. Inherently, the eigenvalue accuracy depends on the chosen time step size, leading to possible long time computation. Apparently it is computationally cumbersome for large-scale nonlinear systems.

Mechanisms of losing stability

So far we have discussed how (local) stability of a particular periodic solution manifests itself through Floquet multipliers. In general, the multipliers and, hence, the stability vary with the control parameter ω. Depending on where the critical multiplier or pair of complex conjugate multipliers crosses the unit circle, different types of bifurcation occur. One distinguishes three ways of crossing the unit circle, with three associated types of bifurcation in Fig. 5.6, which shows the path of the critical multiplier onlythat is, the eigenvalue with $|\rho_j| = 1$:

1. ρ_j gets unity in addition to ρ_{2n}; saddle-node or symmetry breaking bifurcation occurs.

2. $\rho_j = -1$, the multiplier crosses the unit circle at the negative real axis period-doubling or flip bifurcation occurs.

3. the crossing is with nonzero imaginary part, that is, a pair of complex conjugate eigenvalues crosses the unit circle; a bifurcation from a periodic solution to a torus (generalized Hopf bifurcation or Neimark-Sacker bifurcation); a new frequency component is exposed after the bifurcation point.

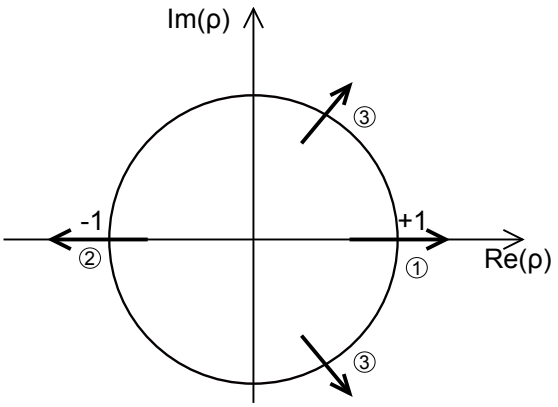

Figure 5.6: Different mechanisms of losing stability

5.3.3 Hill method

Hill method is a harmonic-based numerical approach used to determine the solutions of linear periodic systems like Eq. (5.42). Stability analysis could be also performed with a modification of Hill method [174]. This algorithm transforms a linear time-variant system into an eigenvalue problem of a linear time-invariant system.

Let's recall the second order nonlinear dynamic system with a periodic solution $u_0(t)$:

$$M\ddot{u}_0 + D\dot{u}_0 + Ku_0 + f_{nl}(t, u_0, \dot{u}_0) = f(\omega, t) \tag{5.45}$$

After a harmonic balance procedure, this system is described in the frequency domain:

$$P(\omega)U_0 + F_{nl}(U_0) = F \tag{5.46}$$

The periodic solution $u_0(t)$ is perturbed by a periodic term $w_(t)$ multiplied by a decay term $e^{\rho t}$

$$u(t) = u_0(t) + w(t)e^{\rho t} \tag{5.47}$$

Introducing this solution $u(t)$ into Eq. (5.3), we have:

$$\begin{aligned} &M\ddot{u}_0 + D\dot{u}_0 + Ku_0 + e^{\rho t}[\rho^2 Mw + \rho(2M\dot{w} + Dw)] + \cdots \\ &e^{\rho t}(M\ddot{w} + D\dot{w} + Kw) + f_{nl}[t, u_0(t) + w(t)e^{\rho t}] = f(\omega, t) \end{aligned} \tag{5.48}$$

Applying a harmonic balance procedure with N_h harmonics retained to the above equation yields:

$$P(\omega)U_0 + e^{\rho t}[P(\omega) + \rho\Lambda_1 + \rho^2\Lambda_2]W + F_{nl}(U_0 + We^{\rho t}) = F \tag{5.49}$$

where $w(t) = T(t)W$, and the matrices Λ_1 and Λ_2 are given by:

$$\begin{aligned} \Lambda_1 &= \mathbf{Bdiag}(K, \Lambda_1^1, \ldots, \Lambda_1^k, \ldots, \Lambda_1^{N_h}), \\ \Lambda_2 &= \mathbf{Bdiag}(M, \ldots, M), \end{aligned} \tag{5.50}$$

The subblocks Λ_1^k are written as:

$$\Lambda_1^k = \begin{bmatrix} D & 2k\omega M \\ -2k\omega M & D \end{bmatrix}, \quad k = 1, \ldots, N_h. \tag{5.51}$$

In addition, an expansion of the nonlinear term is performed:

$$F_{nl}(U_0 + We^{\rho t}) = F_{nl}(U_0) + \frac{\partial F_{nl}(U_0)}{\partial U_0} We^{\rho t} + H.O.T \tag{5.52}$$

Substituting Eq. (5.52) into Eq. (5.49) and neglecting terms of higher order, Eq. (5.49) simplifies to the following eigenvalue problem:

$$[P(\omega) + \rho\Lambda_1 + \rho^2\Lambda_2 + \frac{\partial F_{nl}(U_0)}{\partial U_0}]W = 0 \tag{5.53}$$

It is important to note that the term $\partial F_{nl}(U_0)/\partial U_0$ is readily available as a by-product in solving Eq. (5.46) by a quasi-newton algorithm.

Solving for the eigenvalues of Eq. (5.53), one obtains a set of ρ_j with real and imaginary parts, where a negative real part indicates stability of the solution, as the perturbation decays with time, and a positive real part indicates instability.

Obviously, Hill method is more advantageous when one operates in the frequency domain using the harmonic balance method, since no time integration is needed. However, a Fourier expansion of the nonlinear term $F_{nl}(U_0 + We^{\rho t})$ is involved in this method. As a result, the N_h order truncation of Fourier series may have a great impact on the precision of stability analysis, especially in strong nonlinear cases. A comparative study supporting this viewpoint has been conducted by Guskov [171]. Besides, an improved variant of Hill method, based on HBM combined with the asymptotic numerical method has been reported by Lazarus and Thomas [175].

In this thesis, the method based on Floquet theory is adopted for stability analysis of periodic solution in nonlinear dynamic systems.

5.4 Configuration of essentially nonlinear piezoelectric shunt circuit

In this section, we propose an essentially nonlinear piezoelectric shunt circuit as practical realization of nonlinear energy sink system. This kind of NES relying on piezoelectric shunt circuits possesses attractive features. The most significant advantage is that various forms of nonlinearity can be readily achieved by proper circuit design. For instance, on the basis of traditional resonant shunt circuits, cubic nonlinearity can be introduced by an additional ferroelectric capacitance. The small size of the piezoelectric absorber and the compact easy-integration also make nonlinear piezoelectric shunting appealing for practical use.

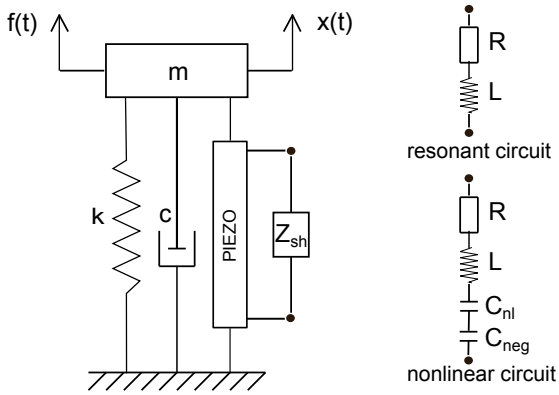

Figure 5.7: Single Degree of freedom system of a mass and a piezoelectric element

We consider once again the simplest SDOF mechanical linear oscillator with a piezoelectric attachment in d_{33} mode depicted in Fig. 5.7. At first the linear piezoelectric shunt circuit, i.e. the resonant circuit in which a resistance R and an inductance L connected in series with the piezoelectric is examined. The governing equations in the time domain are derived in Chapter 2.2.2:

$$m\ddot{x} + c\dot{x} + (k + k^{oc})x - k^c q = f(t) \tag{5.54}$$

$$L\ddot{q} + R\dot{q} + 1/C_p^s q - k^c x = 0 \tag{5.55}$$

where q is the electric charge on the piezoelectric stack, k^{oc} (k^{sc}) is the open

(short) circuit piezoelectric stiffness, k^c reflects the electromechanical coupling effect, C_p^s is the inherent piezoelectric capacitance.

This resonant circuit allows the attenuation of resonance vibration through proper tuning of the electric parameters. Let L_{opt}, R_{opt} denote the tuned inductance and resistance value, respectively. Then we consider introducing the nonlinearity realized by using a ferroelectric capacitance, which is denoted by C_{nl} in Fig. 5.7. Another important component C_{neg} will be explained soon.

Ferroelectric capacitance

Ferroelectric ceramic capacitances are widely used, in particular in circuits where high capacitance precision is not required (rough filtration, etc.). These capacitors have already found also in some nontrivial applications as nonlinear elements. One can characterize the ferroelectric capacitance via its nonlinear voltage-charge characteristic $v_c(q)$ which usually is close to a third degree (or fifth degree) polynomial with positive coefficients [176]:

$$v_c(q) = \frac{1}{C_0} q + \alpha q^3 \tag{5.56}$$

where C_0 is the linearized capacitance near $q = 0$.

We mention at this point that the requirement of essential stiffness nonlinearity of the nonlinear attachment plays a key role in the realization of NES, since it precludes the existence of a preferential resonance frequency of the nonlinear oscillator. This follows from the fact that an essential nonlinear piezoelectric shunt circuit is not a priori tuned to any specific frequency, unlike the linear RL shunt circuit. However, the presence of the inherent capacitance of the piezoelectric material C_p^s undermines the realization of essential nonlinearity. Hence a possible solution is to introduce a negative capacitance, denoted by C_{neg} in Fig. 5.7, connected in series with the piezoelectric capacitance.

Negative capacitance

As mentioned in Chapter 2.3, negative capacitances are widely used to enhance the electromechanical coupling and improve the shunt damping accordingly. Connected in series with the piezoelectric material, the negative capacitance increases the overall capacitance value of the shunt circuit.

With little power consumption, it is an attractive approach in many situations.

Let C_{res} denote the residual capacitance in the essentially nonlinear shunt circuit, which is resulted from the combination of inherent piezoelectric capacitance, ferroelectric capacitance and negative capacitance. Further, we have $1/C_{res} = \mu/C_p^s$, where μ is a small parameter. As pointed out in [139], such a small linear term (usually unavoidable) always appears, however, it does not affect the TET results.

The equations of motion of the nonlinear system are given by:

$$m\ddot{x} + c\dot{x} + (k + k^{oc})x - k^c q = f(t) \tag{5.57}$$

$$\varepsilon L_{opt}\ddot{q} + \beta R_{opt}\dot{q} + 1/C_{res}q + \alpha q^3 - k^c x = 0 \tag{5.58}$$

Hereby the tuned resonant shunt circuit expressed by Eq. (5.54)-(5.55) is taken as a reference system. A critical nonlinear coefficient α^{cr} can be defined by $\alpha^{cr} q_{max}^3 = q_{max}/C_p^s$, where q_{max} is the maximum electric charge exhibited in Eq. (5.55). Consequently the actual nonlinear coefficient α can be measured by α^{cr}.

A series of nondimensional quantities are introduced as follows:

$$\omega_{sc} = \sqrt{\frac{k + k^{sc}}{m}}, \quad \omega_e = \sqrt{\frac{1}{C_p^s L_{opt}}}, \quad \alpha_n^{cr} = \frac{\alpha^{cr} q_{max}^2}{\omega_{sc}^2 L_{opt}^2}, \quad \delta_{sc} = \frac{\omega_e}{\omega_{sc}},$$

$$q = \frac{q_{max}}{\sqrt{L_{opt}}}\bar{q}, \quad x = \frac{q_{max}}{\sqrt{m}}\bar{x}, \quad t = \frac{1}{\omega_{sc}}\bar{t}, \quad \frac{1}{C_{res}} = \mu\frac{1}{C_p^s},$$

$$\lambda_1 = \frac{c}{m\omega_{sc}}, \quad \lambda_2 = \frac{R_{opt}}{L_{opt}\omega_{sc}}, \quad \bar{f}(\bar{t}) = \frac{f(\bar{t}/\omega_{sc})}{\sqrt{m}\omega_{sc}^2 q_{max}}, \quad \alpha_n = \frac{\alpha q_{max}^2}{\omega_{sc}^2 L_{opt}^2} \tag{5.59}$$

Note that a tuning ratio δ_{sc} is defined based on the short circuit natural frequency ω_{sc}, which differs with δ^t described in Chapter 2.2. By use of the piezoelectric constitutive equations, Eq. (5.57)-(5.58) are then nondimensionalised in the following form:

$$\ddot{\bar{x}} + \lambda_1\dot{\bar{x}} + (1 + K_{33}^2)\bar{x} - \delta_{sc}K_{33}\bar{q} = \bar{f}(\bar{t}) \tag{5.60}$$

$$\varepsilon\ddot{\bar{q}} + \beta\lambda_2\dot{\bar{q}} + \mu\delta_{sc}^2\bar{q} + \alpha_n\bar{q}^3 - \delta_{sc}K_{33}\bar{x} = 0 \tag{5.61}$$

Differentiation in Eq. (5.60)-(5.61) is with respect to the nondimensional time $\bar{t}$. Note that $\delta_{sc} \approx 1$ since the linear tuned circuit is chosen as the reference. For the sake of simplicity, the "bar" notation is not used in the rest of this chapter:

$$\ddot{x} + \lambda_1 \dot{x} + (1 + K_{33}^2)x - \delta_{sc} K_{33} q = f(t) \tag{5.62}$$

$$\varepsilon \ddot{q} + \beta \lambda_2 \dot{q} + \mu \delta_{sc}^2 q + \alpha_n q^3 - \delta_{sc} K_{33} x = 0 \tag{5.63}$$

or in a compact matrix form by denoting $y = [x, q]^T$:

$$M_p \ddot{y} + D_p \dot{y} + K_p y + f_{p_{nl}}(y) = f_p(t) \tag{5.64}$$

Several parameters $\lambda_1, \lambda_2, \delta_{sc}$ and K_{33} are fixed because the tuned resonant circuit is chosen as reference. Different configurations of nonlinear shunt circuits could be achieved by assigning proper values of $(\varepsilon, \beta, \mu, \alpha_n)$. Apparently the parameter set $(\varepsilon = 1, \beta = 1, \mu = 1, \alpha_n = 0)$ corresponds to the tuned resonant circuit. We are mainly interested in the essential nonlinear piezoelectric circuit (e.g., $\mu << 1$) with small inductance (e.g., $\varepsilon < 1$). The piezoelectric-based NES possessing linear coupling with the primary structure differs from the the widely investigated mechanical NES configuration in Eq. (5.2). In an effort to understand the dynamics of this simple coupled electromechanical system, we proceed to the analytical and numerical studies in the following sections.

5.5 Nonlinear normal mode and free vibration

As it is known, the dynamics of free vibration of the coupled nonlinear system is governed by the topological structure and bifurcations of the nonlinear normal modes of the undamped and unforced system. For the coupled electromechanical system, the underlying Hamiltonian system is described by:

$$\ddot{x} + (1 + K_{33}^2)x - \delta_{sc} K_{33} q = 0 \tag{5.65}$$

$$\varepsilon \ddot{q} + \mu \delta_{sc}^2 q + \alpha_n q^3 - \delta_{sc} K_{33} x = 0 \tag{5.66}$$

Nonlinear normal modes (NNM) are defined as (not necessarily synchronous)

time-periodic oscillations of a non-dissipative nonlinear dynamic systems. More detailed description of NNM could be found in [139]. In order to have an initial grasp of the dynamics and localization phenomenons that occur in different frequency/energy ranges of the system in Eq. (5.65)-(5.66), we first proceed to the analytical study of the periodic solutions; numerical calculations for NNMs and transient responses are further conducted in the later subsection.

5.5.1 Analytical study of nonlinear normal mode

The analytical study of nonlinear normal modes is performed by employing the Complexification-Averaging methodology [139]. The standard process is initialized by a transition to complex variables:

$$\psi_1 = \dot{x} + i\omega x, \quad \psi_2 = \dot{q} + i\omega q \tag{5.67}$$

The initial undamped and unforced system is thus written as:

$$\dot{\psi}_1 - i\frac{\omega}{2}(\psi_1 + \psi_1^*) + (1 + K_{33}^2)\frac{(\psi_1 - \psi_1^*)}{2i\omega} - \delta_{sc}K_{33}\frac{(\psi_2 - \psi_2^*)}{2i\omega} = 0 \tag{5.68}$$

$$\varepsilon\left[\dot{\psi}_2 - i\frac{\omega}{2}(\psi_2 + \psi_2^*)\right] + \mu\delta_{sc}^2\frac{(\psi_2 - \psi_2^*)}{2i\omega} + \alpha_n\left(\frac{\psi_2 - \psi_2^*}{2i\omega}\right)^3 - \delta_{sc}K_{33}\frac{(\psi_1 - \psi_1^*)}{2i\omega} = 0 \tag{5.69}$$

The Complexification-Averaging methodology essentially involves a slow-fast partition of the dynamics. It is assumed that $1:1$ resonant response is sought with the same fast frequency ω. Then we further introduce the change of variables related with fast oscillation of frequency ω:

$$\psi_1 = \phi_1(t)e^{i\omega t}, \quad \psi_2 = \phi_2(t)e^{i\omega t} \tag{5.70}$$

The above two complex variables indicate that the complex variables $\psi_j, j = 1, 2$ are approximately expressed in terms of fast oscillations $e^{i\omega t}$, modulated by slowly varying complex amplitudes ϕ_j.

Averaging with respect to the fast frequency ω, after which only terms containing the fast frequency remain. This leads to the following set of complex

modulation equations (for the slow dynamics):

$$\dot{\phi}_1 + i\frac{\omega}{2}\phi_1 - i\frac{(1+K_{33}^2)}{2\omega}\phi_1 + i\frac{\delta_{sc}K_{33}}{2\omega}\phi_2 = 0 \quad (5.71)$$

$$\varepsilon\left(\dot{\phi}_2 + \frac{i\omega}{2}\phi_2\right) - i\frac{\mu\delta_{sc}^2}{2\omega}\phi_2 - i\frac{3\alpha_n}{8\omega^3}|\phi_2|^2\phi_2 + i\frac{\delta_{sc}K_{33}}{2\omega}\phi_1 = 0 \quad (5.72)$$

Let's introduce the polar representations $\phi_1 = A_1 e^{i\theta_1}$ and $\phi_2 = A_2 e^{i\theta_2}$ in the above equations, where A_1, A_2 are real amplitudes and θ_1, θ_2 real phases. Equation is balanced by setting the real and imaginary parts of the resulting equations equal to zero, respectively. The following set of real modulation equations is thus obtained:

$$\dot{A}_1 - \frac{A_2\delta_{sc}K_{33}}{2\omega}sin(\theta_2-\theta_1) = 0 \quad (5.73)$$

$$A_1\dot{\theta}_1 + \frac{\omega A_1}{2} - \frac{(1+K_{33}^2)A_1}{2\omega} + \frac{A_2\delta_{sc}K_{33}}{2\omega}cos(\theta_2-\theta_1) = 0 \quad (5.74)$$

$$\varepsilon\dot{A}_2 + \frac{A_1\delta_{sc}K_{33}}{2\omega}sin(\theta_2-\theta_1) = 0 \quad (5.75)$$

$$\varepsilon A_2\dot{\theta}_2 + \frac{\varepsilon\omega A_2}{2} - \frac{\varepsilon\mu\delta_{sc}^2 A_2}{2\omega} - \frac{3\alpha_n}{8\omega^3}A_2^3 + \frac{A_1\delta_{sc}K_{33}}{2\omega}cos(\theta_2-\theta_1) = 0 \quad (5.76)$$

Fix points of the set of real modulation equation is achieved by setting the derivatives with respect to time equal to zero. Let's recall the slow-fast partition of the response Eq. (5.78). Fix points of the slow dynamics imply periodic solution to the initial undamped and unforced system. If we assume identity of phases, $\theta_1 = \theta_2$, the amplitude A_1, A_2 can be estimated, which leads to the following analytic expressions for the nonlinear normal modes (periodic solutions):

$$\begin{aligned} x(t) &= Xcos\omega t = \frac{\psi_1 - \psi_1^*}{2i\omega} = (A_1/\omega)cos\omega t \\ &= \frac{\delta_{sc}K_{33}}{(1+K_{33}^2)-\omega^2}\sqrt{\frac{4}{3\alpha_n}\left[\varepsilon\omega^2 - \mu\delta_{sc}^2 + \frac{(\delta_{sc}K_{33})^2}{(1+K_{33}^2)-\omega^2}\right]}cos\omega t \quad (5.77) \\ q(t) &= Qcos\omega t = \frac{\psi_2 - \psi_2^*}{2i\omega} = (A_2/\omega)cos\omega t \\ &= \sqrt{\frac{4}{3\alpha_n}\left[\varepsilon\omega^2 - \mu\delta_{sc}^2 + \frac{(\delta_{sc}K_{33})^2}{(1+K_{33}^2)-\omega^2}\right]}cos\omega t \quad (5.78) \end{aligned}$$

We reminded that the analytical expressions Eq. (5.77)-Eq. (5.78) are only approximations of the periodic solutions where 1 : 1 fundamental resonance occurs. Then the ratio of the amplitudes of the linear mechanical and nonlinear piezoelectric oscillators is given by:

$$\frac{X}{Q} = \frac{\delta_{sc} K_{33}}{(1 + K_{33}^2) - \omega^2} \tag{5.79}$$

This relation shows that if the frequency ω is not close to $\sqrt{1 + K_{33}^2}$, the motion is always localized to the piezoelectric NES. The oscillation localizes to the mechanical linear oscillator sufficiently close to its resonant frequency $\sqrt{1 + K_{33}^2}$.

NNM is featured by frequency-energy (or amplitude) dependence, as shown in Eq. (5.77)-Eq. (5.78). A suitable graphic representation of the nonlinear normal mode is a frequency-energy plot (FEP). A NNM is represented by a point in the FEP, which is drawn at a frequency corresponding to the minimal period of the period motion and at an energy equal to the conserved total energy during the motion. The analytical approximations of branches in the FEP are computed by noting that the conserved energy of the system is given by:

$$E = \frac{1}{2}(1 + K_{33}^2)X^2 + \frac{1}{2}\mu\delta_{sc}^2 Q^2 - \delta_{sc} K_{33} QX + \frac{\alpha_n}{4} Q^4 \tag{5.80}$$

It is assumed that the essentially nonlinear shunt circuit generating the FEP depicted in Fig. 5.8 has the properties: $\varepsilon = 0.1, \mu = 0.11^3, \alpha_n = 0.1\alpha_n^{cr}$ and $K_{33} \approx 0.035$.

There are two distinct branches of NNMs in this frequency-energy plot, denoted by $S_{11}+$ and $S_{11}-$ respectively. Hereby the notation used in this research is in accordance with the literature: the two subscripts indicate the ratio of the two main frequency components in the periodic solution; the signs indicate the relative phase relationship between the two oscillators during the periodic motion (+ in-phase or − out-of-phase). For instance, in the branch $S_{11}+$, the two oscillators vibrate in an in-phase manner with the same vibratory frequency. In particular, motion along the $S_{11}+$ branch represents the basic targeted energy transfer mechanism, termed *fundamental energy pumping*. It relies on the localization phenomenon in the NNMs. A more intuitive explanation of the fundamental

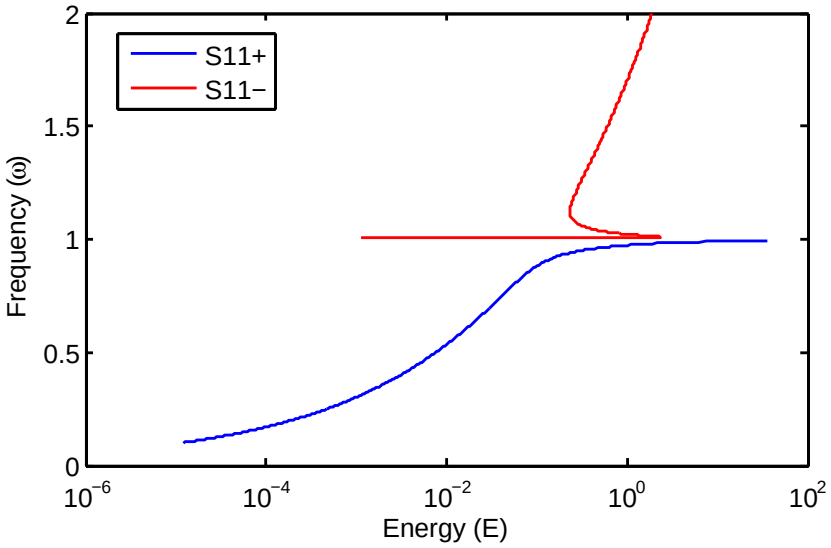

Figure 5.8: Analytic approximation of NNM in the FEP

energy pumping will be given in the next subsection.

For a complete introduction about NNMs in the FEP, readers may refer to the reference [139]. Through this short analytic study, we conclude that the essentially shunted piezoelectrics show considerable potential to perform as a nonlinear energy sink. In order to cope with more complex nonlinear systems, next we present numerical studies on nonlinear normal modes.

5.5.2 Numerical study of nonlinear normal mode

We will discuss numerical computations of nonlinear normal modes by means of HBM in this subsection. The classical harmonic balance method presented in Section 5.2.1 can be directly applied to the non-dissipative autonomous system:

$$M_p\ddot{y} + K_p y + f_{p_{nl}}(y) = 0 \tag{5.81}$$

By expressing $y = T(t)Y$, the task of searching for periodic solution could be

formulated by a set of algebraic equations:

$$G(\omega, Y) = P(\omega)Y + F_{p_{nl}}(Y) = 0 \tag{5.82}$$

where $P(\omega) = \omega^2 N_{M_p} \nabla^2 + N_{K_p}$.

However, Eq. (5.82) does not define an unique periodic solution. This is due to the fact that any solution $y(t) = y(t + \Delta t)$ also satisfies the formulation of HBM for arbitrary but fixed phase shift. Mathematically, the underdetermined system Eq. (5.82) needs a supplementary condition, termed the phase condition.

A suitable phase condition for NNM computation in this thesis is to set all the initial velocities $\dot{y}(0)$ to zero. This can be achieved by retaining only *cosine* terms in the development of y [177], i.e.:

$$Y = [Y^0, Y^{c1}, \ldots, Y^{ck}, \ldots, Y^{cN_h}]^T \tag{5.83}$$

NNMs can then be calculated using HBM combined with the arc-length contin-

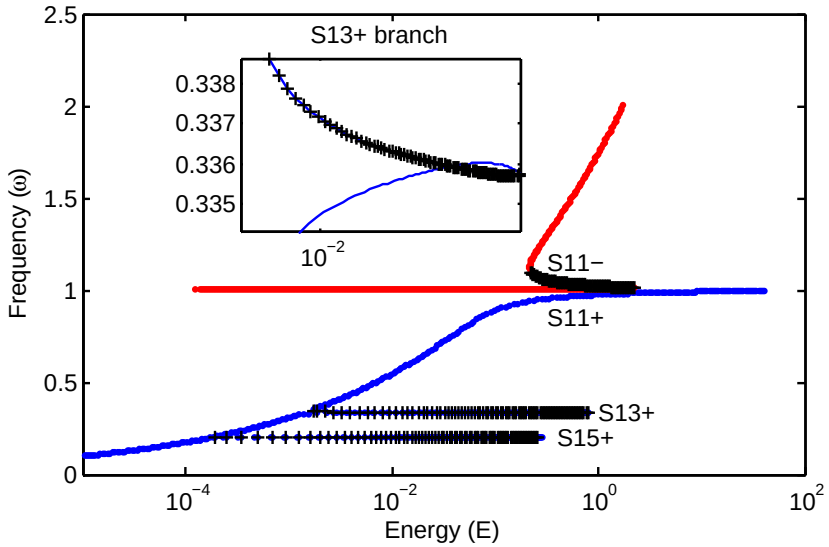

Figure 5.9: Numerical approximation of NNM in the FEP

uation technique. $N_h = 7$ harmonics are retained in the formulation of HBM. Different branches in Fig. 5.9 are computed by starting from the corresponding

linear normal mode at low amplitudes. Stability analysis is also carried out based on Floquet theory. Instable NNMs are denoted by + points. For the electromechanical system, the total energy is expressed by:

$$E = \frac{1}{2}\dot{y}^T M_p \dot{y} + \frac{1}{2} y^T K_p y + \frac{\alpha_n}{4} q^4 \tag{5.84}$$

The backbones $S_{11}+$ and $S_{11}-$ validate the analytic approximation of NNMs in Fig. 5.8. In weakly damped dynamics, as the damped motion follows branch $S_{11}+$ with decaying energy, an irreversible energy transfer could take place from the mechanical oscillator to the piezoelectric-based NES, since Fig. 5.10a-c show that if the frequency is not close to $\sqrt{1+K_{33}^2}$, the motion is always localized to the piezoelectric NES.

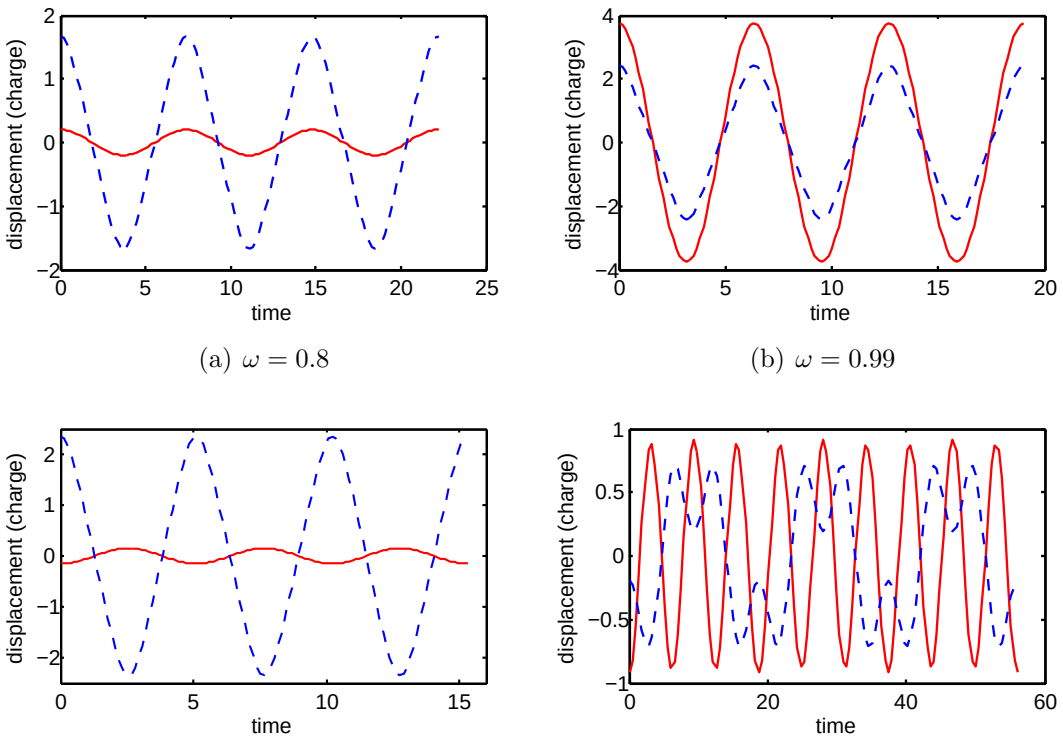

(a) $\omega = 0.8$ (b) $\omega = 0.99$

(c) $\omega = 1.2$ (d) $\omega = 0.34$

Figure 5.10: Periodic motions in: a) S11+, $\omega = 0.8$; b) S11+, $\omega = 0.99$; c) S11-, $\omega = 1.2$; d) S13+, $\omega = 0.34$. (——: x(t); – – –: q(t))

In addition, we can observe a sequence of subharmonic branches $S_{13}+$ and $S_{15}+$. These branches are termed *tongues*, which bifurcate out of the backbone. Unlike the NNM in the backbone, these tongues consist of multifrequency periodic solutions. The tongues highlights the versatility of the NES; it is capable of engaging in $1:3$ or $1:5$ internal resonance with the primary mechanical oscillator. Motion along these tongues represents the second targeted energy transfer mechanism, termed *subharmonic energy pumping*. As examples, Fig. 5.10d also depicts period motions on the $S_{13}+$ tongue.

As declared in the literature, there are two saddle-node bifurcations observed on the branch $S_{11}-$. This is the mechanism responsible for the existence of a critical energy threshold above which the nonlinear vibration absorber is capable of robustly absorbing impulsive loads. It is better explained by plotting amplitudes versus energy of NNMs on this branch in Fig. 5.11. In the low energy region, the motion appears to be nearly localized to the linear mechanical oscillator since the modal curve in FEP is a straight line; with increasing energy, the motion of the linear oscillator jumps from high to low levels around the saddle-node bifurcation point; on the other hand, the amplitude of electrical charge escalate to a higher level. In the high energy region, strong spatial localization of NNMs to the NES is observed. This "jump" phenomenon, occurring at a certain energy level, implies the existence of a critical energy threshold for effective transient response reduction.

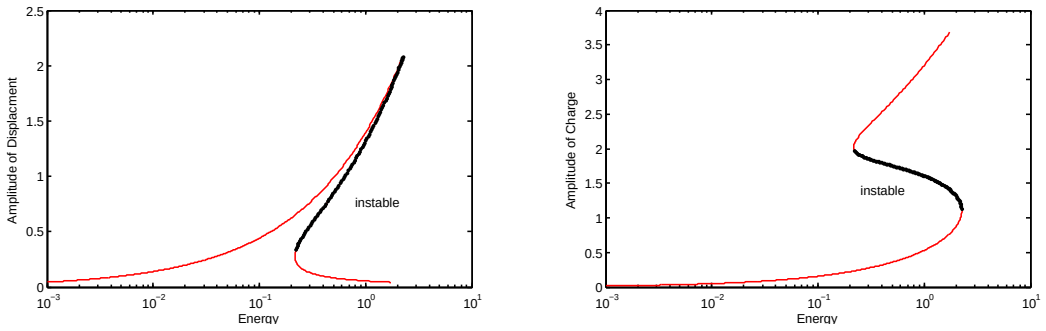

(a) (b)

Figure 5.11: Amplitude versus energy: a) linear mechanical oscillator; b) essentially nonlinear shunt circuit. (———: stable; ———: instable)

The existence of this critical energy level becomes apparent when we consider the transient dynamics of the coupled electromechanical system. Hereby the system is set to be initially at rest, with an impulse of magnitude V applied to the linear mechanical oscillator. This is equivalent to initiate the system with initial conditions $\dot{x}(0) = V$, $x(0) = q(0) = \dot{q}(0) = 0$ and no external forcing. Time integration is carried out for varying values of the impulse of V and fixed parameters $\varepsilon = 0.1, \beta = 0.2, \mu = 0.11^3, \alpha_n = 0.1\alpha_n^{cr}$. Note that weak damping is highlighted since it is necessary for effective realization of targeted energy transfer.

The relative instantaneous amount of energy localized at the piezoelectric oscillator is plotted versus time t, as well:

$$\frac{E_2}{E_1 + E_2} = \frac{\mu\delta_{sc}^2 q^2 + \varepsilon\dot{q}^2 + \frac{\alpha_n}{2}q^4 - 2\delta_{sc}K_{33}xq}{(1 + K_{33}^2)x^2 + \dot{x}^2 + \mu\delta_{sc}^2 q^2 + \varepsilon\dot{q}^2 + \frac{\alpha_n}{2}q^4 - 2\delta_{sc}K_{33}xq} \tag{5.85}$$

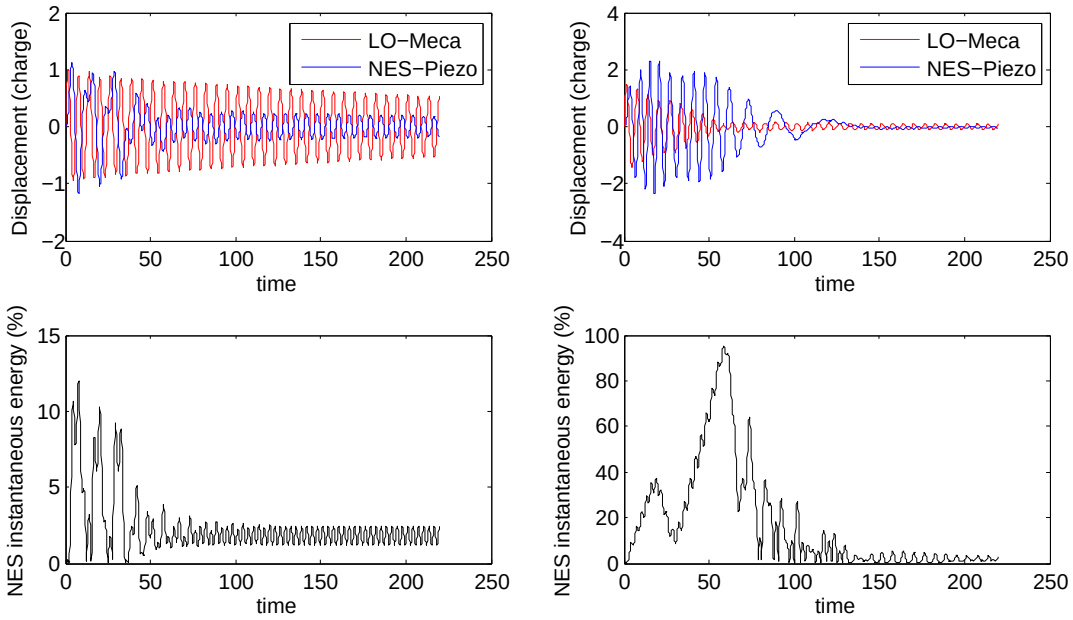

(a) V = 1.0 (b) V = 1.5

Figure 5.12: Transient dynamics of the 2DOF system: a) low energy level, V = 1.0; b) high energy level, V = 1.5.

In Fig. 5.12a we first present the transient damped dynamics at a low-energy level initial condition $V = 1.0$. The mechanical displacement decreases very slowly, since most of the impulsive energy remains localized to the linear mechanical oscillator. Moving to a higher energy level in Fig. 5.12b with $V = 1.5$, a completely different dynamical behavior is realized. In spite of the fact that initially the energy is entirely stored in the mechanical oscillator, a large part of this total system energy (up to 90%) is quickly pumped to the essentially nonlinear piezoelectric shunt circuit and dissipated. This results in a much faster vibration reduction of the mechanical oscillator. Consequently it is clear that above a certain initial energy threshold the dynamics of the system undergo essential change. Then questions naturally arise concerning the quantitative determination of this "energy threshold". Recent research efforts have revealed that the critical energy threshold required for effective targeted energy transfer can be directly related to a similar critical energy value in the underlying undamped system, above which the topological features of NNMs undergo essential changes. However, a definitive criterion for the "energy threshold" is not yet available at this stage.

The numerical studies of NNMs and transient damped dynamics validate the feasibility of essentially nonlinear piezoelectric shunt circuits as practical realization of nonlinear energy sink. Consequently we do not continue to perform an exhaustive calculation of the periodic orbits of the underlying Hamiltonian system. As pointed out in numerous research efforts, the NES performance depends on the impulse magnitude, which is an intrinsic limitation of this type nonlinear absorber. Another attractive feature is that the effectiveness of the NES is not significantly influenced by changes in the natural frequency of the linear primary structure. This prevailing characteristic of the piezoelectric-based NES will be fully addressed in the following section.

5.6 Forced response

The forced response of the coupled electro-mechanical system under harmonic external excitation applied to the mechanical oscillator is investigated in this section.

The steady-state response of the single-DOF linear system with strongly non-

linear attachment to external harmonic forcing loading have been studied via averaging method by Starosvetsky and Gendelman [178]. It is demonstrated that in close vicinity of the main resonance the system with NES can exhibit quasi-periodic rather than simple periodic response, leading to qualitatively different dynamical behavior. In our research, we will first calculate the nonlinear forced response by HBM combined with arc-length continuation. Then a so-called *variable harmonic balance method* is to be proposed in order to precisely predict the quasi-periodic response due to the essential nonlinearity.

5.6.1 Forced response by HBM & arc length continuation

The nonlinear forced response is calculated by applying HBM combined with arc length continuation to the non-autonomous system:

$$M_p\ddot{y} + D_p\dot{y} + K_p y + f_{p_{nl}}(y) = f_p(\omega, t) \tag{5.86}$$

A preliminary convergence study with the number of harmonics shows that a good approximation can be obtained by retaining 3 harmonics in this research. Hence, $N_h = 3$ is chosen due to the cubic nonlinearity in Eq. 5.86. A typical frequency response plot describing the dependence of the vibration amplitude of the system on frequency is depicted in Fig. 5.13. The parameter set ($\varepsilon = 0.1, \beta = 1, \mu = 0.11^3, \alpha_n = 0.1\alpha_n^{cr}$) is chosen for the essentially nonlinear shunt circuit. Special discussion about the nonlinear damping parameter β will be conducted later.

Stability analysis of the periodic solutions is carried out by monitoring the numerical values of Floquet multipliers. Two Neimarker-Sacker bifurcation or generalized Hopf bifurcation points (see Section 5.3.2) are observed in the nonlinear frequency response curves. The branch of stable periodic solutions that exists prior to the bifurcation continues as a branch of unstable periodic solutions after the bifurcation. At these bifurcation points, there emerges a new unknown frequency component and periodic solutions accordingly evolves into a torus. Another branch of stable quasi-periodic solutions is thus created. This can be demonstrated through numerical validation of periodic solutions by direct time integration.

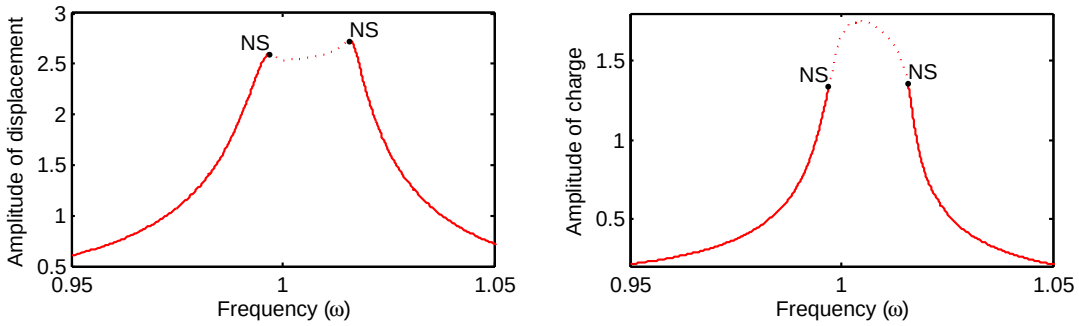

(a) (b)

Figure 5.13: Nonlinear frequency response: a) mechanical displacement; b) electric charge. (———: stable solution; · · · · · · : instable solutions). NS: Neimark-Sacker bifurcation point.

It is seen that at $\omega = 0.99$ (see Fig. 5.14a) a good accuracy of the HBM solution is achieved. However, at $\omega = 1.01$ (see Fig. 5.14b), the nonlinear response initiated from the HBM solution evolves into a modulated, nearly periodic oscillation. It indicates that in the vicinity of $1:1$ fundamental resonance there is a region where a single stable periodic attractor and a stable quasi-periodic response attractor co-exist. It should be pointed out that the quasi-periodic response occurs due to the nonlinear coupling between oscillation modes although the system is single-frequency excited. This result is in agreement with the literature regarding targeted energy transfer in nonlinear systems with periodic excitations. Analytical approach has been proposed for the strongly modulated response description by Starosvetsky and Gendelman [150; 151].

In this thesis, a numerical approach, called *variable-coefficient harmonic balance method*, is proposed to predict the quasi-periodic response precisely.

5.6.2 Variable-coefficient harmonic balance method

In general, a quasi-periodic oscillation that is associated with p different internal frequencies takes place on a p-dimensional invariant torus. Any quasi-periodic solution $x(t)$ can be expressed as a function $x(t) = x(\omega t)$. The tuple $\omega = (\omega_1, \ldots, \omega_p)$ is called the frequency base. Since the solution $x(t)$ is quasi-

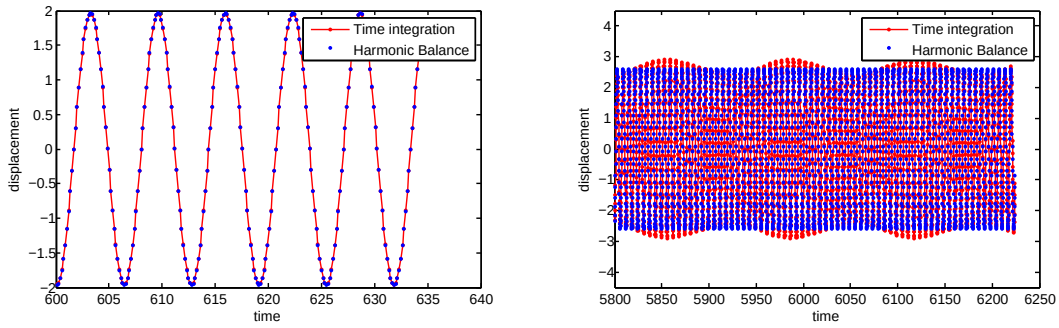

(a) $\omega = 0.99$ (b) $\omega = 1.01$

Figure 5.14: Numerical validation of HBM solutions

periodic, the basic frequencies ω_j must be *incommensurate* (rationally independent), that is, for integers k_j the equation $\langle k, \omega \rangle := \sum_{j=1}^{p} k_j \omega_j = 0$ holds if and only if all $k_j = 0$ for $j = 1, \ldots, p$. For $p = 2$ this means that the ratio ω_1/ω_2 is irrational. Considering the special case of Neimark-Sacker bifurcation in this chapter, we use the term "quasi-periodic solution" for a quasi-periodic solution with a two-dimensional frequency base.

A quasi-periodic function with p-dimensional frequency base can uniformly be approximated by quasi-trigonometric polynomials:

$$x(t) = \sum_{k \in \mathbb{Z}^p} c_k e^{i\langle k,\omega \rangle t}, \quad c_k := \lim_{a \to \infty} \frac{1}{2a} \int_{-a}^{a} x(t) e^{-i\langle k,\omega \rangle t} dt \tag{5.87}$$

It will be showed that a 2-dimensional quasi-periodic solution can be approximated by Fourier polynomials where the coefficients are 2π-periodic functions. To this end, the quasi-periodic solution $x(t)$ is expanded in a Fourier series as follows:

$$\begin{aligned} x(t) &= \sum_{k_1,k_2=-\infty}^{\infty} c_{k_1,k_2} e^{i(k_1\omega_1 + k_2\omega_2)t} = \sum_{k_1=-\infty}^{\infty} \left(\sum_{k_2=-\infty}^{\infty} c_{k_1,k_2} e^{ik_2\omega_2 t} \right) e^{ik_1\omega_1 t} \\ &= \sum_{k_1=-\infty}^{\infty} u_{k_1}(\omega_2 t) e^{ik_1\omega_1 t} \end{aligned} \tag{5.88}$$

The coefficient $u_{k_1}(\omega_2 t)$ is apparently periodic functions. Such a Fourier series is called a generalized Fourier series. The idea is now to approximate $x(t)$ by a truncated series:

$$x(t) = \sum_{k_1=-N_h}^{N_h} u_{k_1}(\omega_2 t) e^{ik_1\omega_1 t} \tag{5.89}$$

For quasi-periodic solutions of the nonautonomous system Eq. (5.86), an approximation $y(\omega_1 t, \omega_2 t)$ could be written equivalently using trigonometric functions:

$$\begin{aligned} y(\omega_1 t, \omega_2 t) &= Y^0(\omega_2 t) + \sum_{k_1=1}^{N_h} Y^{ck_1}(\omega_2 t) cos(k_1\omega_1 t) + Y^{sk_1}(\omega_2 t) sin(k_1\omega_1 t) \\ &= [I, cos(\omega_1 t)I, sin(\omega_1 t)I, \ldots, cos(k_1\omega_1 t)I, sin(k_1\omega_1 t)I, \ldots] \times \\ &\quad [Y^0(\omega_2 t), Y^{c1}(\omega_2 t), Y^{s1}(\omega_2 t), \ldots, Y^{ck_1}(\omega_2 t), Y^{sk_1}(\omega_2 t), \ldots]^T \\ &= T_1(\omega_1 t) Y(\omega_2 t) \end{aligned} \tag{5.90}$$

where the external forcing frequency is denoted by ω_1. The term *variable-coefficient harmonic balance method* (VCHBM) is named after the periodic vector function $Y(\omega_2 t)$. In contrast, the Fourier coefficient vector Y is constant for classical harmonic balance method in Eq. (5.5).

In general, VCHBM is derived from the method of two timescale harmonic balance, which stems from ideas from the method of multiple scales and harmonic balance. The term *variable-coefficient harmonic balance method* has been first reported by Summers [179] in 1995. Similar method can also be found as Fourier method by Schilder [180].

Since one can interpret the coefficient vector Y as time-varying amplitudes of $2N_h + 1$ harmonics with an unknown frequency component ω_2, the first step of VCHBM is to separate $Y(\omega_2 t)$ from the nonlinear system by applying the harmonic balancing procedure in terms of ω_1. Starting from Eq. (5.90), the velocity and acceleration could be expressed as:

$$\dot{y}(t) = \omega_1 T_1 \nabla_1 Y + T_1 Y' \tag{5.91}$$

$$\ddot{y}(t) = T_1(Y'' + 2\omega_1 \nabla_1 Y' + \omega_1^2 \nabla_1^2 Y) \tag{5.92}$$

where $Y' = \partial Y/\partial t, Y'' = \partial^2 Y/\partial t^2$. Subscripts of T_1 and ∇_1 indicate that these functions are defined in terms of ω_1 (see Eq. (5.10)-(5.12)).

Applying the Galerkin procedure to the nonlinear system Eq. (5.86) leads to:

$$N_{M_p}(Y'' + 2\omega_1\nabla_1 Y' + \omega_1^2\nabla_1^2 Y) + N_{D_p}(\omega_1\nabla_1 Y + Y') + N_{K_p}Y + F_{p_{nl}}(Y) - F_p = 0 \tag{5.93}$$

where $f_{p_{nl}}(y) = T_1 F_{p_{nl}}(Y)$ and $f_p(t) = T_1 F_p$.

This equation can be rearranged so that:

$$N_{M_p}Y''+(2\omega_1 N_{M_p}\nabla_1+N_{D_p})Y'+(\omega_1^2 N_{M_p}\nabla_1^2+\omega_1 N_{D_p}\nabla_1+N_{K_p})Y+F_{p_{nl}}(Y)-F_p = 0 \tag{5.94}$$

At this point, we obtain the output of harmonic balancing in terms of ω_1. It is an autonomous second order differential equation of the time-varying coefficient vector $Y(\omega_2 t)$ in a succinct form:

$$M_a Y'' + D_a Y' + K_a Y + F_{p_{nl}}(Y) - F_p = 0 \tag{5.95}$$

the subscript (a) indicates that the matrices or vector correspond to the autonomous system.

We mention that the analytic expression of $F_{p_{nl}}(Y)$ can be obtained by use of Eq. (5.21)-(5.23) due to the cubic form of nonlinearity (see Appendix C). Even though this procedure could be performed by a symbolic manipulator, it will be algebraically tedious for large values of N_h. This is an inherent limitation of this semi-analytic method.

Y is sought by solving the autonomous system of Eq. (5.95) for a periodic solution with frequency component ω_2. Due to the fact that ω_2 is not priori known, a phase condition is needed to fix an unique periodic solution.

Phase condition

Let's express the desired periodic solution $Y(\omega_2 t)$ by $Y(t) = T_2(\omega_2 t)Z$. The classical harmonic balancing method is then applied to Eq. (5.95) with N_{h_2} harmonics

retained, which leads to:

$$G(\omega_2, Z) = P(\omega_2)Z + F_{a,nl}(Z) = 0 \tag{5.96}$$

where $P(\omega_2) = \omega_2^2 N_{M_a} \nabla_2^2 + \omega_2 N_{D_a} \nabla_2 + N_{K_a}$ and $F_{p_{nl}}(Y) - F_p = T_2(\omega_2 t) F_{a,nl}(Z)$.

A well known integral phase condition can be added to obtain an unique periodic solution of this underdetermined equation:

$$\int_0^{2\pi/\omega_2} Y(t)^T \dot{\hat{Y}}(t)\, dt = 0 \tag{5.97}$$

In Eq. (5.97), $\hat{Y}(t)$ is a known nearby approximation of periodic solution. Substituting the relations $Y(t) = T_2 Z$ and $\dot{\hat{Y}}(t) = \omega_2 T_2 \nabla_2 \hat{Z}$ into this phase condition and further simplification yield:

$$h(\omega_2, Z) = \omega_2 Z^T \nabla_2 \hat{Z} = 0 \tag{5.98}$$

In summary, periodic solutions of the autonomous system Eq. (5.95) is sought by solving the following set of algebraic equations:

$$\begin{cases} G(\omega_2, Z) = P(\omega_2)Z + F_{a,nl}(Z) = 0 \\ h(\omega_2, Z) = \omega_2 Z^T \nabla_2 \hat{Z} = 0 \end{cases} \tag{5.99}$$

This algorithm combined with continuation technique are shown to be effective in searching for periodic solutions of autonomous systems. Consecutive branch points are usually treated as precedent known approximation $\hat{Y}(t)$ in a continuation.

Practical aspects

A proper initial condition is of major concern for solving Eq. (5.99). According to the phase condition in Eq. (5.98), it is shown that both static ($\omega_2 = 0$) and dynamic ($\omega_2 \neq 0$) solutions to the autonomous system in Eq. (5.95) coexist. The solver computes either the static solution or the dynamic one, but the static solution is always first achieved without any special consideration for the initial condition. In this thesis, optimized initial conditions based on the complex

nonlinear modal analysis [181] are introduced.

First, stability analysis at a static equilibrium solution is performed for the autonomous system in Eq. (5.95). The static equilibrium solution Y_s is a critical position where the system can lose stability and stationary periodic oscillations, i.e. limit cycles, occur. The corresponding nonlinear static equation is written as:

$$K_a Y_s + F_{p_{nl}}(Y_s) - F_p = 0 \tag{5.100}$$

where the static equilibrium Y_s (a constant vector) is achieved when $Y_s' = 0$ and $Y_s'' = 0$.

The system Eq. (5.95) is then linearized around the static equilibrium position Y_s by the perturbation technique. The perturbation is:

$$Y = Y_s + \Delta Y \tag{5.101}$$

Developing the nonlinear term $F_{p_{nl}}(Y_s + \Delta Y)$ as a Taylor series and retaining the first order leads to:

$$F_{p_{nl}}(Y_s + \Delta Y) = F_{p_{nl}}(Y_s) + J_Y F_{p_{nl}}(Y_s)\Delta Y \tag{5.102}$$

where $J_Y F_{p_{nl}}(Y_s)$ is Jacobian matrix.

Substituting Eq. (5.101)-(5.102) into Eq. (5.95) yields a linearized approximation at the equilibrium point:

$$M_a \Delta Y'' + D_a \Delta Y' + [K_a + J_Y F_{p_{nl}}(Y_s)]\Delta Y = 0 \tag{5.103}$$

The expression above is then written in the state-space form and complex eigenvalues $\lambda = a + i\omega$ of the matrix:

$$A = \begin{bmatrix} \mathbf{0} & I \\ -M_a^{-1}[K_a + J_Y F_{p_{nl}}(Y_0)] & -M_a^{-1} D_a \end{bmatrix} \tag{5.104}$$

are derived.

The real part of the eigenvalue a corresponds to the growth rate of the amplitude and the imaginary part ω corresponds to the pulsation of the mode. A

negative real part indicates that the corresponding mode is stable. In other words, a perturbation about the static equilibrium sliding state will not modify the equilibrium position of the system. A positive real part equivalent to a negative damping leads to an unstable mode. Thus, modifying one of the parameters will induce growing oscillations about the static equilibrium position of the system until the dynamical steady state, i.e., periodic solution, is achieved.

As explained by Sinou [182], the nonlinear unstable mode drives the dynamic solution. The evolution of the approximated periodic solution,defined by considering only the contribution of the unstable mode, is given by:

$$Y(t,p,\lambda) = p(\mathbf{\Psi}e^{\lambda t} + \bar{\mathbf{\Psi}}e^{\bar{\lambda}t}) \tag{5.105}$$

where $\mathbf{\Psi}$ defines the nonlinear unstable mode and $\bar{\mathbf{\Psi}}$ denotes its conjugate; p is an arbitrary chosen coefficient.

As a result, the expression Eq. (5.105) is used as initial condition for solving Eq. (5.99). The trivial static solution can be successfully avoided. Besides, the initial guess of the unknown frequency ω_2 is set to be the unstable mode frequency. Above all, once the periodic solution $Y(\omega_2 t)$ is sought, the quasi-periodic response

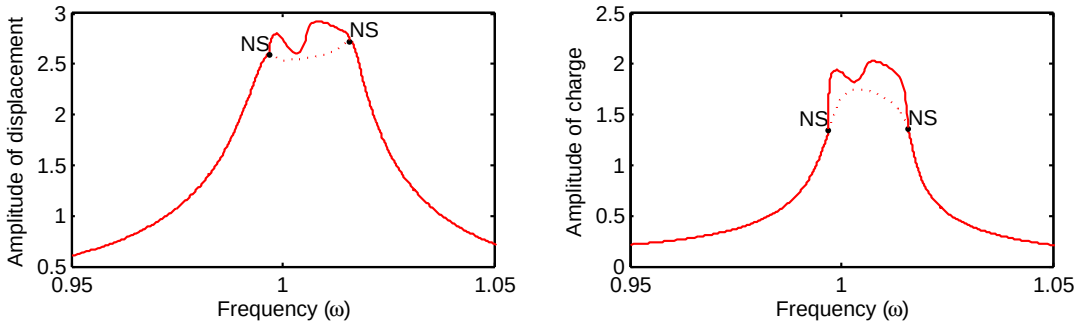

(a) (b)

Figure 5.15: Nonlinear frequency response: a) mechanical displacement; b) electric charge. (——: stable solution; · · · · · · : instable solutions).

is computed by $y(t) = T_1(\omega_1 t)Y(\omega_2 t)$. The complete nonlinear frequency response is depicted in Fig .5.15 and numerical validation of the quasi-periodic response in

the time domain is shown in Fig .5.16. The retained harmonics N_{h_2} in variable-coefficient harmonic balance method is set as 5. It can be seen that the quasi-periodic solution by VCHBM is of good precision.

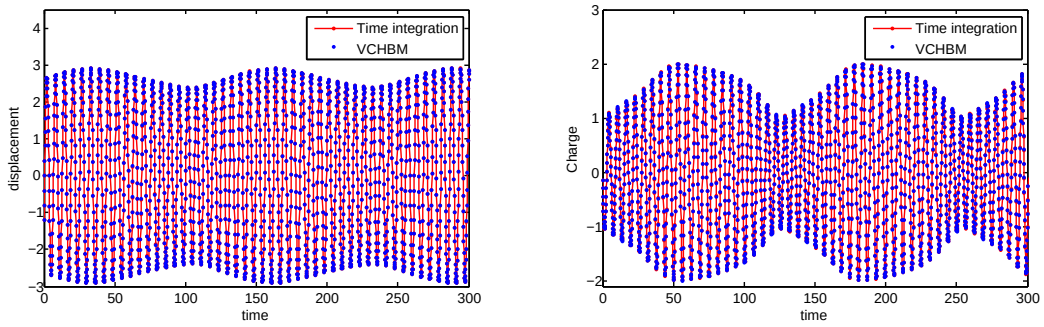

(a) (b)

Figure 5.16: Numerical validation of quasi-periodic solution by VCHBM at $\omega = 1.01$: a) mechanical displacement; b) electric charge

For the purpose of comparison, the performance of the well-tuned resonant shunt circuit (———) and essentially nonlinear shunt circuit (———) are depicted in Fig .5.17. It is clear shown that significant vibration reduction due to the resonant/essentially nonlinear shunt circuit is achieved, compared with the mechanical oscillator without any attachment (———). It appears that the essentially nonlinear shunt circuit performs nearly as well as the well tuned resonant circuit does. However, a relative small inductance requirement advantages the essentially nonlinear circuit over the linear one by noting that $\varepsilon = 0.1$. What is more important, the essentially nonlinear shunt circuit is featured by nonexistence of a preferential resonance frequency. It is assumed that the primary structure undergoes a slight change, i.e., the mechanical stiffness k is increased by 5%. In other words, the mechanical system becomes "mistuned" while these shunt circuits remain unchanged. Performances of both the linear resonant circuit and essentially nonlinear circuit are then revaluated, as shown by dashed lines in Fig .5.17. With a drift of the mechanical system's frequency, performance of the resonant circuit (– – –) undergoes drastic changes. This is due to the fact that the electrical resonance is tuned very close to the original structural resonance. The behavior

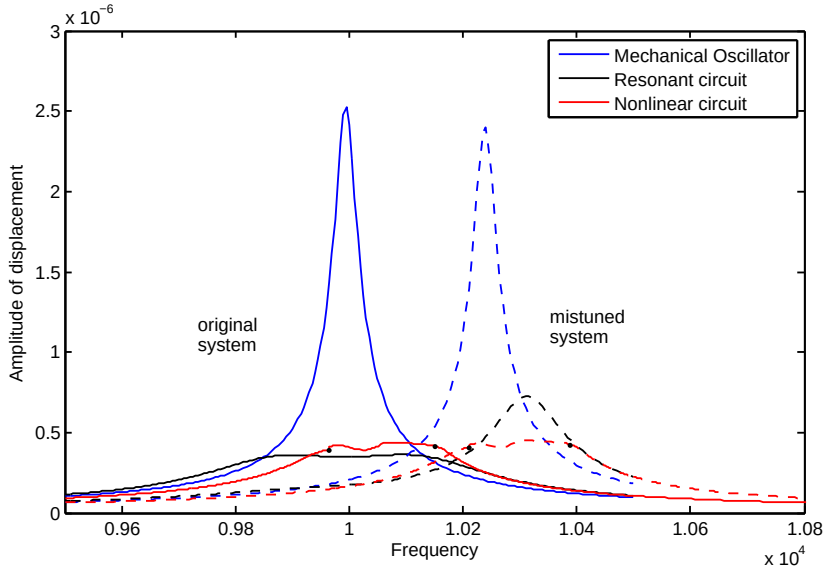

Figure 5.17: Performances of resonant/essentially nonlinear circuit integrated into different primary structures. solid lines: original systems; dashed lines: "mistuned" systems

of resonant shunted piezoelectrics is very sensitive to the deviation of both structural parameters and optimal electrical parameters. It therefore loses its desired damping performance around the "mistuned" structural frequency.

On the contrary, the response curve corresponding to the essentially nonlinear circuit (– – –) shifts to the right as a whole. It means that its performance is barely affected by the drift of the mechanical system's frequency. The reason lies in the lack of a preferential resonance frequency of the nonlinear circuit. As a consequenc, It is able to engage in nonlinear resonance with the linear stucture at broad frequency ranges. Then the essentially nonlinear piezoelectric shunt circuit as practical realization of NES, acts in essence, as a passive, adaptive, broadband vibration absorber.

5.6.3 Nonlinear modal damping

In Section 5.5.2, weak damping $\beta = 0.2$ is briefly addressed in the numerical simulation of transient dynamics of a linear primary structure coupled to NES.

It is true that weak dissipation is necessary for effective target energy transfers. Indeed, weak damping does not generate any new dynamics, but merely influences the damped transitions (jumps) between different branches of NNMs of the underlying Hamiltonian system [139]. A more detailed consideration of this nonlinear damped transition can be found in [183].

It might also be noted that a relatively stronger damping $\beta = 1$ is presented in the forced response calculation (see Section 5.6.1). It seems that the strong damping parameter enables the whole system overdamped. However, nonlinear damping can not be analyzed by only considering the underlying linear system. Hereby the concept of nonlinear modal damping in nonlinear modal analysis is discussed.

The extended definition of *complex nonlinear modes* is proposed by Laxalde and Thouverez [184]. It is in essence related to the definition of nonlinear normal modes; at the same time it is also inspired by the definition of linear complex modes. A complex nonlinear mode is an oscillation of the autonomous nonlinear system with (potentially) a phase difference between its degrees of freedom. This phase difference is the main difference between *complex* and *normal* modes. As second order dynamical systems are considered, the motion takes place on a two-dimensional subspace defined in the system's phase space and is energy-dependent. By analogy with linear complex modes, the eigenvalues of the characteristic equation can be defined in the form:

$$\lambda = a + i\omega \tag{5.106}$$

In Eq. (5.106), $\omega = \omega_0\sqrt{1-\zeta^2}$ is the damped natural frequency, ω_0 the natural frequency and $\zeta = a/\omega_0$ defines the nonlinear modal damping ratio.

This complete definition of complex nonlinear modes essentially emphasizes the frequency-damping-energy dependency. In particular, the damping-energy dependency is addressed in a previous research work [185], in which a hysteretic oscillator is used as NES. This research further illustrates the pertinence of the definition of complex nonlinear modes.

Complex nonlinear modes can be theoretically calculated by a generalized harmonic balance method [184] and the nonlinear damping can be accordingly

quantitatively evaluated. Nonlinear modal parameters can also be obtained experimentally through curve fitting of measured frequency response [186]. In this section, in taking advantage of the obtained nonlinear forced response in Fig .5.15, it is possible to approximate the nonlinear damping ratio based on an equivalent linearization method [187].

We have known the forced response of the nonlinear system:

$$M_p\ddot{y} + D_p\dot{y} + K_p y + f_{p_{nl}}(y) = f_p(\omega, t) \tag{5.107}$$

For each y, an equivalent stiffness matrix $K_{eq}(y)$ can be determined so that an equivalent system description can be written as:

$$M_p\ddot{y} + D_p\dot{y} + K_{eq} y = f_p(\omega, t) \tag{5.108}$$

$K_{eq}(y)$ is a matrix which minimizes the difference ϵ:

$$\epsilon = K_p y + f_{p_{nl}}(y) - K_{eq} y \tag{5.109}$$

This transform refers to the equivalent linearization. ϵ can be minimized by using a least square method.

It is then possible to solve the eigenvalue problem in the standard way:

$$(K_{eq} - \omega_j^2 M_p)\Psi_j = 0 \tag{5.110}$$

The modal damping is written as $d_{p_j} = \Psi_j^T D_p \Psi_j$ and the nonlinear damping ratio is determined by:

$$\zeta_j = \frac{d_{p_j}}{2\omega_j^2} \tag{5.111}$$

Nonlinear damping ratios around the amplitude peaks is calculated in this way. Maximum damping ratio values approach to 3%. Apparently, the overall damping is not too high for the nonlinear system to be overdamped.

On the contrary, if the weak damping $\beta = 0.2$ is kept, the forced response of the coupled electromechanical system becomes further complicated since various coexisting response regimes come out; moreover, no good damping performance

can be obtained compared to the linear resonant shunt circuit.

5.7 Conclusion

In this chapter, an essentially nonlinear shunted piezoelectric is proposed for practical realization of nonlinear energy sink.

It is shown that the addition of a piezoelectric-based NES to a linear mechanical system significantly alters the global dynamics of the resulting integrated system. In transient damped dynamics, targeted energy transfer from the linear system to the NES is observed under certain conditions. When the linear oscillator undergoes harmonic external forcing, the essentially nonlinear shunt circuit can resonantly interact with the primary system in a broadband manner. This feature makes it appealing since it is capable of adapting itself spontaneously according to the structural frequency variation. The piezoelectric-based NES then acts as an adaptive, broadband vibration absorber. Moreover, a relative smaller inductance requirement also benefits this nonlinear shunt circuit over the resonant circuit.

High-dimensional bifurcations in the forced response arise due to the presence of essential nonlinearity. The complicated response regimes are considered related to the damping parameter in the piezoelectric-based NES. With a certain particular parameter set, the performance of NES in terms of vibration reduction is excellent even in the quasi-periodic regime. At this stage, the nonlinear tuning design to seek the best performance of NES under harmonic forcing remains elusive. A complete analytic study is necessary to fully understand energy-dependent nonlinear dynamics and nonlinear tuning design in order to achieve its optimal performance.

Chapter 6

Essentially nonlinear piezoelectric shunt circuits applied in blisks

Essentially nonlinear piezoelectric shunt circuits are applied into mistuned bladed disks as an attempt in this chapter. In the beginning, resonance capture cascades existing in multi-DOF linear primary oscillators coupled to a SDOF nonlinear energy sink, which leads to multi-frequency targeted energy transfers are initially introduced. Similar dynamics is expected to be reproduced in the bladed disk by means of piezoelectric-based NES. For this purpose, essentially nonlinear circuits in tuned bladed disk are first investigated by use of cyclic symmetry. Computational strategy based on harmonic balance method specially for tuned cyclic structures is presented; nonlinear normal modes and forced responses of a single sector will then be discussed. When blade mistuning is considered, nonlinear frequency responses are calculated by HBM in the whole structure. Advantages of essentially nonlinear shunt circuits in mistuned bladed disks over linear resonant circuits are examined in the end of this chapter.

6.1 Multi-frequency TETs and resonance capture cascades

In the previous chapter, we have examined targeted energy transfer in a two-DOF system consisting of SDOF linear mechanical oscillator coupled to an essentially nonlinear piezoelectric shunt circuit, which, acts as nonlinear energy sink. The application of NES is not limited to SDOF structures. The analysis to MDOF linear primary structures with a SDOF essentially nonlinear attachment has been extended in a number of research works. It is reported that the SDOF nonlinear energy sink can interact with multiple linear modes of the linear system, through a so-called mechanism *resonance capture cascades*. The phenomenon that the resonance capture cascades enable the nonlinear energy sink to extract broadband vibration energy from the MDOF linear system is termed *multi-frequency targeted energy transfer* [139].

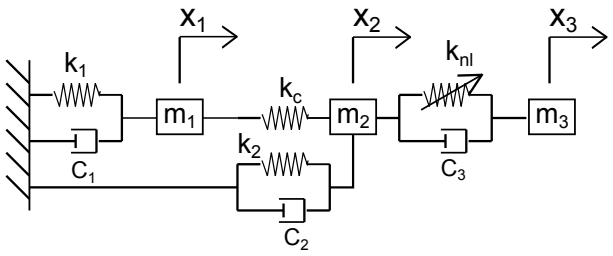

Figure 6.1: A 2DOF primary linear structure coupled with a NES [188]

As an example, a system considered in [188] is depicted in Fig .6.1 and consists of a two-DOF linear primary structure (m_1, m_2) and a SDOF nonlinear energy sink (m_3). The NES is directly linked to m_2 by essentially nonlinear stiffness k_{nl} and viscous damper c_3. The equations of motion are given by:

$$\begin{aligned} m_1\ddot{x}_1 + c_1\dot{x}_1 + k_1 x + k_c(x_1 - x_2) &= 0 \\ m_2\ddot{x}_2 + c_2\dot{x}_2 + c_3(\dot{x}_2 - \dot{x}_3) + k_2 x_2 + k_c(x_2 - x_1) + k_{nl}(x_2 - x_3)^3 &= 0 \\ m_3\ddot{x}_3 + c_3(\dot{x}_3 - \dot{x}_2) + k_{nl}(x_3 - x_2)^3 &= 0 \end{aligned} \quad (6.1)$$

A lightweight NES is considered by requiring that $m_3 << m_1, m_2$, because the

NES is characterized by the strong mass asymmetry.

Since in this case the primary linear structure possesses two degrees of freedom, there exist three backbone branches in the Frequency-Energy Plot in Fig .6.2. These branches represent NNMs during 1:1:1 internal resonance. Detailed descriptions of these branches are referred to the reference [139]. In this chapter, the mechanism for multiple targeted energy transfer is introduced in short. Two specific branches, namely $S111+--$ and $S111++$, are responsible for the realization of fundamental targeted energy transfer. Each branch possesses qualitative similarities with the branch $S_{11}+$ in Fig. 5.9. Along these two branches, there exist transitions of mode localization from the LO to the NES as frequency decreases. Hence, there coexist both in-phase and out-of-phase fundamental TET mechanism in this system. "In-phase" or "out-of-phase" indicates the relative phase between the two degrees of freedom in the primary linear structure.

For the transient damped dynamics, the instantaneous frequency components of the responses can be continuously monitored by superimposing their wavelet transform spectra to the FEP, as shown in Fig .6.3 [139]. Consequently, this plot provides an insight into the energy exchanges and transfers in the global system. It is observed that the NES engages in $1:1:1$ transient response capture (TRC) with the high-frequency out-of-phase linear mode as it moves along the NNM branches $S111+-+$ and $S111+--$ in the initial stage. As the global system energy decreases to a certain level due to energy dissipation, there occurs a transition to the damped NNM branch of $S111++$.

This is a typical example of a *resonance capture cascade*, i.e., a sequential transient resonance interaction of the NES with different modes of the linear primary system. On the contrary, classical linear vibration absorbers is usually limited to a narrowband performance. This once again highlights the broadband feature of nonlinear multi-frequency targeted energy transfer, which renders it suitable for practical applications. For this reason, as an attempt, essential nonlinearity is introduced into the piezoelectric shunted bladed disks in order to improve the damping performance.

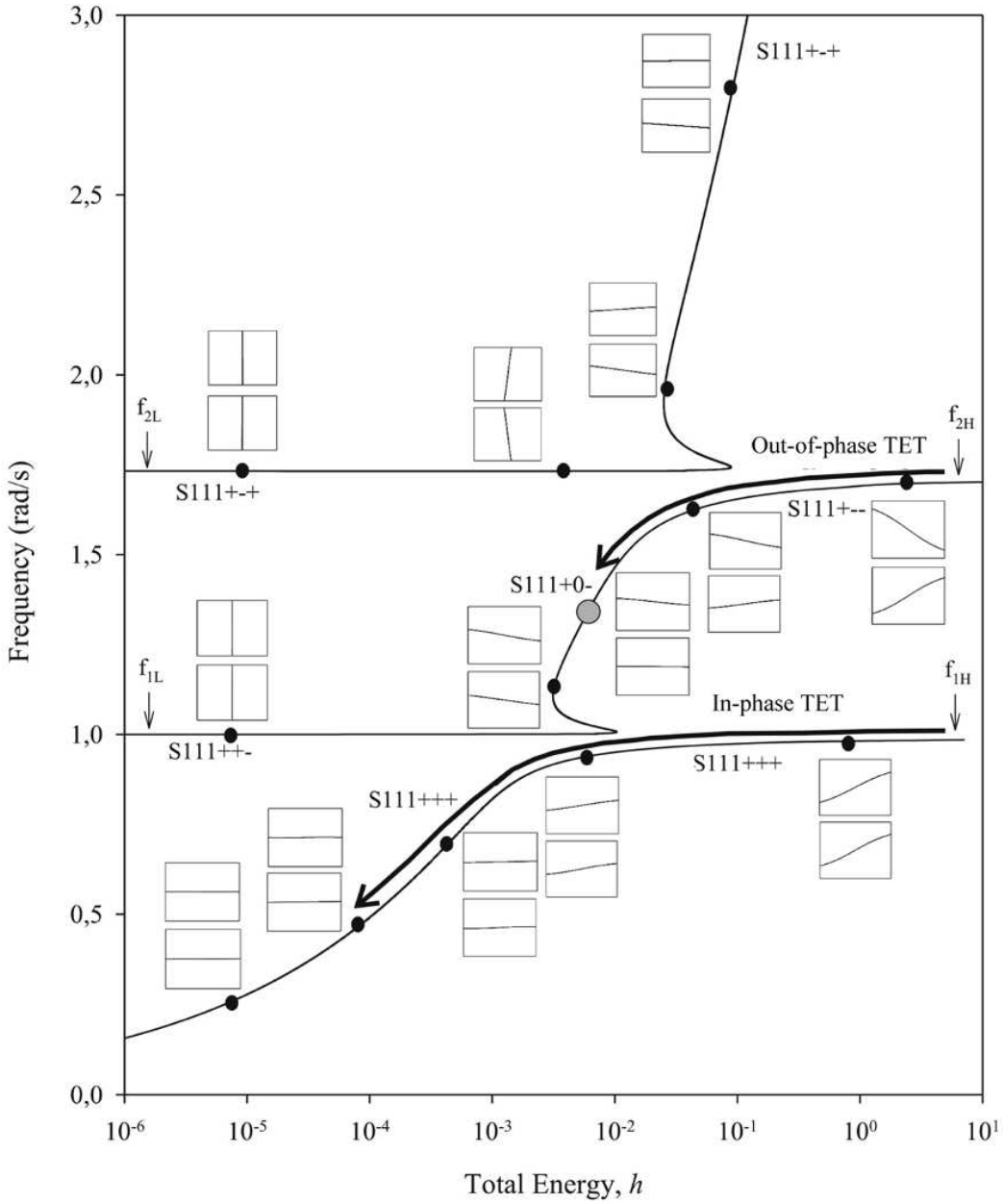

Figure 6.2: NNMs in Frequency-Energy Plot [139]. Mode shapes are projected to the three-dimensional configuration space, respectively. Top window: (x_3, x_1), bottom window (x_3, x_2)]. Vertical axe: x_3.

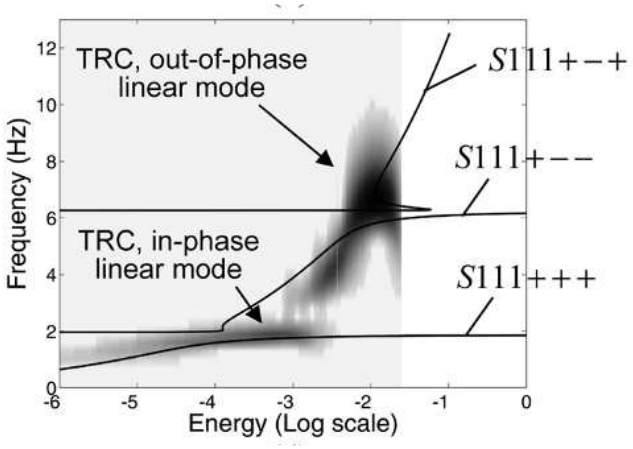

Figure 6.3: Wavelet transform spectra superposed to the Frequency-Energy Plot [139].

6.2 Essentially nonlinear piezoelectric shunt circuits in tuned bladed disks

As an initial step, essentially nonlinear piezoelectric shunt circuits in tuned bladed disks are investigated in this section.

In Chapter 3, we have proposed to reduce the vibration of mistuned bladed disks using resonant shunted piezoelectrics solely attached onto the disk. The optimal resistance R_{opt} and inductance L_{opt} are sought to obtain the best damping performance for the targeted blade-disk mode. In this chapter, we still choose the 1st mode of 1 nodal diameter (low frequency) in Fig. 3.6 as example. Let's recall the equation of motion for the j^{th} sector:

$$\begin{aligned}
m_{1,j}\ddot{x}_{1,j} + k_{1,j}x_{1,j} - k_{1,j}x_{2,j} &= f_{1,j}e^{i\omega t} \\
m_{2,j}\ddot{x}_{2,j} - k_{1,j}x_{1,j} + (k_{1,j}+k_{2,j})x_{2,j} - k_{2,j}x_{3,j} &= 0 \\
m_{3,j}\ddot{x}_{3,j} - k_{3,j-1}x_{3,j-1} - k^{oc}_{j-1}x_{3,j-1} - k^{c}_{j-1}q_{j-1} - k_{2,j}x_{2,j} + (k_{3,j-1} + & \\
k_{2,j} + k_{3,j} + k_{4,j})x_{3,j} + (k^{oc}_{j-1} + k^{oc}_{j})x_{3,j} + k^{c}_{j}q_{j} - k_{3,j}x_{3,j+1} - k^{oc}_{j}x_{3,j+1} &= 0 \\
L_{opt}\ddot{q}_j + R_{opt}\dot{q}_j + \frac{1}{C^{s}_{p,j}}q_j + k^{c}_{j}x_{3,j} - k^{c}_{j}x_{3,j+1} &= 0 \qquad (6.2)
\end{aligned}$$

Weak structural damping in the bladed disk could be readily included in the following analysis.

In a manner similar to Eq. (5.58), essential nonlinearity is introduced into the linear resonant shunt circuit of each piezoelectric attachment by including a nonlinear capacitance and a negative capacitance. By denoting the residual capacitance as C_{res} and further $1/C_{res} = \mu/C^s_{p,j}$, the equation governing the essentially nonlinear shunt circuit is rewritten as:

$$\varepsilon L_{opt}\ddot{q}_j + \beta R_{opt}\dot{q}_j + \mu\frac{1}{C^s_{p,j}}q_j + \alpha q_j^3 + k^c_j x_{3,j} - k^c_j x_{3,j+1} = 0 \tag{6.3}$$

The nonlinear coefficient α can be measured by a critical nonlinear coefficient α^{cr}, which is defined based on the maximum electric charge exhibited in the tuned resonant circuits (see Chapter 5.4). With structure damping γ, a compact matrix form of EOM is presented for the bladed disk shunted with essentially nonlinear piezoelectric shunt circuits:

$$\mathbf{M}_e\,\ddot{y} + \mathbf{D}_e\,\dot{y} + \mathbf{K}_e\,y + f_{e_{nl}}(y) = f_p(t) \tag{6.4}$$

where the subscript (e) indicates that the essentially nonlinear piezoelectric shunt circuits are incorporated into the bladed disk.

We mention at this point that the proposed essentially nonlinear piezoelectric shunt circuits presented in Chapter 5 needs further studies to fully understand the tuning methodology in terms of vibration reduction. Moreover, the purpose in this section is to explore the possibility and potentiality of taking advantage of nonlinear effects in cyclic structures to reduce the blade mistuning vibration. As a consequence, the impact of essentially nonlinear effects in shunt circuits on the blade vibration is examined by a preliminary numerical investigation rather than a detailed and systematic study. Next, the computational strategy based on HBM specially for tuned cyclic structures is presented; nonlinear normal modes and forced responses of a single sector will then be discussed.

6.2.1 HBM applied to structures with cyclic symmetry

Since the bladed disk is under engine order excitation, linear and nonlinear properties of the bladed disk are cyclically symmetric, responses of both mechanical displacements and electric charges can be expressed based on the representation in the reference sector (see Chapter 1.3). The superposition of cyclic components still holds on for the bladed disk. Then considering the system description Eq. (6.4) in physical coordinates, a reformulation in cyclic component can be conducted using the real-valued form of spatial Fourier transform (see Eq. (1.14)). This reformulation consists of a set of independent subproblems for each harmonic order k:

$$\tilde{\mathbf{M}}_e^k \ddot{\tilde{y}}_0^k + \tilde{\mathbf{D}}_e^k \dot{\tilde{y}}_0^k + \tilde{\mathbf{K}}_e^k \tilde{y}_0^k + \tilde{f}_{e_{nl}}^k(\tilde{y}_0^k) = \tilde{f}_p(t) \tag{6.5}$$

where $\tilde{y}_0^k$ is defined on the reference sector for the spatial harmonic index $k = 0, 1, \ldots, \kappa$. $\kappa = (N-1)/2$ if the number of sectors N is odd or $\kappa = N/2 - 1$ if N is even. $\tilde{\mathbf{M}}_e^k$, $\tilde{\mathbf{D}}_e^k$, $\tilde{\mathbf{K}}_e^k$ and $\tilde{f}_{e_{nl}}^k(\tilde{y}_0^k)$ are along with the harmonic index k on the reference sector.

Solving Eq. (6.5) is realized in the frequency domain by means of HBM. The continuity conditions, e.g.,

$$\begin{bmatrix} {}^l\tilde{y}_0^{k,c} \\ {}^l\tilde{y}_0^{k,s} \end{bmatrix} = \begin{bmatrix} cosk\theta & sink\theta \\ -sink\theta & cosk\theta \end{bmatrix} \begin{bmatrix} {}^r\tilde{y}_0^{k,c} \\ {}^r\tilde{y}_0^{k,s} \end{bmatrix} \tag{6.6}$$

can be readily incorporated into the formulation of HBM. $\theta = 2\pi/N$ is the phase difference between two adjacent sectors.

Periodic solutions are sought by solving the following algebraic equation derived from HBM (see Chapter 5.2.1):

$$G(\omega, \tilde{Y}_0^k) = P(\omega)\tilde{Y}_0^k + \tilde{F}_{e_{nl}}^k(\tilde{Y}_0^k) - \tilde{F}_p = 0 \tag{6.7}$$

where $P(\omega)$ is the dynamic stiffness matrix, $\tilde{F}_p$ is the Fourier coefficient vector of the external forcing and $\tilde{F}_{e_{nl}}^k(\tilde{Y}_0^k)$ corresponds to the nonlinear term $\tilde{f}_{e_{nl}}^k(\tilde{y}_0^k)$.

In order to determine the vector $\tilde{F}_{e_{nl}}^k(\tilde{Y}_0^k)$, the alternating frquency/time-domain (AFT) technique (see Fig. 5.3) combined with (inverse) spatial Fourier transform (see Chapter 1.3) are utilized [189]. Starting from an estimation of

the solution $\tilde{Y}_0^k(j)$ during the j^{th} iterative step, an evaluation of the approximate temporal terms $\tilde{y}_0^k(t)$ can be derived using the inverse fast Fourier transform (iFFT). The following step is to evaluate temporarily the nonlinear term $\tilde{f}_{e_{nl}}^k(\tilde{y}_0^k)$ in the time domain. Since the nonlinear function $f_{e_{nl}}(y)$ is expressed in physical coordinates, an intermediate step is needed to bridge the gap between the cyclic coordinates and physical coordinates. To this end, $y(t)$ can be deduced from $\tilde{y}_0^k(t)$ by use of inverse spatial Fourier transform (iSFT):

$$y = ([E]^k \otimes I)\, \tilde{y}_0^k \tag{6.8}$$

where $[E]^k$ is the Fourier transform submatrix corresponding to the harmonic index k.

Once $y(t)$ is obtained, it enable us to calculate the nonlinear function $f_{e_{nl}}(y)$. This function is expressed in physical coordinates for all sectors. In order to seek the expression $\tilde{f}_{e_{nl}}^k$ on the reference sector, the spatial Fourier transform (SFT) is utilized:

$$\tilde{f}_{e_{nl}}^k = [([E]^k)^T \otimes I]\, f_{e_{nl}} \tag{6.9}$$

The last step is to determine the Fourier coefficient vector $\tilde{F}_{e_{nl}}^k(j+1)$ for the $(j+1)^{th}$ iterative step from the approximation $\tilde{f}_{e_{nl}}^k(t)$ in the time domain. This is done by means of fast Fourier transform (FFT). In summary, this complete process is illustrated in Fig .6.4.

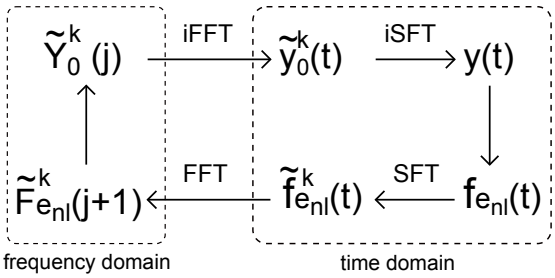

Figure 6.4: Alternating frequency/time-domain technique for tuned bladed disks

This method allows the forced response to be calculated for a whole cyclically symmetric bladed disk using only a reference sector model, while without introduction of any assumptions even for the case of nonlinear vibrations with strong

nonlinear effects.

Condensation

An additional step, called condensation, can reduce the number of equations when solving Eq. (6.7). The condensation lies in the fact that nonlinear effect is exerted only on a part of degrees of freedom in the physical model. Usually this nonlinear DOFs only accounts for a fraction of the total DOFs. For instance, in the essentially nonlinear shunted bladed disk model, only the electric charges q_j can be seen as nonlinear DOFs. The remaining DOFs are called linear DOFs.

During the first step of condensation, all DOFs of the Fourier coefficient vector $\tilde{Y}_0^k$ are reorganized into linear DOFs $\tilde{Y}_0^l$ and nonlinear DOFs $\tilde{Y}_0^n$ using a boolean matrix B:

$$\tilde{Y}_0^k = \begin{bmatrix} B_n & B_l \end{bmatrix} \begin{bmatrix} \tilde{Y}_0^n \\ \tilde{Y}_0^l \end{bmatrix} \tag{6.10}$$

The same operation could be applied to the Fourier coefficient vector $\tilde{F}_{e_{nl}}^k$ so that

$$\tilde{F}_{e_{nl}}^k = B_n \tilde{F}_{e_{nl}}^n \tag{6.11}$$

this is due to the fact that $\tilde{F}_{e_{nl}}^l = 0$.

Eq. (6.7) can then be written as two sub-equations:

$$\underbrace{\begin{bmatrix} B_n^T P B_n & B_n^T P B_l \\ B_l^T P B_n & B_l^T P B_n \end{bmatrix}}_{\begin{bmatrix} P_{nn} & P_{nl} \\ P_{ln} & P_{ll} \end{bmatrix}} \begin{bmatrix} \tilde{Y}_0^n \\ \tilde{Y}_0^l \end{bmatrix} + \begin{bmatrix} \tilde{F}_{e_{nl}}^n \\ 0 \end{bmatrix} = \begin{bmatrix} B_n^T \tilde{F}_p \\ B_l^T \tilde{F}_p \end{bmatrix} \tag{6.12}$$

The bottom line of Eq. (6.12) allows to eliminate $\tilde{Y}_0^l$ from the top line. Consequently a reduced nonlinear algebraic equation containing only nonlinear DOFs is obtained:

$$P_{red} \tilde{Y}_0^n + \tilde{F}_{e_{nl}}^n - \tilde{F}_{red} = 0 \tag{6.13}$$

with

$$P_{red} = P_{nn} - P_{nl}P_{ll}^{-1}P_{ln} \tag{6.14}$$

$$\tilde{F}_{red} = B_n^T\tilde{F}_p - P_{nl}P_{ll}^{-1}B_l^T\tilde{F}_p \tag{6.15}$$

Once $\tilde{Y}_0^n$ is sought by solving Eq. (6.13), the full Fourier coefficient vector is resumed by:

$$\tilde{Y}_0^k = B_n\tilde{Y}_0^n + B_lP_{ll}^{-1}(B_l^T\tilde{F}_p - P_{ln}\tilde{Y}_0^n) \tag{6.16}$$

This condensation technique is an exact reduction of the original problems and can thus greatly reduce nonlinear computational burdens.

6.2.2 Nonlinear normal modes

Relying on the computational strategy presented above, nonlinear normal modes are calculated numerically for a single sector of a tuned bladed disk. The procedure is similar to that for NNMs of 2DOF coupled electromechanical system presented in Chapter 5.5.2. By expressing $\tilde{y}_0^k = T(t)\tilde{Y}_0^k$, the task of searching for periodic solution could be formulated by a set of algebraic equations:

$$G(\omega, \tilde{Y}_0^k) = P(\omega)\tilde{Y}_0^k + \tilde{F}_{e_{nl}}^k(\tilde{Y}_0^k) = 0 \tag{6.17}$$

where $P(\omega) = \omega^2 N_{\tilde{\mathbf{M}}_e^k}\nabla^2 + N_{\tilde{\mathbf{K}}_e^k}$.

A phase condition for NNM computation can be achieved by retaining only *cosine* terms in the development of $\tilde{y}_0^k$. The number of retained harmonics is 5. The backbones of the Frequency-Energy plot of the underlying Hamiltonian system are depicted in Fig. 6.5. Parameters for the essentially nonlinear shunt circuits are: $\varepsilon = 0.05, \mu = 0.185^3, \alpha = 0.05\alpha^{cr}$. Frequencies in this plot are normalized according to the structural frequency of the targeted blade-disk mode. Vibration amplitudes are also rescaled.

It is not necessary to perform an exhaustive search of all the subharmonic branches in this FEP. This is due to the conclusion in Section 6.1 that the dynamics governing targeted energy transfer can be considered by examining the backbone branches under conditions of $1:1:1:1$ internal resonance. Clearly,

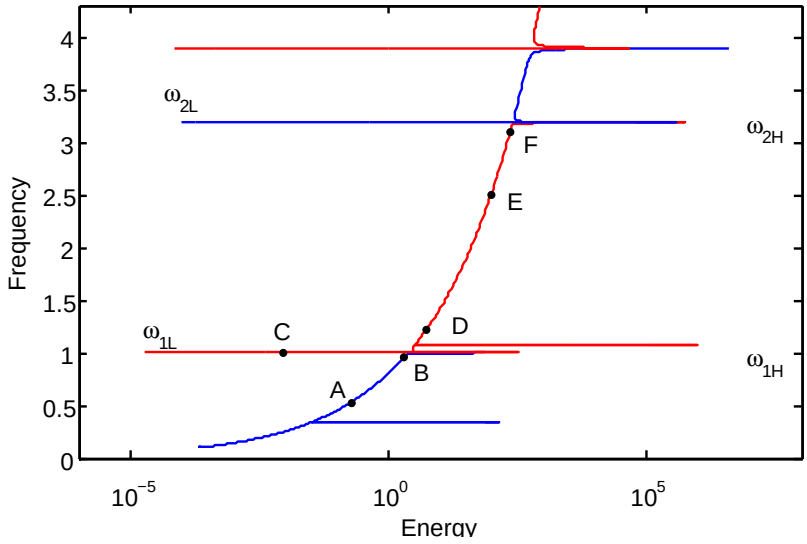

Figure 6.5: Numerical approximation of NNM in the FEP for a single sector of a tuned bladed disk

the FEP of the essentially nonlinear shunted single sector in Fig. 6.5 has strong resemblance with that of the 2DOF primary structure coupled with a mechanical NES in Fig .6.2. At low energy level, the modes behave linearly, whereas, for higher energy levels, the nonlinear characterization increases, and a frequency-energy dependence is exhibited.

Representative periodic orbits along the backbone branches (corresponding to point $A \sim F$) are plotted in Fig .6.6. At points A and B, the primary blade-disk structure vibrates in an in-phase way, and the motion becomes increasingly localized to the mechanical DOFs as $\omega \rightarrow \omega_{1H}$. At point C, the modes almost behave linearly at low energy level. In the region defined by $\omega_{1L} \leq \omega \leq \omega_{2H}$, vibration localizes to the piezoelectric-based NES as ω departs from ω_{1L}, as shown at point D. Around point E, there is supposed to be a phase transition among the mechanical vibration since the motion of blade mass 2 tend to zero. As $\omega \rightarrow \omega_{2H}$, vibration becomes localized to the mechanical DOFs again.

As mentioned in Section 6.1, these branches discussed above (defined by $\omega \leq \omega_{1H}$ and $\omega_{1L} \leq \omega \leq \omega_{2H}$ and so on) play an important role for the realization of multi-frequency targeted energy transfer. Due to the dependence of

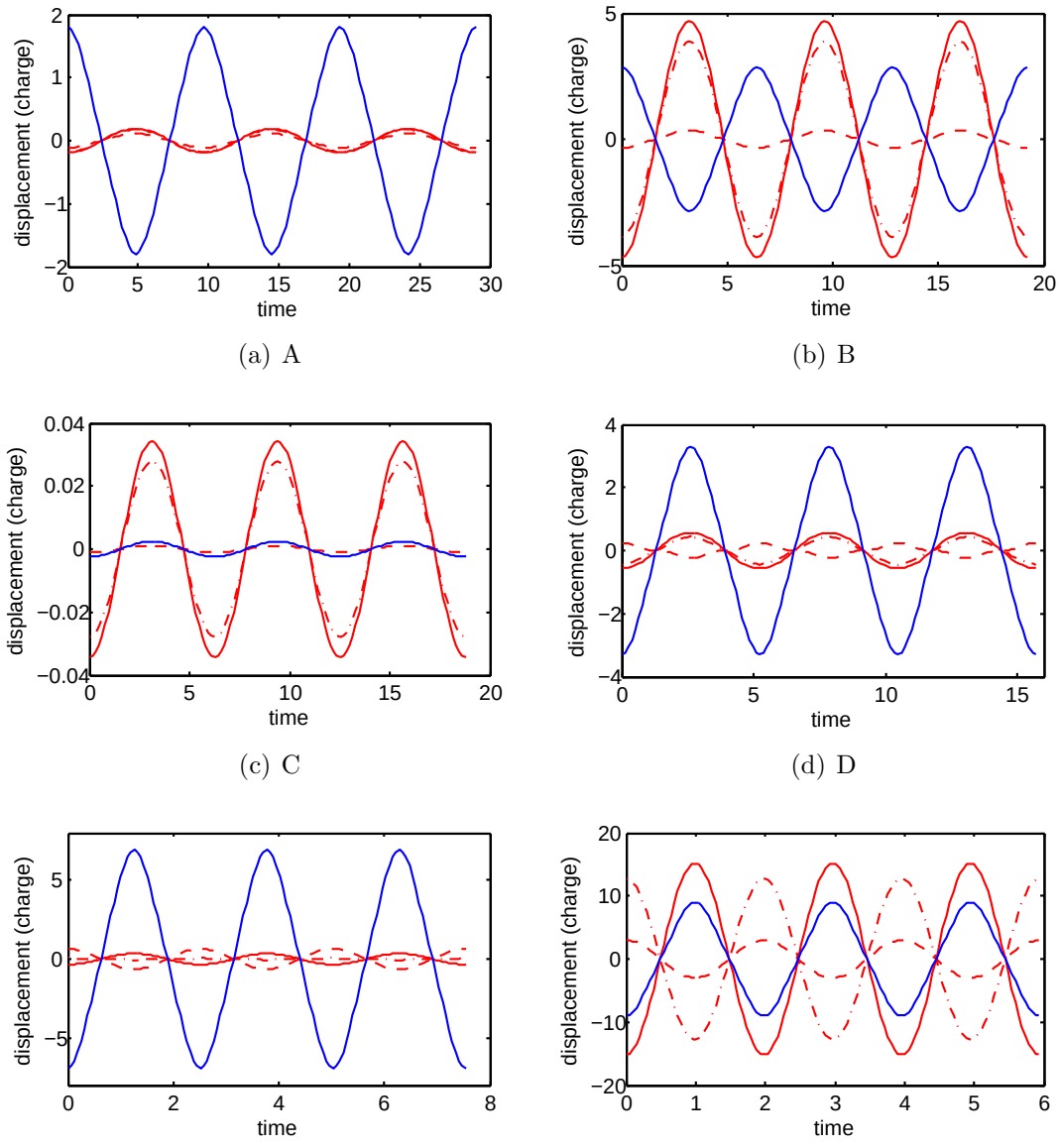

(a) A (b) B

(c) C (d) D

(e) E (f) F

Figure 6.6: Representative periodic orbits; —— blade mass 1; – · – blade mass 2; – – – disk mass; —— electric charge.

the frequency of the damped oscillation on the instantaneous energy, irreversible transfer of vibration energy from the blade-disk sector to the piezoelectric-based NES could take place as the weakly damped continuations of the NNMs are traced from high to low frequencies. This conclusion follows the fact that the shapes of the corresponding NNMs localize from the LO to the NES as frequency decreases along different branches. It also raises the possibility of multi-frequency energy transfer in the transient damped dynamics. As a result, it seems that it is possible to reproduce, using an essentially nonlinear piezoelectric shunt circuit, the dynamics created by an essentially nonlinear mechanical system, which paves the way for applications of the piezoelectric-based NES in bladed disks.

6.2.3 Forced response

Forced responses of the tuned bladed disk with essentially nonlinear shunted circuits are investigated. An engine order 1 excitation is imposed on the bladed disk. Parameters for the essentially nonlinear shunt circuits are: $\varepsilon = 0.05, \beta = 1, \mu = 0.185^3, \alpha = 0.05\alpha^{cr}$. As explained in Chapter 5.6.3, a strong damping parameter β is chosen in order to seek a good damping performance and simple response regimes. Various force responses are compared in Fig. 6.7.

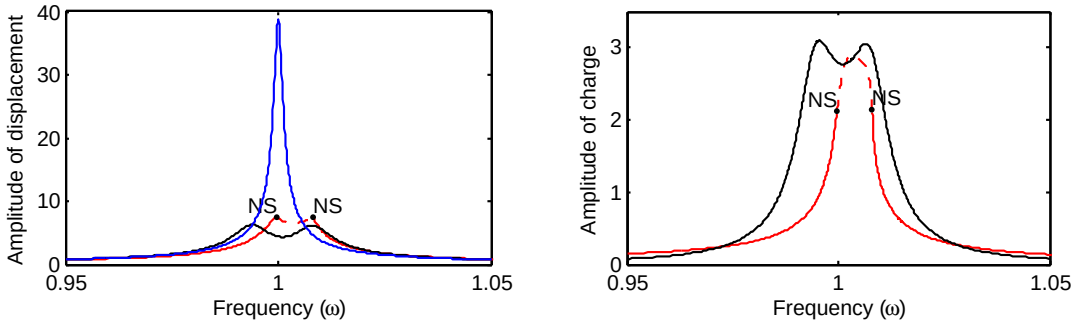

(a) (b)

Figure 6.7: Nonlinear frequency response: a) mechanical displacement of the blade mass m_1; b) electric charge. (———: mechanical bladed disks without piezoelectric attachments; ———: bladed disks shunted with essentially nonlinear circuits; ———: bladed disks shunted with resonant circuits).

For the purpose of comparison, the performance of the well-tuned resonant shunt circuit (———) and essentially nonlinear shunt circuit (———) are depicted in Fig. 6.7. It can be seen that significant vibration reduction due to the resonant/essentially nonlinear shunt circuit is achieved, compared with the mechanical bladed disk without piezoelectric attachment (———). The essentially nonlinear shunt circuit performs nearly as well as the well tuned resonant circuit does. Two Neimark-Sacker bifurcation points are observed. Quasi-periodic response is therefore expected in this region.

According to the preliminary numerical studies on NNMs and forced response for a single sector of a tuned bladed disk, it seems feasible to apply essentially nonlinear piezoelectric shunt circuits into the bladed disks. The dynamics created by the piezoelectric-based NES coupled with a SDOF mechanical oscillator, could be reproduced in the piezoelectric shunted bladed disks. Since essentially nonlinear piezoelectric shunt circuits are featured by nonexistence of preferential resonance frequency, they are expected to exhibit a better performance than the resonant circuit, when structure disorder, i.e., blade mistuning, takes place inevitably.

6.3 Essentially nonlinear piezoelectric shunt circuits in mistuned bladed disks

In this section, the performance of essentially nonlinear piezoelectric shunt circuits in mistuned bladed disks is examined. To capture the blade mistuning phenomenon, one must model the entire blade-disk structure by considering the system:

$$\mathbf{M}_e\,\ddot{y} + \mathbf{D}_e\,\dot{y} + \mathbf{K}_e\,y + f_{e_{nl}}(y) = f_p(t) \tag{6.18}$$

Apparently the mistuned case is much more computationally expensive compared to the tuned case.

As presented in Chapter 3.2, blade mistuning δ is modeled as a variation in blade-alone stiffness k_1 and k_2. Then the response of mistuned bladed disks under engine order 1 excitation is calculated using HBM applied in the whole structure. Three harmonics are retained in the formulation of HBM. Condensation tech-

nique plays an important role in reducing computational burdens. The nonlinear parameter set generating the nonlinear forced response curve in Fig. 6.8 is listed as follows: $\varepsilon = 0.05, \mu = 0.185^3, \beta = 1, \alpha = 0.05\alpha^{cr}$. For the purpose of comparison, response curves of the tuned/mistuned bladed disks, and resonant shunted bladed disk are plotted, as well. Readers may also refer to Fig. 3.8 since the same mistuning pattern δ is imposed on the bladed disk.

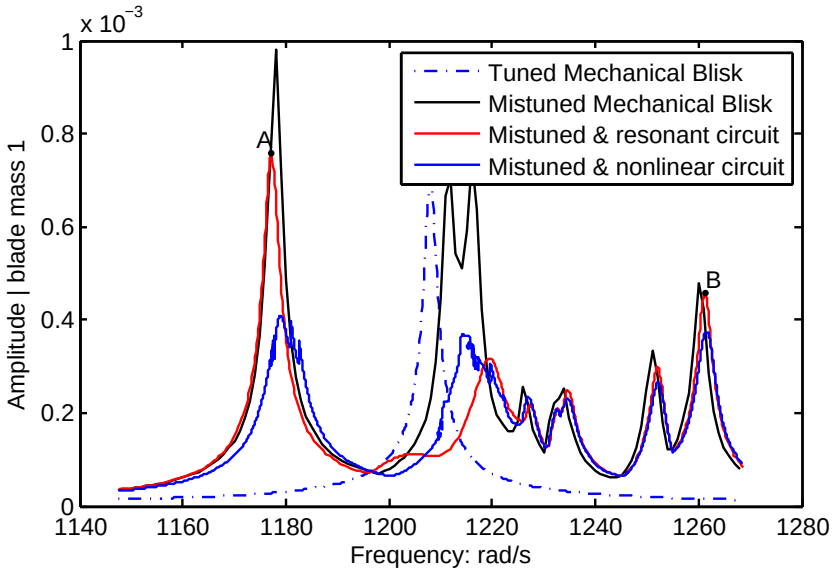

Figure 6.8: Maximum blade amplitude versus frequency

It is seen that in the mistuned bladed disk, the essentially nonlinear piezoelectric shunt circuits (——) perform better than the engine-order tuned resonant circuits (——) since significant vibration reduction is achieved all over the examined frequency range. This is mainly attributed to the adaptive capability of the piezoelectric-based NES since it is not necessary to be a priori tuned to any specified frequency. This feature enables the nonlinear shunted piezoelectric to adaptively interact with each mistuned sector of bladed disks, which finally leads to a sound vibration reduction effect.

The forced responses of this mistuned bladed disk with essentially nonlinear shunted circuits are further validated in the time domain from initial condition at rest at selected excitation frequencies. To highlight the blade mistuning effect, we

choose the excitation frequency as $\omega_1 = 1177 rad/s$, $\omega_2 = 1261 rad/s$, where the maximum blade amplitude (point A) and a secondary peak (point B) are found in Fig. 6.8. A comparison of blade amplitudes between the piezoelectric shunted bladed disk with linear circuits and the one with nonlinear circuits is depicted in Fig. 6.9. Due to the blade mistuning effect, strong localization phenomenons are observed in both cases, i.e., some blades (blade no. 2) undergo excessive vibration level in Fig. 6.9a. While at the same time the vibration level is significantly reduced because of the nonlinear effect. Similar vibration reduction phenomenon is also observed in Fig. 6.9b. These interesting phenomenons demonstrates the possibility that the essentially nonlinear effects could be beneficial in cases where motion localization due to structure disorder is unwanted.

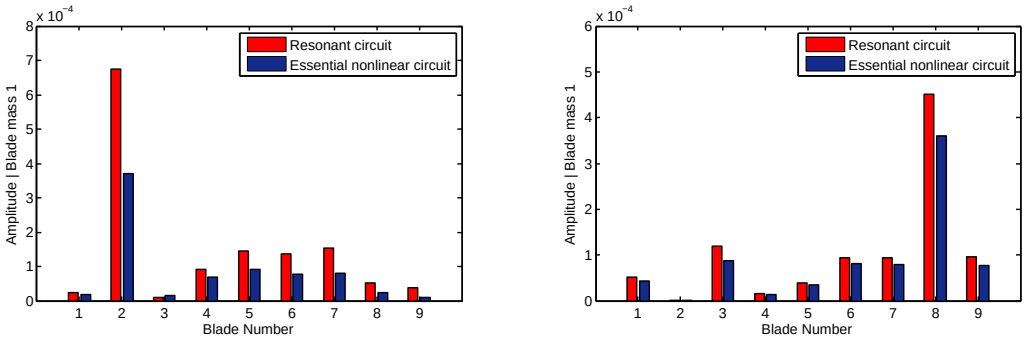

Figure 6.9: Blade amplitude versus blade number: a) at $\omega_1 = 1177 rad/s$, point A; b) at $\omega_2 = 1261 rad/s$, point B.

It is also found that at point B, vibration reduction of the maximum blade amplitude is less effective than that at point A. This phenomenon is probably attributed to the energy-dependent performance of piezoelectric-based NES, since the bladed disk undergoes a higher vibration level at point A. This proves to be a rational conclusion by examining the responses under an augmented excitation. Blade amplitude distribution is given in Fig. 6.10 when the engine order excitation reaches 1.5 times the level in Fig. 6.9. It is shown that in the case of resonant shunt circuit, the maximum blade amplitudes increase linearly with the augmented excitation. As expected, more effective vibration reduction is realized at point B

in Fig. 6.10b.

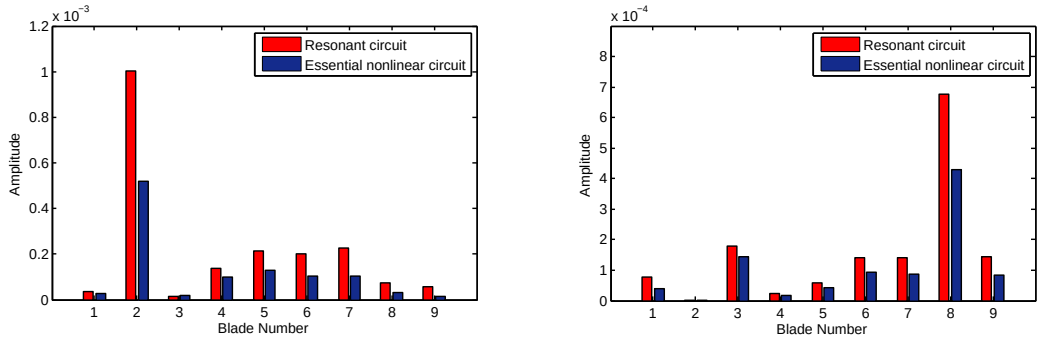

(a) (b)

Figure 6.10: Blade amplitude versus blade number with augmented excitation: a) at $\omega_1 = 1177 rad/s$, point A; b) at $\omega_2 = 1261 rad/s$, point B.

Finally, it should be pointed out that there still exist small fractions of unstable areas in the nonlinear response curve. Since high dimensional bifurcations have been encountered in the global dynamics of SDOF linear oscillator coupled with NES, essentially nonlinear effects in the cyclic structure, along with blade mistuning further complicate the mechanism of losing stability. Despite the existence of unstable periodic solutions, the essential nonlinear piezoelectric shunt circuits yield better performance than the linear resonant circuits do over a broad frequency band.

6.4 Conclusion

Essential nonlinearity is introduced into the piezoelectric shunted bladed disk in this chapter. The computational strategy based on harmonic balance method specially for tuned cyclic structures works well even in the case of strong nonlinear effect. By examining NNMs and forced response of a single sector in a tuned bladed disk, it proves feasible to reproduce, using an essentially nonlinear piezoelectric shunt circuit, the dynamics created by a mechanical NES in the MDOF primary system. This study paves the way for applications of the piezoelectric-based NES in bladed disks.

The appealing feature of NES, i.e., nonexistence of preferential resonant frequency, enables the essentially nonlinear shunt circuits adaptively interact with each sector of mistuned bladed disks in a broadband fashion. Consequently, they yield a better damping performance than the resonant circuits do, when blade mistuning takes place inevitably.

Conclusions and perspectives

Blade mistuning has a dramatic impact on the vibratory behavior of bladed disks, giving rise to vibration localization phenomenons and blade forced response amplitude magnification. On the other hand, piezoelectric materials have been extensively used as sensors and actuators for vibration controls in recent decades because of their ideal properties: light weight, high bandwidths, efficient energy conversion and easy integration. Embedded or bonded onto the vibrating structures, piezoelectric materials can convert mechanical energy into electric energy and vice versa. This thesis is dedicated to applying piezoelectric shunt damping into bladed disks in order to suppress blade mistuning effects.

The main contributions drawn from the research work presented in this thesis are summarized as follows:

- A new piezoelectric damping strategy especially suitable for blisks, i.e., using shunted piezoelectrics solely attached onto the disk, is proposed. This strategy is of engineering interest since the piezoelectric transducers are placed outside of the main stream in turbomachinery in order to avoid disturbing the flow field. It is also important to demonstrate that relatively small inductances are required by resonant circuits for the high-frequency vibration in bladed disks.

- The optimized piezoelectric mistuning, seen as a kind of damping mistuning, is demonstrated effective in blade vibration reduction for a given mistuned bladed disk. Relying on this fact, an adaptive control strategy is developed aiming at adjusting the piezoelectric mistuning pattern to keep "optimal" in terms of maintaining low blade vibration levels during the operation of bladed disks.

- An essentially nonlinear piezoelectric shunt circuit is proposed for practical realization of nonlinear energy sink. This piezoelectric-based NES is characterized by the lack of preferential resonance frequencies. This feature enables it to act as a passive, adaptive, broadband vibration absorber. Furthermore, a relative smaller inductance requirement also advantages this nonlinear shunt circuit over the resonant circuit.

- The variable-coefficient harmonic balance method, namely, a variant of HBM, is effective in searching for quasi-periodic responses arising in the linear mechanical oscillators coupled with a piezoelectric-based NES. It helps gain insights into the complex dynamics of forced response when the coupled electromechanical system is under harmonic external forcing.

- Essentially nonlinear piezoelectric shunt circuits are applied into mistuned bladed disks. They are capable of adaptively interacting with each sector of mistuned bladed disks in a broadband fashion. Consequently, a sound damping performance is obtained. This study paves the way for applications of the piezoelectric-based NES in realistic mistuned bladed disks.

The research work presented in this dissertation also suggests a number of theoretical and experimental work for future studies:

- Experimental validation of the proposed piezoelectric-based damping strategy. Piezoelectric attached onto the disk have been utilized successfully as excitation sources in realistic blade-disk structures. Based on this experimental test rig, resonant circuits could be readily integrated into the structure to provide convincing experimental results in terms of piezoelectric shunt damping for blade vibration.

- Theoretical aspects concerning the piezoelectric-based nonlinear energy sink have been fully addressed in Chapter 5. There are still a number of challenges in the way to practical realization of the proposed essentially nonlinear shunt circuit. The negative capacitance and ferroelectric capacitance are critical issues of major concern.

- The development of variable-coefficient harmonic balance method for quasi-periodic responses also implies its inherent limitation as a semi-analytic method. In the following study, this method might be further generalized by the multi-dimensional harmonic balance method.

- Nonlinear tuning design for the piezoelectric-based NES deserves further studies in order to seek the best performance of NES under harmonic forcing. This perspective is of great importance for realistic application of NES.

In the end, it is expected that the research work presented in this thesis could arise more attention to the piezoelectric shunt damping in the academic and industrial community. As a new damping technique, the piezoelectric shunt damping, especially the proposed essentially nonlinear shunt circuit, might provide practical and effective means for vibration reduction in mistuned bladed disks.

Appendix A

Details on system descriptions of piezoelectric shunted bladed disks

The submatrices of circulant matrices $\mathbf{D_p}$ and $\mathbf{K_p}$ in Eq. (3.3) are given as follows:

$$\mathbf{D_p} = \begin{bmatrix} \mathbf{D}_{\mathbf{p}_{m,1}} & \mathbf{D}_{\mathbf{p}_{r,1}} & \cdots & \mathbf{D}_{\mathbf{p}_{l,1}} \\ \mathbf{D}_{\mathbf{p}_{l,2}} & \mathbf{D}_{\mathbf{p}_{m,2}} & \mathbf{D}_{\mathbf{p}_{r,2}} & \vdots \\ 0 & \ddots & \ddots & 0 \\ \mathbf{D}_{\mathbf{p}_{r,N}} & \cdots & \mathbf{D}_{\mathbf{p}_{l,N}} & \mathbf{D}_{\mathbf{p}_{m,N}} \end{bmatrix}, \quad \mathbf{K_p} = \begin{bmatrix} \mathbf{K}_{\mathbf{p}_{m,1}} & \mathbf{K}_{\mathbf{p}_{r,1}} & \cdots & \mathbf{K}_{\mathbf{p}_{l,1}} \\ \mathbf{K}_{\mathbf{p}_{l,2}} & \mathbf{K}_{\mathbf{p}_{m,2}} & \mathbf{K}_{\mathbf{p}_{r,2}} & \vdots \\ 0 & \ddots & \ddots & 0 \\ \mathbf{K}_{\mathbf{p}_{r,N}} & \cdots & \mathbf{K}_{\mathbf{p}_{l,N}} & \mathbf{K}_{\mathbf{p}_{m,N}} \end{bmatrix}$$

$$\mathbf{D}_{\mathbf{p}_{l,j}} = \begin{bmatrix} 0 & 0 & 0 & 0 \\ 0 & 0 & 0 & 0 \\ 0 & 0 & -\frac{\gamma}{\omega} k_{3,j-1} & 0 \\ 0 & 0 & 0 & 0 \end{bmatrix}, \quad \mathbf{D}_{\mathbf{p}_{m,j}} = \begin{bmatrix} \frac{\gamma}{\omega} \begin{bmatrix} k_{1,j} & -k_{1,j} & 0 \\ -k_{1,j} & k_{1,j}+k_{2,j} & -k_{2,j} \\ 0 & -k_{2,j} & k_{sum} \end{bmatrix} & 0 \\ 0 & R_j \end{bmatrix}$$

$$\mathbf{D}_{\mathbf{p}_{r,j}} = \begin{bmatrix} 0 & 0 & 0 & 0 \\ 0 & 0 & 0 & 0 \\ 0 & 0 & -\frac{\gamma}{\omega} k_{3,j} & 0 \\ 0 & 0 & 0 & 0 \end{bmatrix}, \quad \mathbf{K}_{\mathbf{p}_{l,j}} = \begin{bmatrix} 0 & 0 & 0 & 0 \\ 0 & 0 & 0 & 0 \\ 0 & 0 & -k_{3,j-1} - k_{j-1}^{oc} & -k_{j-1}^{c} \\ 0 & 0 & 0 & 0 \end{bmatrix}$$

$$\mathbf{K}_{\mathbf{p}_{r,j}} = \begin{bmatrix} 0 & 0 & 0 & 0 \\ 0 & 0 & 0 & 0 \\ 0 & 0 & -k_{3,j} - k_{j}^{oc} & 0 \\ 0 & 0 & -k_{j}^{c} & 0 \end{bmatrix}, \mathbf{K}_{\mathbf{p}_{m,j}} = \begin{bmatrix} k_{1,j} & -k_{1,j} & 0 & 0 \\ -k_{1,j} & k_{1,j}+k_{2,j} & -k_{2,j} & 0 \\ 0 & -k_{2,j} & k_{sum} + k_{j-1}^{oc} + k_{j}^{oc} & k_{j}^{c} \\ 0 & 0 & k_{j}^{c} & \frac{1}{C_{P,j}^{S}} \end{bmatrix}$$

where $k_{sum} = k_{3,j-1} + k_{2,j} + k_{3,j} + k_{4,j}$. The damping matrix $\mathbf{D_p}$ is built such that the system has an equivalent structure damping to that in Eq. (3.4).

Alternatively, the frequency-domain system description in Eq. (3.4) is proposed as well. $\mathbf{K}_{mech}$ and $\mathbf{K}_{piezo}$ are also circulant matrices with a similar structure:

$$\mathbf{K}_{mech_{l,j}} = \begin{bmatrix} 0 & 0 & 0 \\ 0 & 0 & 0 \\ 0 & 0 & -k_{3,j-1} \end{bmatrix}, \qquad \mathbf{K}_{mech_{m,j}} = \begin{bmatrix} k_{1,j} & -k_{1,j} & 0 \\ -k_{1,j} & k_{1,j} + k_{2,j} & -k_{2,j} \\ 0 & -k_{2,j} & k_{sum} \end{bmatrix}$$

$$\mathbf{K}_{mech_{r,j}} = \begin{bmatrix} 0 & 0 & 0 \\ 0 & 0 & 0 \\ 0 & 0 & -k_{3,j} \end{bmatrix}, \qquad \mathbf{K}_{piezo_{l,j}} = \begin{bmatrix} 0 & 0 & 0 \\ 0 & 0 & 0 \\ 0 & 0 & -k_{5,j-1} \end{bmatrix}$$

$$\mathbf{K}_{piezo_{r,j}} = \begin{bmatrix} 0 & 0 & 0 \\ 0 & 0 & 0 \\ 0 & 0 & -k_{5,j} \end{bmatrix}, \qquad \mathbf{K}_{piezo_{m,j}} = \begin{bmatrix} 0 & 0 & 0 \\ 0 & 0 & 0 \\ 0 & 0 & k_{5,j-1} + k_{5,j} \end{bmatrix}$$

Appendix B

.1 Linear approximation of the response

For the sake of simplicity, hereafter $X_0^{\delta+\Delta\delta,\delta_L}$ will be substituted by $X(\delta_L)$ or X_0. Similarly, $X^{\delta+\Delta\delta,\delta_L+\Delta\delta_L}$ is replaced by $X(\delta_L+\Delta\delta_L)$. For practical rather than theoretical reasons, the treatment of matrix calculus is based on differentials rather than derivatives. Let A equal the transfer matrix:

$$A = \left[-\omega^2\mathbf{M} + i\gamma\mathbf{K}_{mech}^{\delta+\Delta\delta} + \left(\mathbf{K}_{mech}^{\delta+\Delta\delta} + \mathbf{K}_{piezo}^{\delta_L}\right)\right] \tag{19}$$

Taking the differential of X at δ_L with increment $\Delta\delta_L$ and then using the property of vectorization and Kronecker's product yields:

$$\begin{aligned} dX(\delta_L;\Delta\delta_L) &= d(A^{-1}F) = -A^{-1}d(A)A^{-1}F = -A^{-1}d(\mathbf{K}_{piezo}^{\delta_L})X_0 \\ &= -\left(X_0^T \otimes A^{-1}\right) vec\left(d\mathbf{K}_{piezo}^{\delta_L}\right) \end{aligned} \tag{20}$$

Let's note that $\mathbf{K}_{piezo}^{\delta_L}$ is the separated piezoelectric stiffness matrix that only comprises the stiffness of each piezoelectric patch $k_{5,j}$; we thus have:

$$d\mathbf{K}_{piezo}^{\delta_L} = \sum_{j=1}^{N} \frac{\partial\mathbf{K}_{piezo}^{\delta_L}}{\partial k_{5,j}} \frac{\partial k_{5,j}}{\partial\delta_{L,j}} d\delta_{L,j} \tag{21}$$

Let's denote $V_j = \partial\mathbf{K}_{piezo}^{\delta_L}/\partial k_{5,j}$. $\partial k_{5,j}/\partial\delta_{L,j}$ can then be obtained from

Eq. (2.22). Furthermore we have:

$$\begin{aligned} vec\left(d\mathbf{K}^0_{piezo}\right) &= vec\left(V_1\frac{\partial k_{5,1}}{\partial \delta_{L,1}}d\delta_{L,1}\right)+\cdots+vec\left(V_N\frac{\partial k_{5,N}}{\partial \delta_{L,N}}d\delta_{L,N}\right) \\ &= \left[vec\left(V_1\frac{\partial k_{5,1}}{\partial \delta_{L,1}}\right)\middle|\cdots\middle|vec\left(V_N\frac{\partial k_{5,N}}{\partial \delta_{L,N}}\right)\right]\times[d\delta_{L,1},\cdots,d\delta_{L,N}]^T \\ &= E\,d\delta_L \end{aligned} \tag{22}$$

Now, let's substitute Eq. (22) into Eq. (20):

$$dX_0 = -\left(X_0^T\otimes A^{-1}\right)E\,d\delta_L \tag{23}$$

Obviously, the Jacobian matrix $\mathbf{J}$ is $-\left(X_0^T\otimes A^{-1}\right)E$.

.2 Gauss-Newton method for nonlinear least squares problems

We shall discuss the Gauss-Newton method for nonlinear least squares problems in this section. Given a vector function $X:\mathbb{C}^N\rightarrow\mathbb{C}^N$. We want to minimize $\|X(\delta_L)\|$, or equivalently to find:

$$\delta_L^* = argmin_{\delta_L}\{\mathbb{F}\} = argmin_{\delta_L}\{\frac{1}{2}X^H(\delta_L)X(\delta_L)\} \tag{24}$$

The Gauss-Newton method is based on a linear approximation to the components of X in the neighborhood of δ_L; for small $\|\Delta\delta_L\|$ we see from the Taylor expansion that:

$$X(\delta_L+\Delta\delta_L) = X(\delta_L)+\mathbf{J}\Delta\delta_L == X_0+\mathbf{J}\Delta\delta_L \tag{25}$$

Inserting this expression into the definition Eq. (24) of $\mathbb{F}$ and introducing the

constraint conditionyields:

$$\begin{aligned}\mathbb{F}(\delta_L + \Delta\delta_L) = \mathbb{L}(\Delta\delta_L) &= (X_0 + \mathbf{J}\Delta\delta_L)^H (X_0 + \mathbf{J}\Delta\delta_L) \\ &= \mathbb{F}(\delta_L) + 2\Delta\delta_L^T Re(\mathbf{J}^H X_0) + \Delta\delta_L^T \mathbf{J}^H \mathbf{J}\Delta\delta_L \quad (26)\end{aligned}$$

We herein introduce $\mathbb{L}$ as a function of $\Delta\delta_L$. The Gauss-Newton step $(\Delta\delta_L)_{gn}$ minimizes $\mathbb{L}(\Delta\delta_L)$,

$$(\Delta\delta_L)_{gn} = argmin_{\Delta\delta_L} \{\mathbb{L}(\Delta\delta_L)\} \quad (27)$$

It is easily seen that the gradient and the Hessian of $\mathbb{L}$ are:

$$\mathbb{L}'(\Delta\delta_L) = 2Re(\mathbf{J}^H X_0) + 2Re(\mathbf{J}^H \mathbf{J})\Delta\delta_L \quad (28)$$

$$\mathbb{L}''(\Delta\delta_L) = 2Re(\mathbf{J}^H \mathbf{J}) \quad (29)$$

If there exists a minimum value of $\mathbb{L}(\Delta\delta_L)$, it can be found by solving

$$\mathbb{L}'[(\Delta\delta_L)_{gn}] = 2Re(\mathbf{J}^H X_0) + 2Re(\mathbf{J}^H \mathbf{J})(\Delta\delta_L)_{gn} = 0 \quad (30)$$

The descent direction $(\Delta\delta_L)_{gn}$ for $\mathbb{F}$ could be used in the extensively known algorithm of *descent method*. The typical step is:

$$\begin{aligned}\text{Solve: } Re(\mathbf{J}^H \mathbf{J})(\Delta\delta_L)_{gn} &= -Re(\mathbf{J}^H X_0) \\ \delta_L &:= \delta_L + \beta(\Delta\delta_L)_{gn} \quad (31)\end{aligned}$$

where β is factor that determines how far the next iteration step is to move from a point δ_L in the descent direction $(\Delta\delta_L)_{gn}$. The classical Gauss-Newton method uses $\beta = 1$ in all iterative steps. However, β is found by line search in this thesis. There exist a number of line search algorithms, such as uniform search and golden section search, etc. The Gauss-Newton method with line search can be shown to have guaranteed convergence under certain conditions.

Appendix C

Analytic expressions of Fourier coefficients for nonlinear functions

It is assumed that the electric charge $q(t)$ is expressed by a truncated Fourier series:

$$q(t) = Q_0 + \sum_{k=1}^{N_h} Q^{ck} cos(k\omega t) + Q^{sk} sin(k\omega t) \tag{32}$$

The $(2N_h + 1) \times 1$ vector Q contains Fourier coefficients:

$$\begin{aligned} Q &= [Q^0, Q^{c1}, Q^{s1}, \ldots, Q^{ck}, Q^{sk}, \ldots, Q^{cN_h}, Q^{sN_h}]^T \\ &= [Q_1, Q_2, \ldots, Q_{2N_h+1}]^T \end{aligned} \tag{33}$$

In standard harmonic balance method, the nonlinear term $f_{nl}(t, q) = q^3$ is also expressed by a Fourier expansion:

$$f_{nl}(t) = F_{nl}^0 + \sum_{k=1}^{N_h} F_{nl}^{ck} cos(k\omega t) + F_{nl}^{sk} sin(k\omega t) \tag{34}$$

where

$$F_{nl}^0 = \frac{\omega}{2\pi} \int_0^{2\pi/\omega} q^3(t) dt \tag{35}$$

$$F_{nl}^{ck} = \frac{\omega}{\pi}\int_0^{2\pi/\omega} q^3(t)cos(k\omega t)dt \tag{36}$$

$$F_{nl}^{sk} = \frac{\omega}{\pi}\int_0^{2\pi/\omega} q^3(t)sin(k\omega t)dt \tag{37}$$

Analytical expression of F_{nl} can be readily obtained for small valued N_h. For instance, when $N_h = 3$, we have:

$$F_{nl} = \begin{bmatrix} Q_1^3 + \frac{3}{2}Q_1Q_2^2 + \frac{3}{2}Q_1Q_4^2 + \frac{3}{2}Q_1Q_6^2 + \frac{3}{2}Q_1Q_3^2 + \frac{3}{2}Q_1Q_5^2 + \cdots \\ \frac{3}{2}Q_1Q_7^2 + \frac{3}{2}Q_2^2Q_4 + \frac{3}{2}Q_2Q_4Q_6 + \frac{3}{2}Q_2Q_3Q_5 + \frac{3}{2}Q_2Q_5Q_7 - \cdots \\ \frac{3}{4}Q_4Q_3^2 + \frac{3}{2}Q_4Q_3Q_7 - \frac{3}{2}Q_6Q_3Q_5; \\ 3Q_1^2Q_2 + 3Q_1Q_2Q_4 + 3Q_1Q_4Q_6 + 3Q_1Q_3Q_5 + 3Q_1Q_5Q_7 + \cdots \\ \frac{3}{4}Q_2^3 + \frac{3}{4}Q_2^2Q_6 + \frac{3}{2}Q_2Q_4^2 + \frac{3}{2}Q_2Q_6^2 + \frac{3}{4}Q_2Q_3^2 + \frac{3}{2}Q_2Q_3Q_7 + \cdots \\ \frac{3}{2}Q_2Q_5^2 + \frac{3}{2}Q_2Q_7^2 + \frac{3}{4}Q_4^2Q_6 + \frac{3}{2}Q_4Q_5Q_7 - \frac{3}{4}Q_6Q_3^2 - \frac{3}{4}Q_6Q_5^2; \\ 3Q_1^2Q_3 + 3Q_1Q_2Q_5 - 3Q_1Q_4Q_3 + 3Q_1Q_4Q_7 - 3Q_1Q_6Q_5 + \cdots \\ \frac{3}{4}Q_2^2Q_3 + \frac{3}{4}Q_2^2Q_7 - \frac{3}{2}Q_2Q_6Q_3 - \frac{3}{4}Q_4^2Q_7 + \frac{3}{2}Q_4Q_6Q_5 + \cdots \\ \frac{3}{2}Q_4^2Q_3 + \frac{3}{2}Q_6^2Q_3 + \frac{3}{4}Q_3^3 - \frac{3}{4}Q_3^2Q_7 + \frac{3}{2}Q_3Q_5^2 + \frac{3}{2}Q_3Q_7^2 + \frac{3}{4}Q_5^2Q_7; \\ 3Q_1^2Q_4 + \frac{3}{2}Q_1Q_2^2 + 3Q_1Q_2Q_6 - \frac{3}{2}Q_1Q_3^2 + 3Q_1Q_3Q_7 + \cdots \\ \frac{3}{2}Q_2^2Q_4 + \frac{3}{2}Q_2Q_4Q_6 + \frac{3}{2}Q_2Q_5Q_7 + \frac{3}{4}Q_4^3 + \frac{3}{2}Q_4Q_6^2 + \cdots \\ \frac{3}{2}Q_4Q_3^2 - \frac{3}{2}Q_4Q_3Q_7 + \frac{3}{4}Q_4Q_5^2 + \frac{3}{2}Q_4Q_7^2 + \frac{3}{2}Q_6Q_3Q_5; \\ 3Q_1^2Q_5 + 3Q_1Q_2Q_3 + 3Q_1Q_2Q_7 - 3Q_1Q_6Q_3 + \frac{3}{2}Q_2^2Q_5 + \cdots \\ \frac{3}{2}Q_2Q_4Q_7 - \frac{3}{2}Q_2Q_6Q_5 + \frac{3}{4}Q_4^2Q_5 + \frac{3}{2}Q_4Q_6Q_3 + \frac{3}{2}Q_6^2Q_5 + \cdots \\ \frac{3}{2}Q_3^2Q_5 + \frac{3}{2}Q_3Q_5Q_7 + \frac{3}{4}Q_5^3 + \frac{3}{2}Q_5Q_7^2; \\ 3Q_1^2Q_6 + 3Q_1Q_2Q_4 - 3Q_1Q_3Q_5 + \frac{1}{4}Q_2^3 + \frac{3}{2}Q_2^2Q_6 + \frac{3}{4}Q_2Q_4^2 - \cdots \\ \frac{3}{4}Q_2Q_3^2 - \frac{3}{4}Q_2Q_5^2 + \frac{3}{2}Q_4^2Q_6 + \frac{3}{2}Q_4Q_3Q_5 + \cdots \\ \frac{3}{4}Q_6^3 + \frac{3}{2}Q_6Q_3^2 + \frac{3}{2}Q_6Q_5^2 + \frac{3}{4}Q_6Q_7^2; \\ 3Q_1^2Q_7 + 3Q_1Q_2Q_5 + 3Q_1Q_4Q_3 + \frac{3}{4}Q_2^2Q_3 + \frac{3}{2}Q_2^2Q_7 + \cdots \\ \frac{3}{2}Q_2Q_4Q_5 - \frac{3}{4}Q_4^2Q_3 + \frac{3}{2}Q_4^2Q_7 + \frac{3}{4}Q_6^2Q_7 - \frac{1}{4}Q_3^3 + \cdots \\ +\frac{3}{2}Q_3^2Q_7 + \frac{3}{4}Q_3Q_5^2 + \frac{3}{2}Q_5^2Q_7 + \frac{3}{4}Q_7^3 \end{bmatrix} \tag{38}$$

List of Figures

References

[1] A. S. Rangwala. *Turbo-machinery dynamics design and operation*. McGraw-Hill, New York, 2005. 5

[2] T. Giampaolo. *Gas turbine handbook : principles and practice*. Fairmont Press ; CRC Press, Lilburn, GA; Boca Raton, FL, 2009. 5

[3] A. V. Srinivasan. Flutter and resonant vibration characteristics of engine blades. *Journal of Engineering for Gas Turbines and Power*, 119(4):742–775, 1997. 7, 8, 36, 39

[4] K.C. Hall, R.E. Kielb, and J.P. Thomas. *Unsteady aerodynamics, aeroacoustics and aeroelasticity of turbomachines*. Springer, Dordrecht, 2006. 8

[5] G. B. Sinclair, N. G. Cormier, J. H. Griffin, and G. Meda. Contact stresses in dovetail attachments: Finite element modeling. *Journal of Engineering for Gas Turbines and Power*, 124(1):182–189, 2002. 10

[6] G. B. Sinclair and N. G. Cormier. Contact stresses in dovetail attachments: Physical modeling. *Journal of Engineering for Gas Turbines and Power*, 124(2):325–331, 2002. 10

[7] M. Legrand, C. Pierre, P. Cartraud, and J.P. Lombard. Two-dimensional modeling of an aircraft engine structural bladed disk-casing modal interaction. *Journal of Sound and Vibration*, 319(1):366–391, 2009. 10

[8] A. Batailly, M. Legrand, and C. Pierre. Influence of abradable coating wear mechanical properties on rotor stator interaction. *ASME Conference Proceedings*, 2011(54662):941–950, 2011. 10

[9] D. L. Thomas. Dynamics of rotationally periodic structures. *International Journal for Numerical Methods in Engineering*, 14(1):81–102, 1979. 11

[10] J. Wildheim. Excitation of rotating circumferentially periodic structures. *Journal of Sound and Vibration*, 75(3):397–416, 1981. 11, 24

[11] A. Sternchuss. *Multi-level parametric reduced models of rotating bladed disk assemblies*. PhD thesis, Ecole Centrale Paris, 2009. 11

[12] R. Bladh. *Efficient predictions of the vibratory response of mistuned bladed disks by reduced order modeling*. PhD thesis, University of Michigan, 2001. 18

[13] D. Laxalde. *Étude d'amortisseurs non-linéaires appliqués aux roues aubagées et aux systèmes multi-étages*. PhD thesis, Ecole Centrale de Lyon, 2007. 19

[14] Matthew P. Castanier and Christophe Pierre. Modeling and analysis of mistuned bladed disk vibration: Status and emerging directions. *Journal of Propulsion and Power*, 22(2):384–396, 2006. 19, 21, 26, 30, 77

[15] J. A. Kenyon, J. H. Griffin, and N. E. Kim. Mistuned bladed disk forced response with frequency veering. *Journal of Propulsion and Power*, 20(5):863–870, 2004. 21, 32

[16] J. A. Kenyon, J. H. Griffin, and N. E. Kim. Sensitivity of tuned bladed disk response to frequency veering. *Journal of Engineering for Gas Turbines and Power*, 127(4):835–842, 2005.

[17] M. I. Hussein, Pierre C., and M. P. Castanier. Correlation of tuned free vibration characteristics with mistuning sensitivity for a bladed disk. In *Proceedings of the AIAA/ASME/ASCE/AHS/ASC structures, structural dynamics and materials conference*, volume 2, pages 1341–1358, New York, 2003. AIAA. 21

[18] R. Bladh, C. Pierre, M. P. Castanier, and M. J. Kruse. Dynamic response predictions for a mistuned industrial turbomachinery rotor using reduced-order modeling. *Journal of Engineering for Gas Turbines and Power*, 124(2):311–324, 2002. 21

[19] R. Bladh, M. P. Castanier, and C. Pierre. Effects of multistage coupling and disk flexibility on mistuned bladed disk dynamics. *Journal of Engineering for Gas Turbines and Power*, 125:121–130, 2003. 21

[20] Simon Braun, D. J. Ewins, and S. S. Rao. *Encyclopedia of vibration*. Academic Press, San Diego, 2002. 25

[21] Joseph C. S., Gregory R.M., and A. J. Blair. Forced response of bladed disk assemblies: A survey. *The Shock and Vibration Digest*, 31(1):17–24, 1999. 27

[22] R. E. Kielb and K. R. V. Kaza. Effects of structural coupling on mistuned cascade flutter and response. *Journal of Engineering for Gas Turbines and Power*, 106(1):17–24, 1984. 27

[23] C. Pierre and D. V. Murthy. Aeroelastic modal characteristics of mistuned blade assemblies - mode localization and loss of eigenstructure. *AIAA journal*, 30(10):2483–2496, 1992. 27, 28

[24] J. Judge, C. Pierre, and O. Mehmed. Experimental investigation of mode localization and forced response amplitude magnification for a mistuned bladed disk. *Journal of Engineering for Gas Turbines and Power*, 123(4):940–950, 2001. 27

[25] M. P. Mignolet, A. J. Rivas-Guerra, and J. P. Delor. Identification of mistuning characteristics of bladed disks from free response data-part 1. *Journal of Engineering for Gas Turbines and Power*, 123(2):395–403, 2001. 27

[26] A. J. Rivas-Guerra, M. P. Mignolet, and J. P. Delor. Identification of mistuning characteristics of bladed disks from free response data— part ii. *Journal of Engineering for Gas Turbines and Power*, 123(2):404–411, 2001.

[27] C. Siewert and H. Stuer. Forced response analysis of mistuned turbine bladings. *ASME Conference Proceedings*, 2010(44014):1145–1156, 2010. 27, 70

[28] Marc P. Mignolet and C.-C. Lin. Identification of structural parameters in mistuned bladed disks. *Journal of Vibration and Acoustics, Transactions of the ASME*, 119(3):428–438, 1997. 27, 34

[29] F. Moyroud, T. Fransson, and G. Jacquet-Richardet. A comparison of two finite element reduction techniques for mistuned bladed disks. *Journal of Engineering for Gas Turbines and Power-Transactions of the Asme*, 124(4):942–952, 2002.

[30] E. P. Petrov and D. J. Ewins. Method for analysis of nonlinear multiharmonic vibrations of mistuned bladed disks with scatter of contact interface characteristics. *Journal of Turbomachinery*, 127(1):128–136, 2005. 27, 39

[31] C. Gibert, V. Kharyton, F. Thouverez, and P. Jean. On forced response of a rotating integrally bladed disk: Predictions and experiments. *ASME Conference Proceedings*, 2010(44014):1103–1116, 2010. 29

[32] J. Avalos and Marc P. Mignolet. Maximum amplification of blade response in mistuned multi stage assemblies. *ASME Conference Proceedings*, 2010(44014):981–994, 2010. 27

[33] C. C. Lin and M. P. Mignolet. Effects of damping and damping mistuning on the forced vibration response of bladed disks. *Journal of Sound and Vibration*, 193(2):525–543, 1996. 27

[34] P. Honisch, A. Kuhhorn, and B. Beirow. Experimental and numerical analyses of radial turbine blisks with regard to mistuning. *ASME Conference Proceedings*, 2011(54662):971–980, 2011. 27

[35] A. G. S. Joshi and B. I. Epureanu. Reduced order models for blade-to-blade damping variability in mistuned blisks. *ASME Conference Proceedings*, 2011(54662):1033–1045, 2011. 27

[36] Pierre C. Bladh R. Component-mode-based reduced order modeling techniques for mistuned bladed disks-part 1: Theoretical models. *Journal of Engineering for Gas Turbines and Power*, 123(1):89–99, 2001. 28

[37] Pierre C. Bladh R. Component-mode-based reduced order modeling techniques for mistuned bladed disks-part ii: Application. *Journal of Engineering for Gas Turbines and Power*, 123(1):100–108, 2001. 28

[38] D. M. Feiner and J. H. Griffin. A fundamental model of mistuning for a single family of modes. *Journal of Turbomachinery*, 124(4):597–605, 2002. 28

[39] D. M. Feiner and J. H. Griffin. Mistuning identification of bladed disks using a fundamental mistuning model - part i: Theory. *Journal of Turbomachinery*, 126(1):150–158, 2004.

[40] D. M. Feiner and J. H. Griffin. Mistuning identification of bladed disks using a fundamental mistuning model - part ii: Application. *Journal of Turbomachinery*, 126(1):159–165, 2004.

[41] A. Hohl, B. Kriegesmann, J. Wallaschek, and L. Panning. The influence of blade properties on the forced response of mistuned bladed disks. *ASME Conference Proceedings*, 2011(54662):1159–1170, 2011. 28

[42] E. Capiez-Lernout, C. Soize, J.-P. Lombard, C. Dupont, and E. Seinturier. Blade manufacturing tolerances definition for a mistuned industrial bladed disk. *Journal of Engineering for Gas Turbines and Power*, 127(3):621–628, 2005. 28

[43] A. Bhartiya, Y.and Sinha. Reduced order model of a multistage bladed rotor with geometric mistuning via modal analyses of finite element sectors. *Journal of Turbomachinery*, 134(4):041001, 2012. 28

[44] S.-H. Lim, M. P. Castanier, and C. Pierre. Vibration modeling of bladed disks subject to geometric mistuning and design changes. volume 3 of *Collection of Technical Papers - AIAA/ASME/ASCE/AHS/ASC Structures, Structural Dynamics and Materials Conference*, pages 1931–1950,

Palm Springs, CA, United states, 2004. American Inst. Aeronautics and Astronautics Inc. 28, 34, 90

[45] Y. Bhartiya and A. Sinha. Reduced order model of a bladed rotor with geometric mistuning: Comparison between modified modal domain analysis and frequency mistuning approach. *ASME Conference Proceedings*, 2011(54662):981–992, 2011. 28

[46] M. A. Mayorca, D. M. Vogt, H. Martensson, and T. H. Fransson. A new reduced order modeling for stability and forced response analysis of aero-coupled blades considering various mode families. *ASME Conference Proceedings*, 2010(44014):1209–1219, 2010. 28

[47] E. P. Petrov. Reduction of forced response levels for bladed discs by mistuning: Overview of the phenomenon. *ASME Conference Proceedings*, 2010(44014):1039–1051, 2010. 28, 34

[48] B. W. Huang and J. H. Kuang. Mode localization in a rotating mistuned turbo disk with coriolis effect. *International Journal of Mechanical Sciences*, 43(7):1643–1660, 2001. 29

[49] M. Nikolic, E. P. Petrov, and D. J. Ewins. Coriolis forces in forced response analysis of mistuned bladed discs. *ASME Conference Proceedings*, 2006(42401):821–831, 2006. 29

[50] J. Xin and J. Wang. Investigation of coriolis effect on vibration characteristics of a realistic mistuned bladed disk. *ASME Conference Proceedings*, 2011(54662):993–1005, 2011. 29

[51] C. H. Hodges. Confinement of vibration by structural irregularity. *Journal of Sound and Vibration*, 82(3):411–424, 1982. 30

[52] Gísli Óttarsson. *Dynamic modeling and vibration analysis of mistuned bladed disks*. PhD thesis, University of Michigan, 1994. 30

[53] J. Avalos and Marc P. Mignolet. On damping entire bladed disks through dampers on only a few blades. *Journal of Engineering for Gas Turbines and Power*, 132(9):1–10, 2010. 32, 72

[54] D. S. Whitehead. Effect of mistuning on the vibration of turbo-machine blades induced by wakes. *Journal of Mechanical Engineering Science*, 8(1):15–21, 1966. 32

[55] D. S. Whitehead. The maximum factor by which forced vibration of blades can increase due to mistuning. *Journal of Engineering for Gas Turbines and Power*, 120(1):115–119, 1998. 32

[56] J. A. Kenyon, J. H. Griffin, and D. M. Feiner. Maximum bladed disk forced response from distortion of a structural mode. *ASME Conference Proceedings*, 2002(36096):965–980, 2002.

[57] E. P. Petrov and D. J. Ewins. Analysis of the worst mistuning patterns in bladed disk assemblies. *Journal of Turbomachinery*, 125(4):623–631, 2003. 32, 33, 83

[58] B. Xiao, A. J. Rivas-Guerra, and Marc P. Mignolet. Maximum amplification of blade response due to mistuning in multi-degree-of-freedom blade models. *ASME Conference Proceedings*, 2004(41715):427–438, 2004. 32

[59] Y. Han, B. Xiao, and Marc P. Mignolet. Expedient estimation of the maximum amplification factor in damped mistuned bladed disks. *ASME Conference Proceedings*, 2007(47942):351–365, 2007. 32

[60] J. Avalos and Marc P. Mignolet. Maximum amplification of blade response in mistuned multi stage assemblies. *ASME Conference Proceedings*, 2010(44014):981–994, 2010. 32

[61] D. J. Ewins. The effects of detuning upon the forced vibrations of bladed disks. *Journal of Sound and Vibration*, 9(1):65–79, 1969. 33

[62] E. P. Petrov and R. Vitali. Optimization of mistuned bladed discs using gradient-based response surface approximations. In *AIAA/ASME/ASCE/AHS/ASC Structures, Structural Dynamics, and Materials Conference and Exhibit*, volume 1522, Atlanta, GA, 2000. AIAA. 33

[63] R. Mario and D'Amato F. New tools for analysis and optimization of mistuned bladed disks. In *38th AIAA/ASME/SAE/ASEE Joint Propulsion Conference and Exhibit*, Indianapolis, Indiana, 2002. AIAA. 33

[64] J. Judge, C. Pierre, and S. L. Ceccio. Experimental validation of mistuning identification techniques and vibration predictions in bladed disks. In *CEAS International Forum on Aeroelasticity and Structural Dynamics*, pages 87–98, Madrid, Spain, 2001. 34

[65] F. Pichot, F. Thouverez, L. Jezequel, and E. Seinturier. Mistuning parameters identification of a bladed disk. In K. M. Holford, J. A. Brandon, J. M. DulieuBarton, M. D. Gilchrist, and K. Worden, editors, *Damage Assessment of Structures*, volume 204-2 of *Key Engineering Materials*, pages 123–132. Trans Tech Publications Ltd, Zurich-Uetikon, 2001. 34

[66] F. Pichot, D. Laxalde, J. J. Sinou, F. Thouverez, and J. P. Lombard. Mistuning identification for industrial blisks based on the best achievable eigenvector. *Computers and Structures*, 84(29-30):2033–2049, 2006. 34

[67] D. Laxalde, F. Thouverez, J.-J. Sinou, J.-P. Lombard, and S. Baumhauer. Mistuning identification and model updating of an industrial blisk. *International Journal of Rotating Machinery*, 2007, 2007. 83

[68] J. A. Judge, C.hristophe Pierre, and S. L. Ceccio. Experimental mistuning identification in bladed disks using a component-mode-based reduced-order model. *AIAA journal*, 47(5):1277–1287, 2009. 34, 83

[69] B. Lalanne and M. Touratier. Aeroelastic vibrations and stability in cyclic symmetric domains. *International Journal of Rotating Machinery*, 6(6):445–452, 2000. 34

[70] M. Sadeghi and F. Liu. A method for calculating mistuning effects on cascade flutter. *AIAA journal*, 39(1):22–28, 2001. 34

[71] M. Sadeghi and F. Liu. Computation of cascade flutter by uncoupled and coupled methods. *International Journal of Computational Fluid Dynamics*, 19(8):559–569, 2005. 34

[72] E. P. Petrov. A method for forced response analysis of mistuned bladed discs with aerodynamic effects included. *ASME Conference Proceedings*, 2009(48876):375–386, 2009. 34

[73] M. P Castanier and C. Pierre. Consideration on the benefits of intentional blade mistuning for the forced response of turbomachinery rotors. *Proceedings of the ASME Aerospace Division*, 55:419–425, 1997. 36

[74] M. P. Castanier and C. Pierre. Investigation of the combined effects of intentional and random mistuning on the forced response of bladed disks. In *34th AIAA/ASME/SAE/ASEE Joint Propulsion Conference and Exhibit*, Cleveland, 1998. AIAA. 37

[75] M. P. Castanier and C. Pierre. Using intentional mistuning in the design of turbomachinery rotors. *AIAA journal*, 40(10):2077–2086, 2002.

[76] Marc P. Mignolet, W. Hu, and I. Jadic. On the forced response of harmonically and partially mistuned bladed disks. part i: Harmonic mistuning. *International Journal of Rotating Machinery*, 6(1):29–41, 2000.

[77] M. P. Mignolet, W. Hu, and I. Jadic. On the forced response of harmonically and partially mistuned bladed disks. part ii: Partial mistuning and applications. *International Journal of Rotating Machinery*, 6(1):43–56, 2000. 37

[78] B. K. Choi, J. Lentz, A. J. Rivas-Guerra, and M. P. Mignolet. Optimization of intentional mistuning patterns for the reduction of the forced response effects of unintentional mistuning: Formulation and assessment. In *International Gas Turbine and Aeroengine Congress and Exhibition*, volume 125, pages 131–140, New Orleans, LA (USA), 2003. ASME. 37, 83

[79] J. F. Hou and C. Cross. Minimizing blade dynamic response in a bladed disk through design optimization. *AIAA journal*, 43(2):406–412, 2005. 37

[80] K. Y. Sanliturk, D. J. Ewins, and A. B. Stanbridge. Underplatform dampers for turbine blades: Theoretical modeling, analysis, and comparison with

experimental data. *Journal of Engineering for Gas Turbines and Power*, 123(4):919–929, 2001. 37

[81] J. Szwedowicz, W. Sextro, R. Visser, and P. A. Masserey. On forced vibration of shrouded turbine blades. *ASME Conference Proceedings*, 2003(36878):257–266, 2003. 37

[82] D. Laxalde, C. Gibert, and F. Thouverez. Experimental and numerical investigations of friction rings damping of blisks. *ASME Conference Proceedings*, 2008(43154):469–479, 2008. 37, 69, 70, 184

[83] D. Charleux, C. Gibert, F. Thouverez, and J. Dupeux. Numerical and experimental study of friction damping blade attachments of rotating bladed disks. *International Journal of Rotating Machinery*, 2006, 2006. 38

[84] S. Nacivet, C. Pierre, F. Thouverez, and L. Jezequel. A dynamic lagrangian frequency-time method for the vibration of dry-friction-damped systems. *Journal of Sound and Vibration*, 265(1):201–219, 2003. 38

[85] L. Salles, L. Blanc, F. Thouverez, A. M. Gouskov, and P. Jean. Dynamic analysis of a bladed disk with friction and fretting-wear in blade attachments. *ASME Conference Proceedings*, 2009(48876):465–476, 2009. 39

[86] E. P. Petrov. A method for use of cyclic symmetry properties in analysis of nonlinear multiharmonic vibrations of bladed disks. *Journal of Turbomachinery*, 126(1):175–183, 2004. 39

[87] P. J. Torvik and J. Hansel. Mechanical properties of a ceramic coating with vem infiltration. *Journal of Engineering Materials and Technology*, 131(3):1–10, 2009. 39

[88] J. Sun and L. Kari. Coating methods to increase material damping of compressor blades: Measurements and modeling. *ASME Conference Proceedings*, 2010(44014):1157–1165, 2010. 39

[89] S. Filippi and P. J. Torvik. A methodology for predicting the response of blades with nonlinear coatings. *Journal of Engineering for Gas Turbines and Power*, 133(4):1–7, 2011. 39

[90] J. Laborenz, C. Siewert, L. Panning, J. Wallaschek, C. Gerber, and P.-A. Masserey. Eddy current damping: A concept study for steam turbine blading. *Journal of Engineering for Gas Turbines and Power*, 132(5):1–7, 2009. 39

[91] J. Laborenz, M. Krack, L. Panning, J. Wallaschek, M. Denk, and P.-A. Masserey. Eddy current damper for turbine blading: Electromagnetic finite element analysis and measurement results. *Journal of Engineering for Gas Turbines and Power*, 134(4):1–8, 2011. 39

[92] Tzou H, LEE. H.-J, and Arnold S. Smart materials, precision sensors/actuators, smart structures, and structronic systems. *Mechanics of Advanced Materials and Structures*, 11(4-5):367–393, 2004. 43

[93] N. Jalili. *Piezoelectric-Based Vibration Control From Macro to Micro/Nano Scale Systems*. Springer US, 2010. 43, 46, 48

[94] N. W. Hagood and A. von Flotow. Damping of structural vibrations with piezoelectric materials and passive electrical networks. *Journal of Sound and Vibration*, 146(2):243–268, 1991. 44, 45, 49, 50, 55, 59, 76, 183

[95] B. De Marneffe. *Active and Passive Vibration Isolation and Damping via Shunted Transducers*. PhD thesis, Université libre de Bruxelles, 2007. 47, 59, 61, 183, 184

[96] A. Benjeddou and J.-A. Ranger. Use of shunted shear-mode piezoceramics for structural vibration passive damping. *Computers and Structures*, 84(22-23):1415–1425, 2006. 49

[97] M. A. Trindade and C. E. B. Maio. Multimodal passive vibration control of sandwich beams with shunted shear piezoelectric materials. *Smart Materials and Structures*, 17(5):055015–055025, 2008. 49, 60

[98] R. C. Lawrence and W. Clark. Comparison of low-frequency piezoelectric switching shunt techniques for structural damping. *Smart Materials and Structures*, 11(3):370–376, 2002. 57, 62, 63, 184

[99] C. L. Davis and G. A. Lesieutre. A modal strain energy approach to the prediction of resistively shunted piezoceramic damping. *Journal of Sound and Vibration*, 184(1):129–139, 1995. 59

[100] S.O.R. Moheimani. A survey of recent innovations in vibration damping and control using shunted piezoelectric transducers. *Control Systems Technology, IEEE Transactions*, 11(4):482–494, 2003. 59

[101] H. P. Chul and J. Inman D. Enhanced piezoelectric shunt design. *Shock and Vibration*, 10(2):127–133, 2003. 59

[102] I. Giorgio, A. Culla, and D. Del Vescovo. Multimode vibration control using several piezoelectric transducers shunted with a multiterminal network. *Archive of Applied Mechanics*, 79(9):859–879, 2009. 60

[103] J. J. Hollkamp. Multimodal passive vibration suppression with piezoelectric materials and resonant shunts. *Journal of intelligent material systems and structures*, 5(1):49–57, 1994. 60

[104] S. Wu. Method for multiple mode piezoelectric shunting with single pzt transducer for vibration control. *Journal of intelligent material systems and structures*, 9(12):991–998, 1998. 60

[105] F. A. C. Viana and J. V. Steffen. Multimodal vibration damping through piezoelectric patches and optimal resonant shunt circuits. *Journal of the Brazilian Society of Mechanical Sciences and Engineering*, 28:293–310, 2006. 60

[106] J. Tang and K. W. Wang. Active-passive hybrid piezoelectric networks for vibration control: comparisons and improvement. *Smart Materials and Structures*, 10(4):794–806, 2001. 61

[107] M. Neubauer, R. Oleskiewicz, K. Popp, and T. Krzyzynski. Optimization of damping and absorbing performance of shunted piezo elements utilizing negative capacitance. *Journal of Sound and Vibration*, 298(1-2):84–107, 2006. 61

[108] A. Kazuhiko, A. Yoshifumi, and I. Takuzo. Active control effort of hybrid piezoelectric absorber for structural control. *Applied Acoustics*, 65(3):277–292, 2004. 61

[109] A. J. Fleming and S. O. R. Moheimani. Adaptive piezoelectric shunt damping. *Smart Materials and Structures*, 12(1):36–48, 2003. 62

[110] Niederberger D., Fleming A., S. O. R. Moheimani, and M. Manfred. Adaptive multi-mode resonant piezoelectric shunt damping. *Smart Materials and Structures*, 13(5):1025–1035, 2004. 62

[111] O. Thorp, M. Ruzzene, and A. Baz. Attenuation and localization of wave propagation in rods with periodic shunted piezoelectric patches. *Smart Materials and Structures*, 10(5):979–989, 2001. 62, 184

[112] C. Maurini, F. dell'Isola, and D. Del Vescovo. Comparison of piezoelectronic networks acting as distributed vibration absorbers. *Mechanical Systems and Signal Processing*, 18(5):1243–1271, 2004. 62

[113] P. Bisegna, G. Caruso, and F. Maceri. Optimized electric networks for vibration damping of piezoactuated beams. *Journal of Sound and Vibration*, 289(4-5):908–937, 2006. 62

[114] D. Guyomar and A. Badel. Nonlinear semi-passive multimodal vibration damping: An efficient probabilistic approach. *Journal of Sound and Vibration*, 294(1-2):249–268, 2006. 63

[115] K. Li, J.-Y. Gauthier, and D. Guyomar. Structural vibration control by synchronized switch damping energy transfer. *Journal of Sound and Vibration*, 330(1):49–60, 2010. 63, 184

[116] S. R. Anton and H. A. Sodano. A review of power harvesting using piezoelectric materials (2003-2006). *Smart Materials and Structures*, 16(3), 2007. 64

[117] C. J. Cross and S. Fleeter. Shunted piezoelectrics for passive control of turbomachine blading flow-induced vibrations. *Smart Materials and Structures*, 11(2):239, 2002. 66, 184

[118] S. Livet, M. Collet, M. Berthillier, P. Jean, and J. M. Cote. Turbomachinery blades damping thanks to optimized shunted piezoelectric circuits. In Ahmadian Mehdi, editor, *Active and Passive Smart Structures and Integrated Systems*, volume 6928, page 692812, San Diego, CA, 2008. SPIE. 66

[119] S. M. Schwarwendahl, J. Szwedowicz, M. Neubauer, L. Panning, and J. Wallaschek. On blade damping technology using passive piezoelectric dampers. *ASME Conference Proceedings*, 2012(68600), 2012. 67, 69, 184

[120] T. Watanabe, J. Kazawa, S. Uzawa, and B. Keim. Numerical and experimental study of active flutter suppression with piezoelectric device for transonic cascade. *ASME Conference Proceedings*, 2008(43154):849–859, 2008. 67

[121] K. P. Duffy, A. J. Provenza, J. J. Trudell, and J. B. Min. Passively shunted piezoelectric damping of centrifugally-loaded plates. In *AIAA/ASME/ASCE/AHS/ASC Structures, Structural Dynamics, and Materials Conference*, pages 1–10, Palm Springs, CA, 2009. 67

[122] K. P. Duffyand B. B. Choi, A. J. Provenza, J. B. Min, and N. Kray. Active piezoelectric vibraiton control of subscale composite fan blades. *ASME Conference Proceedings*, 2012(68639), 2012. 67, 69

[123] J. L. Kauffman and G. A. Lesieutre. Vibration reduction for turbomachinery bladed disks under changing excitation using piezoelectric materials. *International Forum of Aeroelasticity and Structural Dynamics (IFASD)*, 081:1–15, 2011. 68

[124] Aurélien Sénéchal. *Réduction de vibrations de structure complexe par shunts piézoélectrique: application aux turbomachines*. PhD thesis, Structural Mechanics and Coupled Systems Laboratory, 2011. 68

[125] H. Yu and K. W. Wang. Vibration suppression of mistuned coupled-blade-disk systems using piezoelectric circuitry network. *Journal of Vibration and Acoustics*, 131(2):1–12, 2009. 68, 76, 184

[126] H. B. Yu, K. W. Wang, and J. H. Zhang. Piezoelectric networking with enhanced electromechanical coupling for vibration delocalization of mistuned periodic structure - theory and experiment. *Journal of Sound and Vibration*, 295(1-2):246–265, 2006.

[127] H. Yu and K. W. Wang. Piezoelectric networks for vibration suppression of mistuned bladed disks. *Journal of Vibration and Acoustics*, 129(5):559–566, 2007. 68

[128] Yu F. and L. Li. Vibration dissipation characteristics of symmetrical piezoelectic networks with passive branches. *ASME Conference Proceedings*, 2012(69208), 2012. 68

[129] R. Viguie A. Preumont B. Mokrani, R. Bastaits. Vibration damping of turbomachinery components with piezoelectric transducers: Theory and experiment. In *ISMA2012 International Conference on Noise and Vibration Engineering*, Leuven, Belgium, 2012. 69

[130] U. Andreaus and M. Porfiri. Effect of electrical uncertainties on resonant piezoelectric shunting. *Journal of intelligent material systems and structures*, 18(5):477–485, 2007. 70

[131] Inc MathWorks. *Genetic Algorithm and Direct Search Toolbox for Use with MATLAB: User's Guide*. MathWorks, 2005. 84

[132] G. C. Goodwin and K. S. Sin. *Adaptive filtering prediction and control*. Prentice-Hall, Englewood Cliffs, N.J., 1984. 90, 96

[133] L. Ljung and T. Soderstrom. *Theory and practice of recursive identification*. MIT Press, Cambridge, Mass., 1983. 92

[134] K. I. Tserpes, P. Papanikos, G. Labeas, and S. Pantelakis. Fatigue damage accumulation and residual strength assessment of cfrp laminates. *Composite Structures*, 63(2):219–230, 2004. 93

[135] V. Kharyton, J.-P. Laine, F. Thouverez, and O. Kucher. Simulation of tip-timing measurements of a cracked bladed disk forced response. *ASME Conference Proceedings*, 2010(44014):845–854, 2010. 95, 97, 98, 185

[136] M. I. Friswell and J. E. Mottershead. *Finite element model updating in structural dynamics*. Kluwer Academic Publishers, Dordrecht; Boston, 1995. 95, 98

[137] K. Madsen, H. B. Nielsen, and O. Tingleff. *Methods for non-linear least squares problems*. Informatics and Mathematical Modelling, Technical University of Denmark, [Lyngby], 2004. 102

[138] O. V. Gendelman. Transition of energy to a nonlinear localized mode in a highly asymmetric system of two oscillators. *Nonlinear Dynamics*, 25(1):237–253, 2001. 107

[139] A.F. Vakakis and O.V. Gendelman. *Nonlinear Targeted Energy Transfer in Mechanical and Structural Systems*. Springer, 2009. 108, 109, 110, 113, 131, 133, 136, 152, 156, 157, 158, 159, 185, 186

[140] O. Gendelman, L. I. Manevitch, A. F. Vakakis, and R. M'Closkey. Energy pumping in nonlinear mechanical oscillators: Part i—dynamics of the underlying hamiltonian systems. *Journal of Applied Mechanics*, 68(1):34–41, 2001. 108

[141] A. F. Vakakis and O. Gendelman. Energy pumping in nonlinear mechanical oscillators: Part ii—resonance capture. *Journal of Applied Mechanics*, 68(1):42–48, 2001. 108

[142] O. V. Gendelman, D. V. Gorlov, L. I. Manevitch, and A. I. Musienko. Dynamics of coupled linear and essentially nonlinear oscillators with substantially different masses. *Journal of Sound and Vibration*, 286(1-2):1–19, 2005. 108

[143] A. F. Vakakis. Inducing passive nonlinear energy sinks in vibrating systems. *Journal of Vibration and Acoustics*, 123(3):324–332, 2001. 110

[144] O. Gendelman, L. I. Manevitch, A. F. Vakakis, and L. Bergman. A degenerate bifurcation structure in the dynamics of coupled oscillators with essential stiffness nonlinearities. *Nonlinear Dynamics*, 33(1):1–10, 2003. 110

[145] A. F. Vakakis and R. H. Rand. Non-linear dynamics of a system of coupled oscillators with essential stiffness non-linearities. *International Journal of Non-Linear Mechanics*, 39(7):1079–1091, 2004. 110

[146] G. Kerschen, M. Peeters, J. C. Golinval, and A. F. Vakakis. Nonlinear normal modes, part i: A useful framework for the structural dynamicist. *Mechanical Systems and Signal Processing*, 23(1):170–194, 2009. 110

[147] M. Peeters, R. Viguié, G. Sérandour, G. Kerschen, and J. C. Golinval. Nonlinear normal modes, part ii: Toward a practical computation using numerical continuation techniques. *Mechanical Systems and Signal Processing*, 23(1):195–216, 2009. 110, 125

[148] G. Kerschen, A. F. Vakakis, Y. S. Lee, D. McFarland, J. Kowtko, and L. Bergman. Energy transfers in a system of two coupled oscillators with essential nonlinearity: 1:1 resonance manifold and transient bridging orbits. *Nonlinear Dynamics*, 42(3):283–303, 2005. 110

[149] Bruno Cochelin and Christophe Vergez. A high order purely frequency-based harmonic balance formulation for continuation of periodic solutions. *Journal of Sound and Vibration*, 324(1-2):243–262, 2009. 110

[150] O. Gendelman, Y. Starosvetsky, and M. Feldman. Attractors of harmonically forced linear oscillator with attached nonlinear energy sink i: Description of response regimes. *Nonlinear Dynamics*, 51(1):31–46, 2008. 111, 143

[151] Y. Starosvetsky and O. Gendelman. Attractors of harmonically forced linear oscillator with attached nonlinear energy sink. ii: Optimization of a nonlinear vibration absorber. *Nonlinear Dynamics*, 51(1):47–57, 2008. 111, 143

[152] A. I. Musienko, C. H. Lamarque, and L. I. Manevitch. Design of mechanical energy pumping devices. *Journal of Vibration and Control*, 12(4):355–371, 2006. 111

[153] E. Gourdon and C. H. Lamarque. Nonlinear energy sink with uncertain parameters. *Journal of Computational and Nonlinear Dynamics*, 1(3):187–195, 2006. 111

[154] A. Kozmin, Y. Mikhlin, and C. Pierre. Localization of energy in nonlinear systems with two degrees of freedom. *International Applied Mechanics*, 43(5):568–576, 2007. 111

[155] E. Gourdon, N. A. Alexander, C. A. Taylor, C. H. Lamarque, and S. Pernot. Nonlinear energy pumping under transient forcing with strongly nonlinear coupling: Theoretical and experimental results. *Journal of Sound and Vibration*, 300(3):522–551, 2007. 111

[156] D. M McFarland, L. A. Bergman, and A. F. Vakakis. Experimental study of non-linear energy pumping occurring at a single fast frequency. *International Journal of Non-Linear Mechanics*, 40(6):891–899, 2005. 111

[157] G. Kerschen, D. M. McFarland, J. J. Kowtko, Y. S. Lee, L. A. Bergman, and A. F. Vakakis. Experimental demonstration of transient resonance capture in a system of two coupled oscillators with essential stiffness nonlinearity. *Journal of Sound and Vibration*, 299(4-5):822–838, 2007. 111

[158] Y. S. Lee, A. F. Vakakis, L. A. Bergman, D. M. McFarland, and G. Kerschen. Suppression of aeroelastic instability by means of broadband passive targeted energy transfers, part i: Theory. *AIAA journal*, 45(3):693–711, 2007. 111

[159] Y. S. Lee, G. Kerschen, D. M. McFarland, A. F. Vakakis, L. A. Bergman, and N. van de Wouw. Suppression of aeroelastic instability by means of broadband passive targeted energy transfers, part ii: experiments. *AIAA journal*, 45:2391–2400, 2007. 111, 112, 185

[160] B. Cochelin, P. Herzog, and P.-O. Mattei. Experimental evidence of energy pumping in acoustics. *Comptes Rendus Mecanique*, 334(11):639–644, 2006. 112

[161] R. Viguié. *Tuning Methodology of Nonlinear Vibration Absorbers Coupled to Nonlinear Mechanical Systems*. PhD thesis, University of Liege, 2010. 112

[162] G. Kerschen R. Viguié and M. Ruzzene. Exploration of nonlinear shunting strategies as effective vibration absorbers. In *SPIE conference on Smart Structures and Materials Nondestructive Evaluation and Health Monitoring*, San Diego, USA, 2009. SPIE. 112

[163] R. E. Mickens. *An introduction to nonlinear oscillations*. Cambridge University Press, Cambridge [Eng.]; New York, 1981. 113

[164] W. Szemplinska-Stupnicka. *The Behavior of nonlinear vibrating systems. I, Fundamental concepts and methods - applications to single-degree-of-freedom systems*. Kluwer Academic, London, 1990. 113

[165] R. Subbiah and N. F. Rieger. On the transient analysis of rotor-bearing systems. *Journal of Vibration Acoustics Stress and Reliability in Design*, 110(4):515–520, 1988. 113

[166] W. Szemplinska-Stupnicka. *The behavior of nonlinear vibrating systems. II. Advanced concepts and applications to multi-degree-of-freedom systems*. Kluwer, Dordrecht, 1990. 113

[167] A. Nassirharand. *Computer-aided nonlinear control system design using describing function models*. Springer, London, 2011. 113

[168] C. S. Hsu. *Cell-to-cell mapping : a method of global analysis for nonlinear systems*. Springer-Verlag, New York, 1987. 113

[169] T. M. Cameron and J. H. Griffin. An alternating frequency/time domain method for calculating the steady-state response of nonlinear dynamic systems. *Journal of Applied Mechanics*, 56(1):149–154, 1989. 117

[170] J. Y. Zhao, I. W. Linnett, and L. J. McLean. Stability and bifurcation of unbalanced response of a squeeze film damped flexible rotor. *Journal of Tribology*, 116(2):361–368, 1994. 118

[171] M. Guskov. *Dynamique non-linéaire des systèmes multi-rotors. Etudes numérique et expérimentale.* PhD thesis, Ecole Centrale de Lyon, 2007. 118, 128

[172] A. H. Nayfeh and B. Balachandran. *Applied nonlinear dynamics: analytical, computational, and experimental methods.* Wiley, New York, 1995. 118, 124

[173] R. Seydel. *Practical bifurcation and stability analysis : from Equilibrium to chaos.* Springer, New York, 1995. 118, 122

[174] G. Von Groll and D. J. Ewins. The harmonic balance method with arc-length continuation in rotor/stator contact problems. *Journal of Sound and Vibration*, 241(2):223–233, 2001. 127

[175] A. Lazarus and O. Thomas. A harmonic-based method for computing the stability of periodic solutions of dynamical systems. *Comptes Rendus Mecanique*, 338(9):510–517, 2010. 128

[176] E. E. Gluskin. A nonlinear resistor and nonlinear inductor using a nonlinear capacitor. *Journal of The Franklin Institute*, 336(7):1035–1047, 1999. 130

[177] Aurelien Grolet and Fabrice Thouverez. Vibration analysis of a nonlinear system with cyclic symmetry. *Journal of Engineering for Gas Turbines and Power*, 133(2):022502, 2011. 137

[178] Y. Starosvetsky and O. V. Gendelman. Response regimes of linear oscillator coupled to nonlinear energy sink with harmonic forcing and frequency detuning. *Journal of Sound and Vibration*, 315(3):746–765, 2008. 142

[179] J. L. Summers. Variable-coefficient harmonic balance for periodically forced nonlinear oscillators. *Nonlinear Dynamics*, 7(1):11–35, 1995. 145

[180] F. Schilder, W. Vogt, S. Schreiber, and H. M. Osinga. Fourier methods for quasi-periodic oscillations. *International Journal for Numerical Methods in Engineering*, 67(5):629–671, 2006. 145

[181] N. Coudeyras, J. J. Sinou, and S. Nacivet. A new treatment for predicting the self-excited vibrations of nonlinear systems with frictional interfaces:

The constrained harmonic balance method, with application to disc brake squeal. *Journal of Sound and Vibration*, 319(3-5):1175–1199, 2009. 148

[182] J. J. Sinou, F. Thouverez, and L. Jezequel. Stability analysis and non-linear behaviour of structural systems using the complex non-linear modal analysis (cnlma). *Computers and Structures*, 84(29-30):1891–1905, 2006. 149

[183] Y.S. Lee, G. Kerschen, A. F. Vakakis, P. Panagopoulos, L. Bergman, and D. M. McFarland. Complicated dynamics of a linear oscillator with a light, essentially nonlinear attachment. *Physica D: Nonlinear Phenomena*, 204(1-2):41–69, 2005. 152

[184] D. Laxalde and F. Thouverez. Complex non-linear modal analysis for mechanical systems: Application to turbomachinery bladings with friction interfaces. *Journal of Sound and Vibration*, 322(4-5):1009–1025, 2009. 152

[185] D. Laxalde, F. Thouverez, and J. J. Sinou. Dynamics of a linear oscillator connected to a small strongly non-linear hysteretic absorber. *International Journal of Non-Linear Mechanics*, 41(8):969–978, 2006. 152

[186] C. Gibert. Fitting measured frequency response using non-linear modes. *Mechanical Systems and Signal Processing*, 17(1):211–218, 2003. 153

[187] C. Gibert. *Analyse modale non linéaire expérimentale*. PhD thesis, Ecole Centrale de Lyon, 2001. 153

[188] G. Kerschen, J. Kowtko, D. M. McFarland, L.A. Bergman, and A.F. Vakakis. Theoretical and experimental study of multimodal targeted energy transfer in a system of coupled oscillators. *Nonlinear Dynamics*, 47(1-3):285–309, 2007. 156, 186

[189] M. Gruin. *Dynamique non-linéaires d'une roue de turbine basse pression soumise à des excitation structural d'un turboréacteur*. PhD thesis, Ecole Centrale de Lyon, 2011. 161

dernière page de la thèse

AUTORISATION DE SOUTENANCE

Vu les dispositions de l'arrêté du 7 août 2006,

Vu la demande du Directeur de Thèse

Monsieur F. THOUVEREZ

et les rapports de

Monsieur G. KERSCHEN
Professeur - Université de Liège - LTAS - chemin des Chevreuils, 1 - Bât. B52 - B-4000 LIEGE 1 BELGIQUE

Et de

Monsieur L. PANNING-VON SCHEIDT
Professeur - Gottfried Wilhelm Leibniz Universität Hannover - Institut für Dynamik und Schwingungen Appelstrasse 11 - D-3067 HANNOVER

Monsieur ZHOU Biao

est autorisé à soutenir une thèse pour l'obtention du grade de **DOCTEUR**

Ecole doctorale MECANIQUE, ENERGETIQUE, GENIE CIVIL ET ACOUSTIQUE

Fait à Ecully, le 27 novembre 2012

P/Le directeur de l'E.C.L.
La directrice des Etudes

M-A. GALLAND